

2006

## Numerical and analytical techniques in modeling nonlinear dispersive media: emphasis on NLS type equations

Georges Nehmetallah  
*University of Dayton*

Follow this and additional works at: [https://ecommons.udayton.edu/graduate\\_theses](https://ecommons.udayton.edu/graduate_theses)

---

### Recommended Citation

Nehmetallah, Georges, "Numerical and analytical techniques in modeling nonlinear dispersive media: emphasis on NLS type equations" (2006). *Graduate Theses and Dissertations*. 4650.  
[https://ecommons.udayton.edu/graduate\\_theses/4650](https://ecommons.udayton.edu/graduate_theses/4650)

This Dissertation is brought to you for free and open access by the Theses and Dissertations at eCommons. It has been accepted for inclusion in Graduate Theses and Dissertations by an authorized administrator of eCommons. For more information, please contact [mschlange1@udayton.edu](mailto:mschlange1@udayton.edu), [ecommons@udayton.edu](mailto:ecommons@udayton.edu).

**Numerical and Analytical Techniques in Modeling Nonlinear  
Dispersive Media: Emphasis on NLS Type Equations**

**DISSERTATION**

**Submitted to**

**The School of Engineering of the**

**UNIVERSITY OF DAYTON**

**In Partial Fulfillment of the Requirements for**

**The Degree**

**Doctor of Philosophy in Electrical Engineering**

**By**

**Georges Nehmetallah**


**UNIVERSITY OF DAYTON**

**Dayton, Ohio**

**August, 2006**

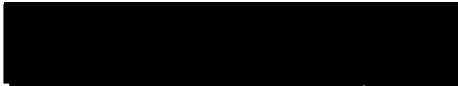
# **Numerical and Analytical Techniques in Modeling Nonlinear Dispersive Media: Emphasis on NLS Type Equations**

**APPROVED BY:**



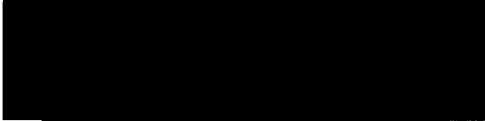
---

**Partha P. Banerjee, Ph.D.**  
Advisory Committee Chairman  
Professor  
Electrical and Computer Engineering




---

**Monish Chatterjee, Ph.D.**  
Committee member  
Professor  
Electrical and Computer




---

**Youssef Raffoul, Ph.D.**  
Committee member  
Associate Professor  
Mathematics Department



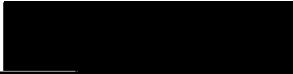
---

**Frank Scarpino, Ph.D.**  
Committee member  
Professor  
Electrical and Computer




---

**Malcolm Daniels, Ph.D.**  
Chair, Electrical and Computer  
Engineering Department



---

**Donald L. Moon, Ph.D.**  
Associate Dean  
Graduate Engineering Programs & Research  
School of Engineering



---

**Joseph E. Saliba, Ph.D, P.E.**  
Dean, School of Engineering

## ABSTRACT

The purpose of the proposed work is to develop new numerical and analytical techniques applied to different partial differential equations (PDEs) modeling wave propagation in nonlinear dispersive (or diffractive) environments and compare the results with classical methods that exist in the literature. Examples of PDEs include the nonlinear Schrödinger (NLS) and Gross-Pitaevskii (GP) family of equations, since they model soliton propagation in fibers, self-focusing of beams, optical shocks, optical “bullets”, and the Bose-Einstein condensates (BEC) dynamics in the mean field approximation in 2 and 3D lattices.

Traditional numerical techniques used to tackle these nonlinear PDEs, like the NLS and GP equations, which model pulse and beam propagation in fiber and Kerr bulk media, and periodic lattices, range from separation of variables, finite difference (FD), perturbation, to methods of weighted residuals (MWR). These traditional techniques fail to track sharp slopes and periodic focusing and defocusing of beams due to their lack of adaptability, computational complexity and large computational times. Also, exact analytical techniques are often unavailable because these types of equations are not integrable in higher dimensions, so approximate analytical techniques based on the variational methods and Kapitza approximation are sought. This study is motivated from the need of soliton stabilization during propagation in D-dimensions. Stabilization may be achieved by (a) incorporating the non-paraxial approximation, (b) including saturating

nonlinearity, (c) dispersion management (DM) through alternating layered structures of the local group velocity dispersion (GVD), or (d) nonlinearity management (NLM) through modulation of the nonlinearity based on periodically alternating self-focusing (SF) and self-defocusing (SDF) layers, or even periodic SF layers with different values of the Kerr coefficient. In 1-D, the purpose of DM is to reduce radiation from the pulse due to amplifiers compensating fiber loss, modulation instability reduction in bandwidth and in gain, jitters due to signal collisions in different channels of wavelength division multiplexed systems, etc. In Kerr type media, there are no stable solitons in 2 or 3 D, and optical bullets eventually collapse. The same can be said about 2 and 3-D BECs, where NLM can be achieved through periodic modulation of the sign of the nonlinearity in time via the Feshback resonance in the GP equation.

In this work we develop new adaptive wavelet transform (AWT) for 1-D NLS and compared the results with FFT, FD and FEM methods. The nonlinear effects considered were self-steepening, third order nonlinearity, and DM. Also, we develop new adaptive split step Fourier Bessel transform (ASSFBT) methods, for 2 and 3-D NLS, to investigate pulse, beam and optical bullets propagation in waveguides and bulk media, and self-focusing of beams to distances very close to the point of collapse, a feature that has not been achievable by existing classical methods was considered. Moreover, we investigate soliton stabilization effects in 2 and 3-D by using the Kapitza approximation and numerically by using the above numerical methods. Cases considered were nonparaxial beams and media containing saturating nonlinearity, periodic nonlinearity and D-dimensional DM.

## ACKNOWLEDGMENTS

First, I would like to thank my family for their continual love, support, and understanding during my studying period all my life till now. Also, I would like to thank all my friends during my stay in Dayton, namely Youssef Dib, Morad El-saleh, Aziz Mahfoud, Prathan Buranasiri, which made my life easier, happier and kept me company, and of course our valuable scientific debates.

Also, I would like to thank my advisor Prof. Partha Banerjee for his continual support and his vast knowledge and expertise in different areas, for without him the completion of my dissertation would have been impossible. Also, I would like to thank Prof. Monish Chatterjee for his time and valuable comments and suggestions during different stages of the work. Moreover, I would like to thank Prof. Frank Scarpino for introducing me to wavelets in his valuable course in which it was a great help to me in my dissertation. Also, I would like to thank Prof. Joe Haus, Prof. Qiwen Zhan and Prof. Andrew Sarangan for their help in my coarse work and their time, even when I wasn't registered in some of their classes, and their big heart and vast knowledge and experience, which I benefited from a lot. Last but not least, I would like to thank Prof. Youssef Raffoul for his caring, both in the personal and academic life, and for his important mathematics courses I took under him which helped me greatly during my dissertation.

Finally, I would like to thank Dr. Malcolm Daniels, Dr. Joseph Saliba and the University of Dayton for giving the opportunity for foreign students to pursue their studies and dreams, in a caring, well understanding environment, where a lot of financial opportunities and assistantships are offered to students according to their academic standards and needs without prejudice and discrimination, namely the DAGSI scholarship, which I greatly benefited from during my stay at the University of Dayton.

# TABLE OF CONTENTS

	Page
ABSTRACT.....	iii
ACKNOWLEDGEMENTS.....	v
LIST OF TABLES.....	xii
LIST OF FIGURES.....	xiii
LIST OF SYMBOLS.....	xxii.
LIST OF ACRONYMS.....	xxxiii
CHAPTERS:	
1. INTRODUCTION: THEORY AND BJECTIVES.....	1
1.1 Introduction.....	1
1.2 PDEs Analyzed in this Work.....	4
1.2.1 The Heat Equation.....	6
1.2.2 The First Order Nonlinear Kinematic Equation.....	6
1.2.3 The Burger's Equation.....	7
1.2.4 The KdV Equation.....	7
1.2.5 Pulse Propagation in Fiber: The 1-D NLS Equation.....	8
1.2.6 Beam Propagation in Bulk Media: Self-focusing.....	11
1.2.7 Nonparaxial Assumption in the NLS Equation.....	16
1.2.8 Beam Propagation in Saturating Nonlinearity.....	17
1.2.9 Dispersion Management in D-dimensions.....	18
1.2.10 Nonlinearity Management in D-dimensions.....	19
1.2.11 Self-Steepening and Raman Scattering Phenomena.....	20



1.3	Organization of the Dissertation.....	22
1.4	What is New in this Work.....	23
2.	CLASSICAL NUMERICAL METHODS: A REVIEW.....	24
2.1	Introduction.....	24
2.2	Application.....	25
2.3	Summary.....	28
3.	BASIC WAVELET THEORY AND APPLICATION TO PDEs.....	31
3.1	Introduction.....	31
3.2	Multi-Resolution Analysis.....	33
3.3	Evaluation of Connection Coefficients.....	36
3.4	Wavelet Method for Solving Some of the Classical PDEs.....	39
3.4.1	The Heat Equation (HE).....	40
3.4.2	The First Order Nonlinear Wave Equation.....	42
3.4.3	The Burger's Equation.....	45
3.4.4	The KdV Equation.....	45
3.4.5	The 1-D NLS Equation.....	47
3.4.6	The 2-D NLS or Self-Focusing Equation.....	54
3.4.7	The Self-steepening Equation.....	57
3.5	Summary.....	58
4.	HANKEL OR FOURIER BESSEL TRANSFORM METHODS.....	61
4.1	Introduction.....	61
4.2	Calculation of the Fourier Bessel Transform.....	65
4.2.1	Siegman's or Magni's Method.....	65
4.2.2	Yu or Guizar's Method.....	67
4.2.3	Ferrari's Method.....	68

4.3	Summary.....	69
5.	VARIATIONAL METHOD.....	70
5.1	Introduction.....	70
5.2	Summary.....	73
6.	FOCUSING ARREST MECHANISMS.....	74
6.1	Introduction.....	74
6.2	Nonparaxiality.....	75
6.2.1	Introduction.....	75
6.2.2	Beam Collapse.....	76
6.2.3	Adaptive Hankel Split Step Method.....	79
6.2.4	Numerical Results and Conclusions.....	80
6.3	Saturating Nonlinearity.....	84
6.3.1	Introduction.....	87
6.3.2	Spatio-Temporal Collapse.....	89
6.3.3	Saturating Nonlinearity and Optical Bullets.....	93
6.3.4	Adaptive Spherical Fourier Bessel Split Step Method.....	96
6.3.5	Numerical Results and Conclusions.....	96
6.4	Summary.....	97
7.	DISPERSION MANAGEMENT IN 1, 2 AND 3-D.....	101
7.1	Introduction.....	101
7.2	Dispersion Management in 1-D.....	101
7.2.1	Introduction.....	102
7.2.2	Variational Technique.....	104
7.2.2.1	Weak Nonlinearity.....	108
7.2.2.2	Strong Nonlinearity.....	110
7.2.3	Adaptive Wavelet Method.....	113

7.2.4	Numerical Results and Conclusion.....	115
7.3	Dispersion Management in 2 and 3 –D.....	126
7.3.1	Introduction.....	126
7.3.2	Variational Technique.....	129
7.3.3	Adaptive Fast Hankel Split Step Method.....	140
7.3.4	Numerical Results and Conclusion.....	140
7.4	Summary.....	151
8.	NONLINEARITY MANAGEMENT IN 2 AND 3-D.....	153
8.1	Introduction.....	153
8.2	Variational Technique.....	157
8.3	Adaptive Fast Hankel Split Step Method.....	164
8.4	Numerical Results.....	164
8.5	Summary.....	172
9.	CONCLUSION AND FUTURE WORK.....	173
9.1	Conclusions.....	173
9.2	Future Work.....	174
	REFERENCES.....	176
	APPENDICES:	
A.	USEFUL HANKEL TRANSFORM PROPERTIES.....	186
B.	MATLAB CODE.....	188
B.1	Wavelet Transform Codes.....	188
B.1.1	NLS Equation in 1-D.....	188
B.1.2	NLS Equation in 2-D: Self-focusing Phenomena.....	191
B.1.3	Self-steepening Equation.....	196
B.1.4	Dispersion Management in 1-D.....	199

B.2	Fourier Bessel Transform Codes.....	202
B.2.1	Non-paraxial NLS Equation.....	202
B.2.2	Saturating Nonlinearity Equation.....	204
B.2.3	Dispersion Management in 2 and 3D.....	206
B.2.3.1	2D Case.....	206
B.2.3.2	3D Case.....	209
B.2.4	Nonlinearity Management in 2 and 3-D.....	211
B.2.4.1	2D Case.....	211
B.2.4.2	3D Case.....	213

## LIST OF TABLES

Table 3.1	Some of the wavelet families and their associated properties.....	36
Table 9.1	Plan for future work.....	175

## LIST OF FIGURES

Figure 1.1	Dispersion curve in fibers.....	10
Figure 1.2	Townes soliton profiles.....	14
Figure 1.3	(a) Initial Gaussian profile. (b) Self-focusing of a beam after some time..	15
Figure 1.4	Optical bullet propagation.....	16
Figure 1.5	Townes soliton profiles for $D=1, 2, 3$ .....	16
Figure 1.6	Schematic of Self-steepening.....	21
Figure 2.1	Classical numerical methods diagram related to AWT method.....	25
Figure 2.2	SSFFT algorithm for 1-D NLS.....	29
Figure 2.3	SSFFT algorithm for 2-D NLS.....	30
Figure 3.1	Wavelet transform use and properties.....	31
Figure 3.2	MRA diagram.....	34
Figure 3.3	(a) Symlet (Sym4) scaling function and (b) Sym4 wavelet function.....	35
Figure 3.4	(a) Low pass reconstruction filter $h(k)$ and (b) High pass reconstruction filter $g(k)$ .....	35
Figure 3.5	(a) Initial function profile, (b) Wavelet scaling functions at level $J$ , (c) approximated function using $a_{J,l}$ 's as expansion coefficients.....	40
Figure 3.6	Heat equation evolution with time.....	42
Figure 3.7	First order nonlinear kinematic equation at times (a) 0.5, (b) 0.7.....	44
Figure 3.8	Burger's equation evolution at time $t=1$ (a) $\alpha = 0.05$ , (b) $\alpha = 0.01$ .....	46

Figure 3.9	The KdV evolution equation with a soliton initial condition.....	47
Figure 3.10	Wavelet method algorithm for 1-D NLS.....	49
Figure 3.11	First order 1-D soliton evolution using the wavelet method.....	50
Figure 3.12	Exponential input to the 1-D NLS equation using the wavelet method...	50
Figure 3.13	2 <sup>nd</sup> order soliton propagation and amplitude variation using the wavelet method at times (a) 0.75, (b) 2 (c) On-axis amplitude variation,(d) 3-D view.....	53
Figure 3.14	Wavelet method algorithm for 2-D NLS.....	55
Figure 3.15	Self-focusing wavelet approximation method, (a) 3 <sup>rd</sup> level, (b) 5 <sup>th</sup> level..	56
Figure 3.16	Wavelet method algorithm for self-steepening equation.....	58
Figure 3.17	Evolution of optical shocks using self-steepening Eq. , at (a) $\xi = 0.005$ , (b) $\xi = 0.5$ .....	59
Figure 4.1	The AFHSS algorithm, a symmetrized version of the split step FFT using cylindrical or spherical Fourier Bessel transform instead, and using adaptive longitudinal stepping and transverse grid management.....	62
Fig. 6.1	The AFHSS algorithm, a symmetrized version of the split step FFT using Hankel transform instead, and using adaptive longitudinal stepping and transverse grid management.....	81
Fig. 6.2	Maximal focusing as a function of grid size.....	84
Fig. 6.3	On-axis intensity of $\tilde{u}_{e0} = 4e^{-r^2/2}$ as a function of propagation for fixed values of $\varepsilon$ ranging from $10^{-2}$ to $10^{-8}$ where $z = z_c = 0.1481$ for $\varepsilon = 10^{-8}$ , and for an adaptive $\varepsilon$ varying as $\varepsilon = (\lambda/4\pi r)^2$ , using AFHSS with $S = 2\pi R_1 R_2 = 2\pi \times 2000$ (4000 cylindrical samples).	

	$\lambda$ in inset is normalized to $r_0$ .....	85
Fig. 6.4	On-axis intensity of $\tilde{u}_{e0} = 4e^{-r^2}$ as a function of propagation for fixed values of $\varepsilon$ ranging from $10^{-2}$ to $10^{-8}$ where $z = z_c = 0.1461$ for $\varepsilon = 10^{-8}$ , and for an adaptive $\varepsilon$ varying as $\varepsilon = (\lambda/4\pi r)^2$ using AFHTSS with $S = 2\pi R_1 R_2 = 2\pi \times 2000$ (4000 cylindrical samples). $\lambda$ in inset is normalized to $r_0$ .....	85
Fig. 6.5	On-axis intensity of $\tilde{u}_{e0} = 4e^{-r^2/2}$ as a function of propagation for fixed values of $\varepsilon$ ranging from $10^{-2}$ to $10^{-8}$ where $z = z_c = 0.1581$ for $\varepsilon = 10^{-8}$ , and for an adaptive $\varepsilon$ varying as $\varepsilon = (\lambda/4\pi r)^2$ , using AFFSS with $1024^2$ samples. $\lambda$ in inset is normalized to $r_0$ .....	86
Fig. 6.6	On-axis intensity of $\tilde{u}_{e0} = 4e^{-r^2}$ as a function of propagation for fixed values of $\varepsilon$ ranging from $10^{-2}$ to $10^{-8}$ where $z = z_c = 0.15596$ for $\varepsilon = 10^{-8}$ , and for an adaptive $\varepsilon$ varying as $\varepsilon = (\lambda/4\pi r)^2$ using AFFSS with $1024^2$ samples. $\lambda$ in inset is normalized to $r_0$ .....	86
Fig. 6.7	Radial dependence of the self-trapped normalized field in 1, 2, 3 transverse dimensions.....	91
Fig. 6.8	Stability regions for the 2 and 3 D spatiotemporal solitons in saturating nonlinearity medium.....	95
Fig. 6.9	The AFBSS algorithm, a symmetrized version of the split step FFT using spherical Fourier Bessel transform instead, and using adaptive longitudinal stepping and transverse grid management..	98



Fig. 6.10	Stable light-bullet generation with initial focusing for $N_0 = 50, A_0^2 = 0.4$ , $w_0 = 5, w_e < w_H < w_0 \Rightarrow H < 0$ .....99
Fig. 6.11	Stable light-bullet generation with initial defocusing for $w_0 = 3.684$ , $N_0 = 50, A_0^2 = 1, w_H < w_0 < w_e \Rightarrow H < 0$ .....99
Fig. 6.12	Stable light-bullet generation with initial focusing for $N_0 = 50, A_0^2 = 0.36$ , $w_0 = 4.8, w_e < w_0 < w_H \Rightarrow H > 0$ .....100
Fig. 7.1	Adaptive wavelet transform (AWT) method for DMS.....119
Fig. 7.2	Comparison between on-axis pulse amplitude using the AWT and FFT techniques when propagating according to the accompanying dispersion map and initial conditions.....120
Fig. 7.3	Variation of the on-axis pulse amplitude for two different pulses where $f = [-2, 2]$ and an increasing nonlinearity coefficient using the AWT techniques when propagating according to the accompanying dispersion map and initial conditions.....120
Fig. 7.4	Variation of the on-axis pulse amplitude for two different pulses where $f = [-4, 4]$ and an increasing nonlinearity coefficient using the AWT techniques when propagating according to the accompanying dispersion map and initial conditions.....121
Fig. 7.5	Variation of the on-axis pulse amplitude for two different dispersion maps and an increasing nonlinearity coefficient when the initial pulse $\tilde{u}_e = \exp(-2\tau^2)$ using the AWT techniques when propagating according to the accompanying dispersion maps and initial conditions.....121

Fig. 7.6	Variation of the on-axis pulse amplitude for two different dispersion maps amplitude keeping the same period and an increasing nonlinearity coefficient with the initial pulse $\tilde{u}_e = \exp(-\tau^2)$ using the AWT techniques when propagating according to the accompanying dispersion maps and initial conditions.....	122
Fig. 7.7	Comparison between on-axis pulse amplitude using the AWT and FFT techniques when propagating according to the accompanying dispersion map and initial conditions as found in Kutz et al [63] .....	122
Fig. 7.8	Variation of the on-axis pulse amplitude for two different dispersion map periods keeping the same amplitude in the anomalous dispersion regime with the initial pulse $\tilde{u}_e = \exp(-\tau^2)$ using the AWT techniques when propagating according to the accompanying dispersion maps and initial conditions.....	123
Fig. 7.9	Variation of the on-axis pulse amplitude for two different dispersion map periods keeping the same amplitude with the initial pulse $\tilde{u}_e = \exp(-\tau^2)$ using the AWT techniques when propagating according to the accompanying dispersion maps and initial conditions. The first two are in the AD regime and the third one is in the normal regime.....	123
Fig. 7.10	Variation of the on-axis pulse amplitude for two different dispersion map periods, keeping the same amplitude in the anomalous dispersion regime according to condition in Section 7.2.2.2, with the initial pulse $\tilde{u}_e = \exp(-\tau^2)$ , using the AWT techniques according to the accompanying initial conditions.....	124

- Fig. 7.11 Variation of the on-axis pulse amplitude for three different dispersion map periods, keeping the same amplitude in the anomalous dispersion regime according to condition in Section 7.2.2.2, with the initial pulse  $\tilde{u}_e = 2 \exp(-\tau^2)$ , using the AWT techniques according to the accompanying initial conditions.....124
- Fig. 7.12 Variation of the on-axis pulse amplitude for three different dispersion Map amplitudes, keeping the same period in the anomalous dispersion regime according to condition in Section 7.2.2.2, with different initial pulses, using the AWT techniques according to the accompanying initial conditions.....125
- Fig. 7.13 Variation of the on-axis pulse amplitude for three different dispersion map periods, keeping the same amplitude in the normal dispersion regime contradicting the condition in 7.2.2.2, using the AWT techniques according to the accompanying same initial conditions.....125
- Fig. 7.14 The AFHSS algorithm, a symmetrized version of the split step FFT Using cylindrical or spherical Fourier Bessel transform instead, and using adaptive longitudinal stepping and transverse grid management..143
- Fig. 7.15 (a), (b) and (c) on-axis amplitude stable 2-D soliton evolution through the sign alternating dispersion when  $D=2$  with the parameters  $f = [-1, 2]$ ,  $\Delta z = 0.001$ ,  $M = 4000$ ,  $A_0 = 1.5$ ,  $w_0 = 1$ , for different values of the dispersion period ranging from  $L = 0.004$  to  $L = 0.2$ , using AFHSS with  $\tilde{S} = 2\pi R_1 R_2 = 2\pi \times 200$  (400 cylindrical samples)..144
- Fig. 7.16 Stable 2-D soliton generation through the sign alternating dispersion.

	3(a) shows the pulse evolution with the parameters $M = 8000$ , $f = [-1, 2], \Delta z = 0.001, A_0 = 1.5, w_0 = 1, L = 0.04$ . 3(b) shows the on-axis amplitude for both the AFFSS and the AFHSS methods for the same parameters, using AFHSS with $\tilde{S} = 2\pi R_1 R_2 = 2\pi \times 200$ (400 cylindrical samples) ..... 145
Fig. 7.17	Stable 2-D soliton generation through the sign alternating dispersion. 4(a) shows the pulse evolution with the parameters $M = 8000$ $f = [-2, 4], \Delta z = 0.001, A_0 = 2, w_0 = 1, L = 0.002$ . 4(b) shows the on- axis amplitude for the AFHSS methods for the same parameters, using AFHSS with $\tilde{S} = 2\pi R_1 R_2 = 2\pi \times 200$ (400 cylindrical samples).....146
Fig. 7.18	(a-c) shows the comparison of the on-axis amplitude between the AFFSS and the AFHSS for the parameters shown in each inset, using AFHSS with $\tilde{S} = 2\pi R_1 R_2 = 2\pi \times 200$ (400 cylindrical samples), and $N^2 = (2^8)^2$ for the AFFSS 2D mesh.....147
Fig. 7.19	Stable 3-D soliton generation through the sign alternating dispersion when $f = [-2, 4], \Delta z = 0.005, M = 4000, A_0 = 0.2, w_0 = 15, L = 4$ , using AFHSS with $\tilde{S} = 2\pi R_1 R_2 = 2\pi \times 800$ (1600 radial samples). (6a) is pulse evolution. (6b) is on-axis amplitude.....148
Fig. 7.20	Stable 3-D soliton generation through the sign alternating dispersion When $f = [-2, 4], \Delta z = 0.005, M = 7200, A_0 = 1, w_0 = 5, L = 0.015$ , using AFHSS with $\tilde{S} = 2\pi R_1 R_2 = 2\pi \times 800$ (1600 radial samples). (7a) is pulse evolution. (7b) is on-axis amplitude.....149

Fig. 7.21	Decay of a 3-D optical pulse when $w_0 = 5$ , $L = 0.01$ , $f = [2, -4]$ , $\Delta z = 0.005$ , $M = 1200$ , $A_0 = 2$ , using AFHSS with $\tilde{S} = 2\pi R_1 R_2$ $= 2\pi \times 800$ (1600 radial samples). (8a) is pulse evolution. (8b) is on-axis amplitude.....	150
Fig. 7.22	Collapse of a 3-D optical pulse when $f = [2, -5]$ , $\Delta z = 0.005$ , $M = 1800$ , $A_0 = 1$ , $w_0 = 10$ , $L = 0.015$ , using AFHSS with $\tilde{S} = 2\pi R_1 R_2 = 2\pi \times 800$ (1600 radial samples). (9a) is pulse evolution. (9b) is on-axis amplitude.....	151
Fig. 8.1	The AFHSS algorithm, a symmetrized version of the split step FFT using cylindrical or spherical Fourier Bessel transform instead, and using adaptive longitudinal stepping and transverse grid management..	167
Fig. 8.2	Stable 2-D soliton generation through the sign alternating nonlinearity when $\Delta z = 0.01$ , $A_0 = 0.2$ , $w_0 = 10$ , $g_0 = 0.5$ , $g_1 = -1.5$ , $L_+ = L_- = 0.1$ , using AFHSS with $\tilde{S} = 2\pi R_1 R_2 = 2\pi \times 800$ (1600 cylindrical samples).....	168
Fig. 8.3	Stable 2-D soliton generation through the sign Alternating nonlinearity when $\Delta z = 0.01$ , $A_0 = 2.1$ , $w_0 = 1$ , $g_0 = 1$ , $g_1 = -2$ , $L_+ = L_- = 0.01$ , using AFHSS with $\tilde{S} = 2\pi R_1 R_2 = 2\pi \times 800$ (1600 cylindrical samples).....	168
Fig. 8.4	Decay of 2-D beams when $\Delta z = 0.01$ , $A_0 = 1$ , $w_0 = 1$ , $g_0 = 1.7$ , $g_1 = -2.7$ , $L_+ = L_- = 0.4$ , using AFHSS with $\tilde{S} = 2\pi R_1 R_2 = 2\pi \times 800$ (1600 cylindrical samples).....	169

- Fig. 8.5 Self-focusing of a 2-D optical pulse when  $g_I = -0.5$ ,  $L_+ = L_- = 0.1$ ,  
 $\Delta z = 0.01$ ,  $A_0 = 3$ ,  $w_0 = 1$ ,  $g_0 = 1.5$ , using AFHSS with  
 $\tilde{S} = 2\pi R_1 R_2 = 2\pi \times 800$  (1600 radial samples).....169
- Fig. 8.6 The variation of the main beam ( $D=2$ ) period  $\Lambda_z$  with respect to the  
nonlinearity map period  $L = [0.02, 0.04, 0.08, 0.16, 0.32]$ , for different  
initial width ranging from  $w_0 = [1, 1.5, 2, 2.5]$  keeping the same initial  
beam power  $N_0$ . Superposed on the data are empirical fits of the form  
 $\Lambda_z = c_1 + c_2 L^n$  obtained through fitting the first, third and fifth points  
for each  $w_0$  .....170
- Fig. 8.7 Stable 3-D soliton generation through the sign Alternating nonlinearity  
when  $\Delta z = 0.01$ ,  $A_0 = 0.18$ ,  $w_0 = 10$ ,  $g_0 = 1$ ,  $g_I = -4$ ,  $L_+ = L_- = 0.2$ ,  
using AFHSS with  $\tilde{S} = 2\pi R_1 R_2 = 2\pi \times 800$  (1600 radial samples).....170
- Fig. 8.8 Self-focusing of a 3-D optical pulse when  $g_I = -1$ ,  $L_+ = L_- = 0.2$ ,  
 $\Delta z = 0.01$ ,  $A_0 = 0.5$ ,  $w_0 = 5$ ,  $g_0 = 1$ , , using AFHSS with  
 $\tilde{S} = 2\pi R_1 R_2 = 2\pi \times 800$  (1600 radial samples) ..... 171
- Fig. 8.9 Decay of a 3-D optical pulse when  $\Delta z = 0.01$ ,  $A_0 = 1$ ,  $w_0 = 10$ ,  $g_0 = -1$ ,  
 $g_I = -4$ ,  $L_+ = L_- = 0.2$ , using AFHSS with  $\tilde{S} = 2\pi R_1 R_2 = 2\pi \times 800$   
(1600 radialsamples).....171

## LIST OF SYMBOLS

Symbol	Definition
$v_p$	Nonlinear Phase velocity
$v_{p0}$	Linear Phase velocity
$u$	Base band wave
$Z, T, X, Y$	Propagation, time, and transverse dimension variables of base band signal
$Z', T', X', Y', r'$	Propagation, time and transverse and radial dimension variables in a moving frame of reference
$x, \tau, x, y, r$	Propagation, time, transverse and radial dimension variables of normalized envelope signal
$\hat{\beta}_2, \hat{\beta}_3$	Quadratic and cubic nonlinearity parameters
$n, n_0, n_2$	Total, linear and nonlinear refractive indexes respectively
$u_e$	Slowly varying envelope of the base band signal
$\tilde{u}_e$	Normalized envelope of the base band signal
$E, (= E \hat{a}_x)$	Optical field and $x$ component of the optical field
$P^L, P^{NL}, P$	Linear Polarization, nonlinear polarization, and total polarization respectively.
$\chi$	Linear susceptibility tensor
$\chi^{(3)}$	Third order susceptibility
$\chi^{(2)}$	Quadratic Nonlinearity

$\tilde{\epsilon}, \epsilon_0$	Permittivity tensor, and free space permittivity constant.
$\hat{\alpha}^2$	Thermal diffusivity
$\hat{\eta}$	Nonlinearity coefficient of the nonlinear kinematic and KdV equations
$\tilde{\alpha}$	Dispersion coefficient in the KdV equation
$\hat{V}$	Velocity of the moving frame of reference of the solitary wave solution of the KdV equation
$u_\infty, u_0$	Base band signal at time zero and infinity
$A, K', K$	Amplitude, inverse width and normalized inverse width of envelope signal respectively
$\omega_0$	Optical carrier frequency
$k_0, k_1$ or $k'$	Propagation constant, and group velocity (GV) parameter
$k_2$ or $k''$ , $k_3$ or $k'''$	Group velocity dispersion parameter (GVD), and group velocity slope
$n_g$	Group index of refraction
$v_g$	Group velocity
$\bar{a} \approx  u_e $	Constant amplitude of the envelope signal that doesn't depend on propagation (solitary wave solution)
$K, \Omega$	Side band propagation constant and frequency
$\gamma'$	Kerr nonlinearity coefficient proportional to $\hat{\beta}_3$
$\kappa$	Coefficient of the linear phase of the constant amplitude soliton solution
$P_c$	Normalized critical power of a beam or spatiotemporal soliton for self focusing



$N_0, \mathcal{N}, \mathcal{N}_c$	Initial, normalized, and critical beam power respectively
$P_0$	Initial power
$P_c^{ub}$	Upper bound of the critical power
$P_c^{lb}$	Lower bound of the critical power
$G(\tilde{u}_{e0})$	Function proportional to $P_c^{ub}$
$z_r$	Theoretical collapse distance
$z_c$	Empirically calculated collapse distance
D	Dimension of the space
$\tilde{a}, \tilde{r}$	Normalized solitary wave solution and normalized radial coordinate
$A_1, A_3$	Constants of the Klein-Gordon equation
$v, \hat{a}$	Nonstationary velocity and amplitude of a traveling frame of reference in the Klein-Gordon Equation
$r_0$	Initial Beam radius
$\varepsilon$	Beam nonparaxiality coefficient
$\lambda$	Optical wavelength
$L_r$	Linear operator
$N_{nl}$	Nonlinear operator
$\Delta_T$	Transverse divergence
$\tilde{\sigma}$	Nonlinearity order parameter
$\mathfrak{K}$	General nonlinearity function
$\mathfrak{N}( u_e ^2)$	Cubic-quintic nonlinearity function

$L_d$	Diffraction length
$w, w_0$	Beam width and waist
$f(z), g(z)$	Periodic dispersion and nonlinearity functions respectively
$s_d$	Sign of $k_2$
$s_z$	Zakharov's similarity constant
$\mu$	Saturation coefficient
$\Delta K$	Alternating signs of phase mismatch
$\chi_{eff}^{(3)}$	Effective cubic nonlinearity coefficient
$\hat{\gamma}$	Nonlinear parameter responsible for self-phase modulation (SPM)
$L$	Period of the periodic functions $f(z)$ , and $g(z)$
$s$	Dictates the amount of self-steepening
$\tau_R, T_R$	Normalized and not normalized intra pulse Raman scattering coefficient
$T_0$	Pulse width
$\theta_k$	Weighting function
$\hat{\sigma}_k$	Ansatz functions
$X_k(x)$	Unit compact support pulse function used in finite volume method
$E$	Intensity of the normalized envelope of the base band signal
$\Delta\tau, \Delta z, \Delta r, \Delta x, \Delta y$	Time, longitudinal, radial, transverse in $x$ and $y$ spatial steps in the finite difference method respectively
$U_F$	Fourier transform of the normalized envelope function
$k_x, k_y$	Transverse components of the propagation vector

$\psi(z), \psi^{(n)}(z)$	Mother wavelet and its nth order derivative
$\tilde{a}, \tilde{b}$	Scaling and shifting factors
$L^2(R)$	Set of all functions which are square-integrable (Hilbert space)
$\in$	An element of
$\infty$	Infinity
$\Psi(\omega)$	Fourier transform of the mother wavelet
$\{\psi_{\tilde{a}, \tilde{b}}(z)\}$	Set of wavelet basis functions
$c_{j,k}, a_{j,k}, b_{j,k}$	Expansion coefficients, scaling, and wavelet coefficients at level $j$ , shift $k$
$\phi(z), \phi^{(n)}(z)$	Scaling function and its nth order derivative
$h(k), g(k)$	Finite impulse response low pass and high pass filters respectively
$V_j, W_j$	Scaling and wavelet subspaces at level $j$ respectively
$\delta(k)$	Kronecker delta function
$\bar{\alpha}, \bar{\beta}, \bar{\gamma}, \bar{r}$	Connection coefficients
$\hat{L}$	Filter order which is related to the number of vanishing moments
$\oplus$	Direct vector sum
$\hat{q}$	Autocorrelation coefficient of the low pass filter
$\forall$	For all elements
$\mathbf{Z}$	Set of all integers
$a', \tilde{a}'$	Scaling coefficient vector and its derivative

$\bar{K}, \bar{C}, \bar{D}, \bar{Q}, \bar{U}$ $\bar{S}, \bar{R}, \bar{T}, \bar{G}, \bar{M}$ $\bar{Y}, \bar{L}, \bar{B}_1, \bar{B}_2$	Different Matrices used in the adaptive wavelet method
$MX$	Maximum range of the original SYM4 wavelet
$\rho$	Radial frequency
$\nu_{\mathcal{H}}, \tilde{u}_{e\mathcal{H}}$	Fourier Bessel or Hankel transform of $\nu, \tilde{u}_e$ respectively
$\Delta r_{max}$	Grid spatial range
$\mathcal{H}_l$	Fourier Bessel or Hankel transform of order $l$
$j_l(x), J_l(x)$	$l^{th}$ order spherical Bessel function and $l^{th}$ order Bessel function of the first kind
$Y_l$	Bessel transform of the second kind
$\bar{x}, \bar{y}, \hat{u}, \hat{u}_{\mathcal{H}}, \hat{J}_l$	The Gardner transform of $r, \rho, \tilde{u}_e, \tilde{u}_{e\mathcal{H}}, J_l$
$\bar{x}_n, \bar{y}_m, \hat{u}_n, \hat{u}_{\mathcal{H}m},$ $\hat{J}_l(\bar{x}_n + \bar{y}_m)$	Discretized Gardner transform of $r, \rho, \tilde{u}_e, \tilde{u}_{e\mathcal{H}}, \hat{J}_l(\bar{x} + \bar{y})$
$\tilde{b}, \tilde{\beta}$	Highest radial, frequency component
$\rho_0, r_0, \tilde{\alpha}$	Lowest frequency, radial coordinate, and a parameter calculated in Siegman's method respectively
$\bar{N}, \bar{K}_1, \bar{K}_2$	Number of samples, number of samples per cycle, parameters chosen in Siegman's method
$\Delta r_n, \Delta \rho_N$	Grid step in radial and frequency domains
$\bar{\alpha}, N_f$	Parameters defined in Magni's method
$\bar{\phi}_n$	Function defined in Magni's method
$p$	Is the maximum radial point in Yu's method

$\tilde{c}_{lm}$	Bessel series coefficients of the function $\tilde{u}_e$
$R_1, R_2$	Radial and frequency ranges in Yu's method
$\kappa_{ln}$	$n^{th}$ root of the $l^{th}$ order Bessel function
$\tilde{S}$	Parameter proportional to the Band width in Yu's method
$U(n), U_{\mathcal{H}}(m)$	Discretized forms of $\tilde{u}_e$ , and $\tilde{u}_{e\mathcal{H}}$ respectively in Yu's method
$\check{\Phi}_n(x)$	Integral used in Ferrari's method to find the Hankel transform
$\mathcal{F}$	Fourier transform
$\tilde{J}$	Is a stationary quantity to be extremized
$\tilde{\sigma}$	Is a parameter which we need to extremize the function with.
$\partial$	Partial derivative
$\delta\tilde{u}_e$	The variation of $\tilde{u}_e$
$\tilde{\eta}(x)$	Quantity proportional to $\delta\tilde{u}_e$
$\mathcal{L}$	Lagrangian density
$\mathcal{T}_k$	Kinetic Energy
$\mathcal{E}_p$	Potential Energy
$H$	Hamiltonian
$\mathcal{M}$	Momentum
$\mathcal{V}(z), \tilde{\sigma}(z)$	Variance of the wave and standard deviation measure of the spatial and temporal spreads associated with an optical pulse
$\tilde{p}$	Ratio of Initial power $\mathcal{N}_0$ to critical power $\mathcal{N}_c$
$V_p$	Constant representing the volume in which most of the pulse is located

$F(\tilde{u}_e)$	Integral of the general nonlinearity function in the NLS equation
$\mathcal{R}, \mathcal{K}$	Functions proportional to the Integral of $F(\tilde{u}_e)$
$\tilde{\phi}(z)$	Phase as unknown functions of the propagation distance $z$
$b(z)$	Chirp or front curvature of the input wave
$\alpha_s, \beta_s$	Constant numbers proportional to $D(2^{-D/2}, 2 \times 3^{-D/2-1})$ respectively
$w_e, w_H$	Equilibrium and zero Hamiltonian widths respectively
$\Omega_s^2$	Optical Bullet Parameter
$N_c$	Quantity proportional to $\mathcal{N}_c$
$\vartheta(z)$	Simple harmonic function
$T$	Potential Energy
$\tilde{V}$	Normalized width
$\tilde{\mu}$	Parameter proportional to dispersion coefficient
$\tilde{\nu}$	Parameter proportional to power over the cube of the pulse width
$\tilde{K}$	Quantity proportional to Hamiltonian over the square of the pulse width
$\tilde{c}$	Ratio of $\tilde{\nu}$ to $\tilde{\mu}$
$\tilde{P}$	Quadratic polynomial in $\tilde{V}$
$f_+, f_-$	PWC dispersion function
$g_+, g_-$	Nonlinearity function corresponding to $L_+, L_-$ respectively
$L_+, L_-$	Dispersion (nonlinearity) half period in $z$ where $f$ is $f_+, f_-$ or $g$ is $g_+, g_-$ respectively

$\alpha_D, \beta_D$	Coefficients of integration of the Dth moment of the input wave or the square of the input wave respectively
$\gamma_D$	Coefficient related to $\alpha_D, \beta_D$
$w_+, w_-$	Pulse width in each half period $L_+, L_-$ respectively
$\bar{f}$	Mean value of dispersion
$\sigma$	Constant proportional to the ratio of $\gamma_D$ and $\alpha_D$
$H_+, H_-$	Hamiltonians in each half period $L_+, L_-$ respectively
$T_+, T_-$	Potential in each half period $L_+, L_-$ respectively
$w_{min}^2$	Minimum pulse width during the periodic variation of the pulse width in dispersion managed pulses
$\langle w \rangle$ or $\bar{w}_0, \delta w$	Mean and rapidly varying pulse width terms respectively
$\omega_s$	Soliton width oscillating frequency
$\tilde{\Omega}$	Dispersion or nonlinearity function period
$f_l, f_0, g_0, g_1$	Maximum/Minimum and average value of the dispersion and nonlinearity functions respectively
$\langle b \rangle, \delta b$	Mean and rapidly varying pulse front curvature terms respectively
$\tilde{\kappa}$	Function of power and width of the pulse
$\tilde{d}$	Function of width, chirp and dispersion excursion $f_l$
$S_1, S_2, S_3, S_4, \tilde{M}$	Functions of width, chirp, dispersion frequency, power
$c_1, c_2, c_3, c_4$	Coefficients function of $\alpha_D, \beta_D, \gamma_D$ and $N_0$
$F_+, F_-$	PWC functions proportional to $f_+, f_-$ respectively
$T_{0+}, T_{0-}$	Potential Energy in each half period $L_+, L_-$ respectively

$\tilde{v}, \tilde{v}'$	Square of the beam width and the square of its derivative
$\tilde{v}_j, \tilde{v}'_j$	Are the values of $\tilde{v}, \tilde{v}'$ at $z = L_+$
$\tilde{v}_0, \tilde{v}'_0$	Are the values of $\tilde{v}, \tilde{v}'$ at $z = 0$
$\bar{v}_0, \bar{v}'_0$	Are the values of $\tilde{v}, \tilde{v}'$ at $z = L_+ + L_-$
$\tilde{v}_{jr}, \tilde{v}'_{jr}$	Normalization of $\tilde{v}_j, \tilde{v}'_j$
$F_r, L_r$	Ratios of $F_+$ to $F_-$ and $L_+$ to $L_-$
$\tilde{v}_{0FP}, \tilde{v}'_{0FP}$	Fixed point solution of $\tilde{v}, \tilde{v}'$
$\tilde{w}, \tilde{b}$	Slowly varying width and curvature
$\langle \dots \rangle$	Symbol denoting the average
$\tilde{\kappa}$	Function of the $w, f_0, c_1, c_2$
$\tilde{\eta}$	Function of the $w, f_l, b, c_1$
$S_5, S_6, S_7, S_8, \hat{M}$	Functions of width, chirp, dispersion frequency, power
$\hat{\mu}$	Coefficient function of $f_0, c_1, c_2$
$T_{eff}$	Effective Potential
$\varpi$	$w \times b$
$\tilde{\varpi}, \delta\varpi$	Slowly varying and rapidly varying parts of $\varpi$
$\bar{\kappa}$	Function of the $w, f_0, c_3, c_4$
$\bar{\eta}$	Function of the $w, f_l, c_3$
$S_9, S_{10}, S_{11}, S_{12}$	Functions of width, chirp, dispersion frequency, power
$\bar{\mu}$	Function of $w, f_0, c_3, c_4$



$\Gamma(z)$	Function proportional to $\alpha_D, \beta_D, \gamma_D, g(z)$ , and $N_0$
$\bar{g}$	Average nonlinearity
$w_{eN}$	Equilibrium width proportional to $\beta_D, \gamma_D, g_0$ , and $ A $
$\zeta^2, \hat{\zeta}^2$	Second derivative of the $T_{eff}$ with respect to the $w$
$\bar{\epsilon}_0$	Coefficient function of $g_0, \gamma_1, \beta_1, \alpha_3, N_0$
$\bar{\epsilon}$	Coefficient function of $g_1, \beta_1, \alpha_3, N_0$
$\tilde{\mu}$	Coefficient function of $\gamma_2, \alpha_4$
$\nu_z$	Function of $g(z), \beta_2, \alpha_4, N_0$
$\hat{\epsilon}_0$	Coefficient function of $g_0, \beta_2, \alpha_4, N_0$
$\hat{\epsilon}$	Coefficient function of $g_1, \beta_2, \alpha_4, N_0$
$\tilde{\eta}$	Coefficient function of $\gamma_2 \alpha_4$

## LIST OF ACRONYMS

<b><u>Symbol</u></b>	<b><u>Definition</u></b>
HE	Heat Equation
KdV	Korteweg-deVries
KP	Kadomtsev-Petviashvili
BE	Burgers' Equation
BBM	Benjamin-Bona-Mahony
BO	Benjamin-Ono
NLS	Nonlinear Schrödinger
NKG	Nonlinear Klein-Gordon
MWR	Methods of Weighted Residuals
FDM	Finite Difference method
FEM	Finite Element Method
FFT	Fast Fourier Transform
AFHSS	Adaptive Fast Hankel Split Step
AFBSS	Adaptive Fourier Bessel Split Step
AFFSS	Adaptive Fast Fourier Split Step
MRA	Multi-Resolution Analysis
ND	Normal Dispersion
AD	Anomalous Dispersion

GVD	Group Velocity Dispersion
SPM	Self Phase Modulation
DMSS	Dispersion Managed Soliton Systems
SF	Self-focusing
SFD	Self-defocusing
WDM	Wavelength Division Multiplexing
PWC	Piece Wise Continuous

# CHAPTER 1

## INTRODUCTION: THEORY AND OBJECTIVES

### 1.1 Introduction

In the last four decades there has been extensive research to model natural phenomena through different evolution equations<sup>1</sup> like the heat equation (HE), Burger's equation (BE), Korteweg-deVries (KdV) equation, Kadomtsev-Petviashvili (KP) equation, Boussinesq equation, Benjamin-Bona-Mahony (BBM) equation, Benjamin-Ono (BO) equation, nonlinear Schrödinger (NLS) equation, nonlinear Klein-Gordon (NKG) equation, etc., and the field of nonlinear optics is no exception. Traditional numerical techniques used to tackle these nonlinear partial differential equations, like the NLS and NKG equations, which model nonlinear pulse and beam propagation in fiber and Kerr bulk media, range from separation of variables, finite difference (FD)<sup>2,3</sup>, and perturbation, to variational methods or methods of weighted residuals (MWR)<sup>4,5,6</sup>.

The first technique that we describe in this dissertation is a modification of an adaptive wavelet transform (AWT) technique<sup>7,8</sup>, which is based on a mixture of finite difference (FD) method in time domain and using a new wavelet set of ansatz functions following the finite element method (FEM) technique. The wavelets are generated by translation and dyadic scaling, utilizing properties given by some kinds of Daubechies wavelets<sup>9,10,11</sup> namely, symmetry, orthogonality, completeness, compactness, differentiability, number of vanishing moments, and multiresolution<sup>12,13</sup>. This allows for

high adaptability to track extremely large gradients that might develop in special cases, as in pulse self steepening<sup>14,15</sup> (or optical shock formation), which describes the asymmetric steepening of an optical pulse with an initial Gaussian profile as the pulse propagates along the fiber, and the problem of optical beam self-focusing<sup>16-22</sup> in a bulk optical medium where a critical power<sup>23,24</sup> is necessary for beam collapse to occur because of the continuous narrowing of the Gaussian beam width. This new technique takes the advantages offered by the wavelet theory through its multiresolution<sup>13</sup> capability of shifting and scaling in order to solve complex nonlinear partial differential equations associated with pulse and beam propagation, where adaptability is needed to track steep gradients in the numerical solution by switching through different resolution levels as these steep gradients develop. There is, however, a trade off between computation time and accuracy, and a compromise is required.

The second new technique is the adaptive fast Hankel split step (AFHSS) or adaptive Fourier Bessel split step (AFBSS) method, which is a pseudo-spectral method<sup>6,25-29</sup>, and is based on the fast Fourier transform<sup>30-34</sup> (FFT) which assumes the diffraction or dispersion and the nonlinear effect are independent from each other during a small time or spatial step. This is true depending on the problem and the step size. So, the diffraction or dispersion part is solved in the Fourier transform domain, while the nonlinearity is solved in the spatial domain. This method is fast and accurate and can be used either for the case of one spatial dimension, or even when we have some kind of radial symmetry, which may be the case when we model beam propagation through the NLS equation as stated above assuming two transverse dimensions. Using fast algorithms for cylindrical/spherical Fourier Bessel transforms along with adaptive longitudinal

stepping and transverse grid management in a symmetrized split-step technique, it is possible to accurately study many nonlinear effects, including the possibility of self-focusing, spatio-temporal collapse, collapse-arresting mechanism due to saturable nonlinearity or beam nonparaxiality, variable Kerr nonlinearity, and variable dispersion managed systems. We compare results of the new numerical technique with those obtained using the straightforward fast Fourier split step (FFSS) technique.

Also in this dissertation, we develop an averaged variational technique to reduce the governing  $(D+1)$ -dimensional NLS equation to a coupled set of nonlinear ordinary differential equations (ODEs), rigorously solve these equations, and study their stability from the stability of the fixed points of the variational equations. The long term dynamics of the solitons are studied by the averaged equations obtained using the Kapitza approach. The system of ODEs obtained accurately predict the pulse dynamics in a medium of saturating nonlinearity, periodic nonlinearity and/or dispersion. Note that this variational method is used as a guideline for how to select stable initial conditions for the pulse, and compare it with the exact numerical technique developed. The importance of this work is in generating optical solitons which may become important in telecommunication systems due to their self-confined structure. Also, this work is applied to the stabilization of the Bose-Einstein condensate in  $(2+1)$  and  $(3+1)$ -dimensional optical lattice.

One should not forget that the above techniques when applied to the NLS equation assume some constraints like the slowly varying amplitude assumption<sup>35</sup> in which the second derivative of the complex field amplitude with respect to the axial propagation is supposed to be small. Also, we assume that the higher order terms in the

nonlinear polarization of the electric field are ignored. So, as long as the pulse width, in the case of pulse propagation for example, is considered wide enough so that its spectral width is negligible with respect to the central optical frequency (commonly referred to as the slowly varying envelope approximation or SVEA), the above methods are valid<sup>7,36</sup>.

It is worth noting that the numerical and analytical methods developed in this dissertation are useful in many fields of science, ranging from classical mechanics, fluid mechanics<sup>6</sup>, ocean acoustics<sup>35,36</sup>, nonlinear optics<sup>37-39</sup>, plasma physics<sup>40-42</sup>, electrodynamics, to many other domains of science which are based on these kinds of evolution equations or their modifications.

The purpose of this work is to investigate and compare between classical methods that exist in the literature<sup>3,43-47</sup> and the above mentioned techniques applied to different PDEs modeling wave propagation in nonlinear dispersive (or diffractive) environments. Examples include the linear HE, the nonlinear evolution equation, the BE<sup>48</sup>, the KdV equation<sup>49,50</sup>, and finally, the NLS<sup>38,50</sup> family of equations. Emphasis is placed on the last set since they model soliton propagation in fibers, self-focusing of optical beams leading to collapse, optical shocks, and optical “bullets”<sup>51-53</sup>.

In the next Section, we summarize the theoretical background and list the PDEs to be analyzed numerically and analytically in the dissertation, along with a brief narration of the physical phenomena that they model.

## **1.2 PDEs Analyzed in This Work**

In its simplest terms, nonlinearity can be attributed to the dependence of the phase velocity  $v_p$  on the amplitude of the propagating wave  $u$ <sup>37</sup>. If we denote the 1-D wave equation with an initial condition as:

$$\frac{\partial u}{\partial T} + v_p \frac{\partial u}{\partial Z} = 0, u(Z, 0) = u_0, \quad (1.1)$$

and if we let:

$$v_p = v_{p0} (1 + \hat{\beta}_2 u + \hat{\beta}_3 u^2), \quad (1.2)$$

be the nonlinearly modified velocity, where we consider only the quadratic and cubic nonlinearities, then Eq. (1.1) becomes<sup>48</sup>:

$$\frac{\partial u}{\partial T} + v_{p0} \frac{\partial u}{\partial Z} + \frac{v_{p0} \hat{\beta}_2}{2} \frac{\partial u^2}{\partial Z} + \frac{v_{p0} \hat{\beta}_3}{3} \frac{\partial u^3}{\partial Z} = 0, u(Z, 0) = u_0, \quad (1.3)$$

where  $\hat{\beta}_2$  is responsible for shock formation and also for second harmonic generation,  $\hat{\beta}_3$  is responsible for self refraction, bistability, phase conjugation, and soliton propagation<sup>37</sup>. If  $\hat{\beta}_2 \neq 0, \hat{\beta}_3 \neq 0$ , then after some manipulation and extension in 3-D we get:

$$\frac{\partial^2 u}{\partial T^2} - v_{p0}^2 \nabla^2 u \equiv \hat{\beta}_2 \frac{\partial^2 u^2}{\partial T^2} + \frac{2}{3} \hat{\beta}_3 \frac{\partial^2 u^3}{\partial T^2}, \quad (1.4)$$

which is a general starting point. Eq. (1.4) may represent the wave equation of a component of the electric field ( $E$ ) in nonlinear optics, where the RHS are the source terms due to the nonlinear polarization of the medium. For  $\hat{\beta}_2 = 0$ , the description of the nonlinearities may sometimes be given in terms of the nonlinear induced polarization in the medium or an amplitude dependent refractive index<sup>18,23</sup>

$$n(x, y, z, \omega, |u_e|^2) = n_0 + n_2 |u_e|^2, \text{ where } u = \text{Re}[u_e e^{j(\omega_0 T - k_0 Z)}].$$

Rigorously speaking, we can derive the optical field  $E (= E \hat{a}_x)$  starting from Maxwell's equations in terms of the nonlinear polarization  $P^{NL}$ . We know that the induced polarization  $P = P^L + P^{NL} = \epsilon_0 \chi E + P^{NL}$ , where  $\chi$  denotes the linear



susceptibility and  $\tilde{\epsilon} = \epsilon_0(1 + \chi)$ . If we consider only Kerr media with  $\chi_{ijk} = 0, \forall i, j, k$ ,  $\chi_{ijkl} = 0$ , for  $i, j, k, l \neq 1$ , and  $\chi_{1111} = \chi^{(3)}$  is the only nonvanishing cubic nonlinear susceptibility coefficient, we obtain an equation for  $E$  similar to (1.4) with:  $\hat{\beta}_2 = 0, \hat{\beta}_3 = -3 \frac{\epsilon_0}{\tilde{\epsilon}} \chi^{(3)} = -\frac{2n_2}{n_0}, n_2 = \frac{3}{4n_0} \chi^{(3)}$ .

### 1.2.1 The Heat Equation

The heat equation (HE) is defined as:

$$\frac{\partial u}{\partial T} - \hat{\alpha}^2 \frac{\partial^2 u}{\partial Z^2} = 0, \quad (1.5)$$

where  $u$  denotes the temperature, to be solved along with the initial conditions:  $u(Z, 0) = e^{-Z^2}$ , with  $-\infty < Z < \infty, 0 < T < \infty$ . This equation admits an analytical

solution:  $u(Z, T) = \frac{1}{\sqrt{1 + 4\hat{\alpha}^2 T}} e^{\frac{-Z^2}{1 + 4\hat{\alpha}^2 T}}$ . Eq. (1.5) is linear, and represents heat propagation

in an infinite bar with Gaussian initial conditions, and it is used for the sake of demonstrating the wavelet method only.

### 1.2.2 The First Order Nonlinear Kinematic Equation<sup>1</sup>

This equation is the same as the 1-D wave equation in a traveling frame reference, similar to Eq. (1.1) with  $\hat{\beta}_2 \neq 0, \hat{\beta}_3 = 0$ , defined as:

$$\frac{\partial u}{\partial T'} + \hat{\eta} u \frac{\partial u}{\partial Z'} = 0, \quad Z' = Z - v_{p_0} T, T' = T, \hat{\eta} = \hat{\beta}_2 v_{p_0}, \quad (1.6)$$

to be solved along with the initial conditions:  $u(Z', 0) = e^{-Z'^2}$ , with  $-\infty < Z' < \infty, 0 < T' < \infty$ . Eq. (1.6) represents unidirectional wave propagation in nonlinear media.

### 1.2.3 The Burger's Equation<sup>48</sup>

The Burger's equation (BE) is defined as:

$$\frac{\partial u}{\partial T'} + \hat{\eta} u \frac{\partial u}{\partial Z'} - \hat{\alpha}^2 \frac{\partial^2 u}{\partial Z'^2} = 0, \quad \hat{\eta} = \hat{\beta}_2 v_{p0}, \quad (1.7)$$

to be solved along with the initial conditions:  $u(Z', 0) = e^{-Z'^2}$ , with  $-\infty < Z' < \infty, 0 < T' < \infty$ . This equation is like the nonlinear kinematic wave equation with a dissipation term added. It is used in fluid dynamics and in engineering as a simplified model for turbulence, boundary layer behavior, shock wave formation, and mass transport<sup>48</sup>. It has been studied and applied for many decades. Many different closed-form, series approximation, and numerical solutions are known for particular sets of boundary conditions.

### 1.2.4 The KdV Equation<sup>1,49,50</sup>

The Kortweg-deVries (KdV) equation is a nonlinear partial differential equation of third order, as follows:

$$\frac{\partial u}{\partial T'} + \hat{\eta} u \frac{\partial u}{\partial Z'} + \tilde{\alpha} \frac{\partial^3 u}{\partial Z'^3} = 0. \quad (1.8)$$

In a moving frame of reference with a velocity  $\hat{V}$ , we have the analytic solitary wave solution (also called the one-soliton solution):  $u = u_\infty + (u_0 - u_\infty) \operatorname{sech}^2[K(Z' - Z_0)]$ ,

where  $K = \sqrt{\left(\frac{u_0 - u_\infty}{12\tilde{\alpha}}\right)} \hat{\eta}$ ,  $\hat{V} = \left(u_\infty + \frac{u_0 - u_\infty}{3}\right) \hat{\eta}$ , and where  $u = u_\infty$  at  $Z' = \pm\infty$ .

This equation was formulated as part of an analysis of shallow-water waves in canals<sup>1,49,50</sup>, it has subsequently been found to be involved in a wide range of physical phenomena, especially those exhibiting shock waves, traveling waves, and solitons. Certain theoretical physical phenomena in the quantum mechanics domain are explained

by means of a KdV model. It is used in fluid dynamics, aerodynamics, and continuum mechanics as a model for shock wave formation, solitons, turbulence, and mass transport<sup>49,50</sup>. It has been studied and applied for many decades. Many different closed form, series approximation, and numerical solutions are known for particular sets of boundary and initial conditions.

### 1.2.5 Pulse Propagation in Fiber: The 1-D NLS Equation<sup>38,48,50</sup>

We know that pulses traveling in a nonlinear medium distort due to the effect of nonlinearity. Also we know from linear theory that pulses distort due to dispersion that exist in the medium. This phenomenon is due to the fact that different frequency components constituting the pulse travel with different velocities in a dispersive medium. So, it is surmised that nonlinearity and dispersion together can accommodate distortionless propagation of pulses, called solitons. For both nonlinearity and dispersion, chirping in frequency develops during propagation. Appropriate amounts of each ensures soliton-like propagation.

Fiber dispersion can be best understood by realizing that the propagation constant  $k$  is not a constant but depends on frequency<sup>7,37</sup> according to the dispersion relation

$k(\omega) = k_0 + (\omega - \omega_0)k_1 + \frac{1}{2}(\omega - \omega_0)^2 k_2 + \frac{1}{6}(\omega - \omega_0)^3 k_3 + \dots$  where  $k_0$  is the propagation constant at frequency  $\omega_0$ ,  $k_1 = k'(\omega_0)$  is the group velocity (GV) parameter,  $k_2 = k''(\omega_0)$  is the group velocity dispersion parameter (GVD), and  $k_3 = k'''(\omega_0)$  is the slope of the group velocity.

An optical pulse propagating in a single mode fiber will have a spectral width  $\Delta\omega$ , since  $n = n(\omega, |u_e|^2)$  depends on frequency. Then  $n_g = n_0 + \omega \frac{dn_0}{d\omega}$ , where  $n_g$  is the

group index. Hence, the pulse amplitude  $u_e$  travels at a group velocity  $v_g = \frac{1}{k_1} = \frac{c}{n_g}$ .

Thus, different spectral components travel at different speeds along the fiber causing dispersion. This phenomenon is called GVD and is denoted by parameter  $k_2 = k''(\omega_0)$ .

There are two kinds of dispersion: normal dispersion (ND), and anomalous dispersion (AD), as shown in Figure 1.1.<sup>38</sup> We note that dispersion broadens the pulse shape.

The effect of the nonlinearity is due to intensity dependence of refractive index  $n(\omega, |u_e|^2) = n_0 + n_2 |u_e|^2 = n_0 - \frac{n_0 \hat{\beta}_3}{2} |u_e|^2$ . The third order  $\chi^{(3)}$  susceptibility is the nonlinearity present in optical fibers, and is the physical component responsible for nonlinear refraction. This phenomenon is called self phase modulation (SPM)<sup>7,38</sup>, where the optical pulse experiences spectral broadening or self-focusing in time domain. Now, we can use a heuristic way to derive the NLS equation by using the dispersion relation method<sup>1,37</sup> outlined as the following:

$$\omega(k) = \omega(k_0) + v_g(k - k_0) + \frac{v'_g}{2}(k - k_0)^2 + \dots + \frac{\partial \omega}{\partial |a|^2} \bigg|_{\omega_0} |a|^2, \bar{a} \approx |u_e| \quad (1.9)$$

where  $v_g = \frac{d\omega}{dk} \bigg|_{k_0}$ ,  $v'_g = \frac{d^2\omega}{dk^2} \bigg|_{k_0}$ ,  $u(X, Y, Z, T) = \text{Re}[u_e(X, Y, Z, T)e^{j(\omega_0 T - k_0 Z)}]$ . If we make the

following change of variables:  $\Omega(K) = \omega(k) - \omega(k_0) = v_g K + \frac{v'_g}{2} K^2 + \dots$ , and the

following operator equivalence:  $\Omega \rightarrow -j \frac{\partial}{\partial T}$ ,  $K \rightarrow j \frac{\partial}{\partial Z}$ , Eq. (1.9) becomes:

$$j \frac{\partial u_e}{\partial T} - \frac{v'_g}{2} \frac{\partial^2 u_e}{\partial Z^2} = 0, \quad (1.10)$$

where  $Z' = Z - v_g T, T' = T$ .

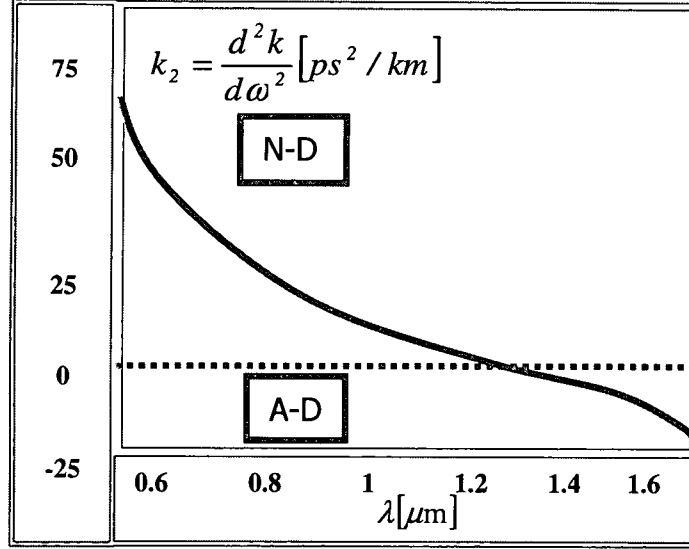


**Figure 1.1:** Dispersion curve in fibers.

Also, from Eq. (1.3) in Kerr media, or when  $\hat{\beta}_2 = 0, \hat{\beta}_3 \neq 0$ , we get:

$$\frac{\partial u}{\partial T} + v_{p0} \frac{\partial u}{\partial Z} + v_{p0} \frac{\hat{\beta}_3}{3} \frac{\partial u^3}{\partial Z} = 0. \quad (1.11)$$

Now, let  $u(Z, T) = \text{Re}[u_e(Z, T)e^{j(\omega_0 T - k_0 Z)}] = \frac{1}{2}[u_e e^{j(\omega_0 T - k_0 Z)} + u_e^* e^{-j(\omega_0 T - k_0 Z)}]$ , and after some

simple algebra and assuming  $v_{p0} = v_g$ , and retaining terms of frequency  $\omega_0$  we arrive

at:

$$j \frac{\partial u_e}{\partial T'} + \frac{\omega_0 \hat{\beta}_3}{4} |u_e|^2 u_e = 0, \quad (1.12)$$

where  $\frac{\omega_0 \hat{\beta}_3}{4} = \left( \frac{\partial \omega}{\partial |a|^2} \right)_{\omega_0}$ ,  $n_2 = -\frac{n_0 \hat{\beta}_3}{2} = -\frac{2n_0}{\omega_0} \left( \frac{\partial \omega}{\partial |a|^2} \right)_{\omega_0}$ ,  $\bar{a} \approx |u_e|$ . So, by heuristically

adding nonlinearity to Eq. (1.10) in accordance with Eq. (1.12) we get:

$$j \frac{\partial u_e}{\partial T'} - \frac{v'_g}{2} \frac{\partial^2 u_e}{\partial Z'^2} + \frac{\omega_0 \hat{\beta}_3}{4} |u_e|^2 u_e = 0, \quad (1.13)$$

which is the 1-D NLS equation. If  $n_2 > 0$ , or equivalently  $\frac{\omega_0 \hat{\beta}_3}{4} = \left( \frac{\partial \omega}{\partial |\vec{a}|^2} \right) \Big|_{\omega_0} < 0$ , and

$k_2 < 0$ , implying  $v'_g > 0$ , since  $v'_g = -v_g^3 k_2$ , we have a solitary wave or one-soliton solution of the form:

$$\tilde{u}_e = 2K' \sqrt{-\frac{v'_g}{\omega_0 \beta_3}} \operatorname{sech}(K'Z') e^{-j \frac{v'_g K'^2 T'}{2}}. \quad (1.14)$$

Let  $\gamma' = -\frac{\omega_0 \hat{\beta}_3}{4}$ ,  $z = \frac{T'}{T_0}$ ,  $\tau = \frac{Z'}{L_D}$ ,  $\tilde{u}_e = \left( \frac{\gamma L_D^2 u_e^2}{|v'_g|} \right)^{\frac{1}{2}}$ ,  $L_D^2 = |v'_g| T_0$ . Upon replacing these

quantities in Eq. (1.13), we get <sup>7</sup>:

$$j \frac{\partial \tilde{u}_e}{\partial z} - \frac{1}{2} \frac{\partial^2 \tilde{u}_e}{\partial \tau^2} - |\tilde{u}_e|^2 \tilde{u}_e = 0, \quad (1.15)$$

which is the normalized form of the NLS equation, and correspondingly has a single soliton solution of the form<sup>38</sup>:

$$\tilde{u}_e = K \operatorname{sech}(K\tau) e^{-j \frac{K^2 z}{2}}. \quad (1.16)$$

### 1.2.6 Beam Propagation in Bulk Media: Self-focusing Equation<sup>54,55</sup>

Self-focusing is a nonlinear phenomenon, which has been studied for the last four decades<sup>54,55</sup>. The effect of nonlinearity on the refractive index is similar to that discussed before. Self-focusing results in the narrowing of the beam width and increase in the on-axis intensity. For powers above a certain threshold<sup>18,23</sup>  $P_c$ , the beam undergoes collapse with intensity so high that it can either cause breakdown in the material, or some other

physical effects are triggered, such as saturation of the index of refraction<sup>39</sup> or breakdown of the assumptions about slowly varying amplitude and paraxial approximation, causing no further focusing to occur. Zakharov and Shabat<sup>19</sup> point out that due to a higher index of refraction, on-axis rays undergo total internal reflection and are thereby trapped if the nonlinearity is strong enough. In one dimension nonlinearity can balance diffraction of a beam, resulting to the formation of first order spatial solitons. Also, if the nonlinear effect is higher than diffraction, periodic focusing occurs, or may result in higher order solitons. This may not be the case in two or three dimensions where spatial collapse may occur.

In Chapter 6, we will discuss the self-focusing phenomenon in more detail where we formulate conditions for the self-focusing to occur and estimate the collapse time. Here, we shall derive the self-focusing equation in 1, 2, and 3-D. From Eq. (1.4) and assuming a slowly varying function of  $Z'$  :  $\left| \frac{d^2 u_e}{dZ'^2} \right| \ll k_0 \left| \frac{du_e}{dZ'} \right|$ , we get the following relation:

$$2jk_0 \frac{du_e^*}{dZ'} = \nabla_T^2 u_e^* - \frac{\hat{\beta}_3 k_0^2}{2} u_e^2 u_e^*. \quad (1.17)$$

If  $u_e(X', Y', Z') = \bar{a}(X', Y') e^{-j\kappa Z'}$  is the solution of the above equation then we have:

$$\nabla_T^2 \bar{a} = 2\kappa k_0 \bar{a} + \hat{\beta}_3 \frac{k_0^2}{2} \bar{a}^3. \quad (1.18)$$

Three cases need to be discussed:

#### A. 1 Transverse Dimension<sup>37,56</sup>

Eq. (1.18) becomes:

$$\frac{d^2 \bar{a}}{dX'^2} = +2\kappa k_0 \bar{a} + \hat{\beta}_3 \frac{k_0^2}{2} \bar{a}^3, \quad (1.19)$$

implying  $X' = \int \frac{d\bar{a}}{\left[2\kappa k_0 \bar{a}^2 + \left(\hat{\beta}_3 \frac{k_0^2}{4}\right) \bar{a}^4\right]^{\frac{1}{2}}}$ , which is an elliptic integral, having a spatial

soliton solution of the form:  $\bar{a}(X') = A \operatorname{sech}(KX')$ , where

$A = \left(-\frac{8\kappa}{\hat{\beta}_3 k_0}\right)^{\frac{1}{2}}$ , and  $K = (2\kappa k_0)^{\frac{1}{2}}$ .  $A, K$  are positive for  $\hat{\beta}_3 < 0$  &  $\kappa > 0$ . The soliton

forms as a balance between focusing due to nonlinearity or self refraction, and spreading due to diffraction.

## B. 2 Transverse Dimensions<sup>1,56,57</sup>

If we make the transformations:  $\bar{a} = \left(-\frac{2\kappa}{\hat{\beta}_3 k_0}\right)^{\frac{1}{2}} \tilde{a}$ ,  $r' = \frac{1}{(2\kappa k_0)^{\frac{1}{2}}} \tilde{r}$ , and if we

consider problems of cylindrical symmetry where:  $\nabla_r^2 = \frac{\partial}{\partial X'^2} + \frac{\partial}{\partial Y'^2} = \frac{d^2}{dr'^2} + \frac{1}{r'} \frac{d}{dr'}$ ,

Eq. (1.18) becomes:

$$\frac{d^2 \tilde{a}}{d\tilde{r}^2} + \frac{1}{\tilde{r}} \frac{d\tilde{a}}{d\tilde{r}} - \tilde{a} + \tilde{a}^3 = 0, \quad (1.20)$$

which has no analytic solution, and is very sensitive to initial conditions. The envelope  $\tilde{a}$  is called the Townes "soliton" and is given by the solution of Eq. (1.20) with the conditions:  $\tilde{a}'(0) = 0, \tilde{a}(\infty) = 0$ . The first three modes are shown in Figure 1.2.<sup>1,56,57</sup>

Figure 1.3 describes the self-focusing of a beam after propagation for some distance. We will describe in detail the simulation of 2 D case later in Chapter 6.

## C. 3 Dimensions<sup>1</sup>



To find a stationary particular solution in this case, it is better to start with the NKG equation which may be used to describe the envelope propagation in the presence of a cubic nonlinearity<sup>1</sup>. Hence, the linear part of the carrier envelope equation can be derived from the dispersion relation:  $\omega^2 = c_0^2 k^2 - A_1$ , by replacing  $\omega, k$ , by the equivalent operators, and upon introducing a cubic nonlinear term (similar to the NLS), we get the general form of the NKG equation:

$$\frac{\partial^2 u}{\partial T^2} - v_{p0}^2 \nabla^2 u = A_1 u + A_3 u^3, \quad (1.21)$$

where  $A_1 > 0, A_3 < 0$ . If we consider radial symmetry, stationary solutions may be obtained by substituting:

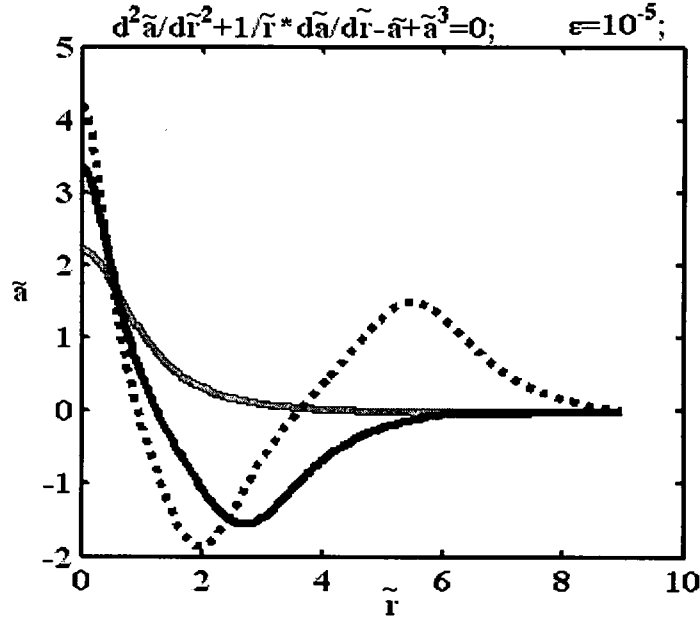


**Figure 1.2:** Townes soliton profiles.

$u \rightarrow u(X, Y, Z - vT), (Z - vT) = (1 - v^2/v_{p0}^2)^{1/2} Z', X' = X, Y' = Y$ . Upon neglecting all angular dependences, we get:

$$\nabla^2 u = \frac{\partial^2 u}{\partial r'^2} + \frac{D-1}{r'} \frac{\partial u}{\partial r'} = \frac{(A_1 u + A_3 u^3)}{v_{p0}^2}. \quad (1.22)$$

If  $(D-1)=1$ , the problem is one similar to the previous case with cylindrical symmetry.

If  $(D-1)=2$ , the equation models the spherical symmetry case, which can give 3-D spatio-temporal solitons or optical bullets. Also, if we make this final substitution:

$$u = \left( -\frac{A_1}{A_3} \right)^{\frac{1}{2}} \hat{a}, \quad \tilde{r} = A_1^{\frac{1}{2}} \frac{r'}{v_{p0}} \text{ in Eq. (1.22) we get:}$$

$$\frac{\partial^2 \hat{a}}{\partial \tilde{r}^2} + \frac{D-1}{\tilde{r}} \frac{\partial \hat{a}}{\partial \tilde{r}} - \hat{a} + \hat{a}^3 = 0. \quad (1.23)$$

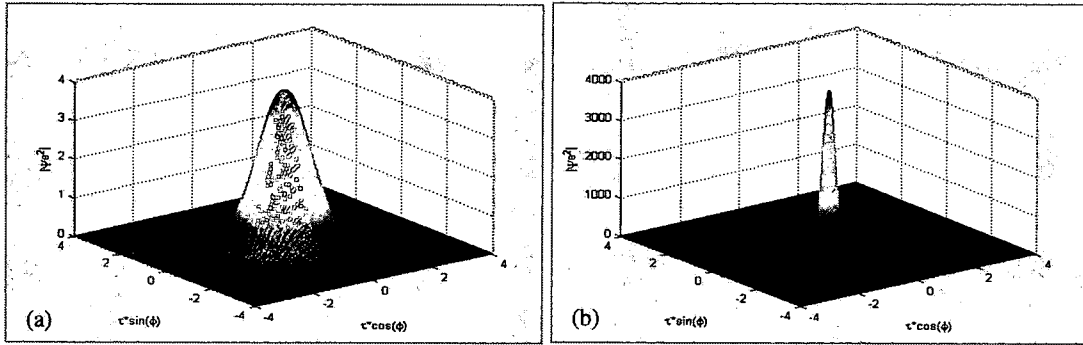


**Figure 1.3:** (a) Initial Gaussian profile. (b) Self-focusing of a beam after some time.

Figure 1.4 shows the 3D in time and space or optical bullet propagation in bulk media where the solution tends to self-focus after propagation for some time. Figure 1.5

shows particular solitary- wave solution by plotting  $\frac{\hat{a}(\tilde{r})}{\hat{a}(0)}$  versus  $\tilde{r}$  and compares it to

with corresponding solutions for  $D = (1, 2)$ .<sup>18,51</sup>

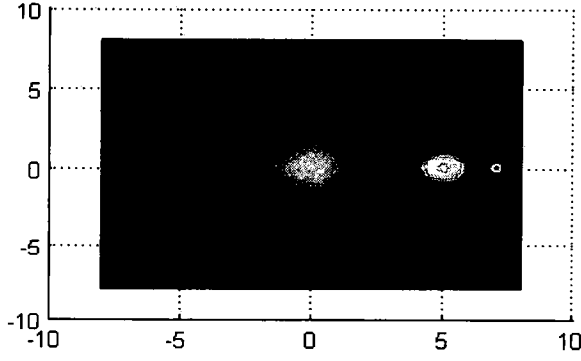


**Figure 1.4:** Optical bullet propagation.

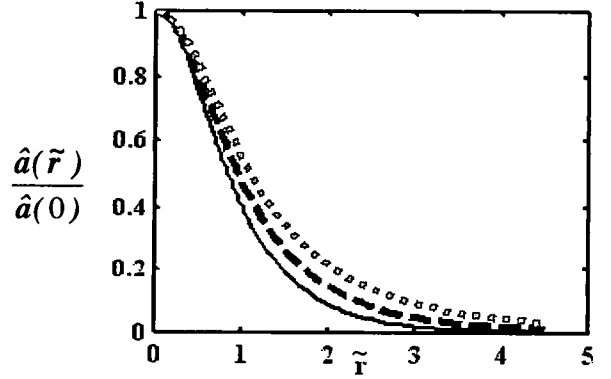


**Figure 1.5:** Townes soliton profiles for  $D=1,2,3$ .

### 1.2.7 Nonparaxial Assumption in the NLS Equation

The assumptions about slowly varying amplitude and the paraxial approximation may not be valid for large focusing angles during the last stages of self-focusing, and it has been proposed that there is no singularity if one accounts for nonparaxiality<sup>58,59</sup>. Starting from Eq. (1.17) the paraxial and nonparaxial nonlinear Schrodinger (NLS) equation which is classically used to model the self-focusing phenomenon given in the general operator form<sup>58</sup>:

$$\frac{\partial \tilde{u}_e}{\partial z} - j\varepsilon \frac{\partial^2 \tilde{u}_e}{\partial z^2} = jL_r \tilde{u}_e + jN_{nl}(\tilde{u}_e) \tilde{u}_e, \quad \tilde{r} \in \mathbb{R}^D, \quad z \geq 0; \quad \tilde{u}_e(r, z=0) = \tilde{u}_{e0}(r) \quad (1.24)$$

where  $D$  is the transverse dimension in space,  $\varepsilon = (\lambda/4\pi r_0)^2$  and  $r_0$  is the initial beam radius, and where  $L_r \tilde{u}_e = \Delta_r \tilde{u}_e$ ,  $N_{nl}(\tilde{u}_e) = |\tilde{u}_e|^{2\sigma}$ . In Chapter 6, we will discuss the implication of nonparaxiality.

### 1.2.8 Beam Propagation in Saturating Nonlinearity

As we mentioned earlier, self-focusing results in the narrowing of the spatiotemporal pulse width in dimensions and increase in the on-axis intensity. For powers above a certain threshold the spatiotemporal pulse undergoes collapse. In reality, the high pulse intensity may either cause breakdown in the material, or some other

physical effects may be triggered, such as saturating of the index of refraction<sup>39</sup>, so that no further focusing may occur. The time-dependent (3+1)-dimensional (D=3) paraxial wave equation, in the presence of group velocity dispersion is<sup>51,60,61</sup>:

$$i \frac{\partial u_e}{\partial Z'} + \frac{1}{2k_0} \left( \frac{\partial^2 u_e}{\partial X'^2} + \frac{\partial^2 u_e}{\partial Y'^2} \right) - \frac{k_2}{2} \frac{\partial^2 u_e}{\partial T'^2} + \Re(u_e)^{2\bar{\sigma}} u_e = 0, \quad (1.25)$$

where  $u_e$  is the slowly varying envelope of the optical field,  $T'$  is the reduced time in a moving frame of reference,  $k_1$  is the group velocity parameter,  $k_0 = \frac{n_0 \omega}{c}$  is the propagation constant,  $k_2$  is the group-velocity dispersion (GVD) parameter, and  $\Re(u_e)^{2\bar{\sigma}} = \frac{k_0}{n_0} \delta n(u_e)^{2\bar{\sigma}}$  is the nonlinear parameter responsible for self-phase modulation (SPM). Note that  $k_2$  can be positive or negative depending on the nature of the dispersion in the medium, corresponding to normal dispersion (ND) and anomalous dispersion (AD) respectively. Also, for  $\bar{\sigma} = 1$ ,  $\delta n(u_e)^2 = n_2 |u_e|^2 + n_4 |u_e|^4$  is the intensity induced change in index where  $n_4 \neq 0$  and negative in the case of saturable nonlinearity.

Introducing the following normalization<sup>61</sup> for Eq. (1.25):  $z = \frac{Z'}{L_d}$ ,  $x = \frac{X'}{w_0}$ ,

$y = \frac{Y'}{w_0}$ ,  $\tau = \frac{T'}{(w_0^2 k_0 k_2)^{1/2}}$ ,  $f(u_e)^{2m} = L_d \Re(u_e)^{2\bar{\sigma}}$ ,  $L_d = 2k_0 w_0^2$ , we arrive at

$$j \frac{\partial \tilde{u}_e}{\partial z} + \left( \frac{\partial^2 \tilde{u}_e}{\partial x^2} + \frac{\partial^2 \tilde{u}_e}{\partial y^2} - s_d \frac{\partial^2 \tilde{u}_e}{\partial \tau^2} \right) + f(\tilde{u}_e)^{2\bar{\sigma}} \tilde{u}_e = 0, \quad (1.26)$$

where  $s_d = \text{sgn}(k_2)$ ,  $w_0$  is the initial transverse spatial width, and  $L_d$  is the diffraction length. If  $s_d = -1$  we can assume spherical symmetry of the field distribution and introduce the radial variable  $r = (x^2 + y^2 + \tau^2)^{1/2}$  to recast Eq. (1.26) as<sup>60</sup>

$$j \frac{\partial \tilde{u}_e}{\partial z} + \frac{1}{r^{D-1}} \frac{\partial}{\partial r} \left( r^{D-1} \frac{\partial \tilde{u}_e}{\partial r} \right) + f(|\tilde{u}_e|^2) \tilde{u}_e = 0, \quad (1.27)$$

where  $D$  is 3 and  $\tilde{\sigma} = 1$  and  $f(\tilde{u}_e) = \frac{\tilde{u}_e}{1 + \mu \tilde{u}_e^2} \approx u - \mu \tilde{u}_e^2$  in our case. In Chapter 6, we will discuss this phenomenon in detail.

### 1.2.9 Dispersion Management in D-dimensions

In recent years, dispersion management (DM) techniques have received a lot of attention due to its benefits in high speed nonlinear wave propagation in optical communication systems because it allows one to reach the zero dispersion limit where inter-pulse effects are reduced enormously<sup>62</sup>. In 1 dimension (1D) DM reduces radiation from the pulse due to amplitude compensating fiber loss, modulation instability reduction in bandwidth and in gain, jitter due to collisions between signals in different channels of wavelength division multiplexed systems (WDMS), and many other effects which provides stabilizing pulse propagation for very long distances<sup>63-65</sup>. Hence, DM is sometimes considered to be the future of soliton-based communication systems. The time-dependent paraxial wave equation, in the presence of periodic modulation of dispersion and nonlinearity has the form of a modified (D+1)-dimensional NLS with a dimensionless envelope of the optical field according to

$$j \frac{\partial \tilde{u}_e}{\partial z} + \frac{f(z)}{2} \frac{1}{r^{D-1}} \frac{\partial}{\partial r} \left( r^{D-1} \frac{\partial \tilde{u}_e}{\partial r} \right) + |\tilde{u}_e|^2 \tilde{u}_e = 0, \quad (1.28)$$

where  $r = (x^2 + y^2)^{1/2}$  or  $r = (x^2 + y^2 + \tau^2)^{1/2}$  for cylindrical or spherical symmetry of the field distribution respectively, and  $D$  can be 2 or 3, respectively. In Chapter 7, we will discuss this technique in details.

### 1.2.10 Nonlinearity Management in D-dimensions

It has been shown<sup>66</sup> that a beam can be stabilized if the nonlinearity coefficient is weakly modulated along the propagation direction where the beam power oscillates about the modulated critical value. Moreover, a better stabilization occurs if a more radical modulation of the nonlinearity is done based on a periodically alternating self-focusing (SF) and self defocusing (SDF) layers or even a periodic SF layers with different values of the Kerr coefficient as shown in Towers and Malomed<sup>67</sup>. Note that in a quadratically nonlinear medium with phase mismatch  $\Delta K$ , it has been shown that the effective cubic nonlinearity coefficient,  $\chi_{\text{eff}}^{(3)}(z) \propto (\chi^{(2)})^2 \left( \frac{1 - \exp(-j\Delta K z)}{\Delta K} \right)$ , will be automatically periodic<sup>68</sup>.

The time-dependent  $(D+1)$ -dimensional ( $D=3$ ) paraxial wave equation in the presence of group velocity dispersion is<sup>18,51,61</sup>:

$$j \frac{\partial u_e}{\partial Z'} + \frac{1}{2k_0} (\nabla_{\perp}^2 u_e) - \frac{k_2}{2} \frac{\partial^2 u_e}{\partial T'^2} + \hat{\gamma}(Z') |u_e|^2 u_e = 0, \quad (1.29)$$

where  $u_e$  is the slowly varying envelope of the optical field,  $T'$  is the reduced time in a moving frame of reference,  $k_1$  is the group velocity parameter,  $k_0 = \frac{n_0 \omega}{c}$  is the propagation constant,  $k_2$  is the GVD parameter, and  $\hat{\gamma} = n_2 k_0 / n_0$  is the nonlinear parameter responsible for SPM and is either piecewise continuous in layers of width  $L$  or

harmonic function of period  $L$ . Note that  $k_2$  can be positive or negative depending on the nature of the dispersion in the medium, corresponding to ND and AD, respectively.

Introducing the following normalization<sup>61</sup> for Eq. (1.29):  $z = \frac{Z'}{L_d}$ ,  $x = \frac{X'}{w_0}$ ,  $y = \frac{Y'}{w_0}$ ,

$\tau = \frac{T'}{(w_0^2 k_0 k_2)^{1/2}}$ ,  $\tilde{u}_e = (L_d)^{1/2} u_e$ ,  $L_d = k_0 w_0^2$ , we arrive at

$$i \frac{\partial \tilde{u}_e}{\partial z} + \frac{1}{2} \left( \nabla_{\perp}^2 \tilde{u}_e - s_d \frac{\partial^2 \tilde{u}_e}{\partial \tau^2} \right) + \hat{\gamma}(z) |\tilde{u}_e|^2 \tilde{u}_e = 0, \quad (1.30)$$

where  $s_d = \text{sgn}(k_2)$ ,  $w_0$  is the initial transverse spatial width,  $L_d$  is the diffraction length.

If we assume  $s_d = -1$  and spherical symmetry of the field distribution, and introduce the radial variable  $r = (x^2 + y^2 + \tau^2)^{1/2}$ , Eq. (1.30) can be written as

$$i \frac{\partial \tilde{u}_e}{\partial z} + \frac{1}{2} \frac{1}{r^{D-1}} \frac{\partial}{\partial r} \left( r^{D-1} \frac{\partial \tilde{u}_e}{\partial r} \right) + \hat{\gamma}(z) |\tilde{u}_e|^2 \tilde{u}_e = 0, \quad (1.31)$$

where  $D$  can be 1, 2, 3, and we are in the AD regime. In Chapter 8, we will discuss this technique in detail.

### 1.2.11 Self-Steepening and Raman Scattering Phenomena <sup>7</sup>

Self-steepening is described as the asymmetric steepening of an optical pulse with an initial Gaussian amplitude profile as the pulse propagates along a fiber. Oliveira et al <sup>14</sup> have derived exact analytic solutions for the modified NLS equation, which is the

standard NLS equation with an additional term  $s \frac{\partial(|\tilde{u}_e|^2 \tilde{u}_e)}{\partial \tau}$  added. Thus the equation

becomes:

$$j \frac{\partial \tilde{u}_e}{\partial z} + \frac{1}{2} \frac{\partial^2 \tilde{u}_e}{\partial \tau^2} + js \frac{\partial(|\tilde{u}_e|^2 \tilde{u}_e)}{\partial \tau} + |\tilde{u}_e|^2 \tilde{u}_e = 0, \quad (1.32)$$

where  $s$  dictates the amount of self-steepening experienced by the pulse during propagation along the fiber. If  $s$  is positive, the pulse develops a shock front in the trailing edge, i.e., it steepens on the right, if  $s$  is negative, then it will steepen on the left. Hence, the last term is due to the intensity dependence of the GVD which leads to self steepening (shock fronts) of the pulse, see Figure 1.6, when  $s > 0$ . The wavelet method becomes handy in such circumstances, since the steepening causes numerical problems, and special techniques are used to track the shock fronts, such as the methods we talked about in the previous Section. In addition also, Zaspel<sup>15</sup> has given solutions to the higher order NLS equation which adds another additional third order dispersion term to the self-steepening equation, viz.,  $-j\left(\frac{k_3}{6k_2T_0}\right)\frac{\partial^3\tilde{u}_e}{\partial\tau^3}$ , which modifies the equation to:

$$j\frac{\partial\tilde{u}_e}{\partial z} + \frac{1}{2}\frac{\partial^2\tilde{u}_e}{\partial\tau^2} - j\left(\frac{k_3}{6k_2T_0}\right)\frac{\partial^3\tilde{u}_e}{\partial\tau^3} + js\frac{\partial(\tilde{u}_e^2|\tilde{u}_e)}{\partial\tau} + |\tilde{u}_e^2|\tilde{u}_e = 0. \quad (1.33)$$

Also, intrapulse Raman scattering plays an important role among the higher order nonlinearities which lead to the phenomenon called soliton self-frequency shift, and its effect is denoted by even another added term to Eq. (1.33), which then becomes

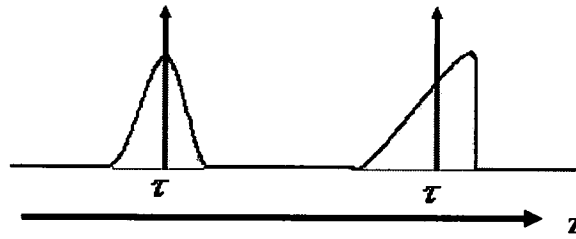


**Figure 1.6:** Schematic of self-steepening.

$$j\frac{\partial\tilde{u}_e}{\partial z} + \frac{1}{2}\frac{\partial^2\tilde{u}_e}{\partial\tau^2} - j\left(\frac{k_3}{6k_2T_0}\right)\frac{\partial^3\tilde{u}_e}{\partial\tau^3} + js\frac{\partial(\tilde{u}_e^2|\tilde{u}_e)}{\partial\tau} - \tau_R\tilde{u}_e\frac{\partial|\tilde{u}_e|^2}{\partial\tau} + |\tilde{u}_e^2|\tilde{u}_e = 0, \quad (1.31)$$



where  $\tau_R = \frac{T_R}{T_0}$ ,  $T_0 (<< 1ps)$  is the pulse width. Physically stimulated Raman scattering leads to a continuous downshift of the soliton carrier frequency when the pulse spectrum becomes so broad that the high frequency components of a pulse transfers energy to the low-frequency components of the same pulse through Raman amplification.

### 1.3 Organization of the Dissertation

The roadmap of the dissertation is as follows. In Chapter 2 we review classical numerical methods namely, finite difference, finite element and pseudo spectral techniques, and discuss their advantages and disadvantages. In Chapter 3 we introduce our first numerical technique based on wavelet theory and its applications to PDEs. Thereafter in Chapter 4 we introduce our second technique based on the Hankel or Fourier Bessel transform methods in cylindrical and spherical coordinates. We also study different numerical methods used to evaluate such integral transforms and discuss their advantages and disadvantages. In Chapter 5 we study the stability of the PDEs in hand using a semi-analytical technique based on a variational approach. Thereafter in Chapter 6 we study two different focusing arrest mechanisms, namely the nonparaxial approximation and the saturating nonlinearity. In Chapters 7 and 8 we continue with other two focusing arrest mechanisms namely dispersion management and nonlinearity management respectively, which we study numerically using Fourier Bessel transform technique and analytically using the variational technique introduced in Chapter 5. Finally, in Chapter 9 we summarize the work presented in the dissertation and outline selected future work.

#### **1.4 What is New in this Work**

In this work we develop new adaptive wavelet transform (AWT) for 1-D NLS and compare the results with FFT, FD and FEM methods. The nonlinear effects considered are self-steepening, third order nonlinearity, and DM. Also, we develop new adaptive split step Fourier Bessel transform (ASSFBT) methods, for 2 and 3-D NLS, to investigate pulse, beam and optical bullets propagation in waveguides and bulk media, and self-focusing of beams to distances very close to the point of collapse, a feature that has not been achievable by existing classical methods. Moreover, we investigate soliton stabilization effects in 2 and 3-D by using the Kapitza approximation and numerically by using the above numerical methods. Cases considered are nonparaxial beams and media containing saturating nonlinearity, periodic nonlinearity and D-dimensional DM.

## CHAPTER 2

### CLASSICAL NUMERICAL METHODS: A REVIEW

#### 2.1 Introduction

Traditional numerical techniques are basically divided between finite difference methods, where differentiation discretization is done in time and space with different stencil formulas depending on the accuracy and time consuming criteria, and the function approximation methods, or methods of weighted residuals (MWR). In MWR, we multiply the PDE by a weighting function  $\theta_k$ , and then integrate the whole equation resulting in a system of ODEs, where the function which is the solution of the PDE, is expressed as a series of ansatz functions  $\hat{\sigma}_k$ . Depending on the type of the weighting functions the method's name changes accordingly to<sup>6,69</sup>:

- *Bubnov-Galerkin or Finite Element method (FEM)*, when  $\theta_k = \hat{\sigma}_k$ , where  $\hat{\sigma}_k$  is any function series that ranges from finite support piecewise continuous functions, like triangular function, to an infinite support continuous series, like trigonometric functions.
- *Petrov-Galerkin or Point Wise Collocation method*, when  $\theta_k = \delta(x - x_k)$ , where  $\delta(x)$  is the Dirac delta function.

- *Finite Volume method (FVM) or Subdomain Collocation method*, when

$$\theta_k = X_k, \text{ where } X_k(x) = \begin{cases} 1 & x_k \leq x \leq x_{k+1} \\ 0 & \text{else where} \end{cases}.$$

- *Spectral or Pseudo-spectral method*<sup>70</sup>, when the ansatzfunctions are trigonometric functions, (like the Fourier method). Also, the ansatzfunctions might be any set of orthogonal polynomials like the Legendre, Bessel, Laguerre, Chebychev... or even piecewise polynomials like B-splines.

Often, these spectral or pseudo-spectral methods are considered to have their own category and branches, but in general we always have undefined borders, and mixed and interlaced features that may all come from a single unified theory. Figure 2.1, explains our categorization of methods which varies according to emphasis needed.

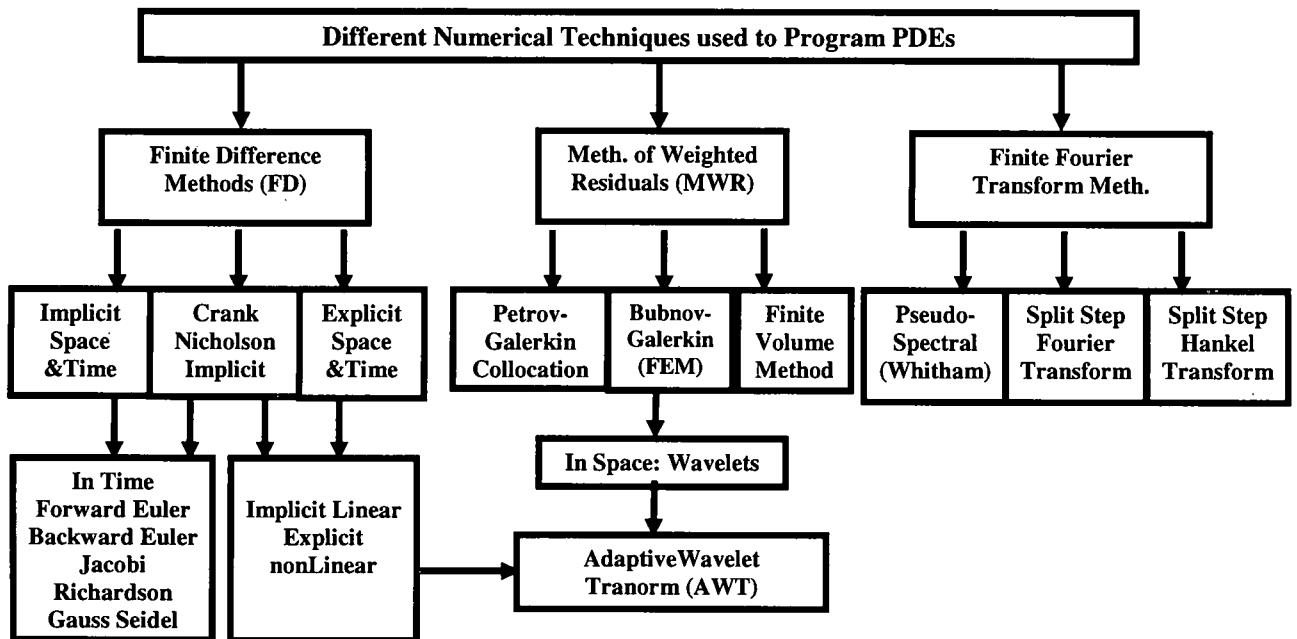


**Figure 2.1:** Classical numerical methods diagram related to AWT method.

## 2.2 Application

An example of a classical technique for 1-D NLS equation:

$$j \frac{\partial \tilde{u}_e}{\partial z} + \frac{1}{2} \frac{\partial^2 \tilde{u}_e}{\partial \tau^2} + \gamma |\tilde{u}_e|^2 \tilde{u}_e = 0 \quad (2.1)$$

is, finite difference in time and space method, which has a lot of versions that range from stable, to unstable, to conditionally stable. If we consider two stable techniques, and if we let  $E = |\tilde{u}_e|^2$ , then Eq. (2.1) becomes:

$$1. \quad j \frac{\tilde{u}_{en}^{m+1} - \tilde{u}_{en}^m}{\Delta z} + \frac{1}{4} \left( \frac{\tilde{u}_{en+1}^{m+1} - 2\tilde{u}_{en}^{m+1} + \tilde{u}_{en-1}^{m+1}}{\Delta \tau^2} + \frac{\tilde{u}_{en+1}^m - 2\tilde{u}_{en}^m + \tilde{u}_{en-1}^m}{\Delta \tau^2} \right) + \frac{\gamma'}{4} (E_n^m + E_n^{m+1}) (\tilde{u}_{en}^{m+1} + \tilde{u}_{en}^m) = 0. \quad (2.2)$$

$$2. \quad j \frac{\tilde{u}_{en}^{m+1} - \tilde{u}_{en}^m}{\Delta z} + \frac{1}{2} \left( \frac{\tilde{u}_{en+1}^m - 2\tilde{u}_{en}^m + \tilde{u}_{en-1}^m}{\Delta \tau^2} \right) + \frac{\gamma'}{2} (E_n^m) (\tilde{u}_{en-1}^m + \tilde{u}_{en+1}^m) = 0, \quad (2.3)$$

where,  $\Delta \tau = \text{time step}$  and  $\Delta z = \text{longitudinal spatial step}$ . Stability and validity of the above methods can be found in the literature<sup>3,47</sup>. For a 2-D NLS equation or self-focusing equation:

$$j \frac{\partial \tilde{u}_e}{\partial z} + \nabla_\tau^2 \tilde{u}_e + |\tilde{u}_e|^2 \tilde{u}_e = 0, \quad (2.4)$$

with cylindrical symmetry, the PDE has the form:

$$j \frac{\partial \tilde{u}_e}{\partial z} + \frac{1}{r} \frac{\partial \tilde{u}_e}{\partial r} + \frac{\partial^2 \tilde{u}_e}{\partial r^2} + |\tilde{u}_e|^2 \tilde{u}_e = 0. \quad (2.5)$$

Two methods to solve Eqs. (2.4) or (2.5) are:

#### A. A Crank-Nicholson Alternating Direction Implicit (ADI) method<sup>71</sup>

Eq. (2.4) becomes:  $\frac{\partial \hat{u}_e}{\partial z} = j \left( \frac{\partial^2 \tilde{u}_e}{\partial x^2} + \frac{\partial^2 \tilde{u}_e}{\partial y^2} \right) + j |\tilde{u}_e|^2 \tilde{u}_e$ . After discretization we have:

$$\begin{aligned}
\frac{\tilde{u}_{ek,l}^{n+1} - \tilde{u}_{ek,l}^n}{\Delta z} &= j \left[ \frac{(\tilde{u}_{ek+1,l}^n - 2\tilde{u}_{ek,l}^n + \tilde{u}_{ek-1,l}^n)}{\Delta x^2} + \frac{(\tilde{u}_{ek,l+1}^{n+1} - 2\tilde{u}_{ek,l}^{n+1} + \tilde{u}_{ek,l-1}^{n+1})}{\Delta y^2} \right] + \frac{j}{2} |\tilde{u}_{ek,l}^n|^2 (\tilde{u}_{ek,l}^{n+1} + \tilde{u}_{ek,l}^n), \\
\frac{\tilde{u}_{ek,l}^{n+2} - \tilde{u}_{ek,l}^{n+1}}{\Delta z} &= j \left[ \frac{(\tilde{u}_{ek+1,l}^{n+2} - 2\tilde{u}_{ek,l}^{n+2} + \tilde{u}_{ek-1,l}^{n+2})}{\Delta x^2} + \frac{(\tilde{u}_{ek,l+1}^{n+1} - 2\tilde{u}_{ek,l}^{n+1} + \tilde{u}_{ek,l-1}^{n+1})}{\Delta y^2} \right] + \frac{j}{2} |\tilde{u}_{ek,l}^{n+1}|^2 (\tilde{u}_{ek,l}^{n+2} + \tilde{u}_{ek,l}^{n+1}).
\end{aligned}
\tag{2.6}$$

### B. ADI (With Cylindrical Symmetry)<sup>46</sup>

Eq. (2.5) becomes after discretization:

$$\begin{aligned}
\frac{\tilde{u}_{ek}^{n+1} - \tilde{u}_{ek}^n}{\Delta z} &= j \left[ \left( \frac{\tilde{u}_{ek-1}^n - 2\tilde{u}_{ek}^n + \tilde{u}_{ek+1}^n}{2\Delta r^2} \right) + \left( \frac{\tilde{u}_{ek-1}^{n+1} - 2\tilde{u}_{ek}^{n+1} + \tilde{u}_{ek+1}^{n+1}}{2\Delta r^2} \right) \right] \\
&+ j \left[ \frac{\tilde{u}_{ek+1}^n - \tilde{u}_{ek-1}^n + \tilde{u}_{ek+1}^{n+1} - \tilde{u}_{ek-1}^{n+1}}{4\Delta r \cdot r_k} \right].
\end{aligned}
\tag{2.7}$$

Also, another kind of classical technique for 1 and 2-D NLS equation is a pseudo-spectral technique, called a Split Step Fast Fourier Transform (FFTSS)<sup>43,57</sup> method. This method is based on the following theory. Consider the general form of an evolution equation:

$$\frac{\partial \tilde{u}_e}{\partial z} = jL\tilde{u}_e + jN_{nl}(\tilde{u}_e)\tilde{u}_e, \quad \vec{r} \in \mathfrak{R}^D, \quad z \geq 0,
\tag{2.8}$$

where  $D$  is the transverse dimension in space, and where  $L_r(\tilde{u}_e) = \Delta_T \tilde{u}_e$ ,  $N_{nl}(\tilde{u}_e) = |\tilde{u}_e|^2$ . Eq.

(2.8) needs to be solved with the initial condition  $\tilde{u}_e(\vec{r}, z=0) = \tilde{u}_0(\vec{r})$ . So the above equation

can be written as:  $\tilde{u}_{e,t} = j[L_r + N_{nl}(\tilde{u}_e)](\tilde{u}_e)$ , and the solution can be advanced in space as:

$\tilde{u}_e(\vec{r}, z + \Delta z) \approx \exp\{j\Delta z[L_r + N_{nl}(\tilde{u}_e)]\}\tilde{u}_e(\vec{r}, z)$ . Note that, the previous equation is exact if

$|\tilde{u}_e|^2$  is not a function of  $z$ . Applying the split step technique we get:

$\tilde{u}_e(\vec{r}, z + \Delta z) \approx \exp(j\Delta z L_r) \times \exp[j\Delta z N_{nl}(\tilde{u}_e)]\tilde{u}_e(\vec{r}, z)$ , which is true only if  $L_r$  and  $N_{nl}$  are

two

commuting

operators

$$\exp(j\Delta z L_r) \exp[j\Delta z N_{nl}(\tilde{u}_e)] = \exp\left\{j\left[L_r \Delta z + N_{nl} \Delta z + \frac{1}{2}[L_r, N_{nl}](\Delta z^2) + \dots\right]\right\}, \quad \text{where,}$$

$[L_r, N_{nl}] = L_r N_{nl} - N_{nl} L_r$ , represents the commutation of  $L_r$  and  $N_{nl}$  according to Baker-Housdorff formula. So up to second order, and when the operators commute, we have:  $\exp\{j\Delta z [L_r + N_{nl}(\tilde{u}_e)]\} = \exp(j\Delta z L_r) \exp[j\Delta z N_{nl}(\tilde{u}_e)]$ , and the split step method is valid.

So, we can successively solve the equations:  $\frac{\partial \tilde{u}_e}{\partial z} = jL_r \tilde{u}_e, \frac{\partial \tilde{u}_e}{\partial z} = jN_{nl}(\tilde{u}_e) \tilde{u}_e$ . Hence,

$$\tilde{u}_e^{n+\frac{1}{2}} = \exp\left(j\frac{\Delta z}{2} L_r\right) \tilde{u}_e^n, \quad \tilde{u}_e^{n+\frac{3}{2}} = \exp[j\Delta z N_{nl}(\tilde{u}_e^n)] \tilde{u}_e^{n+\frac{1}{2}}, \quad \text{and} \quad \tilde{u}_e^{n+2} = \exp\left(j\frac{\Delta z}{2} L_r\right) \tilde{u}_e^{n+\frac{3}{2}},$$

which is a symmetrical form of the split step method. For example, for the 1-D NLS Eq. (2.1), we have the algorithm shown in Figure 2.2, while for the 2-D NLS Eq. (2.4), the algorithm is shown in Figure 2.3.

### 2.3 Summary

In this Chapter we discussed classical numerical techniques that is usually used to solve evolution equations, namely FD and SSFFT. In Chapter 3 we will introduce our first numerical technique based on wavelet theory and its applications to PDEs. We will start by defining the wavelet transform and the multiresolution analysis. Then we shift to the evaluation of the connection coefficients. In the end we apply the method to well known evolution equations in the literature and finally to the NLS equation and its variations.

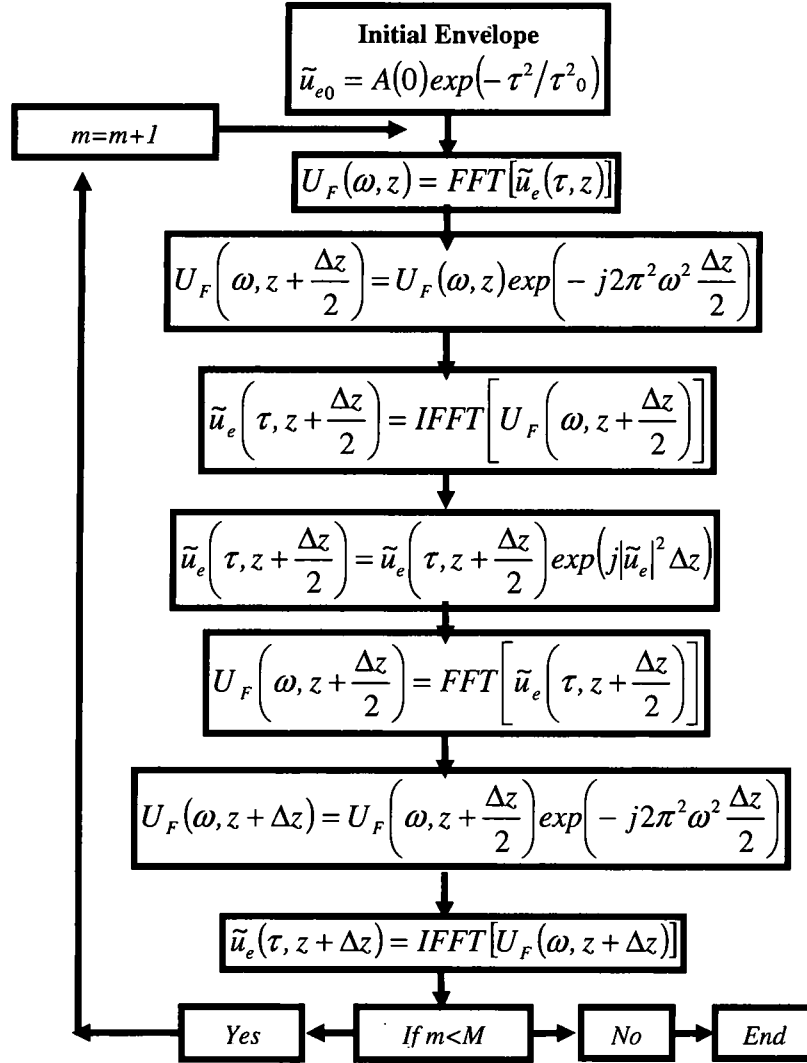


**Figure 2.2:** SSFFT algorithm for 1-D NLS.



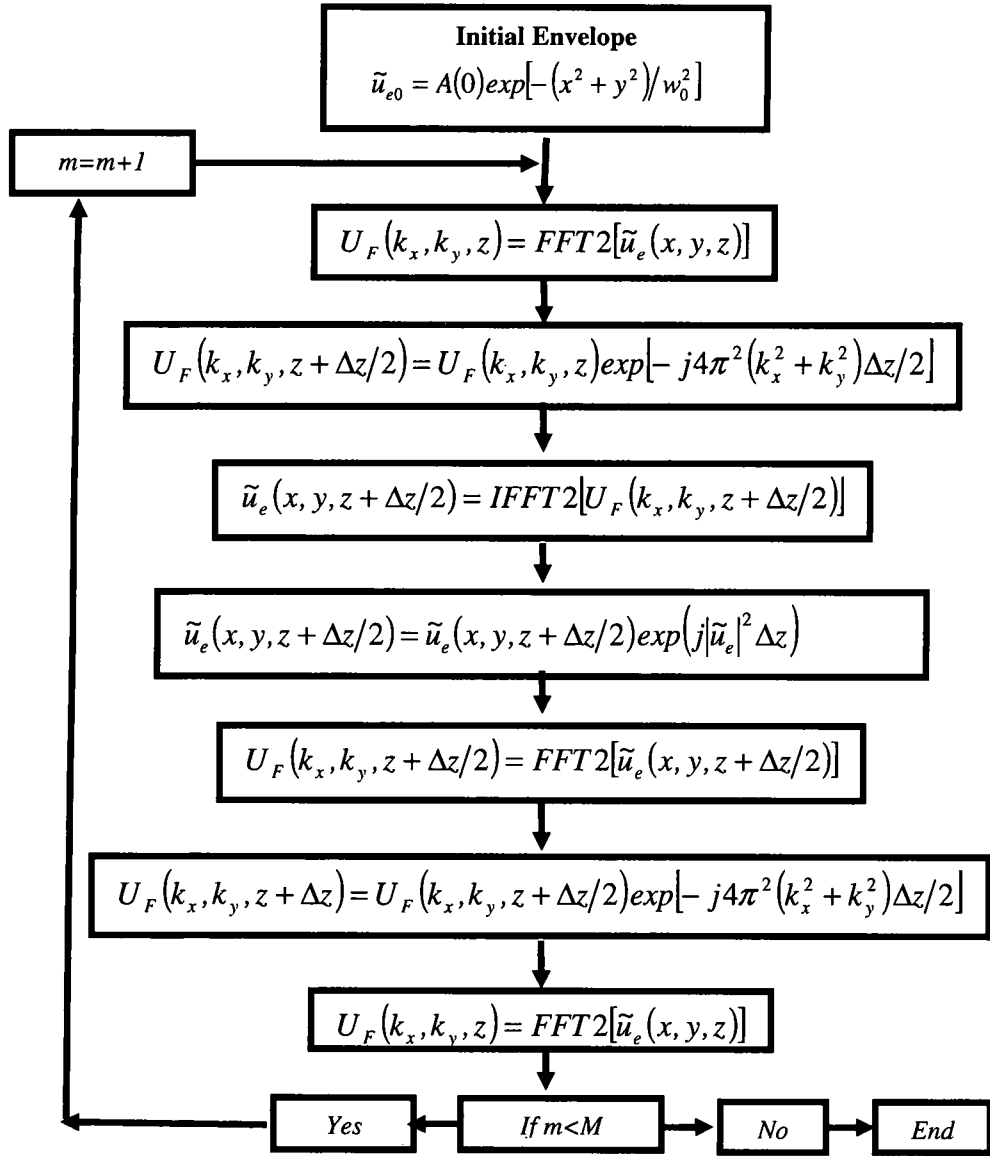


**Figure 2.3:** SSFFT algorithm for 2-D NLS.

## CHAPTER 3

### BASIC WAVELET THEORY AND APPLICATION TO PDEs

#### 3.1 Introduction

As mentioned in Chapter 2, the wavelet method is devised as a combination of FEM in space domain, and FD method in time domain. In the literature, there are many ways to solve PDEs and evolution equations using wavelets<sup>7,12,72</sup>, each with its advantages and disadvantages, and are based on complicated mathematical theories<sup>12,10,11</sup>, which makes deriving simple algorithm a very difficult task. Most of the methods, are also dependent on the specific PDE<sup>73,74,75</sup>, and thus, there is no universal solution for all problems<sup>76</sup>. The various methods that exist range from, collocation<sup>77,78,79</sup>, FEM<sup>80</sup>, FVM, Split Step, Symplectic (higher order FD<sup>81</sup>). Combinations of these methods, are applied to different parts of the PDE and/or different kinds of wavelets are incorporated as weighting or ansatz functions<sup>82,83</sup>.

Before we start to develop the algorithms used to study some of the above evolution equations, we give a brief review of some properties of wavelets and why they are so appealing in many applications, including the numerical solution of PDEs.<sup>7,13</sup>

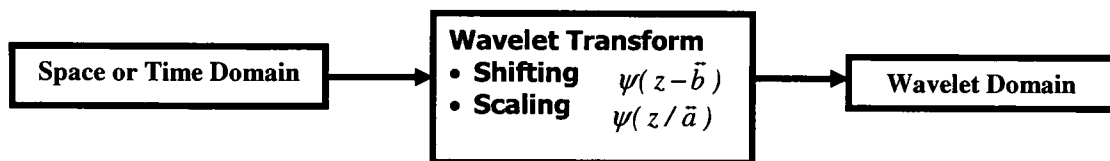


Figure 3.1: Wavelet transform use and properties.

Figure 3.1 shows that wavelets are used as basis functions to perform a transform from one domain (space or time) to another domain called the wavelet domain. The operation is called the wavelet transform. The process begins with a mother wavelet  $\psi(z)$ , followed by shifting  $\psi(z - \vec{b})$ , and scaling,  $\psi(z/\vec{a})$ .

A wavelet is often a compact support function,  $\in L^2(R)$  and satisfies the following<sup>84</sup>:

- $\psi(z)$  is an oscillatory function and drops to zero as  $|z| \rightarrow \infty$ .
- $\Psi(\omega)$ , the Fourier transform of  $\psi(z)$ , satisfies the admissibility criterion:

$$\int_{-\infty}^{\infty} |\Psi(\omega)|^2 d\omega / |\omega|^2 < \infty.$$

- $\int_{-\infty}^{\infty} \psi(z) dz = 0$ , implying that wavelet average value is zero.
- $\Psi(0) = 0$  and  $\Psi(\infty) = 0$ , i.e., it acts like a band pass filter.

Additional useful properties are:

- Symmetry.
- Order of differentiability.
- Number of vanishing moments  $\int_{-\infty}^{\infty} z^j \psi(z) dz = 0$  for  $j = 0, 1, \dots, p-1$ .

Any wavelet satisfying the above criteria, can be used to form a set of wavelet basis functions  $\{\psi_{\vec{a}, \vec{b}}(z)\}$ , generated by scaling and shifting as follows:

$\psi_{\vec{a}, \vec{b}}(z) = \vec{a}^{-1/2} \psi\left[(z - \vec{b})/\vec{a}\right]$ ,  $\vec{a} = 2^{-j}$ ,  $\vec{b} = k \times 2^{-j}$ , if we use the dyadic scale. Then, every

function  $\tilde{u}_e(z)$  can be written in the form:

$\tilde{u}_e(z) = \sum_j \sum_k c_{j,k} \psi_{j,k}(z)$  where  $c_{j,k} = \int_{-\infty}^{\infty} \tilde{u}_e(z) \psi_{j,k}(z) dz$ . However, this formula is

not practical since we have to perform infinite sums to accurately represent the function.

To solve this problem, we introduce a scaling function  $\phi(z)$ . The relation between these functions, are understood from the multi-resolution analysis (MRA) described below.

Indeed, there is a relation between digital filters and the wavelet and scaling functions, where the scaling function comes from the low pass filter (LPF) while the wavelet function comes from the high pass filter (HPF). Thus the properties of the wavelet functions are reflected in digital filters which we use to generate them through dilation and recursion. Thus:

$$\phi(z) = 2 \sum_{k=0}^{\hat{L}-1} h(k) \phi(2z - k), \quad (3.1a)$$

where  $h(k)$  is a FIR LPF, and  $\int_{-\infty}^{\infty} \phi(z) dz = 1$  or  $\sum_k h(k) = 1$ . Also,

$$\psi(z) = 2 \sum_{k=0}^{\hat{L}-1} g(k) \phi(2z - k). \quad (3.1b)$$

It can be proven that  $g(k) = (-1)^k h(1 - k)$ , and that  $\sum_k g(k) = 0$ .

### 3.2 Multi-Resolution Analysis

The goal of multi-resolution analysis (MRA)<sup>13,84</sup> is to decompose the function space into subspaces via projection. There are two types of subspaces: a scaling subspace at level  $j$ ,  $V_j$ , and a wavelet subspace at level  $j$ ,  $W_j$ , defined as:

$$V_j = \sum_k a_{j,k} \phi_{j,k}(z), W_j = \sum_k b_{j,k} \psi_{j,k}(z), \quad (3.2)$$

where

$$a_{j,k} = \langle \tilde{u}_e, \phi_{j,k} \rangle = \int_{-\infty}^{\infty} \tilde{u}_e(z) \phi_{j,k}(z) dz, \quad (3.3a)$$

$$b_{j,k} = \langle \tilde{u}_e, \psi_{j,k} \rangle = \int_{-\infty}^{\infty} \tilde{u}_e(z) \psi_{j,k}(z) dz. \quad (3.3b)$$

So, we can draw a sketch to show how the signal  $V_j = \psi_j(z)$  is decomposed or projected on the corresponding subspaces through the MRA structure as shown in Figure 3.2.

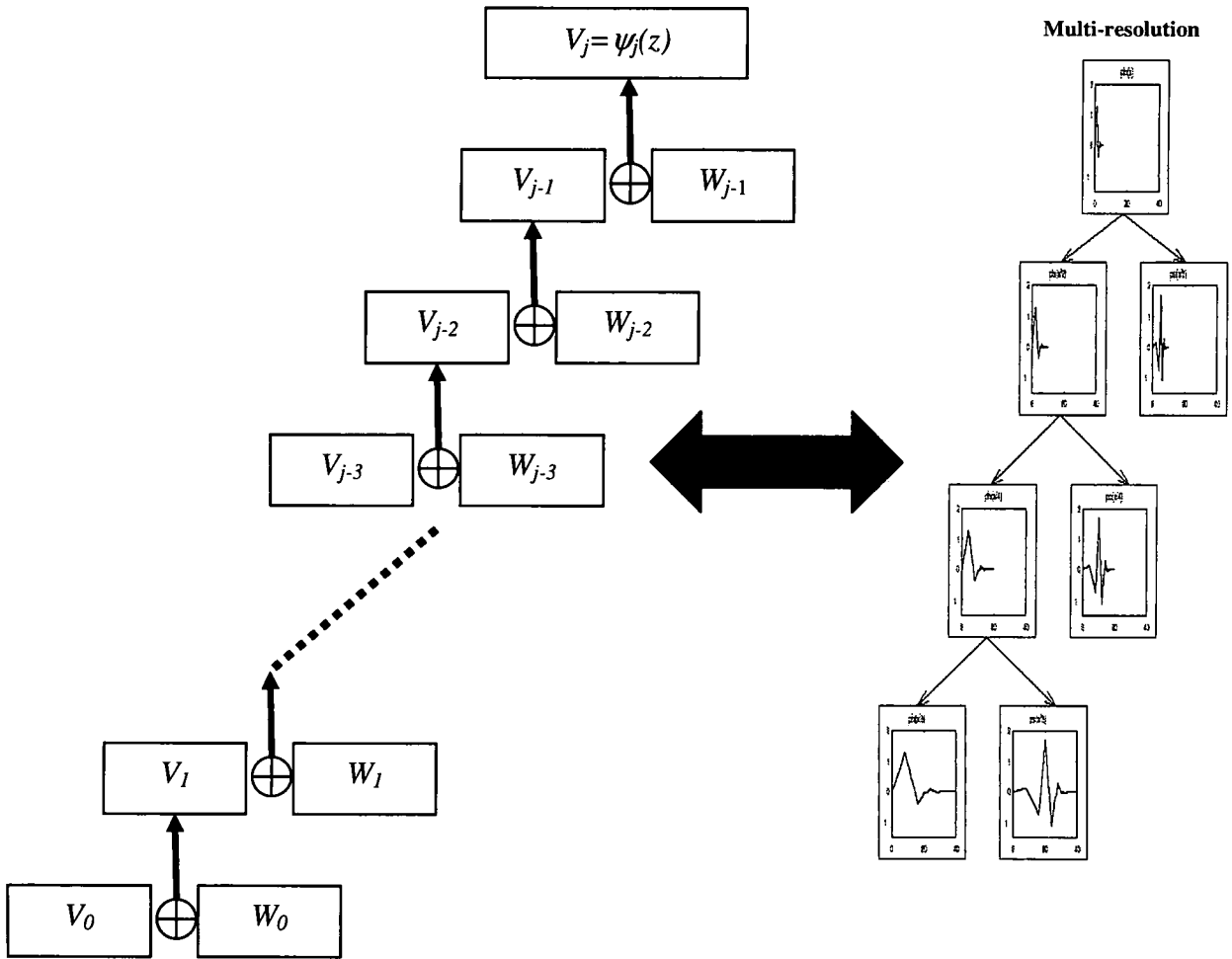


**Figure 3.2:** MRA diagram

For this decomposition to be true, we have to have the completeness property, and that can happen if the scaling and the wavelet functions form an orthonormal basis for the subspace decomposition<sup>11,9</sup>. This can be stated as follows:

$$\begin{aligned}
\int_{-\infty}^{\infty} \phi(z-n) \phi(z-m) dz &= \delta(m-n), \\
\int_{-\infty}^{\infty} \phi(z-n) \psi(z-n) dz &= 0, \\
\int_{-\infty}^{\infty} \psi_{j,k}(z) \psi_{m,n}(z) dz &= \delta(j-m) \delta(k-n).
\end{aligned} \tag{3.3}$$

Figure 3.3a shows the Symlet (derived by Daubechies)<sup>10</sup> scaling and wavelet function respectively. Figure 3.3b shows the coefficients of the reconstruction low pass and high pass filters defined in Eqs.(3.1a) and (3.1b) using MATLAB<sup>84</sup>.

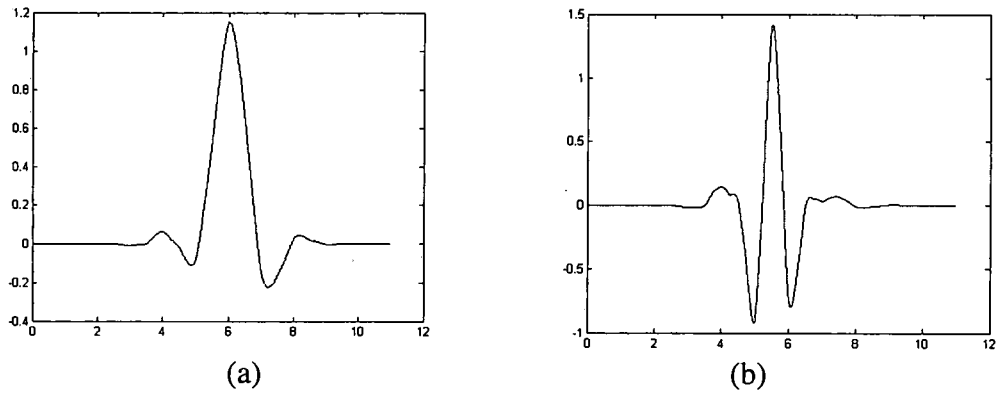


**Figure 3.3:** (a) Symlet (Sym4) scaling function and (b) Sym4 wavelet function.

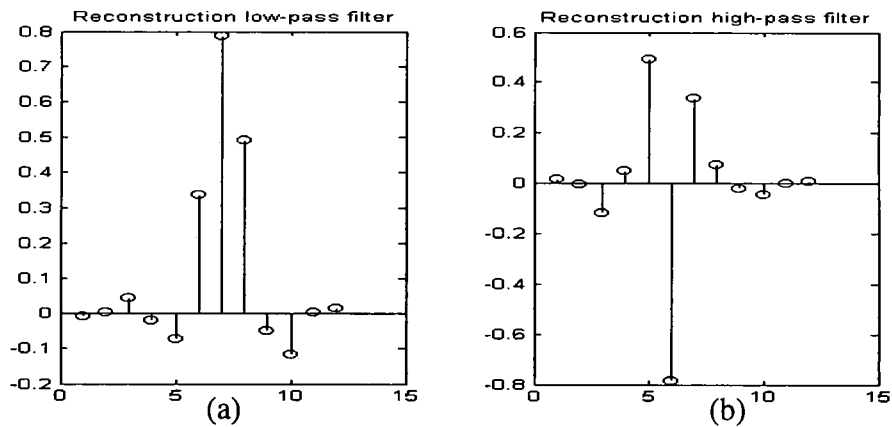


**Figure 3.4:** (a) Low pass reconstruction filter  $h(k)$  and (b) High pass reconstruction filter  $g(k)$ .

We use a MATLAB supplied Symlet family of wavelets for our subsequent calculations. Symlet wavelets are compactly supported wavelets with the least asymmetry and highest number of vanishing moments for a given support width, with scaling filters are near linear phase filters.

**Table 3.1:** Some of the wavelet families and their associated properties<sup>1</sup>

Wavelet Family	Symmetry	Analytic Expression	Compact Support	# of Zero Moments	Regularity
Coiflet	Near	No	Yes	Yes	Yes
Daubechies	No	No	Yes	Yes	Yes
Gaussian	Yes	Yes	No	No	No
Haar	Yes	Yes	Yes	No	No
Mexican Hat	Yes	Yes	No	No	No
Meyer	Yes	Yes	No	No	No
Morlet	Yes	Yes	No	No	No
Symlet	Near	No	Yes	Yes	Yes

### 3.3 Evaluation of Connection Coefficients<sup>72,85,86,87</sup>

Although we know from the previous Section how to calculate the wavelet or scaling coefficients of the series representation of the function in question, it remains to know also how can one efficiently compute derivatives of the function in terms of the wavelet or scaling expansion coefficients. Not only that, one also needs to evaluate nonlinear operators on functions in terms of the coefficients of the original function. The connection coefficients are used to evaluate the coefficients of the matrices that we obtain while applying our method to the different evolution equations. As an example, if we

want to represent  $\tilde{u}_e(z)$  in terms of a wavelet series:

$$\tilde{u}_e(z) = \sum c_k \phi_k(z) + \sum \sum c_{jk} \psi_{jk}(z), \quad \text{and} \quad \text{differentiate}$$

$$\tilde{u}'_e(z) = \sum c_k \phi'_k(z) + \sum \sum c_{jk} \psi'_{jk}(z). \quad \text{Expand the derivatives of the scaling and wavelet functions in a wavelet series:}$$

$$\begin{aligned} \phi'_l(z) &= \sum_i \bar{r}_{il} \phi_i + \sum_{ij} \bar{\beta}_{il}^j \psi_{ij}, \\ \psi'_{jl}(z) &= \sum_i \bar{\gamma}_{il}^j \phi_i + \sum_{ij} \bar{\alpha}_{il}^j \psi_{ij}, \end{aligned} \quad (3.4)$$

where:

$$\begin{aligned} \bar{\alpha}_{il}^j &= 2^{-j} \int_{-\infty}^{\infty} \psi(2^{-j}z - i) \psi'(2^{-j}z - l) 2^{-j} dz = 2^{-j} \bar{\alpha}_{i-l}, \\ \bar{\beta}_{il}^j &= 2^{-j} \int_{-\infty}^{\infty} \psi(2^{-j}z - i) \phi'(2^{-j}z - l) 2^{-j} dz = 2^{-j} \bar{\beta}_{i-l}, \\ \bar{\gamma}_{il}^j &= 2^{-j} \int_{-\infty}^{\infty} \phi(2^{-j}z - i) \psi'(2^{-j}z - l) 2^{-j} dz = 2^{-j} \bar{\gamma}_{i-l}, \\ \bar{r}_{il}^j &= 2^{-j} \int_{-\infty}^{\infty} \phi(2^{-j}z - i) \phi'(2^{-j}z - l) 2^{-j} dz = 2^{-j} \bar{r}_{i-l}. \end{aligned} \quad (3.5)$$

Renaming the coefficients of  $\bar{\alpha}$ ,  $\bar{\beta}$ ,  $\bar{\gamma}$ ,  $\bar{r}$ , we get:

$$\begin{aligned} \bar{\alpha}_l &= \int_{-\infty}^{\infty} \psi(z-l) \frac{d}{dz} \psi(z) dz, \quad \text{where} & \bar{\alpha}_l &= 2 \sum_{k=0}^{\hat{L}-1} \sum_{k'}^{\hat{L}-1} g_k g_{k'} \bar{r}_{2l+k-k'}, \\ \bar{\beta}_l &= \int_{-\infty}^{\infty} \psi(z-l) \frac{d}{dz} \phi(z) dz, \quad \text{where} & \bar{\beta}_l &= 2 \sum_{k=0}^{\hat{L}-1} \sum_{k'}^{\hat{L}-1} g_k h_{k'} \bar{r}_{2l+k-k'}, \\ \bar{\gamma}_l &= \int_{-\infty}^{\infty} \phi(z-l) \frac{d}{dz} \psi(z) dz, \quad \text{where} & \bar{\gamma}_l &= 2 \sum_{k=0}^{\hat{L}-1} \sum_{k'}^{\hat{L}-1} h_k g_{k'} \bar{r}_{2l+k-k'}, \\ \bar{r}_l &= \int_{-\infty}^{\infty} \phi(z-l) \frac{d}{dz} \phi(z) dz, \quad \text{where} & \bar{r}_l &= 2 \left[ \bar{r}_{2l} + \frac{1}{2} \sum_{k=1}^{\hat{L}/2} q_{2k-1} (\bar{r}_{2l-2k+1} + \bar{r}_{2l+2k-1}) \right], \\ & \text{and} & & \sum_l l \bar{r}_l = -1. \end{aligned} \quad (3.6)$$



Here it is sufficient to calculate  $\bar{r}_l$  only since  $\bar{\alpha}, \bar{\beta}, \bar{\gamma}$ , are functions of  $\bar{r}$ , and  $g, h$ , are as defined before. In a similar fashion if we have a second derivative of the function  $\tilde{u}_e(z)$ ,

we get:  $\bar{r}_l^{(n)} = \int_{-\infty}^{\infty} \phi(z-l) \frac{d^n}{dz^n} \phi(z) dz$ , where

$$\begin{aligned} \bar{r}_l^{(n)} &= 2^n \left[ \bar{r}_{2l} + \frac{1}{2} \sum_{k=1}^{\hat{L}/2} \hat{q}_{2k-1} \left( \bar{r}_{2l-2k+1}^{(n)} + \bar{r}_{2l+2k-1}^{(n)} \right) \right], \\ \text{and} \quad \sum_l l^n \bar{r}_l^{(n)} &= (-1)^n n!, \end{aligned} \quad (3.7a)$$

where  $\hat{q}_{2k-1} = 2 \sum_{i=0}^{\hat{L}-2k} h_i h_{i+2k-1}$ ,  $k = 1, \dots, \hat{L}/2$ , is the autocorrelation coefficient of  $\{h_k\}_{k=0}^{\hat{L}-1}$ .

Two possible cases must be considered:

1. If  $n$  is even,

$$\begin{aligned} \bar{r}_l^{(n)} &= \bar{r}_{-l}^{(n)}, \\ \sum_l l^{2\tilde{n}} \bar{r}_l^{(n)} &= 0, \text{ for } \tilde{n} = 1, \dots, \frac{n}{2} - 1. \\ \text{and } \sum_l \bar{r}_l^{(n)} &= 0, \end{aligned} \quad (3.7b)$$

2. If  $n$  is odd,

$$\begin{aligned} \bar{r}_l^{(n)} &= -\bar{r}_{-l}^{(n)}, \\ \text{and } \sum_l l^{2\tilde{n}-1} \bar{r}_l^{(n)} &= 0, \text{ for } \tilde{n} = 1, \dots, \frac{n-1}{2}. \end{aligned} \quad (3.7c)$$

Note that, there are also *three* and *four* factor connection coefficients:

$$\bar{r}_{lm} = \int_{-\infty}^{\infty} \phi^{(n)}(z) \phi_l(z) \phi_m(z) dz. \quad (3.8)$$

### 3.4 Wavelet Method for Solving Some of the Classical PDEs

The unknown function  $\tilde{u}_e$ , which is expanded in terms of a linear combination of

orthogonal functions  $\phi(k)$ :  $\tilde{u}_e = \tilde{u}_{e,J} = \sum_{k=-\infty}^{\infty} c_{J,k} \phi_k = \sum_{k=0}^{N-1} c_{J,k} \phi_k$  where  $c_{J,k}$ 's are the expansion coefficients at level  $J$  in the transform space and are calculated by:

$$c_{J,k} = \langle \tilde{u}_e, \phi_{J,k} \rangle = \int_{-\infty}^{\infty} \tilde{u}_e(z) \phi_{J,k}(z) dz, \text{ where } \phi_{J,k} \text{ plays the role of } \hat{\sigma}_k, \text{ which is the ansatz}$$

function as discussed earlier. The weighted functions introduced here are  $\theta_k$ , force the truncated series expansion to satisfy the PDE, with a minimized norm. A necessary and sufficient condition for the MWR is the orthogonality between  $\{\phi \perp \theta : \forall k \in \mathbf{Z}\}$ . The choice of the proper expansion functions and weighting functions, leads to the spectral accuracy which we wish to minimize.

The three most used spectral methods are the Galerkin, the Tau and the collocation methods. Basically they are the same, but they differ in the choice of the weighting functions. In the Galerkin method that we have adopted, we use the same expansion and weighting functions. The Tau method uses different weighting functions to satisfy the boundary conditions and the collocation method uses Dirac delta functions as the weighting functions as indicated in Figure 2.1. The basic equation in this method

$$\text{is: } \int_{-\infty}^{\infty} \{PDE[\tilde{u}_e(z, \tau)]\} \theta_j(z) dz = \int_{-\infty}^{\infty} \{PDE[\tilde{u}_e(z, \tau)]\} \phi_j(z) dz = 0, \text{ if we use the Galerkin}$$

method. Figure 3.5, shows how the initial profile  $\tilde{u}_e(\tau, z) = \sum_{l=0}^{N-1} a_{J,l}(\tau) \phi_l(z)$  is expressed

in terms of the scaling wavelets at level  $J$  resulting in a sampling of the initial function,

which eventually will evolve according to the corresponding PDE. In the next subSections we will apply this method to some of the PDEs mentioned earlier.

### 3.4.1 The Heat Equation (HE)

The HE is defined as:  $\frac{\partial u}{\partial T} - \hat{\alpha}^2 \frac{\partial^2 u}{\partial Z^2} = 0$ , which is solved along with the initial conditions:  $u(Z,0) = \exp(-Z^2)$ , with  $-\infty < Z < \infty, 0 < T < \infty$ . This equation admits the solution:

$$u(Z,T) = \frac{1}{\sqrt{1+4\hat{\alpha}^2 T}} \exp\left(\frac{-Z^2}{1+4\hat{\alpha}^2 T}\right). \quad (3.9)$$

Now, if we apply the wavelet method and expand the function  $u(Z,T)$  in terms of the wavelet scaling functions as explained before we get:

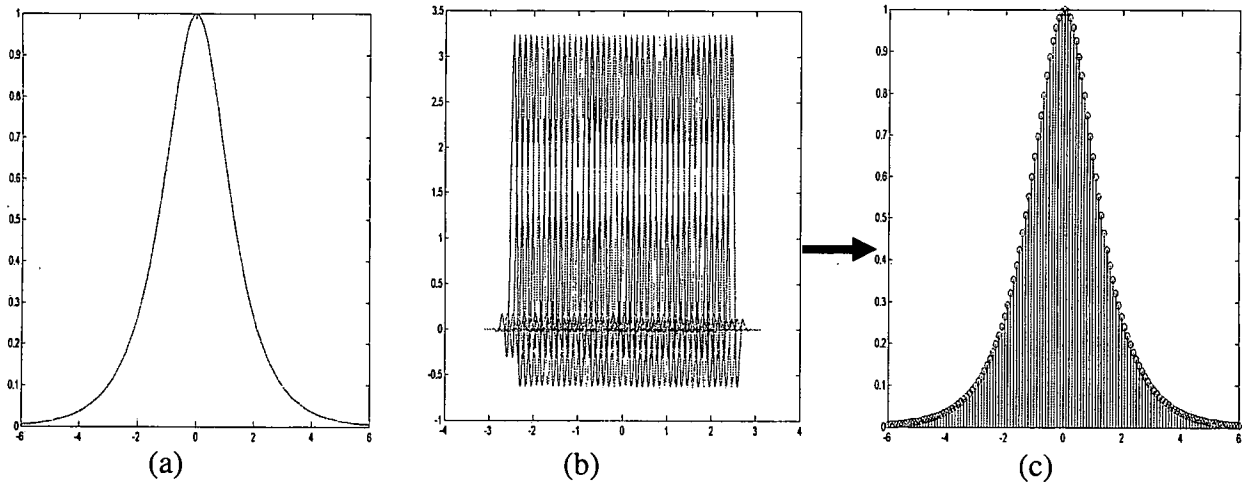


**Figure 3.5:** (a) Initial function profile, (b) Wavelet scaling functions at level  $J$ , and (c) Approximated function using  $a_{J,l}$ 's as expansion coefficients.

$$u(Z,T) = \sum_{l=0}^{N-1} a_l(T) \phi_l(Z), \quad (3.10)$$

and the coefficients  $a_i$  are found by the equation:  $a_i(T_0) = \int_{Z_{min}}^{Z_{max}} u(Z, T_0) \phi_i(Z) dZ$ .

Applying the MWR to the HE we get:

$$\int_{Z_{min}}^{Z_{max}} [u_T - \hat{\alpha}^2 u_{ZZ}] \phi_k(Z) dZ = 0. \quad (3.11)$$

Replacing  $u(Z, T)$  or its derivatives by its value from Eq. (3.10) we get for the first term

of Eq. (3.11):  $\int_{Z_{min}}^{Z_{max}} u_T \phi_k(Z) dZ = \sum_i \frac{d}{dT} a_i \int \phi_i(Z) \phi_k(Z) dZ = I \bar{a}'(T)$ , where

$$\bar{a}'(T) = \frac{\bar{a}(T + \Delta T) - \bar{a}(T)}{\Delta T}, \bar{a} = \begin{bmatrix} a_1 \\ \vdots \\ a_M \end{bmatrix}. \quad (3.12)$$

In a similar way, for the second term of Eq. (3.11) we get:

$$\int_{Z_{min}}^{Z_{max}} u_{ZZ} \phi_k(Z) dZ = \int_{Z_{min}}^{Z_{max}} \frac{\partial^2}{\partial Z^2} [\sum a_i(T) \phi_i(Z)] \cdot \phi_k(Z) dZ = \sum a_i(T) \cdot \int_{Z_{min}}^{Z_{max}} \frac{\partial^2 \phi_i}{\partial Z^2} \phi_k(Z) dZ = \bar{K} \cdot \bar{a}(T),$$

where

$$\bar{K}(l, k) = \int \phi_l'' \phi_k dZ, \bar{K} = \begin{bmatrix} \bar{K}(1,1) & & \\ & \ddots & \\ & & \bar{K}(N,N) \end{bmatrix}^T. \quad (3.13)$$

Applying these results to Eq. (3.11) and using a forward Euler scheme in time we arrive at:

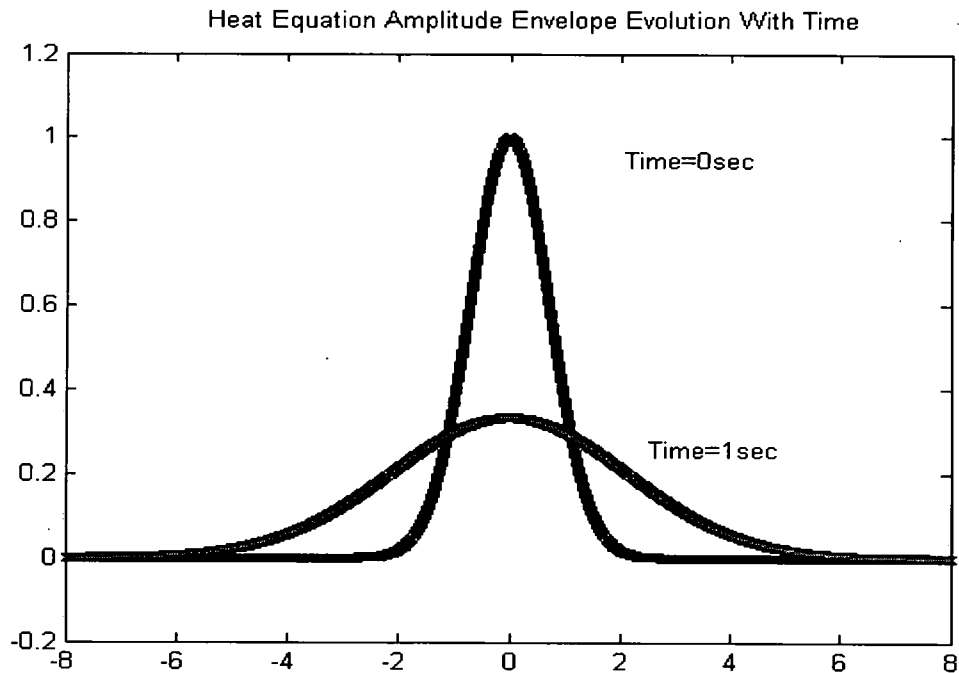
$$\bar{a}(T + \Delta T) = \bar{a}(T) + \hat{\alpha}^2 \Delta T \bar{K} \bar{a}(T). \quad (3.14)$$

Figure 3.6, at  $T=0$ , and at  $T=1$  shows the analytical solution along with the wavelet approximation solution which coincides perfectly with the analytical result. This equation is used to verify the validity of the algorithm. Note that the only matrix to be computed here is the  $\bar{K}$  matrix which is  $N \times N$ , where  $N$  is the length of the vector

containing the elements of the scaling coefficients  $a_l(T)$  that change with time as defined in Eq. (3.12). This matrix is only computed once before time stepping, hence, there is no need to go to higher *levels* in this type of PDE where no steepening or focusing occurs. This reduces computation time to (minutes). Depending on the *level* chosen, the number of coefficients calculated  $N$ , is doubled if the *level* is increased by one according to the following formula:  $N = Z_{max} \times 2^{level} - (MX - 1)$ , where  $Z_{max}$  is the maximum range of the initial profile, and  $MX$  is equal to the maximum range of the original SYM4 wavelet which is equal to 11 as shown in Figure 3.4a. Since the program execution time is  $\propto N^2$  according to Eq. (3.14), where we have  $N^2$  multiplications in every pass or time step, then increasing the *level* by one makes the execution time 4 times slower.

### 3.4.2 The First Order Nonlinear Wave Equation

The first order nonlinear wave equation is defined as:



**Figure 3.6:** Heat equation evolution with time.

$\frac{\partial u}{\partial T'} + \hat{\eta} u \frac{\partial u}{\partial Z'} = 0$ ,  $Z' = Z - v_{p0} T$ ,  $T' = T$ ,  $\hat{\eta} = \hat{\beta}_2 v_{p0} = 1$ , is solved along with the initial conditions:  $u(Z', 0) = \exp(-Z'^2)$ , with  $-\infty < Z' < \infty$ ,  $0 < T' < \infty$ . This equation admits as a general solution:  $u(Z', T') = u(Z' - uT')$ . In a fashion similar to the heat equation we obtain:

$$\int_{Z'_{min}}^{Z'_{max}} [u_{T'} + uu_{Z'}] \phi_k(Z') dZ' = 0. \quad (3.15)$$

The only difference is that in the second term of Eq. (3.15) we have:

$$\begin{aligned} \int_{Z'_{min}}^{Z'_{max}} u_{Z'} u \phi_k(Z') dZ' &= \int_{Z'_{min}}^{Z'_{max}} \frac{\partial}{\partial Z'} [\sum a_l(T') \phi_l(Z')] \cdot [\sum a_n(T') \phi_n(Z')] \phi_k(Z') dZ' \\ &= \int_{Z'_{min}}^{Z'_{max}} \left[ \sum a_l(T') \frac{d}{dZ'} \phi_l(Z') \right] \cdot [\sum a_n(T') \phi_n(Z')] \phi_k(Z') dZ' \\ &= \sum a_l \cdot \left\{ \sum a_n \int \frac{d\phi_l}{dZ'} \cdot \phi_k(Z') \phi_n(Z') dZ' \right\} = \{\tilde{\Psi}_{l,k} \cdot \bar{a}(T')\} \bar{a}(T') \\ &= \bar{D}(T') \cdot \bar{a}(T'), \end{aligned}$$

where  $\tilde{\Psi}_{l,k}(n) = \int \frac{d\phi_l}{dZ'} \cdot \phi_k(Z') \phi_n(Z') dZ'$ ,  $\tilde{\Psi}_{l,k} = \begin{bmatrix} \int \frac{d\phi_l}{dZ'} \cdot \phi_k(Z') \phi_1(Z') dZ' \\ \vdots \\ \int \frac{d\phi_l}{dZ'} \cdot \phi_k(Z') \phi_N(Z') dZ' \end{bmatrix}^T$ , and

$$\bar{D}(T') = \begin{bmatrix} \tilde{\Psi}_{1,1} \bar{a}(T') & & \\ & \ddots & \\ & & \tilde{\Psi}_{N,N} \bar{a}(T') \end{bmatrix}^T. \quad (3.16)$$

Applying these results to Eq. (3.15) and using a forward Euler scheme in time domain as mentioned earlier we arrive at:

$$\bar{a}(T' + \Delta T') = \bar{a}(T') - \Delta T' \bar{D}(T') \cdot \bar{a}(T'). \quad (3.17)$$

Also, this equation will develop a shock wave at a certain time and we use the wavelet method to track the steepening as shown in Figure 3.7. In this PDE, we have to calculate at every time step a matrix  $\tilde{D}$  which is an  $N \times N$  matrix, where each element in the matrix needs  $N$  multiplications to be calculated and hence  $N^3$  multiplications for all the elements of  $\tilde{D}$ . Also we need  $N^2$  multiplications for updating  $N \times 1$  scaling coefficients, as in Eq. (3.17), in each time step of the algorithm. So in total each time step is  $\propto (N^3 + N^2)$ . Also there is memory management issue where  $N^2$   $\tilde{\Psi}_{l,k}$ 's which are  $N \times 1$  vectors, as defined in Eq.(3.16), are calculated once using connection coefficients as explained in Section 3.3, and hence reducing the total memory space from  $N^3 \times 8 \text{ bytes}$  matrix for all the  $\tilde{\Psi}_{l,k}$ 's to  $(2MX - 1)^2 \times 8 \text{ bytes}$  by exploiting symmetry properties of the connection coefficients (every element in a long type matrix in MATLAB needs 8 bytes of space). As with respect to *level* change it has the effect of making the program slower by 8 times this time due to  $N^3$ .

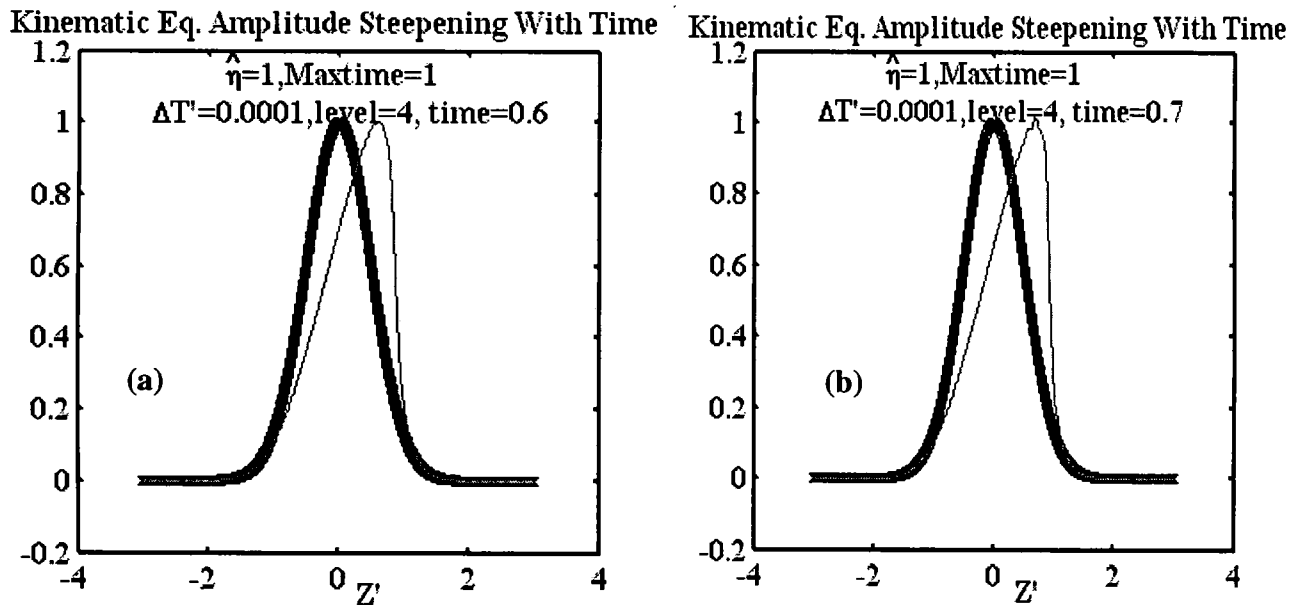


**Figure 3.7:** First order nonlinear kinematic equation at times (a) 0.6, (b) 0.7.

### 3.4.3 The Burger's Equation

The Burger's equation is defined as:  $\frac{\partial u}{\partial T'} + \hat{\eta}u \frac{\partial u}{\partial Z'} - \hat{\alpha}^2 \frac{\partial^2 u}{\partial Z'^2} = 0$ , is solved along with the initial conditions:  $u(Z', 0) = \exp(-Z'^2)$ , with  $-\infty < Z' < \infty$ ,  $0 < T' < \infty$ . Similar to above, we obtain:

$$\int_{Z'_{min}}^{Z'_{max}} \left[ u_{T'} + \hat{\eta}uu_{Z'} - \hat{\alpha}^2 u_{Z'Z'} \right] \phi_k(Z') dZ' = 0. \quad (3.18)$$

Here, the matrices  $\tilde{K}$  and  $\tilde{D}$  are as defined by Eqs. (3.13) and (3.16) respectively. Applying these results to Eq. (3.18) and using a forward Euler scheme in time domain we arrive at:

$$\bar{a}(T' + \Delta T') = \bar{a}(T') - \Delta T' (\hat{\eta} \cdot \tilde{D}(T') - \hat{\alpha}^2 \cdot \tilde{K}) \bar{a}(T'). \quad (3.19)$$

This equation is similar to the previous case; however, the third term which is like a diffusion term makes the shock dissipate in time. We have used the wavelet transform method to solve this equation; the solution is shown in Figure 3.8a and b for two values of  $\hat{\alpha}^2 = 0.05$ , and 0.01 respectively. Computation wise, this PDE is a combination of the HE and the nonlinear kinematic equation where both  $\tilde{K}$  and  $\tilde{D}$  are to be calculated, and a similar discussion applies in memory and computation time complexity.

### 3.4.4 The KdV Equation

The KdV equation is defined as:  $\frac{\partial u}{\partial T'} + \hat{\eta}u \frac{\partial u}{\partial Z'} + \tilde{\alpha} \frac{\partial^3 u}{\partial Z'^3} = 0$ , which is solved along with the solitary type initial condition:  $u(Z', 0) = A \sec h^2(KZ')$ , with  $-\infty < Z' < \infty$ ,  $0 < T' < \infty$ . We obtain:



$$\int_{Z'_{min}}^{Z'_{max}} [u_{T'} + \hat{\eta} u u_{Z'} + \tilde{\alpha} u_{Z'Z'Z'}] \phi_k(Z') dZ' = 0. \quad (3.20)$$

The difference from the Burger's equation is in the third term, which we compute as:

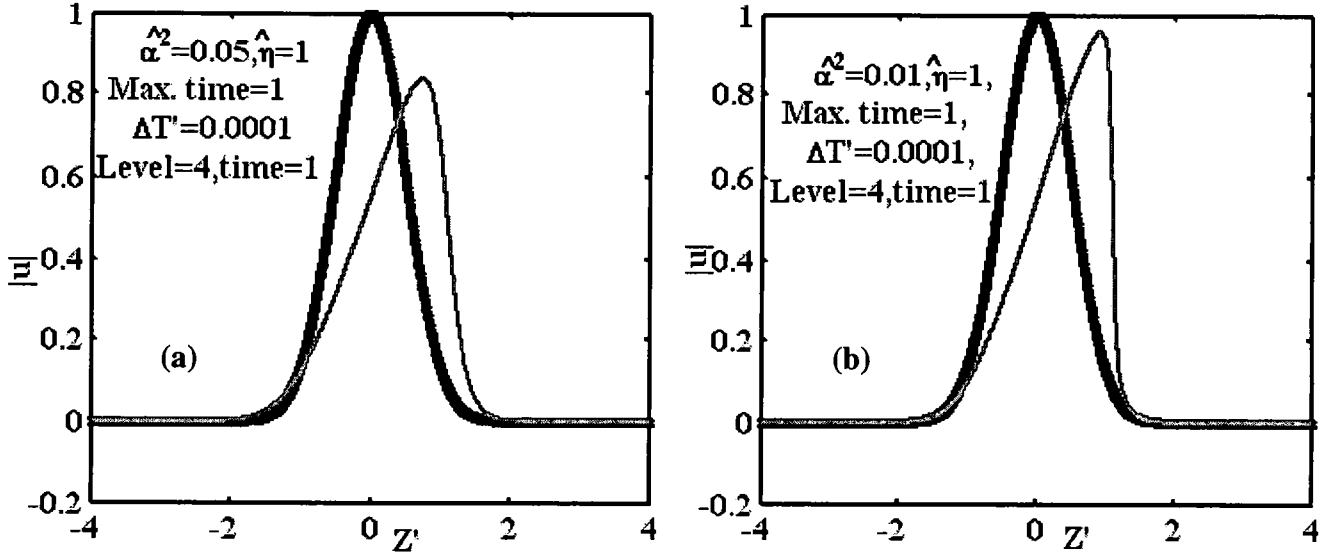


**Figure 3.8:** Burger's equation evolution at time  $T' = 1$  (a)  $\hat{\alpha}^2 = 0.05$ , (b)  $\hat{\alpha}^2 = 0.01$ .

$$\begin{aligned} \int_{Z'_{min}}^{Z'_{max}} u_{Z'Z'Z'} \phi_k(Z') dZ' &= \int_{Z'_{min}}^{Z'_{max}} \frac{\partial^3}{\partial Z'^3} [\sum a_l(T') \phi_l(Z')] \cdot \phi_k(Z') dZ' \\ &= \sum a_l(T') \cdot \int_{Z'_{min}}^{Z'_{max}} \frac{\partial^3 \phi_l}{\partial Z'^3} \phi_k(Z') dZ' = \tilde{G} \cdot \bar{a}(T'), \end{aligned}$$

where

$$\tilde{G}(l, k) = \int \phi_l''' \phi_k dZ' = - \int \phi_l'' \phi_k' dZ', \quad \tilde{G} = \begin{bmatrix} \tilde{G}(1,1) \\ \vdots \\ \tilde{G}(N,N) \end{bmatrix}^T. \quad (3.21)$$

Applying these results to Eq. (3.20) and using a forward Euler scheme in time we obtain

$$\bar{a}(T' + \Delta T') = \bar{a}(T') - \Delta T' (\hat{\eta} \cdot \bar{D}(T') + \tilde{\alpha} \cdot \tilde{G}) \bar{a}(T'). \quad (3.22)$$

For proper choice of A and K, the one soliton solution results, as shown in Figure 3.9.

Computation wise, this PDE is similar to the Burger's equation in the nonlinear part or

the  $\tilde{D}$  matrix, but for the linear part instead of calculating  $\tilde{K}$ , we calculate  $\tilde{G}$  as defined in Eq. (3.21), and we step in time following Eq. (3.22).

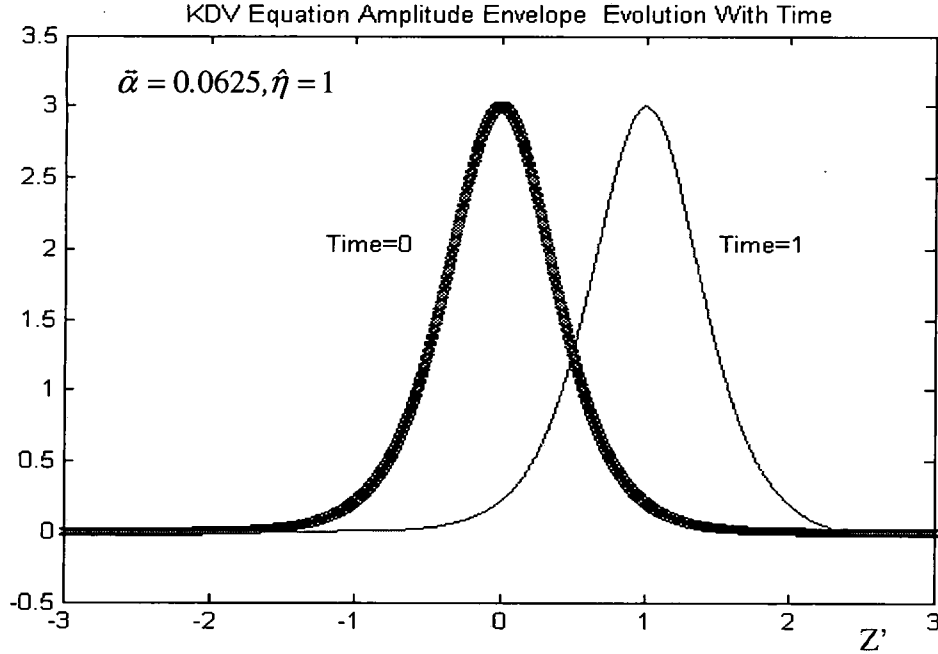


**Figure 3.9:** The KdV evolution equation with a soliton initial condition.

### 3.4.5 The 1-D NLS Equation<sup>88</sup>

The NLS equation is defined as:  $j \frac{\partial \tilde{u}_e}{\partial z} + \frac{1}{2} \frac{\partial^2 \tilde{u}_e}{\partial \tau^2} + \gamma |\tilde{u}_e|^2 \tilde{u}_e = 0$ , to be solved along with the solitary type initial condition:  $\tilde{u}_e(\tau, 0) = K \operatorname{sech}(K\sqrt{\gamma'}\tau)$ , with  $-\infty < \tau < \infty$ ,  $0 < z < \infty$ . For the NLS, and when,  $\gamma' = 1$ , we obtain

$$\int_{\tau_{min}}^{\tau_{max}} \left[ j\tilde{u}_{ez} + \frac{1}{2}u_{\tau\tau} + |\tilde{u}_e|^2 \tilde{u}_e \right] \phi_k(\tau) d\tau = 0. \quad (3.23)$$

The only term to be calculated is the new nonlinear term, which is computed as:

$$\begin{aligned}
\int_{\tau \min}^{\tau \max} |\tilde{u}_e|^2 \tilde{u}_e \phi_k(\tau) d\tau &= \int_{\tau \min}^{\tau \max} \left| \sum a_l(z) \phi_l(\tau) \right|^2 \cdot \left[ \sum a_n(z) \phi_n(\tau) \right] \phi_k(\tau) d\tau \\
&= \int_{\tau \min}^{\tau \max} \left[ \sum a_l(z) \phi_l(\tau) \right] \cdot \left[ \sum a_m^*(z) \phi_m(\tau) \right] \left[ \sum a_n(z) \phi_n(\tau) \right] \phi_k(\tau) d\tau \\
&= \sum a_l \cdot \left\{ \sum a_n \int \phi_l(\tau) \phi_k(\tau) \cdot \phi_m(\tau) \phi_n(\tau) d\tau \right\} \cdot \sum a_m^* = \bar{a}(z) \cdot \{ \bar{a}^*(z) \cdot \bar{\Phi}_{l,k} \cdot \bar{a}(z) \} \\
&= \bar{C}(z) \cdot \bar{a}(z).
\end{aligned}$$

where  $\bar{\Phi}_{l,k}(m,n) = \int \phi_l(\tau) \phi_k(\tau) \cdot \phi_m(\tau) \phi_n(\tau) d\tau$ , and

$$\begin{aligned}
\bar{\Phi}_{l,k} &= \begin{bmatrix} \int \phi_l(\tau) \phi_k(\tau) \cdot \phi_1(\tau) \phi_1(\tau) d\tau & & \\ & \ddots & \\ & & \int \phi_l(\tau) \phi_k(\tau) \cdot \phi_M(\tau) \phi_M(\tau) d\tau \end{bmatrix}^T, \\
\bar{C}(z) &= \begin{bmatrix} \bar{a}^*(z) \bar{\Phi}_{1,1} \bar{a}(z) & & \\ & \ddots & \\ & & \bar{a}^*(z) \bar{\Phi}_{N,N} \bar{a}(z) \end{bmatrix}^T.
\end{aligned} \tag{3.24}$$

Applying these results to Eq. (3.23) we arrive at the following:

$$\bar{a}(z + \Delta z) = \bar{a}(z) + j\Delta z \left( \frac{1}{2} \bar{K} + \bar{C}(z) \right) \cdot \bar{a}(z). \tag{3.25}$$

Note that the different matrices  $\bar{K}$ ,  $\bar{G}$ , and  $\bar{D}$  and  $\bar{C}$  can be calculated using the connection coefficient method discussed earlier. Figure 3.10 shows the algorithm adopted for the NLS case.

#### A- First Order Soliton Input

The first order soliton input  $\tilde{u}_e(\tau, 0) = K \operatorname{sech}(K\tau)$ , with  $-\infty < \tau < \infty$ ,  $0 < z < \infty$  and its evolution in  $z$  is shown in Figure 3.11, using the wavelet transform method.

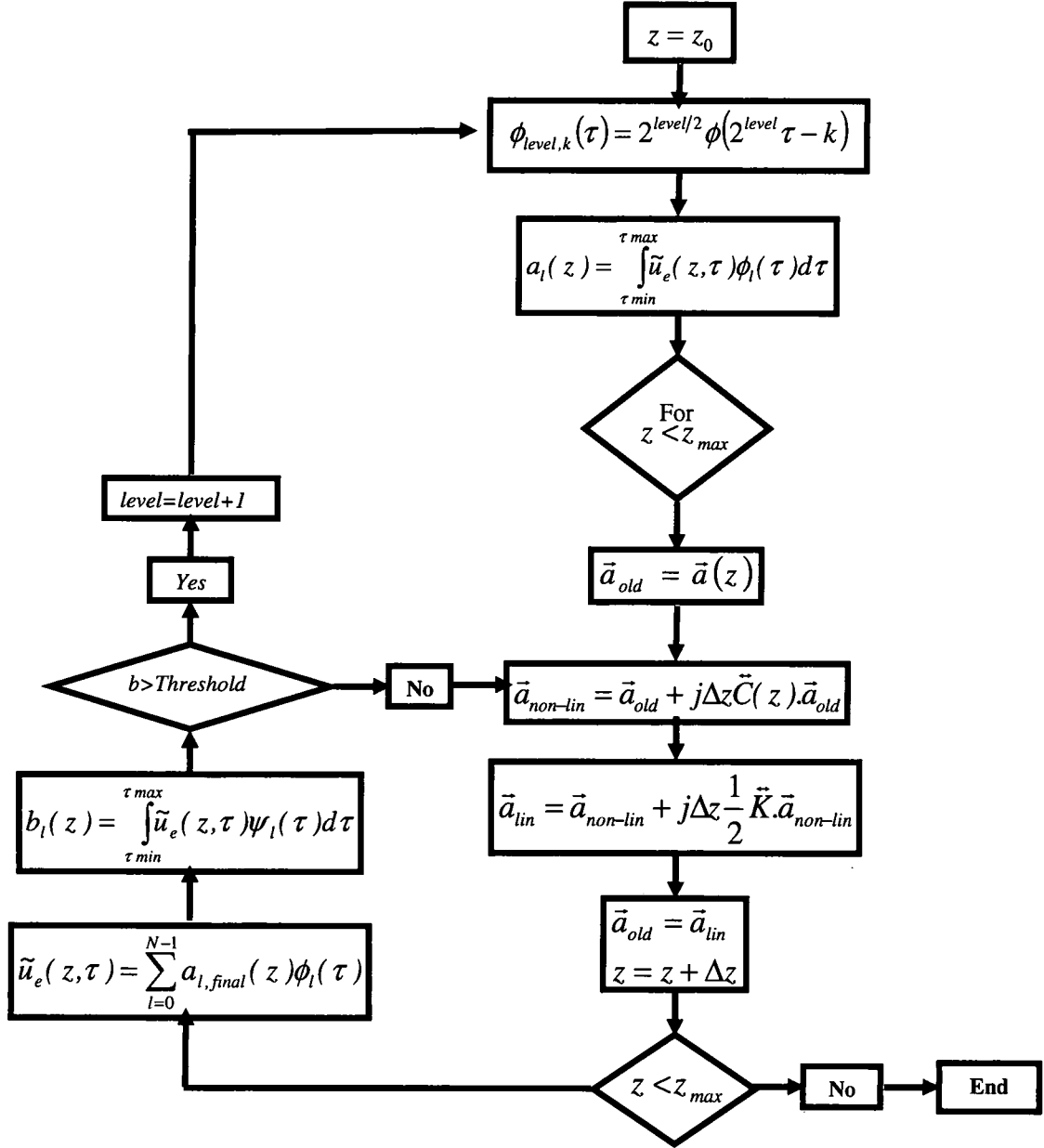


**Figure 3.10:** Wavelet method algorithm for 1-D NLS.

### B- Gaussian Input

Figure 3.12 is the case when the input  $\tilde{u}_e(\tau, 0) = \exp(-\tau^2/2)$  with  $-\infty < \tau < \infty, 0 < z < \infty$ , is a Gaussian. The evolution result using the wavelet method agrees with that found in the literature<sup>7,38</sup> using other classical methods<sup>3,6</sup>.

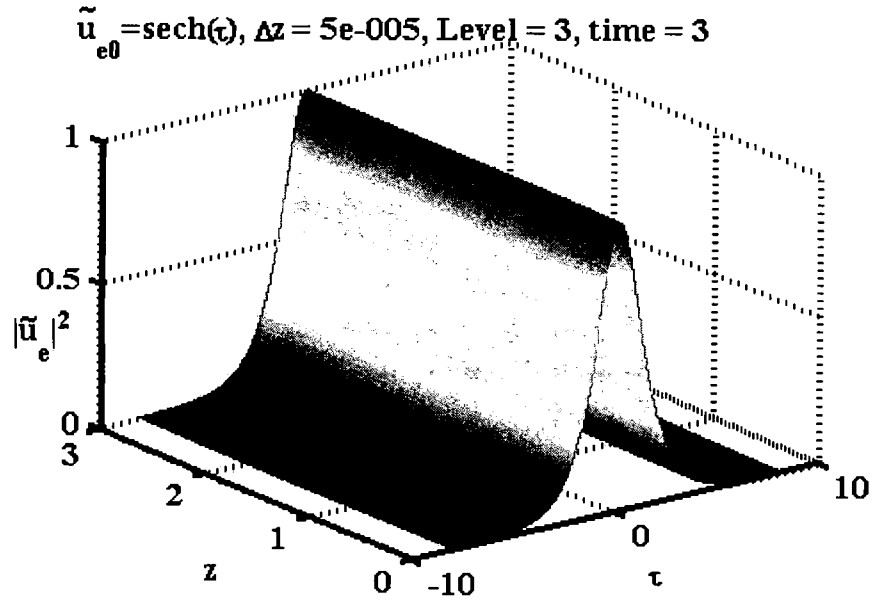


**Figure 3.11:** First order 1-D soliton evolution using the wavelet method.

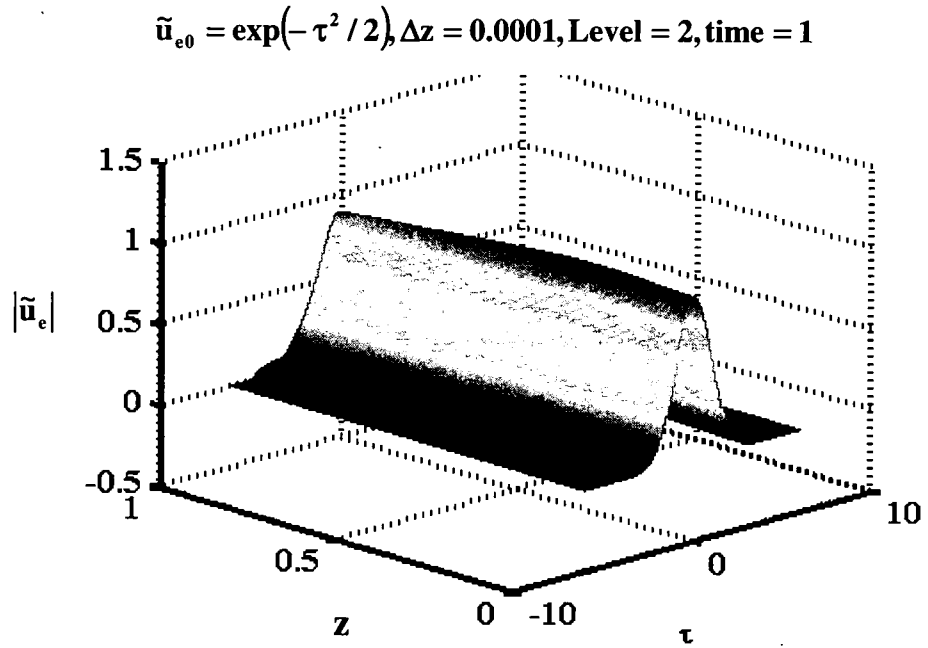


**Figure 3.12:** Exponential input to the 1-D NLS equation using the wavelet method.

Figure 3.12 is the case when the input  $\tilde{u}_e(\tau, 0) = \exp(-\tau^2/2)$  with  $-\infty < \tau < \infty, 0 < z < \infty$ , is a Gaussian. The evolution result using the wavelet method agrees with that found in the literature<sup>7,38</sup> using other classical methods<sup>3,6</sup>.

Computation wise, the  $\tilde{C}$  matrix defined in Eq. (3.24) consists of  $N \times N$  elements and each element needs  $N^2$  multiplications to be computed in each time step, and that makes our algorithm  $\propto N^4$  plus the  $2N^2$  needed for updating the scaling coefficients as in Eq. (3.25). Note that, the later computations are negligible compared to the  $\tilde{C}$  matrix computations. Also here, if we try to move from one level to another, our execution time will be multiplied with  $2^4$ . Memory wise, using the connection coefficient technique, reduces our memory usage for  $\tilde{\Phi}_{l,k}$ 's as defined in Eq. (3.24) from  $N^4 \times 8$  bytes to  $(2MX - 1)^3 \times 8$  bytes, which are computed only once in the beginning of the program. Execution time is in hours in this case, and it depends on the *level*, the number of iterations, spatial dimension of the initial wave, and the number of points approximating each wavelet.

### C- Second Order Soliton Input

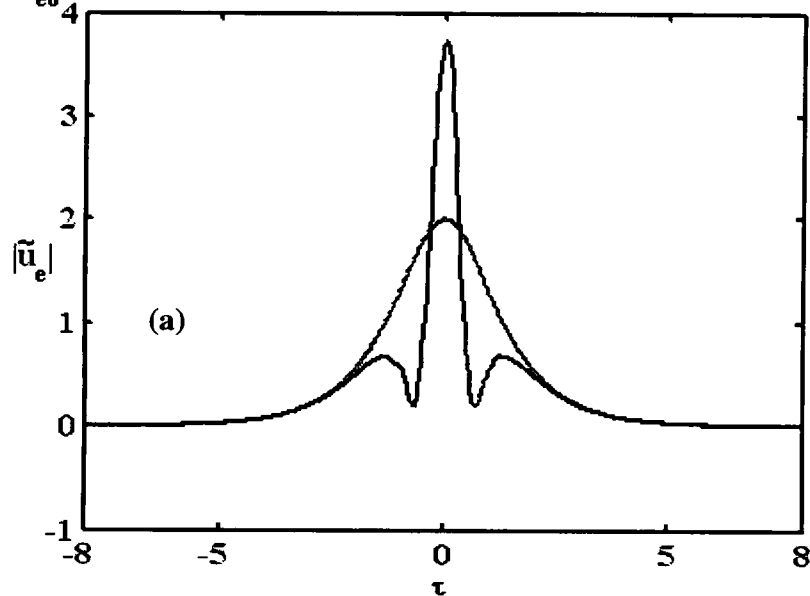
The second order soliton input  $\tilde{u}_e(\tau, 0) = 2K \operatorname{sech}(K\tau)$ , and its evolution in time is shown in Figure 3.13, using the wavelet transform method. Figures 3.13a and b show the pulse shapes at two different times  $z = 0.75$ , and 2. In Figure 3.13c we see the on-axis amplitude variation during propagation, where the pulse returns to its initial value periodically as compared to the FFT method<sup>38</sup>. Figure 3.13d shows a 3-D perspective of the pulse during propagation.

Note that several methods can be used to evaluate  $a'$  and can be used instead of the explicit Euler form, which is conditionally stable. For the NLS equation for example:

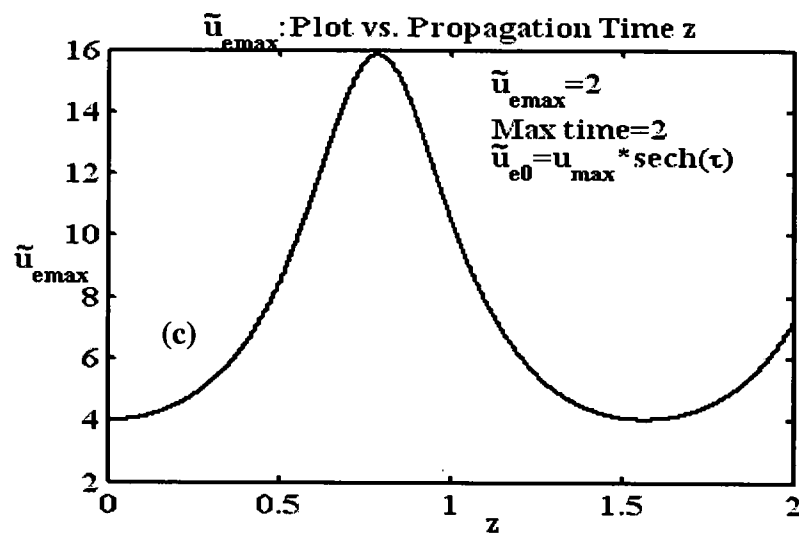
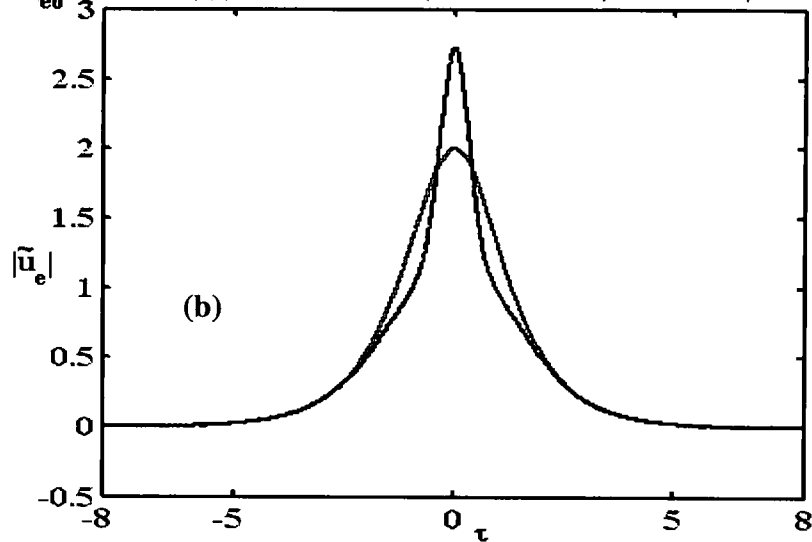
$$\tilde{a}'(z) = \frac{\tilde{a}(z + \Delta z) - \tilde{a}(z)}{\Delta z} = j(1/2\tilde{K} + \tilde{C}(z))\tilde{a}(z) = j\tilde{M}\tilde{a}(z), \quad \text{where}$$

$\tilde{M} = (1/2\tilde{K} + \tilde{C}(z))$ . Thus we can have use of the following:

$\tilde{u}_{e0} = 2 * \text{sech}(\tau)$ , Maxtime=2,  $\Delta z = 0.0001$ , Level=2, time=0.75



$\tilde{u}_{e0} = 2 * \text{sech}(\tau)$ , Maxtime = 2,  $\Delta z = 5e-005$ , Level=3, time=2



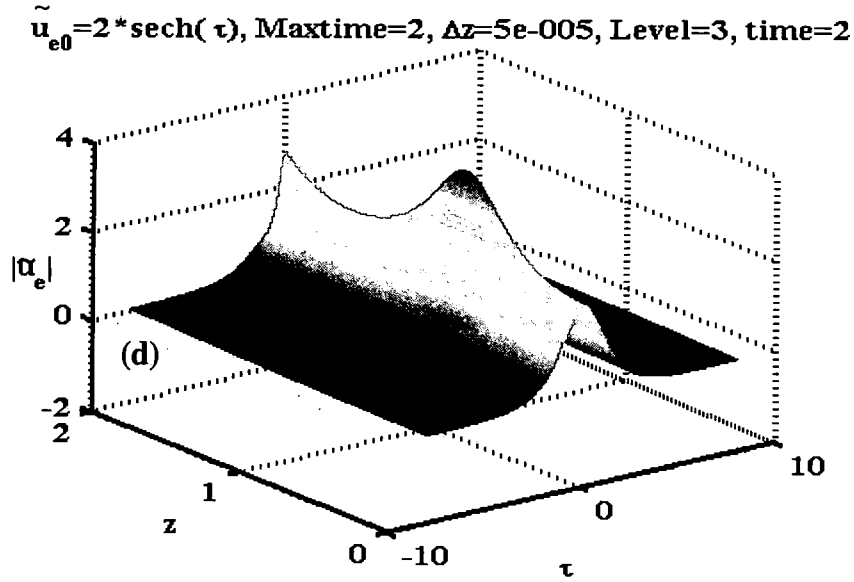


**Figure 3.13:** 2<sup>nd</sup> order soliton propagation and amplitude variation using the wavelet method at times (a) 0.75, (b) 2 (c) On-axis amplitude variation, (d) 3-D view.

**a- Backward Euler**

$$\begin{aligned}\bar{a}_{n+1} &= (I - j\Delta z \bar{M})^{-1} \bar{a}_n = \bar{Q}^{-1} \bar{a}_n, \bar{Q} = \bar{L} \bar{U}, \\ \bar{a}_{n+1} &= \bar{U}^{-1} \bar{L}^{-1} \bar{a}_n,\end{aligned}$$

where we use the  $\bar{L}\bar{U}$  factorization as used in MATLAB.

**b- Jacobi Method**

Let  $\bar{Y} = \text{diag}(\bar{Q})$ ,  $\bar{Q} = -j\bar{M}$ , where  $\bar{M}$  as defined above. Then,  $\bar{Y} \bar{a}_{n+1} = (\bar{Y} - \Delta z \bar{B}) \bar{a}_n$ ,

which can be solved iteratively as:  $a_{n+1}^k = -\frac{1}{q_{kk}} \sum_{k \neq l} q_{kl} a_n^l$ .

**c- Richardson Method**

$$\bar{a}_{n+1} = (I + j\Delta z \bar{M}) \bar{a}_n.$$

**d- Gauss Seidel Method:** ( $\bar{Q}$  as in case (b))



$$a_{n+1}^k = -\frac{1}{q_{kk}} \sum_{l=1}^{k-1} q_{kl} a_{n+1}^l - \sum_{l=k+1}^N q_{kl} a_n^l$$

### e- Crank-Nicholson Method

$$\bar{a}_{n+1} = \left( I - \frac{j}{2} \Delta z \bar{M} \right)^{-1} \left( I + \frac{j}{2} \Delta z \bar{M} \right) \bar{a}_n,$$

$$\text{let } \bar{B}_1 = \left( I - \frac{j}{2} \Delta z \bar{M} \right) = \bar{L} \bar{U}, \bar{B}_2 = \left( I + \frac{j}{2} \Delta z \bar{M} \right), \text{ then, } \bar{a}_{n+1} = \bar{U}^{-1} \cdot \bar{L}^{-1} \cdot \bar{B}_2 \cdot \bar{a}_n.$$

### 3.4.6 The 2-D NLS or Self-Focusing Equation

The 2-D NLS equation in cylindrical coordinates is defined as:

$$j \frac{\partial \tilde{u}_e}{\partial z} + \frac{1}{r} \frac{\partial \tilde{u}_e}{\partial r} + \frac{\partial^2 \tilde{u}_e}{\partial r^2} + |\tilde{u}_e|^2 \tilde{u}_e = 0, \text{ which is to be solved along with the Gaussian initial}$$

conditions:  $u(r, 0) = \exp(-r^2)$ , with  $-\infty < r < \infty$ ,  $0 < z < \infty$ . Applying the MWR to the 2-D NLS we get

$$\int_{r_{min}}^{r_{max}} \left[ j \tilde{u}_{ez} + \frac{1}{r} \tilde{u}_{er} + \tilde{u}_{err} + |\tilde{u}_e|^2 \tilde{u}_e \right] \phi_k(r) dr = 0. \quad (3.26)$$

The only difference from the 1-D NLS is in the second term where it is calculated as:

$$\int_r \frac{1}{r} \frac{\partial \tilde{u}_e}{\partial r} \cdot \phi_k(\tau) d\tau = \int_r \frac{1}{r} \frac{\partial}{\partial r} \left\{ \sum_l a_l(z) \phi_l(r) \right\} \cdot \phi_k(r) dr = \sum_l a_l(z) \cdot \int_r \frac{1}{r} \frac{d\phi_l(r)}{dr} \phi_k(r) dr = \tilde{T} \cdot \bar{a}(z), \text{ wh}$$

ere

$$\tilde{T}(l, k) = \int \frac{\phi_l \phi_k}{r} dr, \tilde{T} = \begin{bmatrix} \tilde{T}(1,1) & \dots & \\ \vdots & \ddots & \vdots \\ \dots & \dots & \tilde{T}(N, N) \end{bmatrix}^T. \quad (3.27)$$

Figure 3.14 shows the algorithm for the self-focusing equation. Figures 3.15a and b show the self-focusing tendency using wavelet method on *levels* 3 and 5 respectively. When the *level* is increased to 5 we can track much higher amplitudes of the beam and

can get closer to the collapse distance. However, the draw back of the wavelet technique is the computation time as compared to the Hankel transform method (which takes minutes) described later. In this simulation we have used as initial profile  $u(\tau, 0) = A(0) \exp(-r^2 / w_0^2)$ , where  $A(0) = (6P_{cr})^{1/2}$ ,  $w_0^2 = 1/2$ .

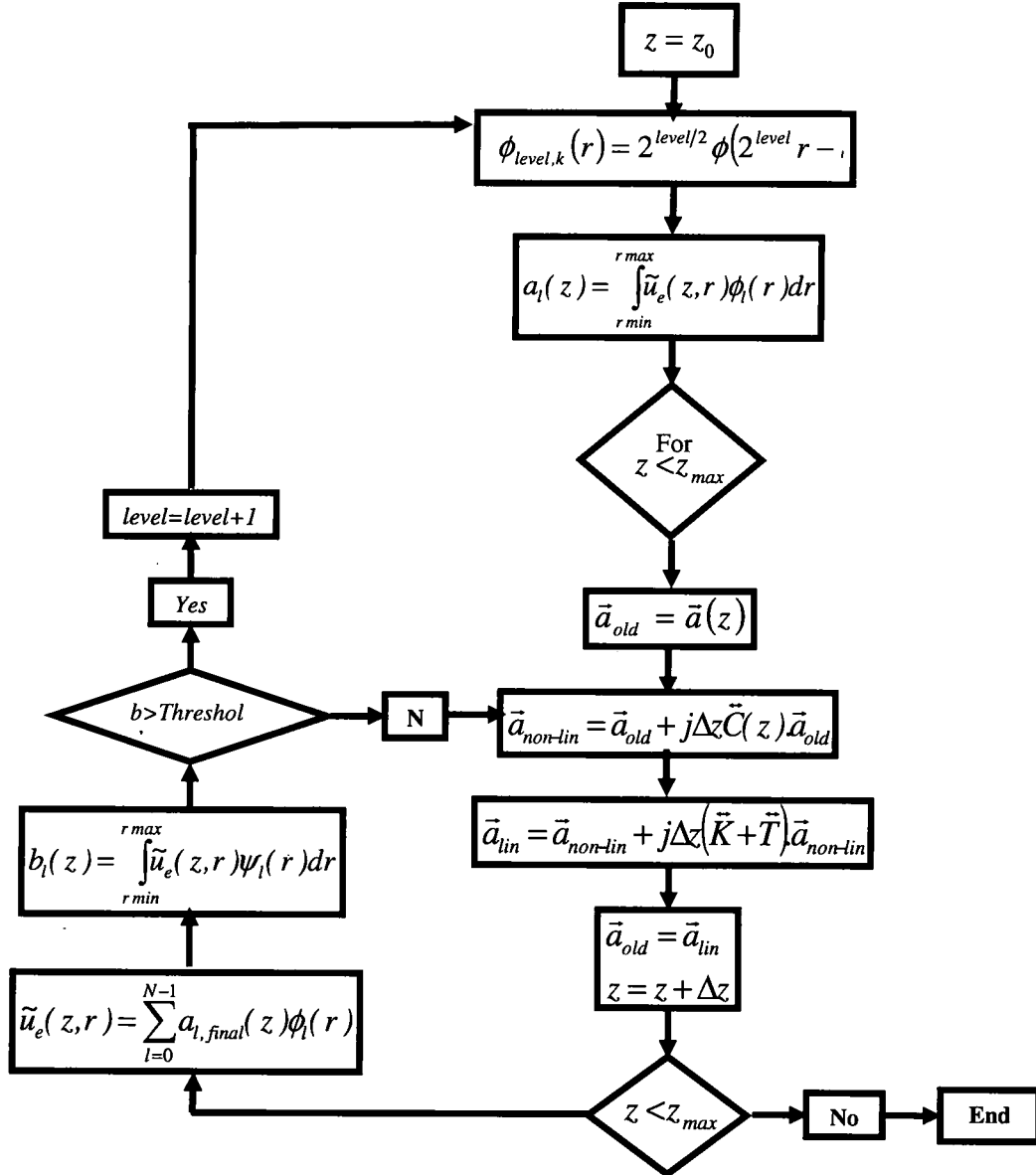


**Figure 3.14:** Wavelet method algorithm for 2-D NLS.

The number of scaling coefficients used here are calculated by the formula given in Section 3.4.1:  $N = r_{\max} \times 2^{\text{level}} - (MX - 1) = 16 \times 2^3 - (10) = 118$ . Since at the 5<sup>th</sup> level the computer which is running the simulation can't support  $N = 502$  memory and speed wise, we used spatial adaptive scaling through interpolation such that the number of wavelets or scaling coefficients  $N$  remains the same but distributed on smaller spatial dimension which is more useful, since outside the focusing region the function is approximately zero. As with respect to the number of computations, the only difference from the 1-D NLS case is in the matrix  $\tilde{T}$  as defined in Eq. (3.27). Although this matrix is computed only once at the beginning of the program, but it gives rise to a lot of problems since it has no known connection coefficients like method to calculate its elements and thus, we are stuck to compute it numerically where precision near zero, which is the focusing point, plays a major role. Note that computation time depends on many factors as we mentioned earlier and it may take a while.

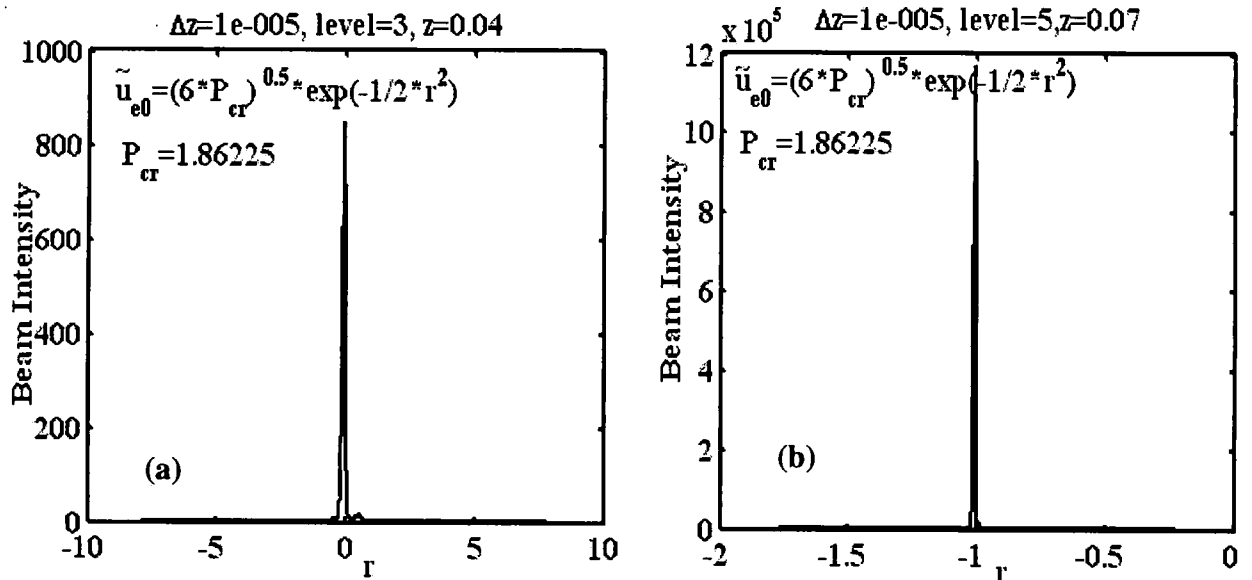


**Figure 3.15:** Self-focusing wavelet approximation method, (a) 3<sup>rd</sup> level, (b) 5<sup>th</sup> level.

### 3.4.7 The Self-steepening Equation

The self-steepening equation is as follows:

$$j \frac{\partial \tilde{u}_e}{\partial z} + \frac{1}{2} \frac{\partial^2 \tilde{u}_e}{\partial \tau^2} + js \frac{\partial (\tilde{u}_e^2 |\tilde{u}_e|)}{\partial \tau} + |\tilde{u}_e|^2 \tilde{u}_e = 0. \quad (3.28)$$

We can derive the algorithm for solving the self-steepening equation as is shown in Figure 3.16. The only new term here is the third term where the corresponding matrix  $\tilde{S}$  is as follows:

$$\tilde{S}(z) = \begin{bmatrix} \bar{a}^*(z) \tilde{R}_{1,1} \bar{a}(z) & & \\ & \ddots & \\ & & \bar{a}^*(z) \tilde{R}_{N,N} \bar{a}(z) \end{bmatrix}, \quad \tilde{R}_{l,k}(m,n) = \int (\phi_l \phi_k \phi_m \phi_n' + \phi_l \phi_k \phi_m' \phi_n + \phi_l' \phi_k \phi_m \phi_n) d\tau.$$

$$\tilde{R}_{l,k} = \begin{bmatrix} \int (\phi_l \phi_k \phi_1 \phi_1' + \phi_l \phi_k \phi_1' \phi_1 + \phi_l' \phi_k \phi_1 \phi_1) d\tau & & \\ & \ddots & \\ & & \int (\phi_l \phi_k \phi_N \phi_N' + \phi_l \phi_k \phi_N' \phi_N + \phi_l' \phi_k \phi_N \phi_N) d\tau \end{bmatrix}^T, \quad (3.29)$$

Finally we arrive at the following algorithm:

$$\bar{a}(z + \Delta z) = \bar{a}(z) + j\Delta z \left( \frac{1}{2} \tilde{K} + js\tilde{S} + \tilde{C}(\xi) \right) \bar{a}(z). \quad (3.30)$$

Using the wavelet method, Figures 3.17a and b show the evolution at  $z = 0.005$  and  $z = 0.5$  respectively. Note that in the later case a shock is developed due to self-steepening of the optical wave. Computation wise since this PDE has two nonlinear matrices  $\tilde{C}$  and  $\tilde{S}$  with similar dimensions, each time step needs  $N^4$  multiplications according to Eqs.(3.29) and (3.30).

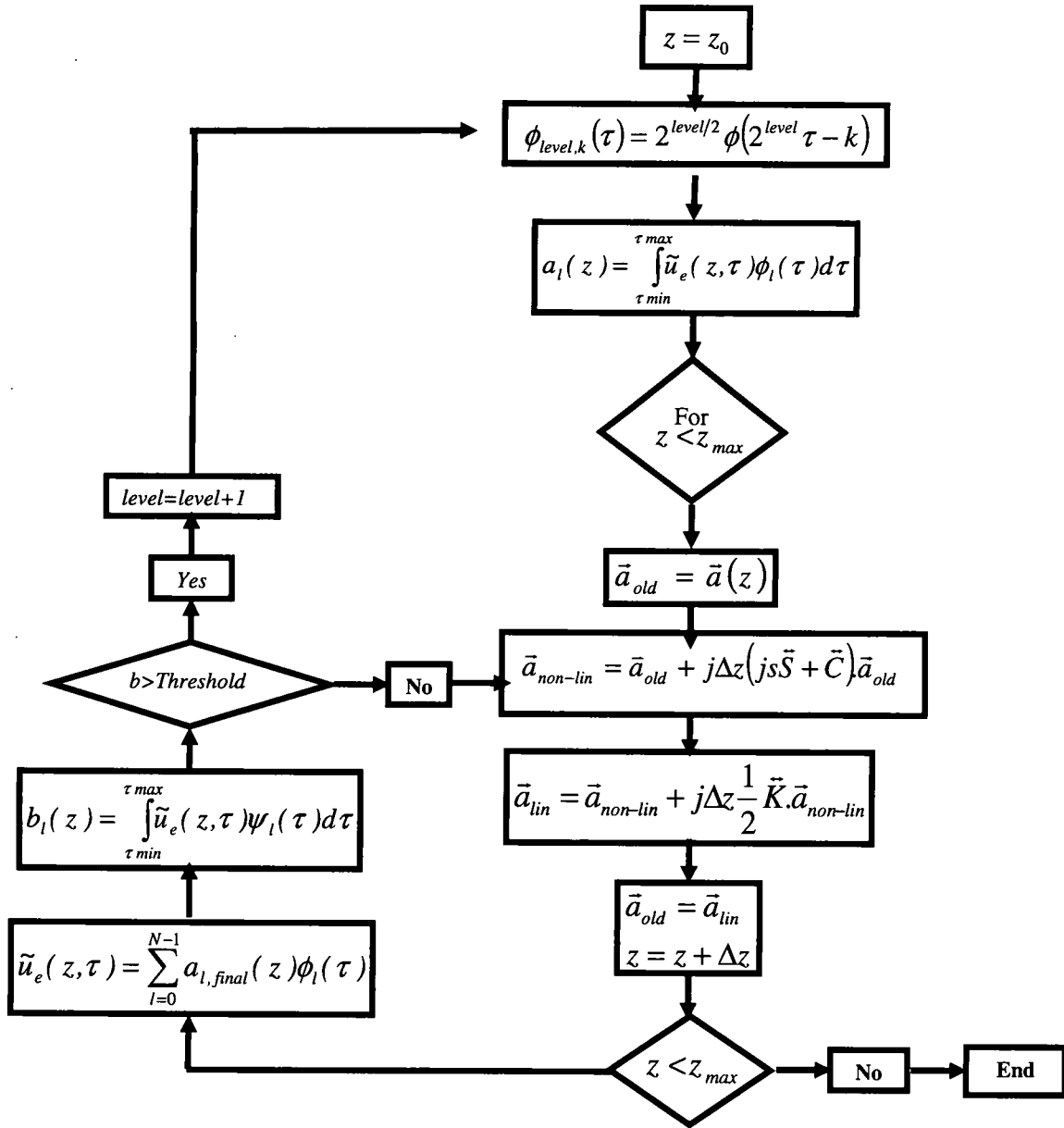


**Figure 3.16:** Wavelet method algorithm for self-steepening equation.

### 3.5 Summary

In this Chapter we studied basic wavelet theory and application to Partial Differential Equations. We also studied the principle of multi resolution and some

numerical techniques to calculate the connection coefficients used in the algorithms developed to solve some typical evolution equations.

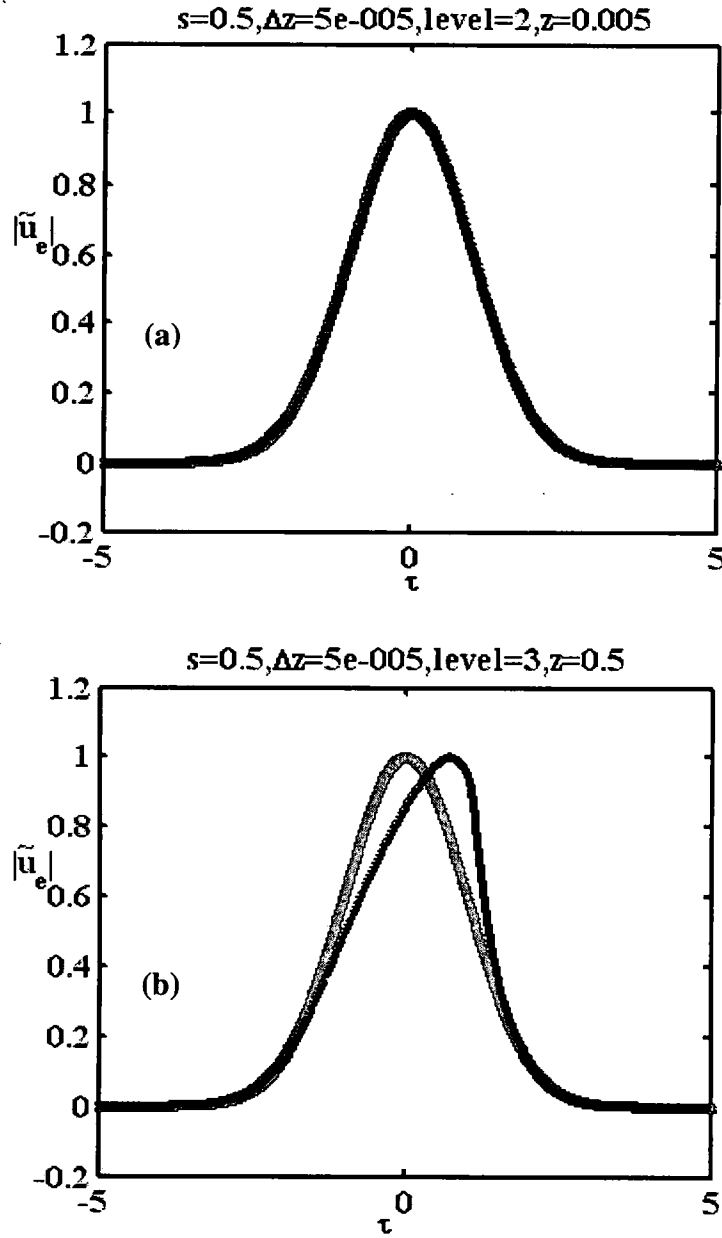


**Figure 3.17:** Evolution of optical shocks using self-steepening Eq. at (a)  $z = 0.005$ , (b)  $z = 0.5$ .

Although the method devised can be very accurate but computational complexity in higher dimensions was a major draw back and was quantified in each case. This lead us to devise new methods based on finite Fourier transform technigues which is the topic of Chapter 4. In this Chapter we introduce our second technique based on the Hankel or Fourier Bessel transform method. We will discuss several methods that are usually used to find the Hankel or the Fourier Bessel transform and we compare between them and develop the AFBSS algorithm and apply it to typical evolution equations.

## CHAPTER 4

### HANKEL OR FOURIER BESSEL TRANSFORM METHODS

#### 4.1 Introduction

Due to the computational complexity problem encountered in higher dimensions in the wavelet method discussed in the previous Chapter we shifted our focus towards integral transform technique and its variations. In this Chapter we outline a new numerical technique called the adaptive fast Hankel split step (AFHSS) or adaptive Fourier Bessel split step (AFBSS) method. This method is used to track, as an example, the solution of the 2 and 3-D NLS equation. Note that this method is based on the combination of the standard split step fast Fourier transform (SSFFT) technique and the use of the Hankel transform which utilizing the cylindrical and spherical symmetry of the problem. This symmetry leads us to use this method applied to the above problem. Also, we notice that the computation time and precision are enhanced enormously, and we will discuss this in the next Chapters. Added to this combination we will also use the similarity criterion developed by Zakharov *et al* <sup>20</sup>. This criterion, which we will outline later, is applied to this method in transverse spatial dimensions and longitudinal propagation step, which will be adaptively updated so that we can track the amplitude to distances very close to collapse distance in the self-focusing case and to track the amplitude dynamics of the spatiotemporal solitons as discussed in the following Chapters.



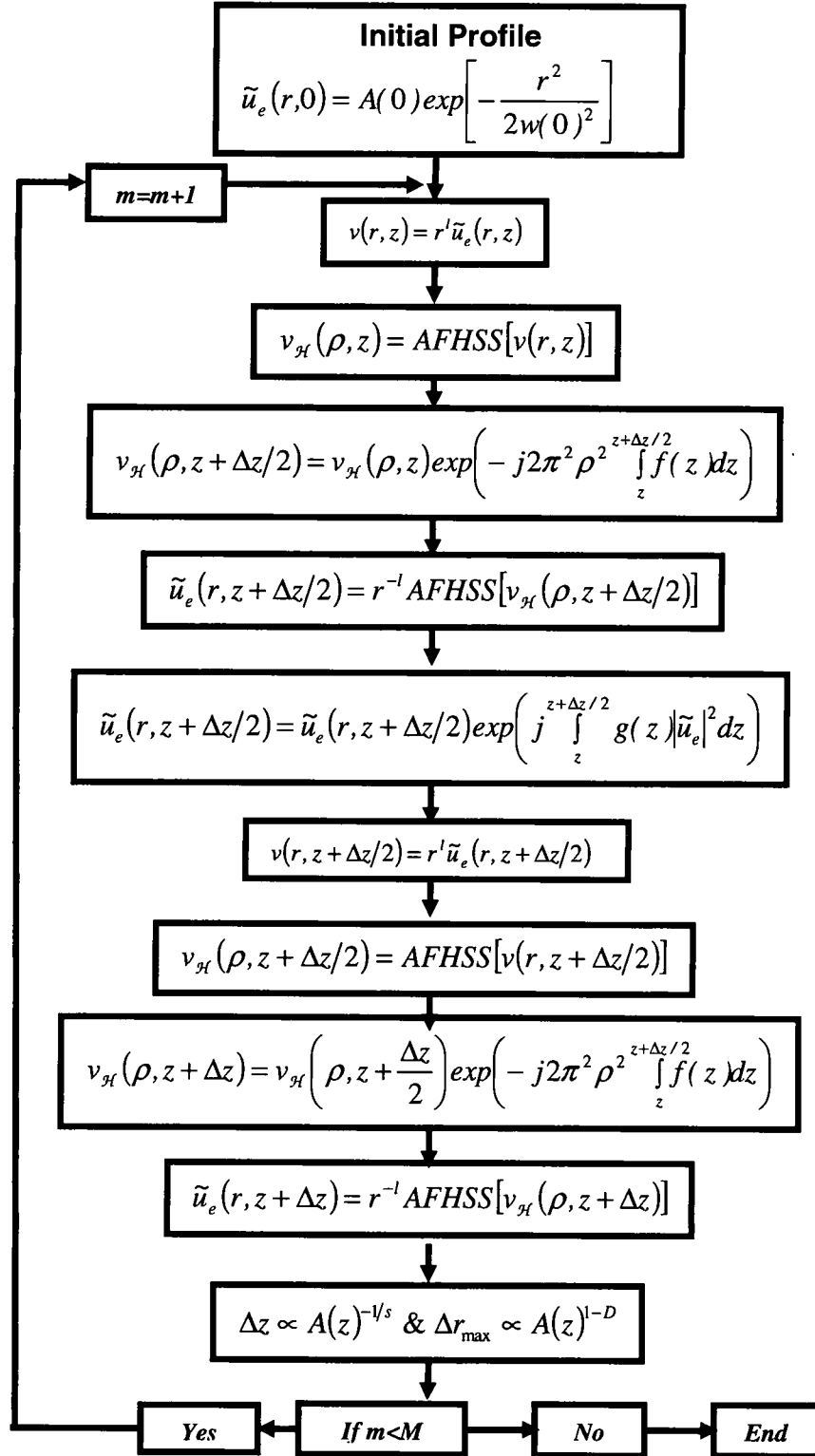


**Figure 4.1:** The AFHSS algorithm, a symmetrized version of the split step FFT using cylindrical or spherical Fourier Bessel transform instead, and using adaptive longitudinal stepping and transverse grid management.

We now outline our numerical spectral techniques used to track the solution of the NLS equation. Our novel scheme is based on the combination of the standard split step fast Fourier transform (FFTSS) and the Hankel transform<sup>89</sup>, which exploits the cylindrical and spherical symmetry of the problem. This enhances the computation time and precision enormously which we discuss later. In addition, we also use the concepts from the similarity solution developed by Zakharov and Synakh<sup>19</sup> and apply them to our split-step spectral methods so that the transverse spatial range and the longitudinal spatial step are adaptively updated.

The AFHSS algorithm in Figure 1 resembles the symmetrized Fourier split-step technique<sup>90,59</sup>, where we change the longitudinal propagation stepping size  $\Delta z \propto A(z_1)^{-1/s} - A(z_2)^{-1/s} \approx A(z_1)^{-1/s}$  when  $A(z_2) \gg A(z_1)$ , adaptively using Zakharov *et al* similarity formula defined in<sup>20</sup> where  $s_z = (2/3, 1/2)$  for  $D = (2, 3)$  respectively, and the grid spatial range  $\Delta r_{\max} \propto A(z)^{1-D}$  as indicated in Fibich and Ilan<sup>2</sup> in order to track the varying amplitude of the spatiotemporal pulse in the medium,. We note that periodic focusing/defocusing or beam trapping occurs when we have a sign-alternating dispersive medium and under the conditions stated above. The time-dependent paraxial wave equation, in the presence of periodic modulation of dispersion and nonlinearity has the form of a modified (D+1)-dimensional NLS with a dimensionless envelope of the electric field

$$j \frac{\partial \tilde{u}_e}{\partial z} + \frac{f(z)}{2} \frac{1}{r^{D-1}} \frac{\partial}{\partial r} \left( r^{D-1} \frac{\partial \tilde{u}_e}{\partial r} \right) + g(z) |\tilde{u}_e|^2 \tilde{u}_e = 0 \quad (4.1)$$

where  $r = (x^2 + y^2)^{1/2}$  or  $r = (x^2 + y^2 + \tau^2)^{1/2}$  for cylindrical or spherical symmetry of the field distribution respectively, and  $D$  can be 2 or 3, respectively. The functions  $f(z), g(z)$  are periodic modulation of dispersion and nonlinearity respectively.

From the linear part of Eq. (4.1) with  $D=2,3$  we have

$$\left( \frac{\partial^2}{\partial r^2} + \frac{D-1}{r} \frac{\partial}{\partial r} \right) \tilde{u}_e. \quad (4.2)$$

The Hankel transform or Fourier Bessel technique can not apply directly to this operator in the case when  $D=3$ , so we have to transform the operator from spherical coordinates to cylindrical ones by letting  $\tilde{u}_e(r, z) = r^{-l} v(r, z)$ , where  $l$  is the order of the Fourier Bessel or

Hankel transform. Eq. (4.2) becomes  $\left( \frac{\partial^2}{\partial r^2} + \frac{1}{r} \frac{\partial}{\partial r} - \frac{l^2}{r^2} \right) v \xrightarrow{AFHSS} -4\pi^2 \rho^2 v_{\mathcal{H}}(\rho, z)$ ,

where  $v_{\mathcal{H}}(\rho, z) = \mathcal{H}_l[v(r, z)] = \mathcal{H}_l[r^l \tilde{u}_e(r, z)] \Rightarrow \tilde{u}_e(r, z) = r^{-l} \mathcal{H}_l[v_{\mathcal{H}}(\rho, z)]$ , with  $l=0, \frac{1}{2}$  in

the case of the cylindrical and spherical Fourier Bessel transform pair respectively, where they are related to each other by:

$$\tilde{u}_e(r, z) = \int_0^\infty \tilde{u}_{e\mathcal{H}}(\rho, z) j_{l-1/2}(\rho r) \rho^{l+3/2} d\rho = \sqrt{\frac{\pi}{2}} r^{-l} \int_0^\infty \rho^{l+1} \tilde{u}_{e\mathcal{H}}(\rho, z) J_l(\rho r) d\rho, \quad (4.3)$$

$$\tilde{u}_{e\mathcal{H}}(\rho, z) = \frac{2}{\pi} \int_0^\infty \tilde{u}_e(r, z) j_{l-1/2}(\rho r) r^{l+3/2} dr = \sqrt{\frac{2}{\pi}} \rho^{-l} \int_0^\infty r^{l+1} \tilde{u}_e(r, z) J_l(\rho r) dr, \quad (4.4)$$

where  $j_l(x) = (-x)^l \left( \frac{1}{x} \frac{d}{dx} \right)^l \frac{\sin(x)}{x} = \sqrt{\frac{\pi}{2x}} J_{l+1/2}(x)$  is the  $l^{th}$  order spherical Bessel

function. The above transform pair is solved by the  $l^{th}$  order finite Hankel Transform method, explained in the next Section.

## 4.2 Calculation of the Hankel Transform

There are many methods to take the Hankel transform numerically with different accuracies. We have found in general that these methods are based on three different theories, as described below:

### 4.2.1 Siegman's<sup>91</sup> or Magni's<sup>92</sup> Method

As for Siegman's method, Eqs. (4.3) and (4.4) can be written after a change of variable called the Gardner transform<sup>93</sup>:

$$\hat{u}_{\mathcal{H}}(\bar{y}) = \int_{-\infty}^{\infty} \hat{u}(\bar{x}) \hat{J}_l(\bar{x} + \bar{y}) dx, \quad (4.5a)$$

where

$$r = r_0 e^{\tilde{\alpha} \bar{x}}, \rho = \rho_0 e^{\tilde{\alpha} \bar{y}}, \quad (4.5b)$$

$$\hat{u}(\bar{x}) = r \tilde{u}_e(r), \hat{u}_{\mathcal{H}}(\bar{y}) = \rho \tilde{u}_{e\mathcal{H}}(\rho), \quad (4.5c)$$

$$\hat{J}_l(\bar{x} + \bar{y}) = 2\pi \tilde{\alpha} r \rho J_l(2\pi r \rho). \quad (4.5d)$$

After discretization of Eq. (4.5) we have:

$$r_n = r_0 e^{\tilde{\alpha} n}, \rho_m = \rho_0 e^{\tilde{\alpha} m}, n, m = 0, \dots, N-1, \quad (4.6a)$$

$$\begin{aligned} \hat{u}_n &= \hat{u}(\bar{x}_n) = r_n \tilde{u}_e(r_n), \hat{u}_{\mathcal{H}m} = \hat{u}_{\mathcal{H}}(\bar{y}_m) = \rho_m \tilde{u}_{e\mathcal{H}}(\rho_m), \\ \hat{J}_{ln+m} &= \hat{J}_l(\bar{x}_n + \bar{y}_m) = 2\pi \tilde{\alpha} r_n \rho_m J_l(2\pi r_n \rho_m). \end{aligned} \quad (4.6b)$$

Let  $\tilde{\beta} = \rho_0 e^{\tilde{\alpha} N}$ ,  $\tilde{b} = r_0 e^{\tilde{\alpha} N}$ , hence,  $r_0 \leq r < \tilde{b}$ ,  $\rho_0 \leq \rho < \tilde{\beta}$ . There are certain criteria for choosing  $r_0$ ,  $\rho_0$ ,  $\tilde{\alpha}$ , which are the following:

- We require that the lower end truncation point in the  $r$  space domain be less than

$$1/\bar{K}_1 \text{ cycles of the highest frequency } \tilde{\beta}, \text{ or } r_0 = (\bar{K}_1 \tilde{\beta})^{-1}.$$

- Also, we require the sample point spacing  $\Delta r_n = r_{n+1} - r_n$  at  $r = \tilde{b}$  less than

$$1/\bar{K}_2 \text{ cycles of } \tilde{\beta}, \text{ or } \Delta r_N \approx \tilde{\alpha}\tilde{b} = (\bar{K}_2\tilde{\beta})^{-1}.$$

- Similar arguments exist in the  $\rho$  transform domain where,

$$\rho_0 = (\bar{K}_1\tilde{b})^{-1}, \Delta\rho_N \approx \tilde{\alpha}\tilde{\beta} = (\bar{K}_2\tilde{b})^{-1}.$$

The above criteria lead to the following set of equations:

$$\bar{N} = \bar{K}_2\tilde{\beta}\tilde{b} \ln(\bar{K}_1\tilde{\beta}\tilde{b}), \tilde{\alpha}e^{\tilde{\alpha}N} = \frac{\bar{K}_1}{\bar{K}_2}, r_0\rho_0 = \left(\frac{\bar{K}_2}{\bar{K}_1^2}\right)\tilde{\alpha}, \quad (4.7)$$

where  $\bar{N}$ ,  $\bar{K}_1$ ,  $\bar{K}_2$ , are parameters to be chosen. Applying the above criteria, it is in our interest to have  $\bar{K}_1$ , as large as possible and  $\bar{K}_2$ , small (as long as  $\bar{K}_1$  and  $\bar{K}_2$  are both  $>2$ ). Now the Hankel transform integral Eq. (4.5a) can be calculated as:

$$\hat{u}_{\mathcal{H}_m} = FFT[FFT(\hat{u}_m) \times IFFT(\hat{J}_{lm})] \quad (4.8)$$

Magni's method similar to Siegman's method where:

$$\tilde{u}_{\mathcal{H}}(\rho) = 2\pi \int_0^1 \tilde{u}_e(r) J_0(2\pi N_f \rho r) r dr. \quad (4.9)$$

So the discrete form of the Hankel Transform is:

$$\hat{u}_{\mathcal{H}}(\rho_m) = \frac{1}{N_f \rho_m} FFT[FFT(\bar{\phi}_n) \times IFFT(J_{ln})] \quad (4.10)$$

where,  $J_l$  is the first order Bessel function,  $N_f$  is a parameter,  $N$  is the number of samples, and  $\bar{\phi}_n$  as defined below:

$$\bar{\phi}_n = \begin{cases} k_0[\hat{u}(r_0) - \hat{u}(r_1)]e^{\tilde{\alpha}(1-N)} & \text{for } n=0 \\ [\hat{u}(r_n) - \hat{u}(r_{n+1})]e^{\tilde{\alpha}(n+1-N)} & \text{for } n=1,2,\dots,N-1 \\ 0 & \text{for } n=N,\dots,2N-1 \end{cases}, \quad (4.11)$$

where

$$\bar{\alpha} = -\ln \left[ \frac{1 - e^{-\bar{\alpha}}}{N-1} \right], r_n = \rho_n = r_0 e^{\bar{\alpha} n}, r_0 = [1 + e^{\bar{\alpha}}] e^{\frac{-\bar{\alpha} N}{2}}, \quad (4.12)$$

$$J_{1n} = J_1(2\pi N_f r_0 e^{\bar{\alpha}(n+1-N)}), n = 0, 1, \dots, 2N-1, k_0 = \frac{2e^{\bar{\alpha}} + e^{2\bar{\alpha}}}{[1 + e^{\bar{\alpha}}]^2 [1 - e^{-2\bar{\alpha}}]}.$$

The importance of these methods related to this problem resides in the fact that depending on the parameters which much be chosen carefully, we have a non-uniform sampling, which is denser near the focusing region, which is advantageous than uniform sampling.

#### 4.2.2 Yu's<sup>94</sup> or Guizar's<sup>95</sup> Method

We use the definition of the  $l^{th}$  order finite Hankel Transform of the third kind<sup>31</sup> :

$$\mathcal{H}[\tilde{u}_e(r, z)] = \tilde{u}_{e\mathcal{H}}(\rho_m, z) = \int_q^p r \tilde{u}_e(r, z) [J_l(r\rho_m)Y_l(q\rho_m) - J_l(q\rho_m)Y_l(r\rho_m)] dr, \quad (4.13)$$

in which  $\rho_m$ 's are the roots of the transcendental equation

$J_l(q\rho_m)Y_l(p\rho_m) - J_l(p\rho_m)Y_l(q\rho_m) = 0$ , the inverse transform can be written as

$$\tilde{u}_e(r, z) = \frac{\pi^2}{2} \sum_m \frac{\rho_m^2 J_l^2(\rho_m p) \tilde{u}_{e\mathcal{H}}(\rho_m, z)}{J_l^2(\rho_m q) - J_l^2(\rho_m p)} \times [J_l(\rho_m r)Y_l(q\rho_m) - J_l(\rho_m q)Y_l(r\rho_m)]. \quad (4.14)$$

For  $q=0$  and  $\rho_m = \frac{\kappa_{lm}}{2\pi p}$  Eq. (4.14) becomes<sup>31,59</sup>  $\tilde{u}_e(r, z) = \sum_m \tilde{c}_{lm} J_l\left(\kappa_{lm} \frac{r}{p}\right)$ ,  $0 \leq r \leq p$ ,

where  $\tilde{c}_{lm} = \frac{1}{p^2 J_{l+1}^2(\kappa_{lm})} \int_0^p r \tilde{u}_e(r, z) J_l\left(\kappa_{lm} \frac{r}{p}\right) dr$  and  $J_l(\kappa_m) = 0$ . Let us evaluate the

radius  $r$  at  $r_n = \frac{\kappa_{ln}}{2\pi R_2}$  and the frequency at  $\rho_m = \frac{\kappa_{lm}}{2\pi R_1}$ ,  $r_n \in r \geq R_1 = p$  &  $\rho_m \in \rho \geq R_2$ ,

we have  $\tilde{u}_e(r_n) = \tilde{u}_{e\mathcal{H}}(\rho_m) = 0$ , where  $R_1, R_2$  are the spatial and transform ranges

respectively, with  $\tilde{S} = 2R_1R_2$ . From above, we can write the expansion of the function and its transform by an  $l^{th}$  order Bessel series<sup>94,95</sup>

$$U_{\mathcal{H}}(m) = \sum_{n=1}^N C_{mn} U(n), U(n) = \sum_{m=1}^N C_{nm} U_{\mathcal{H}}(m), \quad (4.15a)$$

$$C_{mn} = \frac{2}{\tilde{S}} J_l \left( \frac{\kappa_{ln} \kappa_{lm}}{\tilde{S}} \right) \left\| J_1^{-1}(\kappa_{ln}) \right\| \left\| J_1^{-1}(\kappa_{lm}) \right\|, \quad (4.15b)$$

$$U(n) = \tilde{u}_e \left( \frac{\kappa_{ln}}{2\pi R_2}, z \right) \left\| J_{l+1}^{-1}(\kappa_{ln}) \right\| R_1, \quad (4.15c)$$

$$U_{\mathcal{H}}(m) = \tilde{u}_{e\mathcal{H}} \left( \frac{\kappa_{lm}}{2\pi R_1}, z \right) \left\| J_{l+1}^{-1}(\kappa_{lm}) \right\| R_2.$$

Here to it is preferable to choose  $R_2$  as large as possible, and  $R_1$  is determined by the initial profile, which is going to decrease due to focusing in this problem. Also, if we choose  $\tilde{S} = \kappa_{lN+1}$ , then the error is close to zero as  $N$  increases.

#### 4.2.3 Ferrari's<sup>96</sup> Method

Here, the key point is to transform the function  $\tilde{u}_e(r)$  into a function of two variables:  $\tilde{u}_e \left( (x^2 + y^2)^{\frac{1}{2}} \right)$ , and then calculate the following integral:

$$\tilde{\Phi}_n(x) = 2(-j)^n \int_0^\infty \tilde{u}_e \left( (x^2 + y^2)^{\frac{1}{2}} \right) \cos(n\theta(x, y)) dy, \quad (4.16)$$

where  $\theta(x, y)$  is a polar coordinate corresponding to a pair of Cartesian coordinates  $(x, y)$ . After  $\tilde{\Phi}_n(x)$  is generated, its Fourier transform  $\mathcal{F}$  is evaluated by FFT since:

$$\mathcal{F}[\tilde{\Phi}_n(x)] = (-j)^n \int_{-\infty}^\infty \int_{-\infty}^\infty \tilde{u}_e \left( (x^2 + y^2)^{\frac{1}{2}} \right) e^{j(n\theta(x, y))} e^{j2\pi p x} dy dx = (-j)^n \int_0^\infty \int_0^{2\pi} \tilde{u}_e(r) e^{in\theta} e^{i2\pi p r \cos(\theta)} r d\theta dr$$

$$= 2\pi \int_0^{\infty} u(r) J_n(2\pi r \rho) r dr = u_{\mathcal{H}}(\rho), \quad (4.17)$$

$$\text{where } J_n(2\pi r \rho) = \frac{(-j)^n}{2\pi} \int_0^{2\pi} e^{in\theta} e^{i2\pi r \rho \cos(\theta)} d\theta.$$

Thus, the problem of calculating the Hankel transform of the  $n^{\text{th}}$  order resides in calculating a simple integral followed by a 1-D FFT. Also, if the values of  $u$  are known only at a series of discrete values  $r_n$ , as is the case with some of our PDEs, then we have to generate the values of  $\tilde{u}_e\left(\left(x_l^2 + y_m^2\right)^{\frac{1}{2}}\right)$  by making interpolating between discrete values  $\tilde{u}_e(r_n)$ .

### 4.3 Summary

In this Chapter we outlined a new numerical technique called the adaptive fast Hankel split step (AFHSS) or adaptive Fourier Bessel split step (AFBSS) method which is based on the combination of the standard split step fast Fourier transform (SSFFT) technique and the use of the cylindrical and spherical symmetry of the problem. This symmetry leads us to use this method in the next Chapters to solve the different NLS type equations. Also, we notice that the computation time and precision are enhanced enormously, and we will discuss this in the next Chapters. In the next Chapter we study the stability of the PDEs in hand using a semi analytical technique based on the variational approach which we introduce. This semi analytical technique is also used as a guideline to wisely choose the different parameters in the equations modeled by the different numerical techniques discussed in earlier Chapters.



## CHAPTER 5

### VARIATIONAL METHOD

#### 5.1 Introduction

The different numerical techniques discussed so far are not enough to study the type of equations in this work because of the many parameters involved. In order to pick the value of the right parameters for simulation we have to pick them in the region of stability of each equation. For this reason, and since most of these equations under study doesn't have a closed form solution, we thought to use semi analytical methods and the variational techniques is a good candidate. The calculus of variation deals with problems in which the quantity to be extremized appears in integral form as<sup>97-99</sup>

$$\tilde{J}(\bar{\sigma}) = \int_{x1}^{x2} f[\tilde{u}_e(x, \bar{\sigma}), \tilde{u}_{ex}(x, \bar{\sigma}), x] dx, \quad (5.1)$$

where  $\tilde{J}$  is the stationary quantity to be extremized and  $\bar{\sigma}$  is a parameter which we need

to extremize the function with namely  $\left. \frac{\partial \tilde{J}(\bar{\sigma})}{\partial \bar{\sigma}} \right|_{\bar{\sigma}=0} = 0$ . So in most Physical cases we have

to find the path of integration to minimize  $\tilde{J}$ . Hence we assume the existence of an

optimum path for which  $\tilde{J}$  is stationary and compare it with neighboring paths. The

difference between these two for a given  $x$  is called the variation of  $\tilde{u}_e, \delta \tilde{u}_e$ , and is

described by introducing a new quantity  $\tilde{\eta}(x)$  where  $\delta \tilde{u}_e = \bar{\sigma} \tilde{\eta}(x)$ . After some algebra

Eq.(5.1) becomes

$$\delta \tilde{J} = \int_{x_1}^{x_2} \left( \frac{\partial f}{\partial \tilde{u}_e} - \frac{d}{dx} \frac{\partial f}{\partial \tilde{u}_{ex}} \right) \delta \tilde{u}_e dx = 0. \quad (5.2)$$

Thus the condition for stationary solution is  $\left( \frac{\partial f}{\partial \tilde{u}_e} - \frac{d}{dx} \frac{\partial f}{\partial \tilde{u}_{ex}} \right) = 0$ , known as the Euler equation.

#### A- Several Dependent Variables

A first generalization to Eq. (5.1) is to consider the function  $f$  is a function of several dependent variables,  $\tilde{u}_{e1}(x), \tilde{u}_{e2}(x), \tilde{u}_{e3}(x), \dots$ . Hence Eq. (5.1) becomes

$$\tilde{J}(\vec{\sigma}) = \int_{x_1}^{x_2} f[\tilde{u}_{e1}(x, \vec{\sigma}), \tilde{u}_{e2}(x, \vec{\sigma}), \dots, \tilde{u}_{e1x}(x, \vec{\sigma}), \tilde{u}_{e2x}(x, \vec{\sigma}), \dots, x] dx, \quad (5.3)$$

where we end up with a set of Euler equations of the form:

$$\left( \frac{\partial f}{\partial \tilde{u}_{ei}} - \frac{d}{dx} \frac{\partial f}{\partial \tilde{u}_{ei}/\partial x} \right) = 0, i = 1, 2, \dots, n. \quad \text{An important consequence of Eq. (5.3) occurs}$$

when  $f$  is taken to be the Lagrangian  $\mathcal{L}$ , where it is defined as the difference between kinetic and potential energies of a given system,  $\mathcal{L} = \mathcal{T}_k - \mathcal{E}_p$ . Let the independent variable be  $t$  instead of  $x$  and the dependent variable be  $x$  instead of  $u$  then after some algebra Eq. (5.3) becomes

$$\delta \tilde{J} = \delta \int_{t_1}^{t_2} \mathcal{L}(x_1, x_2, \dots, \dot{x}_1, \dot{x}_2, \dots; t) dt = 0. \quad (5.4)$$

Eq.(5.4) is called the Hamilton's principle of classical mechanics which asserts that the motion of a system from time  $t_1$  to  $t_2$  is such that the time integral of the Lagrangian  $\mathcal{L}$  has a stationary value and the resulting equations

$$\frac{d}{dt} \frac{\partial \mathcal{L}}{\partial \dot{x}_i} - \frac{\partial \mathcal{L}}{\partial x_i} = 0, \quad (5.5)$$

are called Euler-Lagrange equations which we use extensively in the following Chapters. Note that Lagrangian equations of a system can be derived from Newton's equations and vice versa but Lagrangian equations are invariant of the coordinate system used. Also, the advantages of using the Hamiltonian formalism is the observation of the relation between a symmetry and a conservation law. For example if our Lagrangian is independent of the azimuthal angle which corresponds to the conservation of the angular momentum, similarly for translation and the linear momentum. Noether's theorem, which is used extensively in later Chapters is the generalization of this symmetry-conservation law relation.

#### **B- Several Independent Variables**

Another generalization of Eq.(5.1) is when we have several independent variables, then Eq. (5.1) becomes

$$\tilde{J} = \iiint f[\tilde{u}_e, \tilde{u}_{ex_1}, \tilde{u}_{ex_2}, \tilde{u}_{ex_3}, x_1, x_2, x_3] dx_1 dx_2 dx_3, \quad (5.6)$$

where this leads to the Euler-Lagrange equations for three variables:

$$\frac{\partial f}{\partial \tilde{u}_e} - \sum_i \frac{\partial}{\partial x_i} \left( \frac{\partial f}{\partial \tilde{u}_e / \partial x_i} \right) = 0. \quad (5.7)$$

#### **C- Several Dependent And Independent Variables**

This case combines the above two cases, the Euler-Lagrange equations become:

$$\frac{\partial f}{\partial \tilde{u}_{ei}} - \sum_j \frac{\partial}{\partial x_j} \left( \frac{\partial f}{\partial \tilde{u}_{ei} / \partial x_j} \right) = 0 \quad (5.8)$$

In Chapter 6 we study two different focusing arrest mechanisms namely the nonparaxial approximation and the saturating nonlinearity by using the methods developed so far namely, the AFBSS and variational techniques in previous Chapters.

## 5.2 Summary

In this Chapter we have briefly introduced the variational technique that we are going to use in the subsequent Chapters to study the different stability regions for the spatiotemporal pulse propagating in periodic dispersion managed and nonlinearity managed media. This technique allows us to wisely choose parameters which lead to stable numerical simulation results. In the next Chapters we will discuss the different self-focusing effects using this semi analytical method and the numerical methods discussed in earlier Chapters.

## CHAPTER 6

### FOCUSING ARREST MECHANISMS

#### 6.1 Introduction

In the previous Chapters we introduced some numerical and analytical techniques to solve and study some typical evolution equations in general and NLS type equations in practical. In this and the following two Chapters we study the propagation of  $(D+1)$ -dimensional optical pulses in bulk media with the assumption of nonparaxiality, saturating nonlinearity, periodic dispersion or nonlinearity, analytically by using the variational approach, and numerically by using the new numerical technique relying on a fast adaptive Fourier Bessel split step (AFBSS) method using cylindrical and spherical symmetry for 2 and 3 dimensions respectively devised in previous Chapters. Stability criteria for  $(2+1)$  and  $(3+1)$ -dimensional solitons are identified, and the long term dynamics of the solitons are studied by the averaged equations obtained using the Kapitza approach. Also, the slow dynamics of the solitons around the fixed points for the width and the chirp are studied. The importance of this work is in generating dispersion or nonlinear managed optical solitons which may become important in telecommunication systems due to their self-confined structure. Also, in the next two Chapters, namely in the case of periodic dispersion and/or nonlinearity this work is applied to the stabilization of the Bose-Einstein condensate in  $(2+1)$  and  $(3+1)$ -dimensional optical lattice. Using fast algorithms for cylindrical/spherical Fourier Bessel transforms along with adaptive

longitudinal stepping and transverse grid management in a symmetrized split-step technique as described in Chapter 4, it is possible to accurately study many nonlinear effects, including the possibility of self-focusing, spatio-temporal collapse, collapse-arresting mechanism due to saturable nonlinearity or beam nonparaxiality, variable Kerr nonlinearity, and variable dispersion managed systems. We compare results of the new numerical technique with those obtained using fast Fourier split step (FFSS) technique.

## 6.2 Nonparaxiality

We present a novel technique to numerically solve beam propagation problems based on the paraxial and nonparaxial scalar nonlinear Schrödinger (NLS) equation in two transverse dimensions with cylindrical symmetry. Using fast algorithms for Hankel transforms along with adaptive longitudinal stepping and transverse grid management in a symmetrized split-step technique, it is possible to accurately track a beam much closer to its physical collapse due to self-focusing for the paraxial NLS than other existing methods, notably the Fast Fourier transform-based standard split-step technique. For the nonparaxial NLS, the adaptive fast Hankel transform based split-step method with an adaptive nonparaxiality parameter yields results comparable to the more rigorous vector nonlinear wave equation.

### 6.2.1 Introduction

Self-focusing, is primarily caused due to a third order nonlinear susceptibility  $\chi^{(3)}$  that is responsible for nonlinear refraction<sup>16</sup>. The nonlinearly modified refractive index can be expressed as  $n(\omega, |\tilde{u}_e|^2) = n_0(\omega) + n_2(|\tilde{u}_e|^2)$ , where  $n_0$  is the linear refractive index,  $n_2(\propto \chi^{(3)})$  is the nonlinear refractive index, and  $|\tilde{u}_e|^2$  is proportional to the intensity of the beam<sup>23,100,2</sup>. Self-focusing results in the narrowing of the beam width in

two transverse dimensions and increase in the on-axis intensity. For powers above a certain threshold the beam undergoes collapse. Although the exact value of the critical power depends on the spatial distribution of the input beam, the critical power of circularly symmetric beams is not more than a few percent above the theoretical lower

bound value<sup>23,100</sup>  $P_c^{lb} = \frac{\lambda^2}{4\pi n_0 n_2} \mathcal{N}_c$ , where  $\mathcal{N}_c$  is the normalized beam power, to be

made more precise later, which is a necessary condition for collapse. In reality, the high beam intensity may either cause breakdown in the material, or some other physical effects may be triggered, such as saturating of the index of refraction<sup>39</sup>, so that no further focusing may occur. Also, the assumptions about slowly varying amplitude and the paraxial approximation may not be valid for large focusing angles during the last stages of self-focusing, and there is no singularity if one accounts for nonparaxiality<sup>58,59</sup>. In one transverse dimension, nonlinearity can balance diffraction of a beam, resulting in the formation of first order spatial solitons. In this case, if the nonlinear effect is higher than diffraction, periodic focusing occurs, and may result in higher order solitons. This may not be the case in two or three dimensions where spatial collapse may occur if we consider the paraxial approximation.

### 6.2.2 Beam Collapse

The nonparaxial NLS is given in the general operator form<sup>58</sup>:

$$\tilde{u}_{ez} - j\varepsilon \tilde{u}_{ezz} = jL_r \tilde{u}_e + jN_{nl}(\tilde{u}_e) \tilde{u}_e, \quad \vec{r} \in \mathbb{R}^D, \quad z \geq 0; \quad \tilde{u}_e(r, z=0) = \tilde{u}_{e0}(r), \quad (6.1)$$

where  $D$  is the transverse dimension in space,  $\varepsilon = (\lambda/4\pi r_0)^2$  and  $r_0$  is the initial beam radius, and where  $L_r \tilde{u}_e = \Delta_T \tilde{u}_e$ ,  $N_{nl}(\tilde{u}_e) = |\tilde{u}_e|^{2\bar{\sigma}}$ . For a problem with cylindrical

symmetry, the Hankel transform technique is preferable over other classical techniques such as finite difference<sup>2,101</sup>, finite element<sup>5</sup>, and wavelet methods<sup>10</sup>, due to the availability of fast algorithms with speeds comparable to one-dimensional fast Fourier transform (FFT) methods. Lax et al.<sup>90</sup> have used Hankel transforms to solve paraxial atmospheric propagation problem for intense light pulses, where the atmospheric response is modeled through hydrodynamic equations. To the best of our knowledge, the Hankel transform technique has not been used to numerically solve the nonparaxial NLS equation in two transverse dimensions. Also, in the paraxial case by incorporating adaptive longitudinal stepping in  $z$  and by employing adaptive transverse grid management, we can track the beam closer to spatial collapse than possible by existing classical techniques. On the other hand, in the nonparaxial case employing the above adaptive grid management techniques along with an adaptive nonparaxial coefficient lead us to results superior to those in Ref. [58] and similar to those of the vector theory of self-focusing method<sup>102</sup>.

Returning to Eq. (6.1) assuming the paraxial case where  $\varepsilon = 0$ , if (a)  $\bar{\sigma}D < 2$  (subcritical case), the solution exists globally and can be solved by the inverse scattering method<sup>19</sup>; (b)  $\bar{\sigma}D = 2$  (critical) or  $\bar{\sigma}D > 2$  (supercritical), the solutions self-focus and attain singularity or collapse within finite distance. For the critical case, Eq. (6.1) with  $\bar{\sigma} = 1$ ,  $D=2$ , is written in the standard form:<sup>101,103</sup>

$$j\tilde{u}_{e_z} + \Delta_T \tilde{u}_e + |\tilde{u}_e|^2 \tilde{u}_e = 0, \quad (6.2)$$

which depicts the unidirectional propagation of a high power laser beam in a nonlinear media<sup>53</sup>. The singularity is often called collapse.

McLaughlin *et al*<sup>103</sup> predict similarity solutions when  $D=2$  of the form:



$$\tilde{u}_e(\vec{r}, z) \propto \frac{1}{(z_r - z)^{1/2}} Q\left(\frac{\vec{r}}{(z_r - z)^{1/2}}\right), \quad (6.3)$$

where  $Q$  is an arbitrary function, and  $z_r$  is the collapse distance. We use this knowledge in order to adaptively vary the longitudinal stepping  $\Delta z$  and the spatial dimension of the beam. A special solution  $R$ , called the Townes soliton<sup>101</sup>, can be found as the positive solution of

$$\Delta_T \tilde{a} - \tilde{a} + \tilde{a}^3 = 0, \tilde{a}'(0) = 0, \tilde{a}(\infty) = 0. \quad (6.4)$$

Also Weinstein<sup>104</sup> has shown that if the initial beam power  $P_0$  is less than the lower

bound for the critical power for blow up  $P_c^{lb} = \frac{\lambda^2}{4\pi n_0 n_2} \mathcal{N}_c$ ,

where  $\mathcal{N}_c = \int |\tilde{a}|^2 r dr = 1.86225$ , there is no collapse of the paraxial NLS equation. Also,

for an arbitrary initial profile  $\tilde{u}_{e0} \neq \tilde{a}$ , Fibich<sup>23</sup> proved that there is an upper bound for the

critical power  $P_c^{ub} = \frac{\lambda^2}{4\pi n_0 n_2} G(\tilde{u}_{e0})$ , where  $G(\tilde{u}_{e0}) = \frac{2 \int |\tilde{u}_{e0}|^2 d\vec{r} \int |\nabla \tilde{u}_{e0}|^2 d\vec{r}}{\int |\tilde{u}_{e0}|^4 d\vec{r}}$  for which

blow up occurs for this initial profile if it has sufficient high power.

There are few known integral invariants for the paraxial NLS equation above when  $\partial D \geq 2$ .<sup>2</sup> These invariants are based on the symmetry of the NLS equation under gauge, space, and time transformations, and may be derived from a Lagrangian density of Eq. (6.2). Three of these invariants are the energy, the Hamiltonian and the variance, defined as:<sup>103,105</sup>

$$\mathcal{N} = \int |\tilde{u}_e|^2 d\vec{r} \quad (6.5a)$$

$$H = \int \left( |\nabla \tilde{u}_e|^2 - \frac{1}{2} |\tilde{u}_e|^4 \right) d\vec{r}, \quad (6.5b)$$

$$\frac{1}{8} \frac{d^2}{dz^2} \int |\tilde{r}|^2 |\tilde{u}_e(\tilde{r}, z)|^2 d\tilde{r} = H - \frac{d-2}{4} \int |\tilde{u}_e(\tilde{r}, z)|^4 d\tilde{r}, \quad (6.5c)$$

where the term  $|\nabla \tilde{u}_e|^2$  results from diffraction and  $|\tilde{u}_e|^4$  from the nonlinear effect. Note that from Eq. (6.5c) blow-up only occurs if  $D \geq 2$ . The “variance” is given as:

$$\mathcal{V}(z) = \int |\tilde{r}|^2 |\tilde{u}_e(\tilde{r}, z)|^2 d\tilde{r} = 4Hz^2 + \frac{d\mathcal{V}(0)}{dz} z + \mathcal{V}(0), \text{ for } D = 2.^8 \text{ Thus, for } H < 0, \text{ the}$$

function  $\mathcal{V}(z)$  vanishes at a distance  $z_r = [\mathcal{V}_0 / -4H_0]^{1/2} > 0$ . A sufficient condition for

blow up is  $H < 0$ , i.e., when the nonlinear effect is stronger than diffraction, the beam self-focuses and collapse occurs at a distance  $z_c \leq z_r$ . For an input Gaussian of the form

$$u_0 = A(0) \exp(-r^2 / 2r_0^2), \quad z_c = 0.317(\tilde{p} - 1)^{-0.6346}, \text{ for } r_0 = 1 \text{ and } z_c = 0.1585(\tilde{p} - 1)^{-0.6346},$$

for  $r_0 = 1 / \sqrt{2}$ , where  $\tilde{p} = \mathcal{N}_0 / \mathcal{N}_c$ .<sup>18</sup>

Note that the condition  $H = 0$ , which leads to  $P_c^{ub}$ , leads to an overestimate of the actual critical power as we shall see in the numerical examples below.

### 6.2.3 Adaptive Hankel Split Step Method

In this Section we use the numerical technique developed in Chapter 4 to numerically solve the two dimensional (2-D) paraxial and nonparaxial nonlinear Schrodinger (NLS) equation for  $\tilde{\sigma} = 1, D = 2$  and variable  $\varepsilon$ , which is classically used to model this phenomenon. This enhances the computation time and precision appreciably, as we discuss later. In addition, we also use the concepts from the similarity solution developed by McLaughlin *et al*<sup>103</sup> and apply them to our split-step spectral method mentioned above, so that the grid transverse spatial range and the longitudinal spatial step are adaptively updated. As its name indicates, we use the Hankel transform instead of the usual Fourier transform, relying on algorithms already developed in the literature.<sup>91,94</sup>

The AFHSS algorithm in Figure 6.1 resembles the symmetrized Fourier split-step technique, where we change the longitudinal spatial step  $\Delta z \propto 1/A(z_1)^2 - 1/A(z_2)^2 \approx 1/A(z_1)^2$  when  $A(z_2) \gg A(z_1)$ , adaptively using McLaughlin's similarity formula (3) and the grid spatial range  $\Delta r_{max} \propto 1/A(z)$  as indicated by<sup>2</sup> in order to track the varying amplitude of the focusing beam when  $\varepsilon = 0$ . We note that periodic focusing/defocusing starts to occur when  $\varepsilon \neq 0$ . Also note that the more general form of Figure 6.1 is found in Figure 4.1.

There are several numerical approaches for implementing the Hankel transform as explained in Chapter 4<sup>91,94</sup>. The importance of Siegman's method<sup>91</sup> resides in the fact that, depending on the parameters, one can employ a non-uniform sampling that is denser near the focusing region, which has advantages over uniform sampling. Yu *et al*'s method<sup>94</sup>, is based on the expansion of the function and its transform by a zero order Bessel series. In this Section we adopt this method.

#### 6.2.4 Numerical Results And Conclusions

We now show sample simulation results using the AFHSS method that uses Yu *et al*'s Hankel transform technique, as well as a novel adaptive version of a symmetric FFT (AFFSS) technique. For purposes of comparison, and for  $\varepsilon = 0$  we choose  $\tilde{u}_{e0} = 4 \exp(-r^2/2)$  and  $\tilde{u}_{e0} = 4 \exp(-r^2)$  as the initial profiles, which should show self-focusing and collapse at  $z_c = [0.1505, 0.1478]$  respectively. Note that  $z_r = [0.288, 0.25]$ , based on the study above which is obviously overestimated. Figure 6.2 shows the maximal focusing as a function of grid size  $h = \Delta r$  which proves the convergence of our methods to the numerical focusing point when  $\Delta r$  decreases by varying the  $\tilde{S}$  parameter

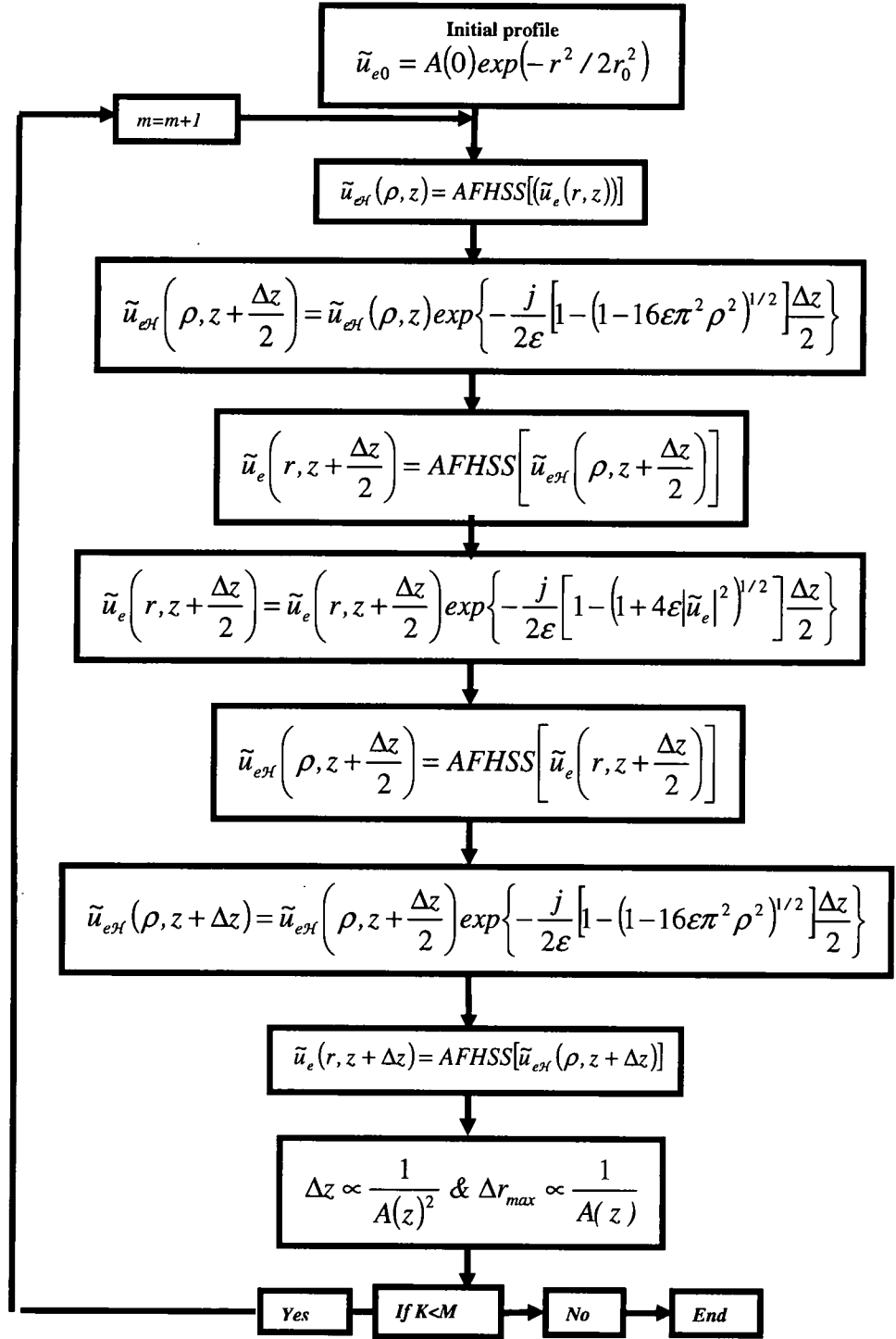


**Figure 6.1:** The AFHSS algorithm, a symmetrized version of the split step FFT using Hankel transform instead, and using adaptive longitudinal stepping and transverse grid management.

defined above. Although the trend is similar, this is a considerable improvement over the convergence test results in Fibich and Ilan <sup>2</sup>. Figure 6.3 and 6.4 shows the growth of the on-axis intensity using AFHSS technique for the two test functions respectively. Also, in these figures AFHSS we take  $\tilde{S} = 2\pi R_1 R_2 = 2\pi \times 2000$  (corresponding to approximately 4000 cylindrical samples) which permits computation for the paraxial case till  $z = z_c = [0.14817, 0.1461]$  corresponding to the expected  $z_c = [0.1505, 0.1478]$  from the empirical equations above<sup>22</sup>, respectively. Figure 6.5 and 6.6 shows the corresponding AFFSS technique for a  $1024 \times 1024$  grid where we get  $z = z_c = [0.1581, 0.15596]$ . This implies that the critical distance  $z_c$  is a little bit over estimated and the maximum intensity reached is also less than the AFHSS method. It is instructive to note that with increase in sampling points, the AFFSS approaches the results from AFHSS but on the expense of calculation time. Also we note that changing the number of samples in both techniques doesn't affect the value of the critical distance drastically but the maximum intensity reached at that point is less or more depending on the number of samples, which is in agreement with the convergence test mentioned above. We stress that in all computations using AFHSS and AFFSS, energy is always conserved. Consequently, AFHSS permits us to track peak intensities higher faster and more accurate than what is achievable by AFFSS. Also, by using adaptive non-paraxiality parameter  $\varepsilon$  in the scalar nonparaxial equation we obtain results similar to those of the more complex vector method<sup>102</sup> and superior to those when  $\varepsilon$  is constant.<sup>58</sup>

Finally, we compare computation speeds of the AFHSS and AFFSS. It can be shown that for Siegman's method, the number of computations is proportional to  $4N \log_2 2N + 2N$ , compared with  $2N^2 \log_2 N$  computations for the two dimensional

FFT as in AFFSS where  $N$  is the number of samples. Care should be taken to implement end corrections in the Hankel transform method, as discussed by Agrawal and Lax<sup>106</sup>. Although at first glance, the number of computations in Yu *et al*'s method is  $\propto N^2$ , we can make the number of computations comparable to Siegman's method by *a priori* computing and storing the zeros of the Bessel function. The advantages of Yu *et al*'s method over Siegman's are the accuracy for the sampled points and a simple retrieval expression. For more comparison between Yu *et al*'s and Siegman's method, we refer readers to Table 1 in Yu *et al.*<sup>94</sup>. Also, we note that the use of the adaptive variation of the longitudinal propagation stepping size  $\Delta z$  and the transverse spatial sampling size according to  $1/A^2(z)$  and  $1/A(z)$  allow us to track on-axis amplitudes, for the paraxial case, up to two orders of magnitude more than what is achievable without the adaptive algorithm, for both the AFHSS and AFFSS methods. Without the adaptive variation, the numerical methods become unstable, and we witness oscillatory focusing and defocusing of the beam from numerical instability. Typical run times on a *Pentium IV 2.4 GHz* processor with a *2 GB RAM* are around *1* minute for AFHSS when  $\tilde{S} = 2\pi R_1 R_2 = 2\pi \times 2000$ , *10* minutes for AFFSS when the mesh size is  $N^2 = (2^{10})^2$ . Note that the Hankel transform based method, which exploits the cylindrical symmetry, is one-dimensional and therefore is expected to be faster than other two-dimensional numerical methods, either FFT based or as in variational approaches such as in Ren and Wang<sup>107</sup>.

In summary, we have outlined a fast and accurate method for tracking beam propagating in a nonlinear Kerr medium in which the beam is expected to collapse for paraxial approximation, and to cyclic focusing and defocusing in the nonparaxial case.

Based on results for the paraxial case, we feel that the AFHSS is an accurate and fast simulation method, and that results similar to the vector method can be achieved using an adaptive  $\varepsilon$  in the scalar equation to account for nonparaxiality.

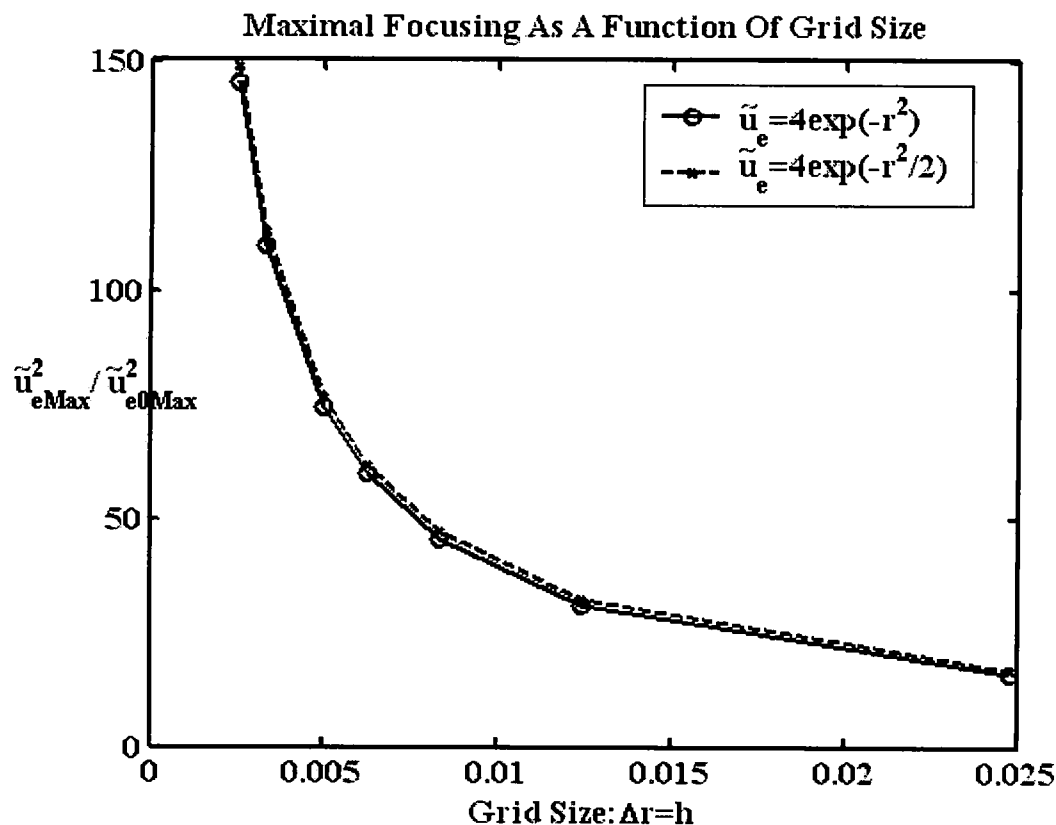
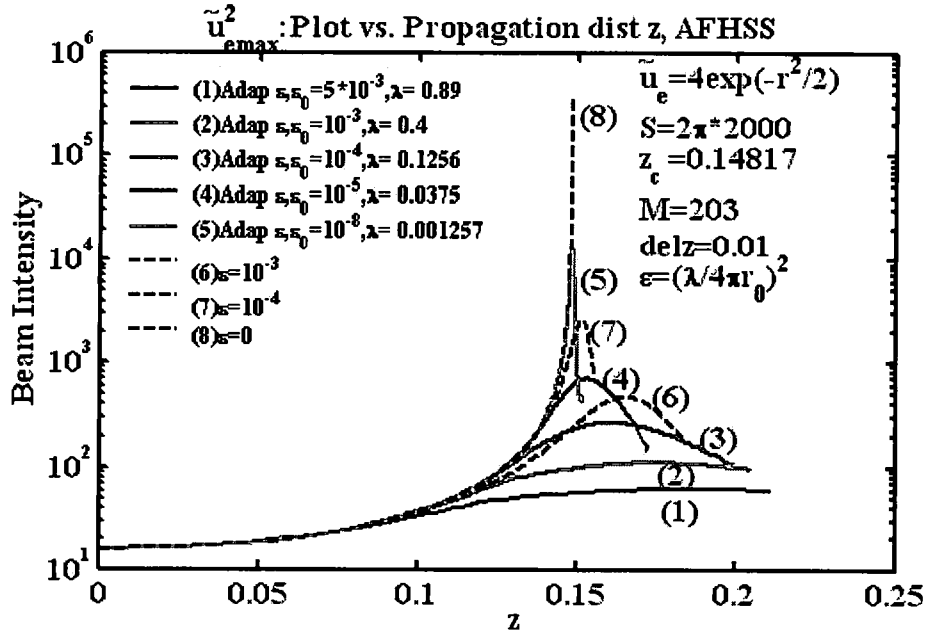


Figure 6.2: Maximal focusing as a function of grid size.

### 6.3 Saturating Nonlinearity

We use the novel technique developed in Chapter 4 to numerically solve pulsed optical beam or “light bullet” propagation in bulk nonlinear media based on the scalar NLSE in three dimensions with spherical symmetry. Using fast algorithms for spherical Fourier Bessel transforms along with adaptive longitudinal stepping and transverse grid management in a symmetrized split-step technique it is possible to accurately study many nonlinear effects, including the possibility of spatiotemporal collapse, or the collapse-arresting mechanism due to saturable nonlinearity.



**Figure 6.3:** On-axis intensity of  $\tilde{u}_{e0} = 4\exp(-r^2/2)$  as a function of propagation for fixed values of  $\varepsilon$  ranging from  $10^{-2}$  to  $10^{-8}$  where  $z = z_c = 0.1481$  for  $\varepsilon = 10^{-8}$ , and for an adaptive  $\varepsilon$  varying as  $\varepsilon = (\lambda/4\pi r)^2$ , using AFHSS with  $\tilde{S} = 2\pi R_1 R_2 = 2\pi \times 2000$  (4000 cylindrical samples).  $\lambda$  in inset is normalized to  $r_0$ .

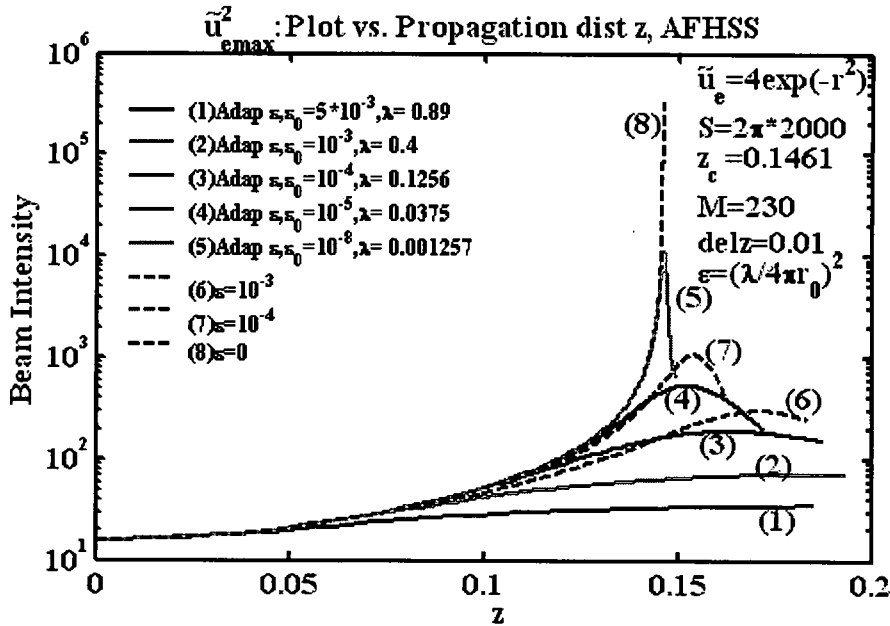


**Figure 6.4:** On-axis intensity of  $\tilde{u}_{e0} = 4\exp(-r^2)$  as a function of propagation for fixed values of  $\varepsilon$  ranging from  $10^{-2}$  to  $10^{-8}$  where  $z = z_c = 0.1461$  for  $\varepsilon = 10^{-8}$ , and for an adaptive  $\varepsilon$  varying as  $\varepsilon = (\lambda/4\pi r)^2$  using AFHSS with  $\tilde{S} = 2\pi R_1 R_2 = 2\pi \times 2000$  (4000 cylindrical samples).  $\lambda$  in inset is normalized to  $r_0$ .



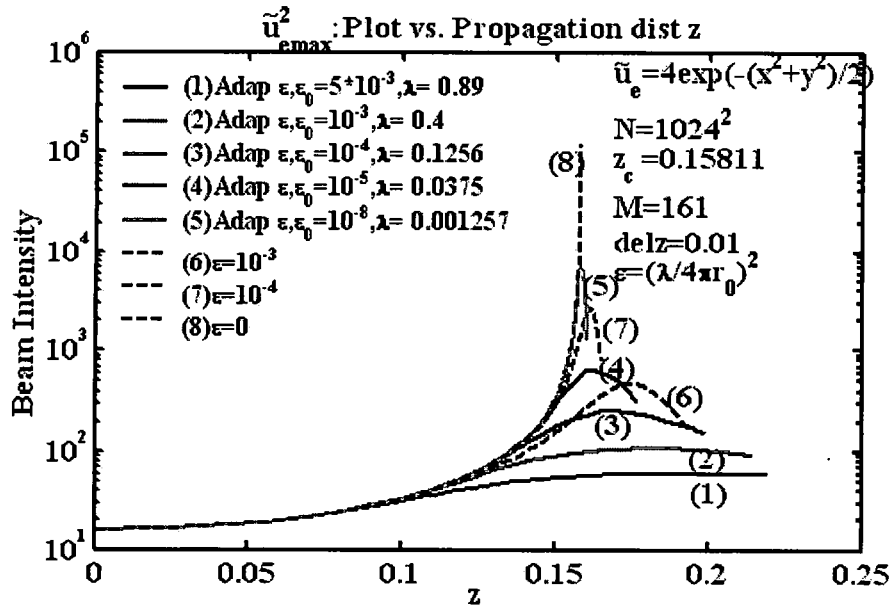


**Figure 6.5:** On-axis intensity of  $\tilde{u}_{e0} = 4 \exp(-r^2/2)$  as a function of propagation for fixed values of  $\varepsilon$  ranging from  $10^{-2}$  to  $10^{-8}$  where  $z = z_c = 0.1581$  for  $\varepsilon = 10^{-8}$ , and for an adaptive  $\varepsilon$  varying as  $\varepsilon = (\lambda/4\pi r_0)^2$ , using AFFSS with  $1024^2$  samples.  $\lambda$  in inset is normalized to  $r_0$ .

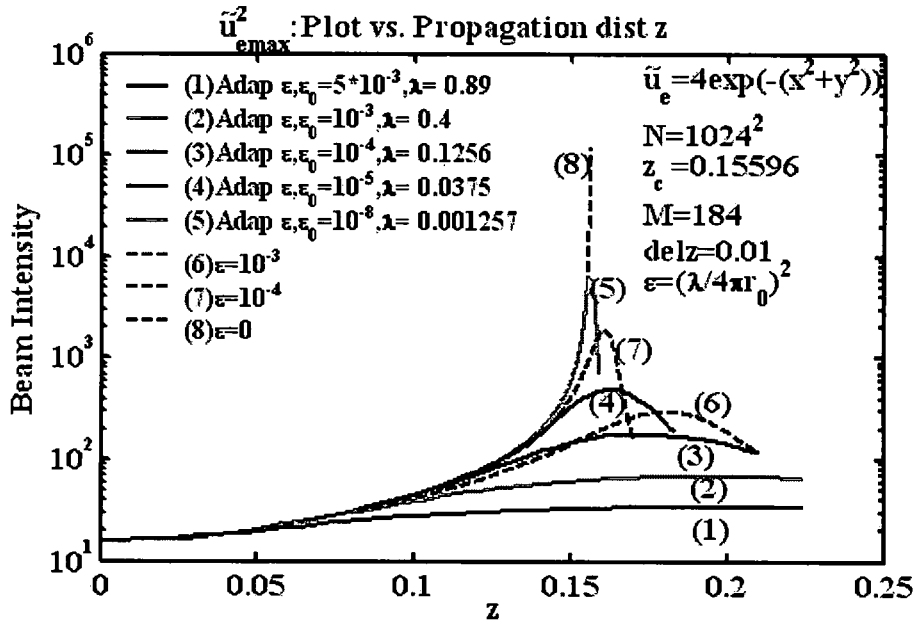


**Figure 6.6:** On-axis intensity of  $\tilde{u}_{e0} = 4 \exp(-r^2)$  as a function of propagation for fixed values of  $\varepsilon$  ranging from  $10^{-2}$  to  $10^{-8}$  where  $z = z_c = 0.15596$  for  $\varepsilon = 10^{-8}$ , and for an adaptive  $\varepsilon$  varying as  $\varepsilon = (\lambda/4\pi r_0)^2$  using AFFSS with  $1024^2$  samples.  $\lambda$  in inset is normalized to  $r_0$ .

### 6.3.1 Introduction

When a pulsed optical beam propagates through a bulk nonlinear medium, it is affected by diffraction, anomalous dispersion, and nonlinear refraction. Such a space-time combined effect leads to many nonlinear phenomena such as spatiotemporal collapse, which can yield short pulses with extremely high optical fields, or formation of three dimensional optical solitons or light bullets<sup>51</sup>. These light bullets represent an extension of self-trapped optical beams into the temporal domain. Such optical solitons may become important in telecommunication systems due to their self-confined structure, by preserving their shape after propagating long distances, where they satisfy the requirement of being self-guided in bulk media. Under the combined and balanced effect of linear diffraction and dispersion and the spatio-temporal nonlinear effect, optical bullets may exist. The above phenomenon is traditionally governed by the (3+1)-dimensional nonlinear Schrodinger equation (NLS), which can be viewed as a limit of the Zakharov system of Langmuir waves in plasmas<sup>42,108</sup>. Note that in (1+1)-dimensions, the NLS equation can be solved explicitly by the inverse scattering method<sup>19</sup> and they are stable, corresponding to temporal or spatial solitons. However, in (2+1) and (3+1)-dimensional cases, solutions are not stable and they can be stabilized by using saturating nonlinearities or graded-index nonlinear media for example<sup>60</sup>. On the experimental front, (2+1)-dimensional spatiotemporal solitons (STSs) that overcome diffraction in one transverse spatial dimension have been created by using the quadratic nonlinearity<sup>109</sup>. Note that, in a quadratically nonlinear medium with phase mismatch  $\Delta K$ , it has been shown<sup>68</sup> that the effective cubic nonlinearity coefficient is

$\chi_{eff}^{(3)}(z) \propto (\chi^{(2)})^2 \left( \frac{1 - \exp(-j\Delta K z)}{\Delta K} \right)$ , which is periodic in the longitudinal dimension. The

same cannot be said for (3+1)-dimensional STSs where there is no experimental evidence for their existence. Also, stabilization of (2+1)D discrete vortex solitons in a SF nonlinear medium has been observed in optically induced photonic lattices and in media with competing nonlinearities (quadratic-cubic or cubic quintic). STSs in (2+1) and (3+1)-dimensions propagating in media with periodic dispersion or nonlinearity can also be stabilized<sup>26,65,67,110-112</sup>. Another way to arrest the collapse in Kerr-type focusing media is to use two-dimensional nonlinear photonic lattices in a three-dimensional environment by harmonic transverse modulation of the refractive index<sup>113</sup>, where it is proven that one parameter families of three-dimensional STSs can be stabilized provided their energy is within a certain interval and the strength of the lattice potential, which is proportional to the refractive index modulation depth, is above a certain threshold value. Note that, the study of coherent wave propagation in lattice systems and its stabilization have generated intense activity in the field of optics and matter waves in optical trapping potentials. Also, it is known that stable solitons with nonzero vorticity may exist in media with competing nonlinearity provided their power exceeds some threshold value<sup>113</sup>. We also note that by computing eigenvalues of the linearized Schrödinger equation, it has been shown that rings with spin  $\hat{s} = 1$  and  $\hat{s} = 2$  are linearly stable, provided that they are very broad<sup>114</sup>. Recently, an extensive survey of experimental and theoretical results has been published on the stabilization of multidimensional solitons in optics and BECs<sup>115</sup>.

In this Section we use the technique developed in Chapter 4 which we call the adaptive Fourier Bessel split-step (AFBSS) method, to numerically solve the (3+1)-dimensional NLS equation with and without saturating nonlinearity, which is classically used to model this phenomenon<sup>19,51,60,108</sup>. This method can also be applied to 2D and 3D

solitons with a nonzero topological charge (or spin) in the cubic quintic model we have at hand and in general models of competing nonlinearities as shown in Section 6.3.4, where it is sufficient to change the order of the Hankel transform to account for the spin of the (D+1)-dimensional solitons of the nonlinear Schrödinger equation.

The time-dependent (3+1)-dimensional (D=3) paraxial wave equation, in the presence of group velocity dispersion is<sup>51,60,61</sup>:

$$j \frac{\partial u_e}{\partial Z'} + \frac{1}{2k_0} \left( \frac{\partial^2 u_e}{\partial X'^2} + \frac{\partial^2 u_e}{\partial Y'^2} \right) - \frac{k_2}{2} \frac{\partial^2 u_e}{\partial T'^2} + \Re(|u_e|^{2\bar{\sigma}}) u_e = 0, \quad (6.6)$$

where  $u_e$  is the slowly varying envelope of the optical field,  $T'$  is the reduced time in a moving frame of reference,  $k_1$  is the group velocity,  $k_0 = \frac{n_0 \omega}{c}$  is the propagation constant,  $k_2$  is the group-velocity dispersion (GVD) parameter, and  $\Re(|u_e|^{2\bar{\sigma}}) = \frac{k_0}{n_0} \delta n(|u_e|^{2\bar{\sigma}})$  is the nonlinear parameter responsible for self-phase modulation (SPM). Note that  $k_2$  can be positive or negative depending on the nature of the dispersion in the medium, corresponding to normal dispersion (ND) and anomalous dispersion (AD) respectively. Also, for  $\bar{\sigma} = 1$ ,  $\delta n(|u_e|^2) = n_2 |u_e|^2 + n_4 |u_e|^4$  is the intensity induced change in index where  $n_4 \neq 0$  in the case of saturable nonlinearity.

### 6.3.2 Spatio-Temporal Collapse

Introducing the following normalization<sup>61</sup> for Eq. (1):  $z = \frac{Z'}{L_d}$ ,  $x = \frac{X'}{w_0}$ ,

$y = \frac{Y'}{w_0}$ ,  $\tau = \frac{T'}{(w_0^2 k_0 k_2)^{1/2}}$ ,  $f(|u_e|^{2m}) = L_d \Re(|u_e|^{2\bar{\sigma}})$ ,  $L_d = 2k_0 w_0^2$ , we arrive at

$$j \frac{\partial \tilde{u}_e}{\partial \tau} + \left( \frac{\partial^2 \tilde{u}_e}{\partial x^2} + \frac{\partial^2 \tilde{u}_e}{\partial y^2} - s_d \frac{\partial^2 \tilde{u}_e}{\partial \tau^2} \right) + f(|\tilde{u}_e|^{2\bar{\sigma}}) \tilde{u}_e = 0, \quad (6.7)$$

where  $s_d = \text{sgn}(k_2)$ ,  $w_0$  is the initial transverse spatial width,  $L_d$  is the diffraction length.

If use the spherical symmetry of the field distribution and introduce the radial variable

$r = (x^2 + y^2 + \tau^2)^{1/2}$ , Eq. (6.7) can be written as<sup>60</sup>

$$j \frac{\partial \tilde{u}_e}{\partial z} + \frac{1}{r^{D-1}} \frac{\partial}{\partial r} \left( r^{D-1} \frac{\partial \tilde{u}_e}{\partial r} \right) + f(|\tilde{u}_e|^2) \tilde{u}_e = 0, \quad (6.8)$$

where  $D$  is 3 and  $\bar{\sigma} = 1$  in our case. The shape preserving solution  $\bar{a}$  of Eq. (6.8) in a Kerr type unsaturated medium can be found by looking for a solution  $u(x, y, z, \tau) = \bar{a}(x, y, \tau) e^{-i\kappa z}$ , where  $\kappa$  is the propagation constant. Since  $\bar{a}$  does not depend on  $z$ , it will not change its spatial or temporal shape during propagation, resulting in what we call an optical bullet. Using the above ansatz in Eq. (6.8), we arrive at<sup>51,61</sup>

$$\frac{d^2 \bar{a}}{dr^2} + \frac{D-1}{r} \frac{d\bar{a}}{dr} - \kappa \bar{a} + \bar{a}^3 = 0, \text{ with } \bar{a}(\infty) = 0. \quad (6.9)$$

Eq. (6.9) has been analytically solved for  $D=1$  and numerically solved for  $D=2,3$ . The lowest order solution  $D=3$  corresponds to the optical bullet. Figure 6.7 shows this

solution by plotting  $\frac{\bar{a}(r)}{\bar{a}(0)}$  versus  $r$  and compares it to with corresponding solutions

obtained for  $D=1$  and  $2^{51,100}$ . The propagation constant is  $\kappa = (0.5, 0.2055, 0.05316)$  and

the pulse energy is  $\mathcal{N} = 2^{D-1} \pi \int |\tilde{u}_e|^2 r^{D-1} dr = (2, 5.85, 28.87)$  for

$D = (1, 2, 3)$  respectively<sup>51,61</sup>. Assuming a Kerr type unsaturated medium we should note

that for  $D=3$  and  $w_0 = 1$ , if the spatiotemporal pulse energy exceeds a certain critical

value  $\mathcal{N}_c \approx 3\pi\sqrt{2\pi} \approx 23.6$  for an unchirped Gaussian input<sup>61</sup>, small fluctuations of the

intensity, beam size or pulse width can grow with propagation and lead to a phenomenon

known as spatiotemporal collapse. In other words, the intensity becomes infinitely large

at a finite distance as the size of the beam diminishes and tends to zero both in the spatial and temporal domains.

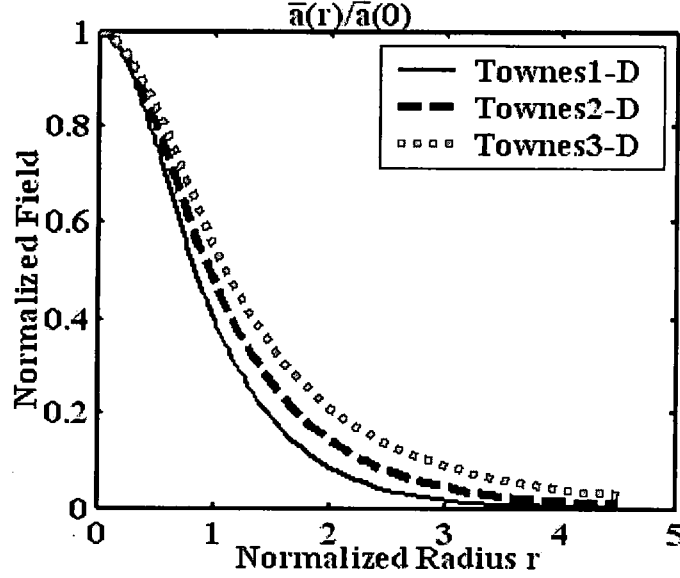


**Figure 6.7:** Radial dependence of the self-trapped normalized field in 1,2,3 transverse dimensions.

There are few known integral invariants for Eq. (6.8) when  $\partial D \geq 2$ . These invariants can be obtained either from the Noether's theorem, or from the symmetry of the NLS equation under gauge, space, and time transformations<sup>61,101,116</sup>. Three of these invariants are the energy, Hamiltonian and the momentum, defined as<sup>60,61,101,116</sup>:

$$\mathcal{N} = 2^{D-1} \pi \int |\tilde{u}_e|^2 r^{D-1} dr, \quad (6.10a)$$

$$H = \int \left( |\nabla \tilde{u}_e|^2 - F(|\tilde{u}_e|^2) \right) r^{D-1} dr, \quad (6.10b)$$

$$\mathcal{M} = -j \int \left( \tilde{u}_e^* \nabla \tilde{u}_e - \tilde{u}_e \nabla \tilde{u}_e^* \right) r^{D-1} dr, \quad (6.10c)$$

where  $F(\tilde{u}_e) = \int_0^{\tilde{u}_e} f(\xi) d\xi$ . Two techniques are traditionally used to study the

spatiotemporal collapse<sup>60,61</sup>. The first is the moment method technique based on the

virial theorem and the second may be derived from a variational technique based on the Lagrangian density corresponding to Eq. (6.8). If we stick to the first technique here then the quantity of most interest to us is<sup>61</sup>

$$\frac{d^2 \tilde{\sigma}^2(z)}{dz^2} = \frac{1}{\mathcal{N}} \left( 8H + 4\mathcal{R} - \frac{4\mathcal{M}^2}{\mathcal{N}} \right) \quad (6.11)$$

due to its relation to the self-focusing effect, where  $\mathcal{R} = \left(1 - \frac{D}{2}\right) \int F(|\tilde{u}_e|^2) r^{D-1} dr < -\frac{\mathcal{N}^2}{2V_p}$

for unsaturated Kerr type media, and the

variance  $\tilde{\sigma}^2(z) = \langle r^2 \rangle - \langle r \rangle^2, \langle r^n \rangle = \frac{\int r^n |\tilde{u}_e|^2 r^{D-1} dr}{\mathcal{N}}$  is the  $n^{th}$  moment of  $r$  and  $\tilde{\sigma}$  is a

measure of the spatial and temporal spreads associated with an optical pulse. If the right hand side of Eq. (6.11) is negative or the initial energy exceeds a threshold

$\mathcal{N}_c \approx \frac{3\pi\sqrt{2\pi}V_p w_0}{V_p + \pi\sqrt{2\pi}w_0^3}$ , where  $V_p$  is a constant representing the volume in which most of

the pulse is located, then the variance  $\tilde{\sigma}^2(z)$  decreases monotonically along the propagation direction, becoming zero at a finite distance associated with the

spatiotemporal collapse, at a distance  $z_c = \tilde{\sigma}_0 \left( \frac{\mathcal{N}V_p}{\mathcal{N}^2 - 4V_p H} \right)^{1/2}$  where  $\tilde{\sigma}_0 = w_0$ .

Zakharov *et al*<sup>20</sup> predict similarity solutions when  $D=3$  of the form:

$$\tilde{u}_e(r, z) \propto \frac{1}{(z_r - z)^{1/2}} Q\left(\frac{r}{(z_r - z)^{1/2}}\right), \quad (6.12)$$

where  $Q$  is an arbitrary function. We use this knowledge in order to adaptively vary the longitudinal stepping  $\Delta z$  and the spatial dimension of the beam.

### 6.3.3 Saturating Nonlinearity And Optical Bullets

In this Section we use the variational approach based on the Lagrangian formalism of classical mechanics in terms of the Lagrangian density<sup>60,61,116</sup>

$$\mathcal{L} = \frac{j}{2} \left( \tilde{u}_e^* \frac{\partial \tilde{u}_e}{\partial z} - \tilde{u}_e \frac{\partial \tilde{u}_e^*}{\partial z} \right) - \frac{1}{2} |\nabla \tilde{u}_e|^2 + F(|\tilde{u}_e|^2), \quad (6.13)$$

where the  $(D+1)$  NLS equation can be derived from  $\mathcal{L}$  using the Euler-Lagrange equation<sup>116</sup>

$$\frac{\partial}{\partial z} \frac{\partial \mathcal{L}}{\partial (\partial \tilde{u}_e / \partial z)} + \sum_{i=1}^3 \frac{\partial}{\partial x_i} \frac{\partial \mathcal{L}}{\partial (\partial \tilde{u}_e / \partial x_i)} - \frac{\partial \mathcal{L}}{\partial \tilde{u}_e} = 0, \quad (6.14)$$

where  $(x_1, x_2, x_3) = (x, y, \tau)$  respectively. Let us assume the initial profile to be<sup>60,61</sup>

$$\tilde{u}_e = \tilde{u}_e(r, z) = A(z) \exp \left[ - (1 + j b(z)) \frac{r^2}{2w^2(z)} + j \tilde{\phi}(z) \right] \quad (6.15)$$

where  $A(z)$  is the amplitude,  $w(z)$  is the beam radius,  $b(z)$  is the wave front curvature, and  $\tilde{\phi}(z)$  is the phase as unknown functions of the propagation distance  $z$ . Following the method<sup>60</sup>, we can derive a set of evolution equations called Euler-Lagrange equations taking into account that the variation with respect to the unknowns in the initial profile should be equal to zero. The evolution of  $w(z)$  is governed by<sup>60</sup>:

$$\frac{d^2 w}{dz^2} = \frac{4}{w^3} - \frac{2}{w} \left[ \mathcal{K}'(A^2) - \frac{\mathcal{K}(A^2)}{A^2} \right] \quad (6.16a)$$

$$A^2 w^D = A_0^2 w_0^D = N_0 \quad (6.16b)$$

where  $\mathcal{K}(\tilde{u}_e) = \frac{4}{\Gamma(D/2)} \int_0^\infty v^{D-1} F(\tilde{u}_e e^{-v^2}) dv$ . If we choose the initial width  $w_0 = w_e$  a

stationary solution to Eq. (6.16a) is obtained as  $w_e = \sqrt{2 \left[ \mathcal{K}'(A_0^2) - \frac{\mathcal{K}(A_0^2)}{A_0^2} \right]^{-1/2}}$ , where



$A_0^2 = N_0 / w_e^3$  for  $D=3$ . Note that for  $D=2$ , the result agrees with the paraxial propagation of a beam in a cubically nonlinear medium as described from the q-formalism approach, as in Banerjee<sup>56</sup>. In this case, there is no unique solution for the width, rather for a critical power, the beam does not diffract.

If now we consider the saturating nonlinearity of the form

$$f(\tilde{u}_e) = \frac{\tilde{u}_e}{1 + \mu \tilde{u}_e} \approx \tilde{u}_e - \mu \tilde{u}_e^2 \quad \text{we get} \quad F(\tilde{u}_e) = \tilde{u}_e^2/2 - \mu \tilde{u}_e^3/3, \mathcal{K}(\tilde{u}_m) = \alpha_s \tilde{u}_e^2 - \beta_s \mu \tilde{u}_e^3,$$

$$\text{where } \alpha_s = 2^{-3/2}, \beta_s = 2 \times 3^{-5/2}, \text{ then } w_e^2 = \frac{2}{\alpha_s A_0^2 - 2\beta_s \mu A_0^4}.$$

Also, from<sup>60</sup> if the bullet parameter defined as

$$\Omega_s^2 = w_0^{-2} \left[ \frac{4 + 2D}{w_0^2} - D A_0^2 \mathcal{K}''(A_0^2) \right] > 0, \text{ then the solution is stable. In the case of}$$

saturating nonlinearity it boils down to  $A_0^2 > \frac{\alpha_s(D-2)}{4\beta_s\mu(D-1)} \approx \frac{0.336}{\mu}$  which corresponds to

$$w_e = \left( \frac{2}{0.12 - 0.03\mu} \right)^{1/2} = 4.716 \text{ which corresponds to } (N_c = 2\mathcal{N}_c/\Gamma(D/2)) = 35.3 \text{ for}$$

$\mu = 1$  and  $D=3$ . Also, from Eq. (6.16a) we can calculate the zero Hamiltonian width

$$w_H^2 = \frac{D}{\alpha_s A_0^2 - \mu \beta_s A_0^2} \text{ where for every } w_0 > w_H \text{ we have } (H_c = 2\mathcal{H}_c/\Gamma(D/2) < 0) \text{ and}$$

the optical pulse forms an oscillating waveguide. Note that when  $D=3$  we have the following cases:

*Case 1:*  $A_0^2 > \frac{\alpha_s}{4\beta_s\mu} \Rightarrow w_e > w_H$ , admits a stable equilibrium solution. If

$w_H < w_e < w_0 \Rightarrow H < 0$  then the beam will initially start to focus and then self-trapping

occurs. Also, if  $w_H < w_0 < w_e \Rightarrow H < 0$  defocusing and then self-trapping occurs, and if  $w_0 < w_H < w_e \Rightarrow H > 0$ , and the beam diffracts monotonically.

*Case 2:*  $A_0^2 < \frac{\alpha_s}{4\beta_s\mu} \Rightarrow w_e < w_H$ , admits a unstable equilibrium solution. If

$w_e < w_H < w_0 \Rightarrow H < 0$  then the beam will initially start to focus and then self-trapping occurs. Also, if  $w_0 < w_e < w_H \Rightarrow H > 0$  and the beam diffracts monotonically, and if  $w_e < w_0 < w_H \Rightarrow H > 0$ , focusing and then self-trapping occurs. Figure 6.8 shows the stability regions for the cases of  $D=2$  and 3.

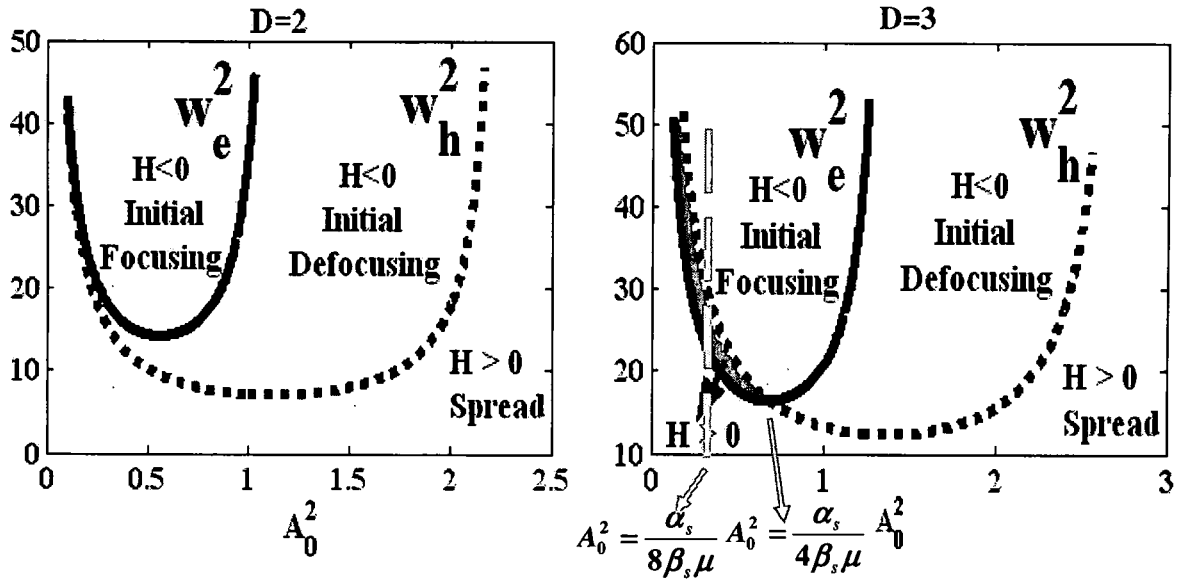


**Figure 6.8:** Stability regions for the 2 and 3 D spatiotemporal solitons in saturating nonlinearity medium.

### 6.3.4 Adaptive Spherical Fourier Bessel Split Step Method

There are several numerical approaches for implementing the Hankel transform as explained in Chapter 4<sup>91,94</sup>. Guizar-Sicairos *et al*'s method<sup>95</sup>, is based on the expansion of the function and its transform by a zero order Bessel series. In this Section we adopt this

method. The AFBSS algorithm in Figure 6.9 resembles the symmetrized Fourier split-step technique<sup>59,90</sup>, where we change the time step and the spatial range adaptively using Zakharov *et al* similarity formula Eq. (6.12)<sup>20</sup> in order to track the varying amplitude of the spatiotemporal pulse in the unsaturated medium. We note that periodic focusing/defocusing or beam trapping occurs when we have a saturated medium and under the conditions stated above.

### 6.3.5 Numerical Results And Conclusions

We now show sample simulation results using the ASFBSS method that uses Guizar-Sicairos et al's Hankel transform technique<sup>31,95</sup>. All the input functions are of the type mentioned in Eq. (6.15) and are mentioned in the work of<sup>90</sup>. Figure 6.10 shows the case when  $N_0 = 50, A_0^2 = 0.4, w_0 = 5$ , which corresponds to *Case 2* where  $w_e < w_H < w_0 \Rightarrow H < 0$ . Here the beam will start focus until  $w < w_e < w_H$  then self-trapping occurs. Figure 6.11 shows the case when  $N_0 = 50, A_0^2 = 1, w_0 = 3.684$ , which corresponds to *Case 1* where  $w_H < w_0 < w_e \Rightarrow H < 0$  and defocusing followed by self-trapping occurs. Figure 6.12 shows the case when  $N_0 = 50, A_0^2 = 0.36, w_0 = 4.8$ ,  $w_e < w_0 < w_H \Rightarrow H > 0$ , focusing and then self-trapping occurs.

Finally, we compare computation speeds of the ASFBSS and the regular 3-D FFT. The number of computations in 3-D FFT is  $\propto M^3 \log_2 M$ . On the other hand we can make the number of computations of Guizar-Sicairos et al's method comparable to Siegman's method<sup>3</sup> namely equal to  $4M \log_2 2M + 2M$  by a priori computing and storing the zeros of the spherical Bessel function. The advantages of Guizar-Sicairos et al's method over Siegman's are the accuracy for the sampled points and a simple retrieval

expression. For more comparison between Guizar-Sicairos et al's and Siegman's method, we refer readers to Table 1 in Yu et al.<sup>94</sup>. Also, we note that the use of the adaptive variation of the longitudinal propagation stepping size  $\Delta z$  and the transverse spatial sampling size according to  $1/A_{max}^{1/2}$  allow us to track on-axis amplitudes, for the paraxial unsaturated case, more precisely than regular 3-D FFT methods. Without the adaptive variation in the case of unsaturated media, the numerical methods become unstable, and we witness oscillatory focusing and defocusing of the beam from numerical instability. Typical run times are around 1 minute for ASFBSS when  $\tilde{S} = 2\pi R_1 R_2 = 1600\pi$ , 1 hour for 3-D FFT when the mesh size is  $M^3 = (2^{10})^3$ .

#### 6.4 Summary

In summary, we have outlined a fast and accurate method for tracking spatiotemporal pulse propagation in a saturated and unsaturated nonlinear Kerr medium in which the spatiotemporal collapse is expected for the paraxial unsaturated medium approximation, and to cyclic focusing and defocusing in the saturating nonlinearity case. The method is based on the novel numerical and semi analytical techniques devised in Chapters 4 and 5 respectively. These methods we find useful in order to obtain better and more accurate results than existing techniques. Based on results for the unsaturated case, we feel that the ASFBSS is the more accurate and faster simulation method<sup>19,117</sup>. In Chapters 7 we continue with other focusing arrest mechanism namely dispersion management which we study numerically using Fourier Bessel transform technique and analytically using the variational technique introduced in Chapters 4 and 5.

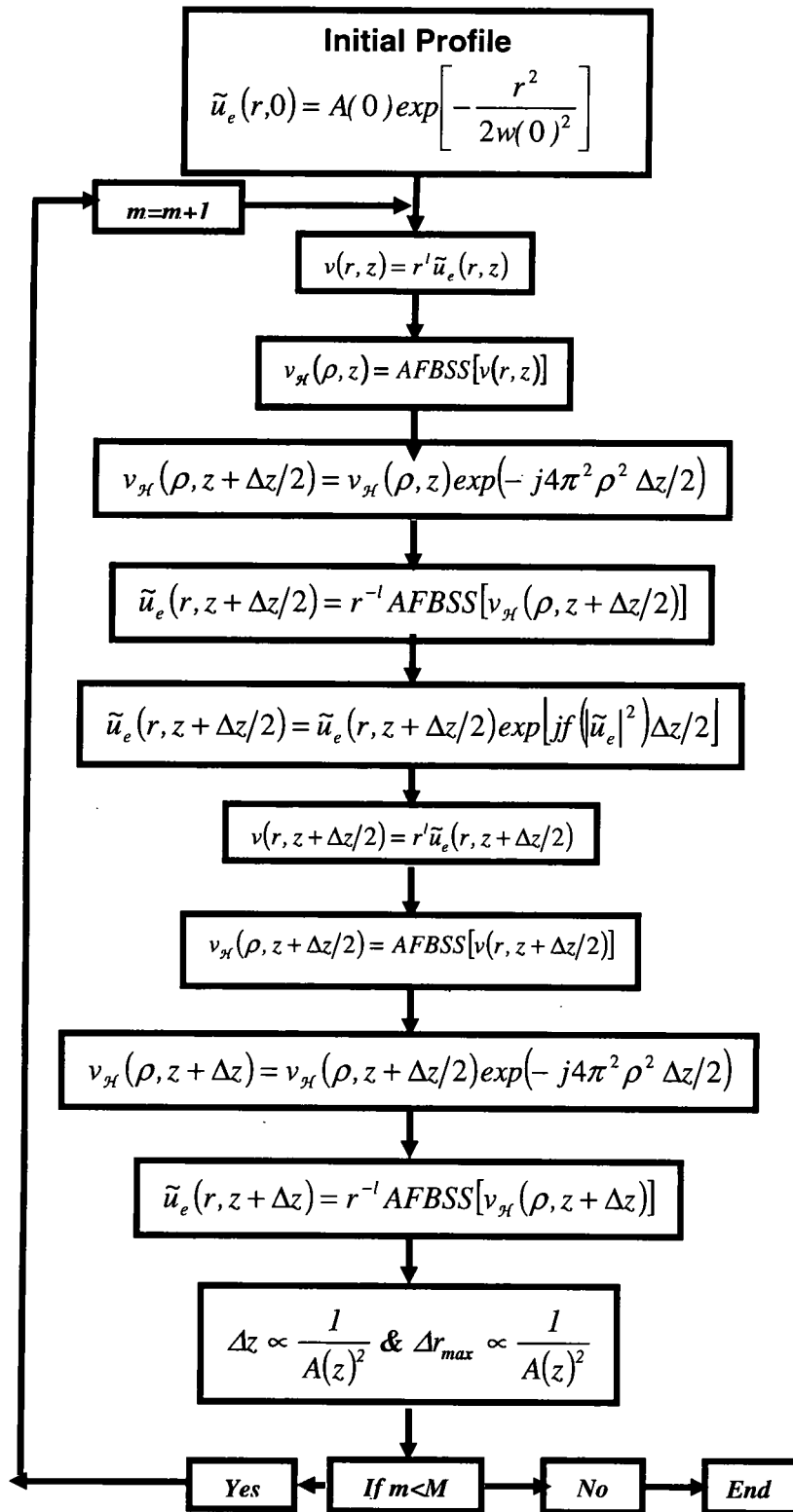


**Figure 6.9:** The AFBSS algorithm, a symmetrized version of the split step FFT using Spherical Fourier Bessel transform instead, and using adaptive longitudinal stepping and transverse grid management.

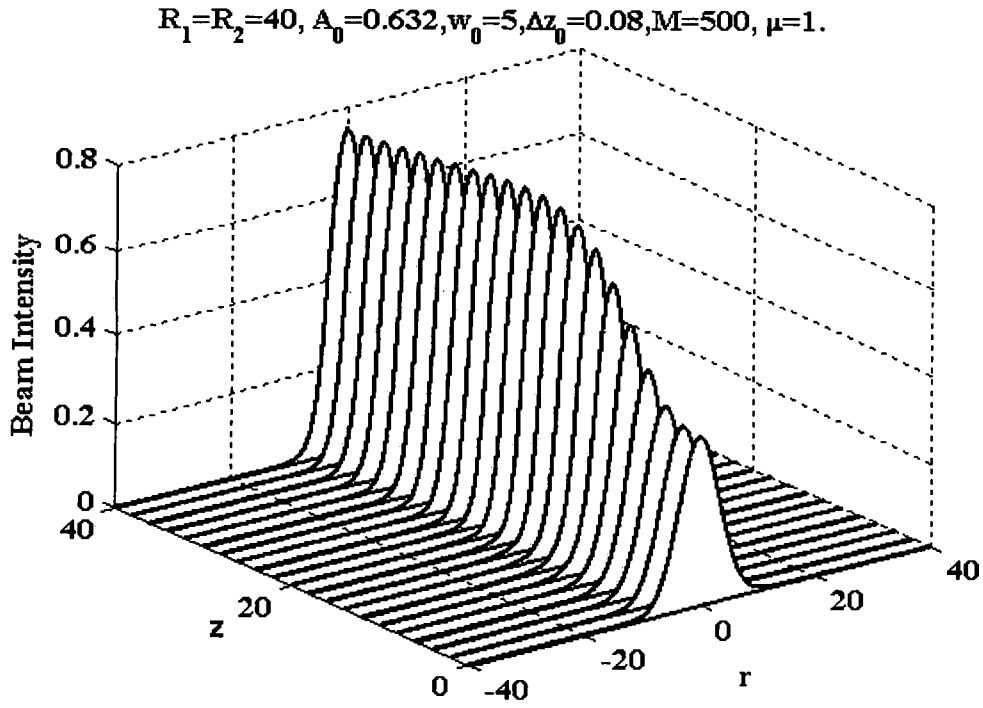


**Figure 6.10:** Stable light-bullet generation with initial focusing for  $N_0 = 50, A_0^2 = 0.4, w_0 = 5, w_e < w_H < w_0 \Rightarrow H < 0$ .

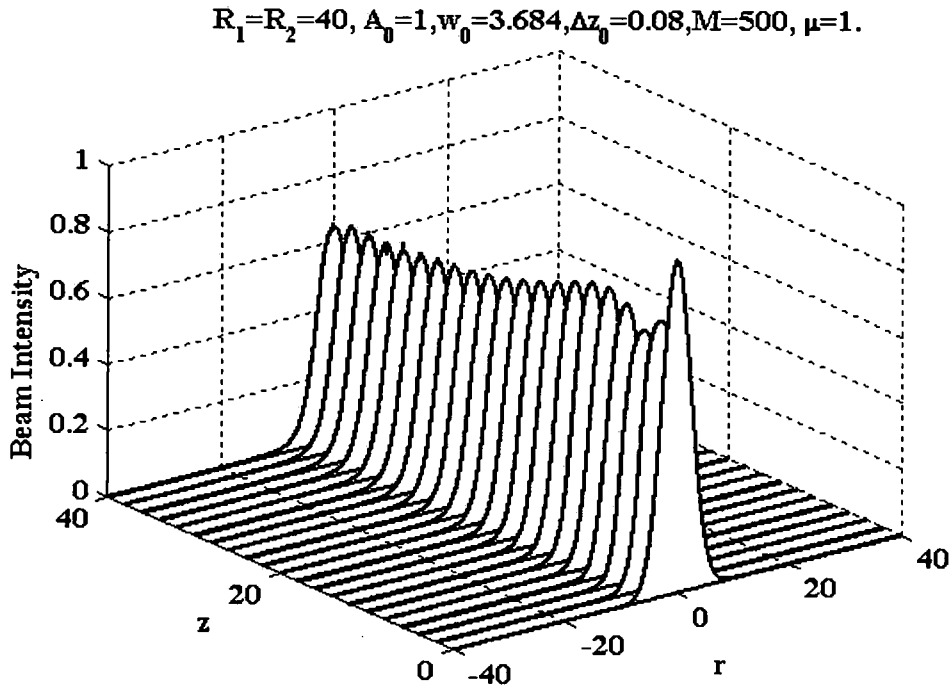


**Figure 6.11:** Stable light-bullet generation with initial defocusing for  $N_0 = 50, A_0^2 = 1, w_0 = 3.684, w_H < w_0 < w_e \Rightarrow H < 0$ .

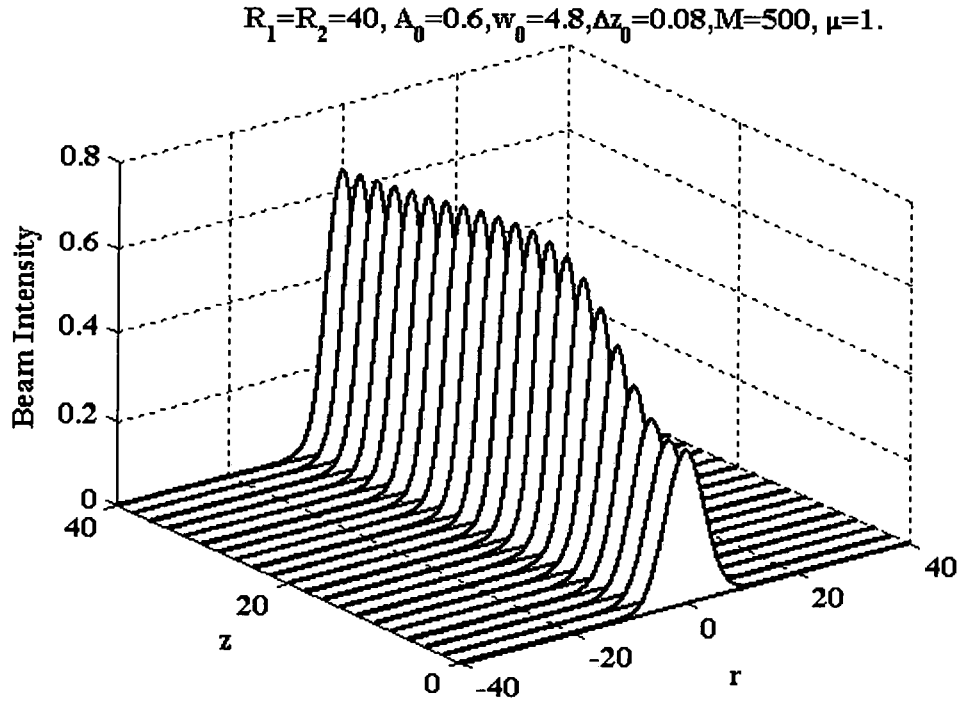


**Figure 6.12:** Stable light-bullet generation with initial focusing for  $N_0 = 50, A_0^2 = 0.36, w_0 = 4.8, w_e < w_0 < w_H \Rightarrow H > 0$ .

## **CHAPTER 7**

### **DISPERSION MANAGEMENT IN 1, 2 AND 3-D**

#### **7.1 Introduction**

In this Chapter we use the two numerical techniques developed in Chapter 3 and 4 namely the wavelet transform and the Fourier Bessel transform respectively and the analytical technique developed in Chapter 5 namely the variational technique to study pulse propagation in dispersion managed environment in  $(D+1)$ -dimensions and to study their stability regions and their propagation dynamics.

#### **7.2 Dispersion management in 1-D**

In 1-D we present a novel technique based on wavelet transform to numerically solve pulse propagation in a nonlinear optical fiber with periodically modulated dispersion. An analytical description for the chirped pulse dynamics based on the Lagrangian theory is also presented, on which the average dispersion is in the anomalous regime, where we obtain good agreement between this analytical method and the new numerical method proposed. Also, we compare results of this new method with those obtained using adaptive fast Fourier split step (AFFSS) technique. Note that the numerical method developed here as indicated in Chapter 3 can be used to approximate any order of nonlinearity in the self-phase modulation or if we have a loss term. Also, the adaptive capability of the discrete wavelet transform technique can be used to track the steep pulse gradients associated with high order terms, if available, by switching to



higher, more accurate wavelet levels. Moreover, by using this numerical technique the analysis will be all limited to the wavelet domain contrary to split-step methods where we switch between frequency and time/spatial domains.

### 7.2.1 Introduction

Recently, dispersion management (DM) technique has received a lot of attention due to its benefits in high-speed optical communications systems. DM purpose is to reduce radiation from the pulse due to amplifiers compensating fiber loss, modulation instability reduction in bandwidth and in gain, jitters due to collisions between signals in different channels of wavelength division multiplexed (WDM) systems, Gordon-Haus effect resulting from noise, suppressing the phase-matched four wave-mixing processes, which leads to detrimental effect in WDM systems. But, if we allow large local dispersion, the efficiency of four wave mixing can be reduced<sup>63,64</sup>. However, the periodic modulation of dispersion leads to the radiative damping of solitons or to the existence of vibrating and splitting of solitons<sup>62</sup>. Also, DM causes a strong perturbation to the nonlinear pulse propagation in the fiber. Despite all this, previous works by<sup>118-121</sup> suggests that the pulse appears to be stable in many numerical simulations especially if we have high-frequency modulation, which will also be shown in this work. For it is crucial in the end to prove that we end up in stable pulses suitable for long distance communication without significant change in shape from their initial launch conditions if observed after each map period. Note that, during each dispersion map period the pulse's width, amplitude, and quadratic phase chirp can change but in a periodic manner where a DM breather is supported. Analytical study is necessary to understand fundamental pulse dynamics and the interaction between dispersion fluctuation and nonlinearity. Several

different methods have been developed to study pulse propagation in DM fibers such as the numerical averaging method<sup>122</sup>, the guiding-center theory<sup>123</sup>, the variational theory<sup>124</sup>, and the multiscale theory<sup>125</sup>. All these methods have their region of applicability to successfully describe the pulse dynamics of the DM solitons. As an example according to precision we obtain: numerical averaging method always gives the exact solution, guiding-center theory gives asymptotically exact results at small energy and small dispersion modulation, multiscale theory is used at large dispersion modulation, and variational (Lagrangian or Hamiltonian) method gives an RMS estimate for a limited or broad energy range depending on the ansatz used. Our proposed numerical method based on the adaptive wavelet transform is an exact numerical solution, which falls in the category of the numerical averaging technique. If the classification is according to computation power: guiding center theory comes first then variational techniques comes next then multiscale method and finally comes the numerical averaging method which uses split step Fourier transform method and our proposed technique which uses wavelet transform comes at last. But a complete theoretical study based on integrability and stability of the DM soliton is yet to come.

In this Section we develop a new adaptive fast wavelet transform (AFWT) to numerically solve the nonlinear Schrödinger (NLS) equation, and we use an averaged variational technique to reduce the governing NLS equation with a periodic dispersion map to a coupled set of nonlinear ordinary differential equations (ODEs). These ODEs accurately predict the pulse dynamics in a weak and strong nonlinear medium, compared to dispersion, in one hand, and slow or fast modulation frequency, compared to the frequency of oscillations of the soliton width, on the other. This analytical method is used

as guidelines for how to select stable initial conditions for the pulse and the dispersion map, and compare it with the exact numerical technique developed.

The time-dependent paraxial wave equation, in the presence of periodic modulation of dispersion and nonlinearity has the form of a modified NLS with a dimensionless envelope of the electric field:

$$j \frac{\partial \tilde{u}_e}{\partial z} - \frac{f(z)}{2} \frac{\partial^2 \tilde{u}_e}{\partial \tau^2} + g(z) |\tilde{u}_e|^2 \tilde{u}_e = 0, \quad (7.1)$$

where  $z, \tau$  are the coordinates along the direction of propagation and time in a moving frame of reference respectively. The functions  $f(z), g(z)$  are periodic modulation of dispersion and nonlinearity respectively. The above functions can be piece wise continuous (PWC) or simple harmonic functions of the form  $\vartheta(z) = 1 + \vartheta_1 \sin \tilde{\Omega} z$ , where we study both cases.

### 7.2.2 Variational Technique

In this Section we use the variational approach to describe the wave evolution based on the Lagrangian formalism of classical mechanics in terms of the Lagrangian density<sup>126</sup>

$$\mathcal{L} = \frac{j}{2} \left( \tilde{u}_j^* \frac{\partial \tilde{u}_j}{\partial z} - \tilde{u}_e \frac{\partial \tilde{u}_e}{\partial z} \right) + \frac{f(z)}{2} \left| \frac{\partial \tilde{u}_e}{\partial \tau} \right|^2 - \frac{g(z)}{2} |\tilde{u}_e|^4, \quad (7.2)$$

where the 1-D NLS equation can be derived from  $\mathcal{L}$  using the Euler-Lagrange equation

$$\frac{\partial}{\partial z} \frac{\partial \mathcal{L}}{\partial (\partial \tilde{u}_e / \partial z)} + \frac{\partial}{\partial \tau} \frac{\partial \mathcal{L}}{\partial (\partial \tilde{u}_e / \partial \tau)} - \frac{\partial \mathcal{L}}{\partial \tilde{u}_e} = 0. \quad (7.3)$$

Note that the application of Eq. (7.3) to the Lagrangian density Eq. (7.2) generates the NLS equation given in Eq. (7.1). Following the Ritz optimization procedure let us assume the initial profile to be one of the following

$$\tilde{u}_e = \tilde{u}_e(\tau, z) = A(z) \exp \left[ -\frac{\tau^2}{2w^2(z)} + jb(z)\tau^2 \right], \quad (7.4a)$$

$$\tilde{u}_e(\tau, z) = A(z) \operatorname{sech} \left( \frac{\tau}{w(z)} \right) \exp[jb(z)\tau^2], \quad (7.4b)$$

where  $A(z)$  is the amplitude,  $w(z)$  is the beam radius,  $b(z)$  is the wave front curvature, as unknown functions of the propagation distance  $z$ . Following the method in Desaix et al<sup>126</sup>, where we insert the trial functions from Eq. (7.4) into the Lagrangian and by integrating:

$$\begin{aligned} \langle \mathcal{L} \rangle = \int_0^\infty \mathcal{L} d\tau = \frac{i}{2} \left( A \frac{dA^*}{dz} - A^* \frac{dA}{dz} \right) w \alpha_0 + 2|A|^2 w^3 \left( \frac{db}{dz} + 2fb^2 \right) \alpha_2 \\ + f|A|^2 w^{-1} \gamma_0 - \frac{1}{2} w \beta_0 g |A|^4, \end{aligned} \quad (7.5)$$

we obtain the reduced Lagrangian, where  $\alpha$ ,  $\beta$ , and  $\gamma$  are given by

$$\alpha_D = \int_0^\infty \tau^D e^{-\tau^2} d\tau, \beta_D = \int_0^\infty \tau^D e^{-2\tau^2} d\tau, \gamma_{D-1} = \alpha_{D+1}, \quad (7.6)$$

for a Gaussian ansatz, and

$$\alpha_D = \int_0^\infty \tau^D \operatorname{sech}^2(\tau) d\tau, \beta_D = \int_0^\infty \tau^D \operatorname{sech}^4(\tau) d\tau, \gamma_D = \alpha_D - \beta_D, \quad (7.7)$$

for a hyperbolic secant one.

We can derive a set of evolution equations called Euler-Lagrange equations taking into account that the variation with respect to the unknowns in the initial profile should be

equal to zero, namely:  $\frac{\delta \langle \mathcal{L} \rangle}{\delta Q} = 0 \Rightarrow \frac{\partial \langle \mathcal{L} \rangle}{\partial Q} - \frac{d}{dz} \left( \frac{\partial \langle \mathcal{L} \rangle}{\partial Q'} \right) = 0$ , where  $Q = (A, w, b, A^*)$ . The

evolution equations obtained are given by:

$$|A|^2 w = A_0^2 w_0 = N_0, \quad (7.8a)$$

$$b = \frac{1}{2fw} \frac{dw}{dz}, \quad (7.8b)$$

$$\frac{d\tilde{\phi}}{dz} = -\frac{\gamma_0}{\alpha_0} \frac{f(z)}{w^2} + \frac{5}{4} g(z) \frac{\beta_0}{\alpha_0} |A|^2, \quad (7.8c)$$

$$\frac{d^2 w}{dz^2} = \frac{\gamma_0}{\alpha_2} \frac{f^2}{w^3} - \frac{N_0 \beta_0}{2\alpha_2} \frac{fg}{w^2} + \frac{w_z f_z}{f}, \quad (7.8d)$$

where  $A(z) = |A(z)| e^{i\tilde{\phi}(z)}$ ,  $N_0$  is the initial pulse energy defined as  $N_0 = \int_0^\infty |u|^2 d\tau$ . In all

what follows, we consider the 1-dimensional cases and  $g(z) = 1$ .

To begin we assume  $f(z) = f = cte.$ , Eq. (7.8d) can be written as

$$\frac{1}{2f} \left( \frac{dw}{dz} \right)^2 = -T + H, \quad (7.9)$$

where  $H$  is the Hamiltonian corresponding to the equivalent Newton equation of motion for a particle with mass  $1/f$  in the time independent nonstationary anharmonic potential

$$T = \frac{\gamma_0}{2\alpha_2} \frac{f}{w^2} - \frac{N_0 \beta_0}{2\alpha_2} \frac{f}{w}. \text{ Let } \tilde{V} = \frac{w}{w_0}, \tilde{\mu} = \frac{\gamma_0 f}{2\alpha_2 w_0^4}, \tilde{\nu} = -\frac{N_0 \beta_0}{2\alpha_2 w_0^3}, \tilde{K} = -\frac{H}{w_0^2} = -(\tilde{\mu} + \tilde{\nu}),$$

Eq. (7.9) becomes

$$\frac{1}{2f} \left( \frac{d\tilde{V}}{dz} \right)^2 = -\frac{\tilde{\mu}}{\tilde{V}^2} - \frac{\tilde{\nu}}{\tilde{V}} - \tilde{K}. \quad (7.10)$$

Integrating Eq. (7.10) we get two cases for the solution according to the number of roots of the polynomial  $\tilde{P} = -\tilde{K}\tilde{V}^2 - \tilde{v}\tilde{V} - \tilde{\mu}$ :<sup>126</sup>

**A- The Case When  $\tilde{c} = \frac{\tilde{v}}{\tilde{\mu}} > -1$  or  $\frac{N_0\beta_0 w_0}{\gamma_0 f} < 1$**

In this case we have monotonous spreading of the pulse, then the solution becomes

$$z\sqrt{2f} = \left[ \frac{\sqrt{\tilde{P}}}{-\tilde{K}} + \frac{\tilde{v}}{2(-\tilde{K})^{3/2}} \ln \frac{(2\sqrt{-\tilde{K}}\sqrt{\tilde{P}} - 2\tilde{K}\tilde{V} - \tilde{v})}{-2\tilde{K} - \tilde{v}} \right] = \left[ \frac{\sqrt{(1+\tilde{c})\tilde{V}^2 - \tilde{c}\tilde{V} - 1}}{1+\tilde{c}} \right. \\ \left. + \frac{\tilde{c}}{2(1+\tilde{c})^{3/2}} \times \ln \frac{2\sqrt{1+\tilde{c}}\sqrt{(1+\tilde{c})\tilde{V}^2 - \tilde{c}\tilde{V} - 1} - 2((1+\tilde{c})\tilde{V} - \tilde{c})}{2+\tilde{c}} \right]. \quad (7.11a)$$

**B- a The Case When  $-2 < \frac{\tilde{v}}{\tilde{\mu}} < -1$  or  $1 < \frac{N_0\beta_0 w_0}{\gamma_0 f} < 2$**

Here we have initial pulse spreading then oscillation between  $1 < \tilde{V} < -\frac{1}{1+\tilde{c}}$ ,

then the solution becomes

$$z\sqrt{2f} = \left[ \frac{\sqrt{\tilde{P}}}{-\tilde{K}} + \frac{\tilde{v}}{2(-\tilde{K})^{3/2}} \left( \sin^{-1} \left( \frac{-2\tilde{K}\tilde{V} - \tilde{v}}{\sqrt{\tilde{v}^2 - 4\tilde{K}\tilde{\mu}}} \right) - \frac{\pi}{2} \right) \right] = \left[ \frac{\sqrt{(1+\tilde{c})\tilde{V}^2 - \tilde{c}\tilde{V} - 1}}{1+\tilde{c}} \right. \\ \left. + \frac{\tilde{c}}{2(-(1+\tilde{c}))^{3/2}} \times \left( \sin^{-1} \left( \frac{2(1+\tilde{c})\tilde{V} - \tilde{c}}{\tilde{c} + 2} \right) - \frac{\pi}{2} \right) \right]. \quad (7.11b)$$

**B- b The Case When  $\frac{\tilde{v}}{\tilde{\mu}} < -2$  or  $\frac{N_0\beta_0 w_0}{\gamma_0 f} > 2$**

Here we have initial pulse compression then oscillation between  $1 < \tilde{V} < -1/(1+\tilde{c})$ , then the solution becomes

$$z\sqrt{2f} = \left[ \frac{\sqrt{(1+\tilde{c})\tilde{V}^2 - \tilde{c}\tilde{V} - 1}}{-(1+\tilde{c})} + \frac{\tilde{c}}{2(-(1+\tilde{c}))^{3/2}} \times \left( \sin^{-1} \left( \frac{2(1+\tilde{c})\tilde{V} - \tilde{c}}{\tilde{c} + 2} \right) - \frac{\pi}{2} \right) \right]. \quad (7.11c)$$

Note that the period of oscillation is found to be  $z_p \sqrt{2\tilde{\mu}f} = \frac{\pi|\tilde{c}|}{(1+\tilde{c})^{3/2}}$ .

Now, let us assume  $f$  is a PWC function of the form

$$f(z) = \begin{cases} f_- & \text{for } -L_- < z < 0 \\ f_+ & \text{for } 0 < z < L_+, \end{cases} \quad (7.12)$$

which is periodic of period  $L = L_+ + L_-$ , and that the width  $w$  and the chirp  $b$  are continuous functions with respect to propagation where as  $w' = dw/dz$  is not<sup>127</sup>, where we get from Eq. (7.8b)

$$\frac{w'_+}{w'_-} = \frac{f_+}{f_-}. \quad (7.13)$$

Next we consider two extreme cases due to the complexity of the solution obtained in Eqs. 7.11(a-c) namely weak and strong nonlinearity as in<sup>127</sup> but the ansatz here can be Gaussian or hyperbolic secant function.

### 7.2.2.1 Weak Nonlinearity

In this case we can deduce that solutions of Eq. (7.9) is periodic with respect to propagation if the mean value of dispersion  $\bar{f} = \frac{f_+L_+ + f_-L_-}{L} = 0$ . This conclusion is drawn from Eq. (7.9) where  $N_0 = 0$  which leads to after integration in each half period and considering the boundary conditions

$$-\frac{L_+f_+}{L_-f_-} = \frac{\sqrt{w^2 - \frac{\check{f}_+}{H_+}} - \sqrt{w_0^2 - \frac{\check{f}_-}{H_-}}}{\sqrt{w^2 - \frac{\check{f}_+}{H_+}} - \sqrt{w_f^2 - \frac{\check{f}_-}{H_-}}}, \quad (7.14)$$

where  $\check{\sigma} = \frac{\gamma_0}{2\alpha_2}$ ,  $w_0, w_f$  are the initial and final width respectively,  $w_+ = w_- = w$  on the

boundary between half periods, since  $w$  is continuous, and  $H_+, H_-$  are the corresponding Hamiltonians in each half period defined as

$$H_+ = \frac{1}{2f_+} w_+'^2 + \frac{\check{\sigma} f_+}{w_+^2}, \quad (7.15a)$$

$$H_- = \frac{1}{2f_-} w_-'^2 + \frac{\check{\sigma} f_-}{w_-^2}, \quad (7.15b)$$

Dividing Eqs. (7.15a) over (7.15b), and using Eq. (7.13) we get

$$\frac{H_+}{H_-} = \frac{\left( \frac{w_-'^2}{2f_-^2} + \frac{\check{\sigma}}{w_-^2} \right) f_+}{\left( \frac{w_-'^2}{2f_-^2} + \frac{\check{\sigma}}{w_-^2} \right) f_-} = \frac{f_+}{f_-}. \text{ Which means that after every period the Hamiltonian}$$

returns to its initial value. Also, if  $w_0 = w_f$  in Eq. (7.14)  $w$  is periodic, and  $-\frac{L_+ f_+}{L_- f_-} = 1$ ,

which leads to the mean dispersion  $\bar{f} = 0$ . Returning back to Eq. (7.11c) with  $N_0 \approx 0$ , at

$z = L, w = w_0$  we arrive at  $L_{\pm} \sqrt{2H_{\pm} f_{\pm}} = \sqrt{w_0^2 - \frac{\check{\sigma} f_{\pm}}{H_{\pm}}}$ . Solving for  $H$  we arrive at

$$H_{\pm} = \frac{1}{4L_{\pm}^2 f_{\pm}} \left( w_0^2 \pm \sqrt{w_0^4 - 8\check{\sigma}(L_{\pm} f_{\pm})^2} \right), \text{ which shows that for a given value of}$$

$f_{\pm}, L_{\pm}, w_0$  we get two solutions of  $H_{\pm}$ . So, a necessary condition of propagation is

$w_0^2 > 2\sqrt{2\check{\sigma}} |f_{\pm}| L_{\pm}$ . Note that, the width of the oscillating pulse will vary between

$$w_{\min}^2 < w^2 < w_0^2, \text{ where } w_{\min}^2 = \frac{\check{\sigma} f_{\pm}}{H_{\pm}} = \frac{4\check{\sigma}(f_{\pm} L_{\pm})^2}{w_0^2 \pm \sqrt{w_0^4 - 8\check{\sigma}(L_{\pm} f_{\pm})^2}}.$$



In conclusion, for weak nonlinearity, which cause perturbation on the width  $w$ , and dispersion to cancel each other we have to have a positive value of  $\bar{f} > 0$  for  $L_+ \neq L_-$ , and  $\bar{f} = 0$  if  $L_+ = L_-$ <sup>127</sup>.

### 7.2.2.2 Strong nonlinearity

Let us assume the width of the pulse has the form  $w(z) = \bar{w}_0 + \delta w$ , where the pulse oscillates around a mean value. Substituting  $w(z)$  in Eq. (7.9) we get<sup>127</sup>

$$\begin{aligned} \frac{d^2 \delta w}{dz^2} = & \frac{f}{\alpha_2} \bar{w}_0^{-2} \left[ \gamma_0 f \bar{w}_0^{-1} - \frac{N_0 \beta_0}{2} \right] + \frac{f}{\alpha_2} \bar{w}_0^{-3} \\ & \times [N_0 \beta_0 - 3\gamma_0 f \bar{w}_0^{-1}] \delta w = T^{(0)} + T^{(1)} \delta w, \end{aligned} \quad (7.16)$$

where  $T = T_{\pm}$ ,  $f = f_{\pm}$  in  $L = L_{\pm}$  respectively. Solving the above equation inside each interval and incorporating the conditions of continuity of  $w$  and the chirp  $b$  and assuming  $\delta w \ll \bar{w}_0$  with rapid oscillation we arrive at  $f_+ T_-^{(0)} L_- + f_- T_+^{(0)} L_+ = 0$ . Replacing  $T_{\pm}$  by there corresponding values we get  $\bar{f} = \frac{L_- f_- + L_+ f_+}{L_- + L_+} = \frac{N_0 \beta_0 \bar{w}_0}{2\gamma_0} > 0$ , which is in the anomalous dispersion regime.

In what follows we consider the case of a harmonic and a high-frequency modulation of the dispersion map of the form  $f = 1 + f_1 \sin \tilde{\Omega} z$ , where  $\tilde{\Omega} > \omega_s$  and  $\omega_s$  is the soliton width oscillating frequency<sup>62</sup>. Also we assume that the ratio  $f_1 / \tilde{\Omega} \ll 1$  and a hyperbolic secant ansatz as an initial pulse. Deriving Eq. (7.8b) and compare it to Eq. (7.8d) we arrive at the following ODE system<sup>62</sup>

$$w_z = 2wbf, \quad (7.17a)$$

$$b_z = \frac{2f}{\pi^2 w^4} - 2b^2 f - \frac{2N_0}{\pi^2 w^3}. \quad (7.17b)$$

Following the Kapitza approach where the width  $w$  and the chirp  $b$  has the form  $w = \langle w \rangle + \delta w$ ,  $b = \langle b \rangle + \delta b$  respectively. Eqs. (7.17a) and (7.17b) become after replacing  $w$  by  $\langle w \rangle$ , and  $b$  by  $\langle b \rangle$  for simplicity.

$$w_z = 2wb + 2w \langle \delta w f_1 \sin \tilde{\Omega} z \rangle + 2b \langle \delta w f_1 \sin \tilde{\Omega} z \rangle + 2 \langle \delta w \delta b \rangle, \quad (7.18a)$$

$$b_z = \frac{2}{\pi^2 w^4} \left( 1 + 10 \frac{\langle \delta w^2 \rangle}{w^2} - 4 \frac{\langle f_1 \delta w \sin \tilde{\Omega} z \rangle}{w} \right) - 2b^2 - 2 \langle \delta b^2 \rangle - 4b \langle \delta b f_1 \sin \tilde{\Omega} z \rangle - \frac{2N_0^2}{\pi^2 w^3} \left( 1 + \frac{6 \langle \delta w^2 \rangle}{w^2} \right), \quad (7.18b)$$

$$\delta w_z = 2wb f_1 \sin \tilde{\Omega} z + 2w \delta b + 2b \delta w, \quad (7.18c)$$

$$\delta b_z = \left( \frac{6N_0}{\pi^2 w^4} - \frac{8}{\pi^2 w^5} \right) \delta w + \left( \frac{2}{\pi^2 w^4} - 2b^2 \right) f_1 \sin \tilde{\Omega} z - 4b \delta b. \quad (7.18d)$$

Let  $\delta b = S_1 \sin \tilde{\Omega} z + S_2 \cos \tilde{\Omega} z$ ,  $\delta w = S_3 \sin \tilde{\Omega} z + S_4 \cos \tilde{\Omega} z$ ,  $\tilde{\kappa} = \left( \frac{6N_0}{\pi^2 w^4} - \frac{8}{\pi^2 w^5} \right)$ ,

$\tilde{d} = \left( \frac{2}{\pi^2 w^4} - 2b^2 \right) f_1$ , then a particular solution to Eqs. (7.18c) and (7.18d) can be found

form the following system of linear equations

$$\begin{bmatrix} 0 & 2w & -\tilde{\Omega} & 2b \\ 2w & 0 & 2b & \tilde{\Omega} \\ \tilde{\Omega} & 4b & 0 & -\tilde{\kappa} \\ 4b & -\tilde{\Omega} & -\tilde{\kappa} & 0 \end{bmatrix} \begin{bmatrix} S_1 \\ S_2 \\ S_3 \\ S_4 \end{bmatrix} = \begin{bmatrix} 0 \\ -2wb f_1 \\ 0 \\ \tilde{d} \end{bmatrix}. \quad (7.19)$$

The Solution of the following system gives

$$S_1 = \frac{-2bw f_1 \tilde{\kappa} (2w \tilde{\kappa} + 8b^2 + \tilde{\Omega}^2)}{\tilde{M}} + 4 \frac{bd (w \tilde{\kappa} + \tilde{\Omega}^2 + 4b^2)}{\tilde{M}}, \quad (7.20a)$$

$$S_2 = -4 \frac{\tilde{\Omega} b^2 w f_1 \tilde{\kappa}}{\tilde{M}} - \frac{\tilde{\Omega} \tilde{d} (2w \tilde{\kappa} + \tilde{\Omega}^2 + 4b^2)}{\tilde{M}}, \quad (7.20b)$$

$$S_3 = \frac{-4b^2 w f_1 (4w \tilde{\kappa} + 16b^2 + \tilde{\Omega}^2)}{\tilde{M}} - 2 \frac{w \tilde{d} (2w \tilde{\kappa} + \tilde{\Omega}^2 + 8b^2)}{\tilde{M}}, \quad (7.20c)$$

$$S_4 = \frac{-2b w f_1 \tilde{\Omega} (2w \tilde{\kappa} + \tilde{\Omega}^2 + 16b^2)}{\tilde{M}} - 4 \frac{b \tilde{d} w \tilde{\Omega}}{\tilde{M}}, \quad (7.20d)$$

where  $\tilde{M} = 4w^2 \tilde{\kappa}^2 + 32wb^2 \tilde{\kappa} + 4w\tilde{\Omega}^2 \tilde{\kappa} + \tilde{\Omega}^4 + 20b^2 \tilde{\Omega}^2 + 64b^4$ . Assuming  $f_1 \gg$  and keeping main terms we arrive at<sup>62</sup>

$$\delta w = \frac{-4f_1}{\tilde{\Omega}^2} \left[ \frac{1}{\pi^2 w^3} + 1 \right] \sin \tilde{\Omega} z - \frac{2w b f_1}{\tilde{\Omega}} \cos \tilde{\Omega} z, \quad (7.21a)$$

$$\delta b = \frac{4b f_1}{\tilde{\Omega}^2} \left[ \frac{1}{\pi^2 w^4} + b^2 \right] \sin \tilde{\Omega} z - \frac{2f_1}{\pi^2 \tilde{\Omega}} \cos \tilde{\Omega} z, \quad (7.21b)$$

$$w_z = 2wb + \frac{f_1^2}{\tilde{\Omega}^2} \left( \frac{4b}{\pi^2 w^3} - 2wb^3 \right), \quad (7.21c)$$

$$b_z = \frac{2}{\pi^2 w^4} - 2b^2 - \frac{2N_0}{\pi^2 w^3} + \frac{4f_1^2}{\pi^2 \tilde{\Omega}^2} \times \left( \frac{12b^2}{w^4} + \frac{3}{\pi^2 w^8} - 2b^4 - 6 \frac{N_0 b^2}{w^3} \right). \quad (7.21d)$$

The above system can be simplified if we consider  $f_1/\tilde{\Omega} \ll$ . We obtain<sup>62</sup>

$$w_{zz} = \frac{4}{\pi^2 w^3} - 4 \frac{N_0}{\pi^2 w^2} + \frac{24f_1^2}{\pi^4 \tilde{\Omega}^2 w^7}, \quad (7.22)$$

which admits a fixed point solution  $w = \frac{1}{N_0} + \frac{6N_0^3 f_1^2}{\pi^2 \tilde{\Omega}^2}$ , which corresponds to the

potential  $T = \frac{2}{\pi^2 w^2} - \frac{4N_0}{\pi^2 w} + \frac{4f_1^2}{\pi^2 w^6 \tilde{\Omega}^2}$ . Compared to the potential in Eq. (7.9) with

( $f=1$ ), we find that the last term is the correction term for dispersion. Note that stabilization is possible when there is a minimum in this effective potential.

### 7.2.3 Adaptive Wavelet Method

As mentioned in Chapter 3, the wavelet method is devised as a combination of finite element method (FEM) in space domain, and finite difference (FD) method in time domain. In the literature, there are many ways to solve PDEs and evolution equations using wavelets<sup>12,72,85</sup>, each with its advantages and disadvantages, and are based on complicated mathematical theories<sup>9,10,11,87</sup>, which makes deriving simple algorithm a very difficult task. Most of the methods are also dependent on the specific PDE<sup>73-75</sup>, and thus, there is no universal solution for all problems. Various methods that exist range from, collocation<sup>77</sup>, FEM<sup>80</sup>, Split Step, Symplectic (higher order FD<sup>81</sup>). Combinations of these methods are applied to different parts of the PDE and/or different kinds of wavelets are incorporated as weighting or ansatz functions<sup>82,83</sup>. A brief review of some properties of wavelets and why they are so appealing in many applications, including the numerical solution of PDEs<sup>7,13</sup> is given in Chapter 3.

Now we study the dispersion modulated NLS equation and apply the wavelet technique to solve the PDE in hand. The basic equation in this method is:

$$\int_{-\infty}^{\infty} \{PDE[\tilde{u}_e(z, \tau)]\} \theta_j(\tau) d\tau = \int_{-\infty}^{\infty} \{PDE[\tilde{u}_e(z, \tau)]\} \phi_j(\tau) d\tau = 0, \text{ if we use the Galerkin}$$

method. The initial profile  $u(z, \tau) = \sum_{l=0}^{M-1} a_{J,l}(z) \phi_l(\tau)$  is expressed in terms of the scaling

wavelets at level  $J$  resulting in a sampling of the initial function, which eventually evolves according to the corresponding PDE. The NLS equation is defined in Eq. (7.1) is solved along with the solitary type initial condition defined in Eq. (7.4). Taking  $g = 1$ , we obtain:

$$\int_{\tau_{\min}}^{\tau_{\max}} [j\tilde{u}_{ez} - f/2\tilde{u}_{e\tau\tau} + |\tilde{u}_e|^2\tilde{u}_e] \phi_k(\tau) d\tau = 0. \quad (7.23)$$

The first term of Eq. (7.23) is computed as the

following  $\int_{\tau_{\min}}^{\tau_{\max}} \tilde{u}_{ez} \phi_k(\tau) d\tau = \sum_l \frac{d}{dz} a_l \int \phi_l(\tau) \phi_k(\tau) d\tau = I \cdot \frac{d}{dz} \bar{a}(z) = \bar{a}'(z)$ , where

$$\bar{a}'(z) = \frac{\bar{a}(z + \Delta z) - \bar{a}(z)}{\Delta z}, \bar{a} = [a_1 \quad \dots \quad a_M]^T. \quad (7.24)$$

For the second term of Eq. (7.23) we get

$$\int_{\tau_{\min}}^{\tau_{\max}} \tilde{u}_{e\tau\tau} \phi_k(\tau) d\tau = \int_{\tau_{\min}}^{\tau_{\max}} \frac{\partial^2}{\partial \tau^2} [\sum_l a_l(z) \phi_l(\tau)] \cdot \phi_k(\tau) d\tau = \sum_l a_l(z) \cdot \int_{\tau_{\min}}^{\tau_{\max}} \frac{\partial^2 \phi_l}{\partial \tau^2} \phi_k(\tau) d\tau = \bar{K} \cdot \bar{a}(z),$$

where

$$\bar{K}(l, k) = \int \phi_l'' \phi_k d\tau, \bar{K} = \begin{bmatrix} \bar{K}(1,1) & & \\ & \ddots & \\ & & \bar{K}(M, M) \end{bmatrix}^T. \quad (7.25)$$

The third term to be calculated is the nonlinear term

$$\begin{aligned} \int_{\tau_{\min}}^{\tau_{\max}} |\tilde{u}_e|^2 \tilde{u}_e \phi_k(\tau) d\tau &= \int_{\tau_{\min}}^{\tau_{\max}} |\sum_l a_l(z) \phi_l(\tau)|^2 \cdot [\sum_n a_n(z) \phi_n(\tau)] \phi_k(\tau) d\tau \\ &= \int_{\tau_{\min}}^{\tau_{\max}} [\sum_l a_l(z) \phi_l(\tau)] \cdot [\sum_m a_m^*(z) \phi_m(\tau)] [\sum_n a_n(z) \phi_n(\tau)] \phi_k(\tau) d\tau \\ &= \sum_l a_l \cdot \left\{ \sum_n a_n \int \phi_l(\tau) \phi_k(\tau) \cdot \phi_m(\tau) \phi_n(\tau) d\tau \right\} \cdot \sum_m a_m^* \\ &= \bar{a}(z) \cdot \{\bar{a}^*(z) \cdot \bar{\Phi}_{l,k} \cdot \bar{a}(z)\} = \bar{C}(z) \cdot \bar{a}(z) \cdot \end{aligned}$$

where

$$\tilde{\Phi}_{l,k}(m,n) = \int \phi_l(\tau) \phi_k(\tau) \cdot \phi_m(\tau) \phi_n(\tau) d\tau,$$

$$\tilde{\Phi}_{l,k} = \begin{bmatrix} \int \phi_l(\tau) \phi_k(\tau) \cdot \phi_1(\tau) \phi_1(\tau) d\tau & & \\ & \ddots & \\ & & \int \phi_l(\tau) \phi_k(\tau) \cdot \phi_M(\tau) \phi_M(\tau) d\tau \end{bmatrix}^T,$$

$$\tilde{C}(z) = \begin{bmatrix} \bar{a}^*(z) \tilde{\Phi}_{1,1} \bar{a}(z) & & \\ & \ddots & \\ & & \bar{a}^*(z) \tilde{\Phi}_{M,M} \bar{a}(z) \end{bmatrix}^T. \quad (7.26)$$

Applying these results to Eq. (7.23) we arrive at

$$\bar{a}(z + \Delta z) = \bar{a}(z) + j\Delta z \left( \tilde{C}(z) - \frac{f}{2} \tilde{K} \right) \bar{a}(z). \quad (7.27)$$

Note that the different matrices  $\tilde{K}$ ,  $\tilde{\Phi}_{l,k}$  can be calculated once using the connection coefficient method discussed earlier, whereas the  $\tilde{C}$  matrix is calculated in every pass of the iteration. Figure 7.1 shows the algorithm adopted for the variable dispersion NLS case.

## 7.2.4 Numerical Results And Conclusion

We now show sample simulation results using the FFT and the AWT methods. Figure 7.1 shows the algorithm of the adaptive wavelet transform (AWT) method for dispersion managed systems (DMS). Figure 7.2 shows the comparison between on-axis pulse amplitude using the AWT and FFT techniques when propagating according to the accompanying dispersion map and initial conditions. Figure 7.3 shows the variation of the on-axis pulse amplitude for two different pulses where  $f = [-2, 2]$  and an increasing nonlinearity coefficient using the AWT techniques when propagating according to the accompanying dispersion map and initial conditions. Figure 7.4 shows the variation of

the on-axis pulse amplitude for two different pulses where  $f = [-4, 4]$  and an increasing nonlinearity coefficient using the AWT techniques when propagating according to the accompanying dispersion map and initial conditions.

Figure 7.5 shows the variation of the on-axis pulse amplitude for two different dispersion maps and an increasing nonlinearity coefficient when the initial pulse  $\tilde{u}_e = \exp(-2\tau^2)$  using the AWT techniques when propagating according to the accompanying dispersion maps and initial conditions. Figure 7.6 shows the variation of the on-axis pulse amplitude for two different dispersion maps amplitude keeping the same period and an increasing nonlinearity coefficient with the initial pulse  $\tilde{u}_e = \exp(-\tau^2)$  using the AWT techniques when propagating according to the accompanying dispersion maps and initial conditions. Figure 7.7 shows the comparison between on-axis pulse amplitude using the AWT and FFT techniques when propagating according to the accompanying dispersion map and initial conditions as found in<sup>1</sup>. Figure 7.8 shows the variation of the on-axis pulse amplitude for two different dispersion map periods keeping the same amplitude in the anomalous dispersion regime with the initial pulse  $\tilde{u}_e = \exp(-\tau^2)$  using the AWT techniques when propagating according to the accompanying dispersion maps and initial conditions. Figure 7.9 shows the variation of the on-axis pulse amplitude for two different dispersion map periods keeping the same amplitude with the initial pulse  $\tilde{u}_e = \exp(-\tau^2)$  using the AWT techniques when propagating according to the accompanying dispersion maps and initial conditions. The first two are in the anomalous dispersion regime and the third one is in the normal regime. Figure 7.10 shows the variation of the on-axis pulse amplitude for two different dispersion map periods, keeping the same amplitude in the anomalous dispersion regime according to condition in Section

7.2.2.2, with the initial pulse  $\tilde{u}_e = \exp(-\tau^2)$ , using the AWT techniques according to the accompanying initial conditions. Figure 7.11 shows the variation of the on-axis pulse amplitude for three different dispersion map periods, keeping the same amplitude in the anomalous dispersion regime according to condition in Section 7.2.2.2, with the initial pulse  $\tilde{u}_e = 2 \exp(-\tau^2)$ , using the AWT techniques according to the accompanying initial conditions. Figure 7.12 shows the variation of the on-axis pulse amplitude for three different dispersion map amplitudes, keeping the same period in the anomalous dispersion regime according to condition in Section 7.2.2.2, with different initial pulses, using the AWT techniques according to the accompanying initial conditions. Figure 7.13 shows the variation of the on-axis pulse amplitude for three different dispersion map periods, keeping the same amplitude in the normal dispersion regime contradicting the condition in Section 7.2.2.2, using the AWT techniques according to the accompanying same initial conditions.

In the 1-D FFT the number of computations is  $\propto M \log_2 M$ , where  $M$  is the number of sampling points. As with respect to the AWT method, the first matrix to be computed here is the  $\tilde{K}$  matrix which is  $M \times M$ , where  $M$  is the length of the vector containing the elements of the scaling coefficients,  $a_l(z)$ , that change with distance as defined in Eq. (7.23). This matrix is only computed once before time stepping. Depending on the *level* chosen, the number of coefficients calculated  $M$ , is doubled if the *level* is increased by one according to the following formula:  $N = \tau_{max} \cdot 2^{level} - (MX - 1)$ , where  $\tau_{max}$  is the maximum range of the initial profile, and  $MX$  is equal to the maximum range of the original SYMLET (SYM4) wavelet which is equal to  $11^{7,10}$ . Computation



wise, the  $C$  matrix defined in Eq. (7.25) consists of  $M \times M$  elements and each element needs  $M^2$  multiplications to be computed in each time step, and that makes our algorithm  $\propto M^4$  plus the  $2M^2$  needed for updating the scaling coefficients as in Eq. (7.26). Note that, the later computations are negligible compared to the  $C$  matrix computations. Also, if we try to move from one *level* to another, our execution time is multiplied with  $2^4$ . Memory wise, using the connection coefficient technique, reduces our memory usage for  $\tilde{\Phi}_{l,k}$ 's as defined in Eq. (7.25) from  $8 \times N^4$  bytes to  $8 \times (2MX - 1)^3$  bytes, which are computed only once in the beginning of the program. Execution time is in hours in this case, and it depends on the *level*, the number of iterations, spatial dimension of the initial wave, and the number of points approximating each wavelet.

In summary, we have outlined a fast and accurate method for tracking the amplitude of a pulse in dispersion modulated media by utilizing an adaptive wavelet transform. Also, we compared our results with traditional methods used to solve such type of equations. Moreover, relying on the semi-analytical study developed using the Lagrangian dynamics we were able to interpret the analytical results and whether they agree with the numerical simulation developed. Note also that by using this adaptive wavelet transform technique, one can solve other complex PDEs associated with nonlinear optics problems taking into advantage the scaling and shifting properties associated with the wavelet transform. Finally, we shall mention that speed versus accuracy, is a common trade-off, and as such, a compromise is usually sought.

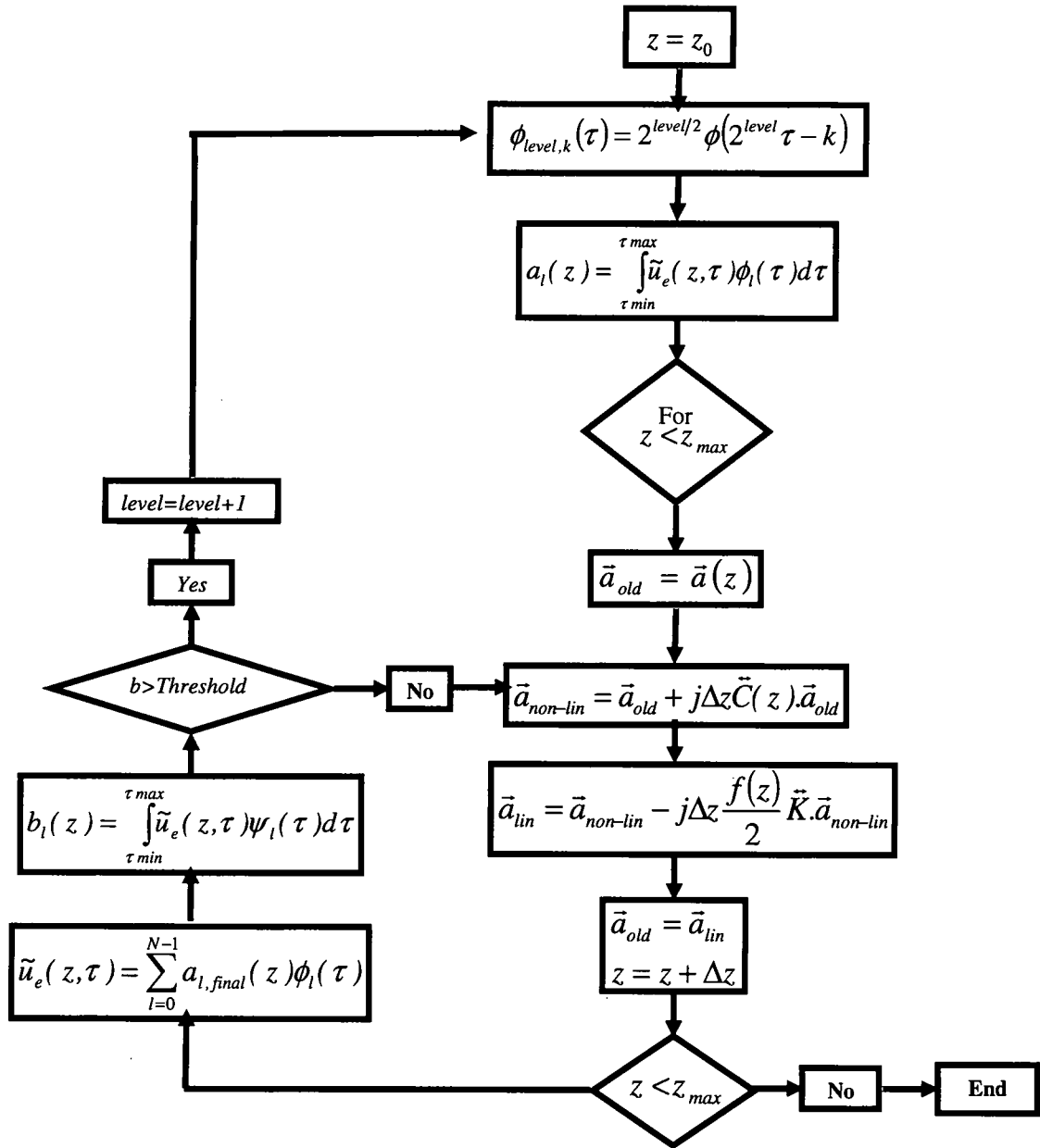


**Figure 7.1:** Adaptive wavelet transform (AWT) method for DMS.

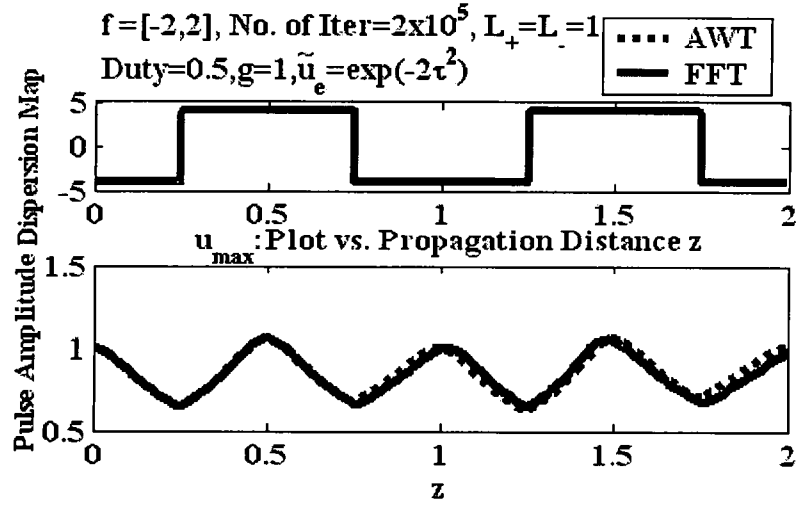


**Figure 7.2:** Comparison between on-axis pulse amplitude using the AWT and FFT techniques when propagating according to the accompanying dispersion map and initial conditions.

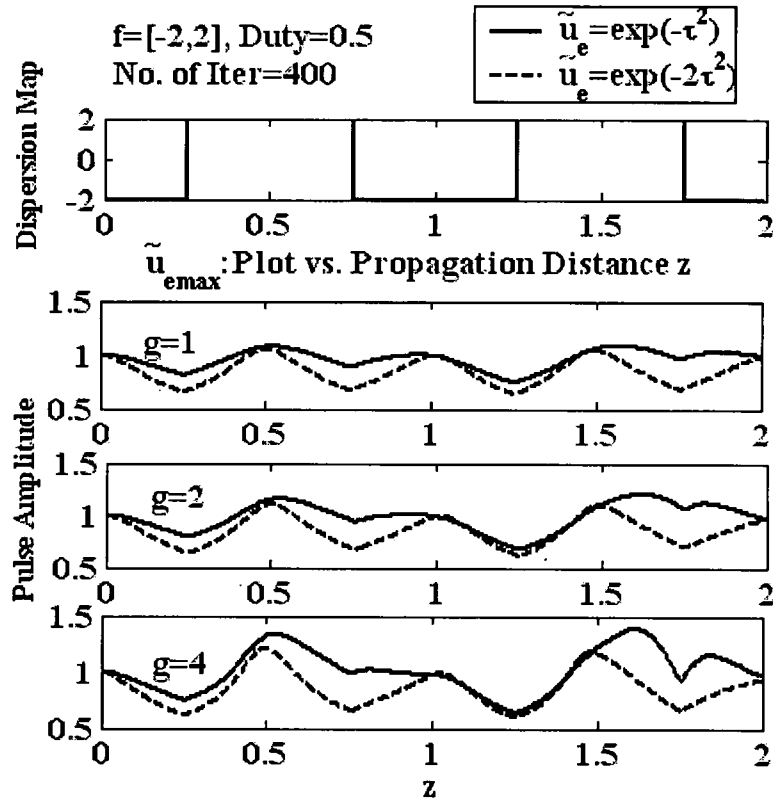


**Figure 7.3:** Variation of the on-axis pulse amplitude for two different pulses where  $f = [-2, 2]$  and an increasing nonlinearity coefficient using the AWT techniques when propagating according to the accompanying dispersion map and initial conditions.

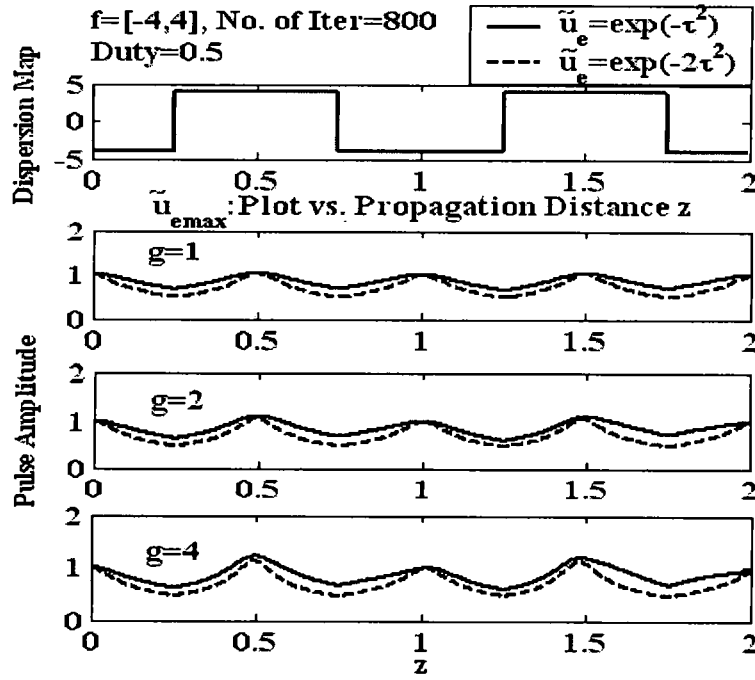


**Figure 7.4:** Variation of the on-axis pulse amplitude for two different pulses where  $f = [-4, 4]$  and an increasing nonlinearity coefficient using the AWT techniques when propagating according to the accompanying dispersion map and initial conditions.

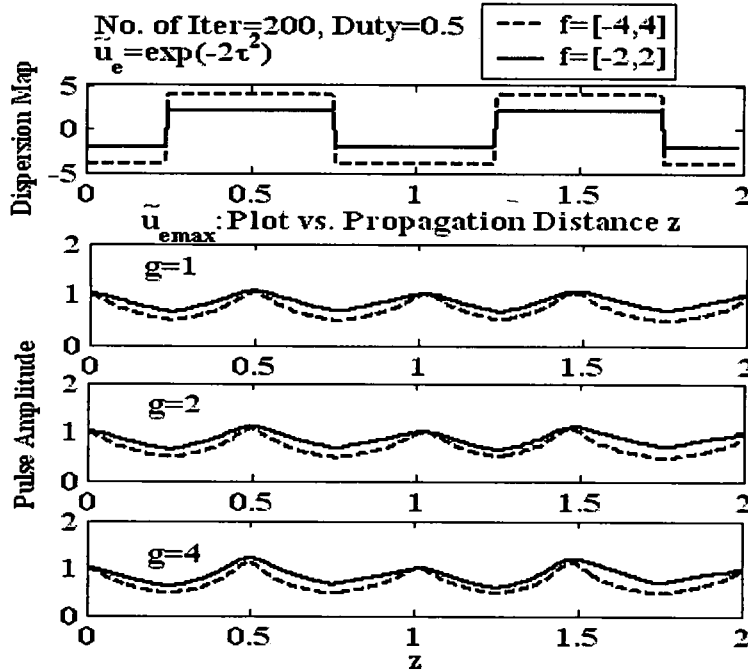


**Figure 7.5:** Variation of the on-axis pulse amplitude for two different dispersion maps and an increasing nonlinearity coefficient when the initial pulse  $\tilde{u}_e = \exp(-2\tau^2)$  using the AWT techniques when propagating according to the accompanying dispersion maps and initial conditions.

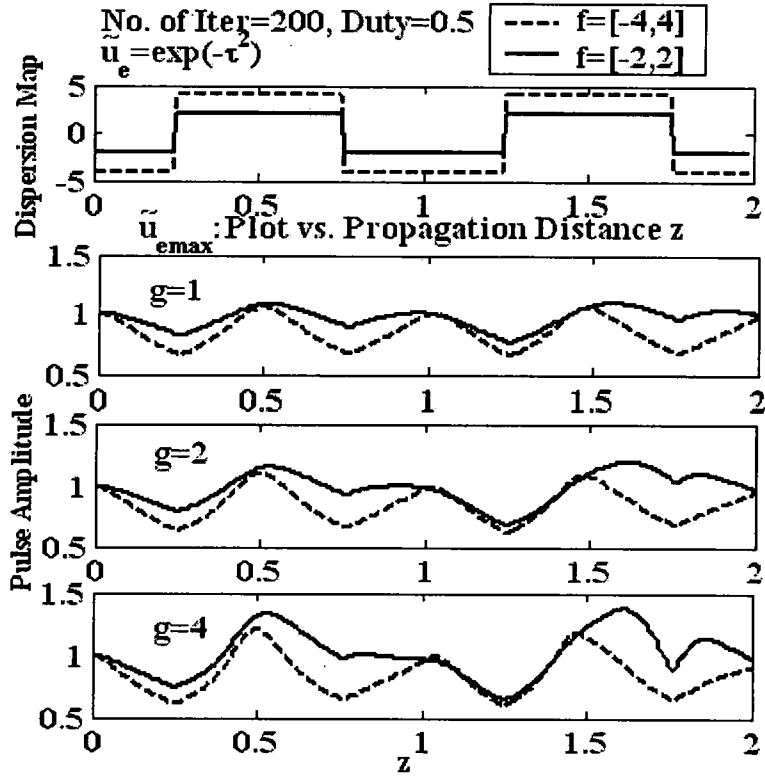


**Figure 7.6:** Variation of the on-axis pulse amplitude for two different dispersion maps amplitude keeping the same period and an increasing nonlinearity coefficient with the initial pulse  $\tilde{u}_e = \exp(-\tau^2)$  using the AWT techniques when propagating according to the accompanying dispersion maps and initial conditions.

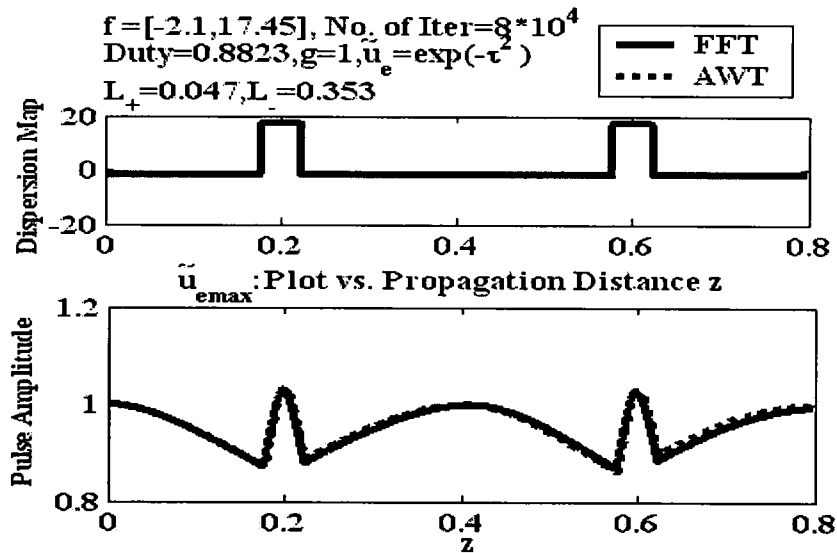


**Figure 7.7:** Comparison between on-axis pulse amplitude using the AWT and FFT techniques when propagating according to the accompanying dispersion map and initial conditions as found in Kutz et al [63].

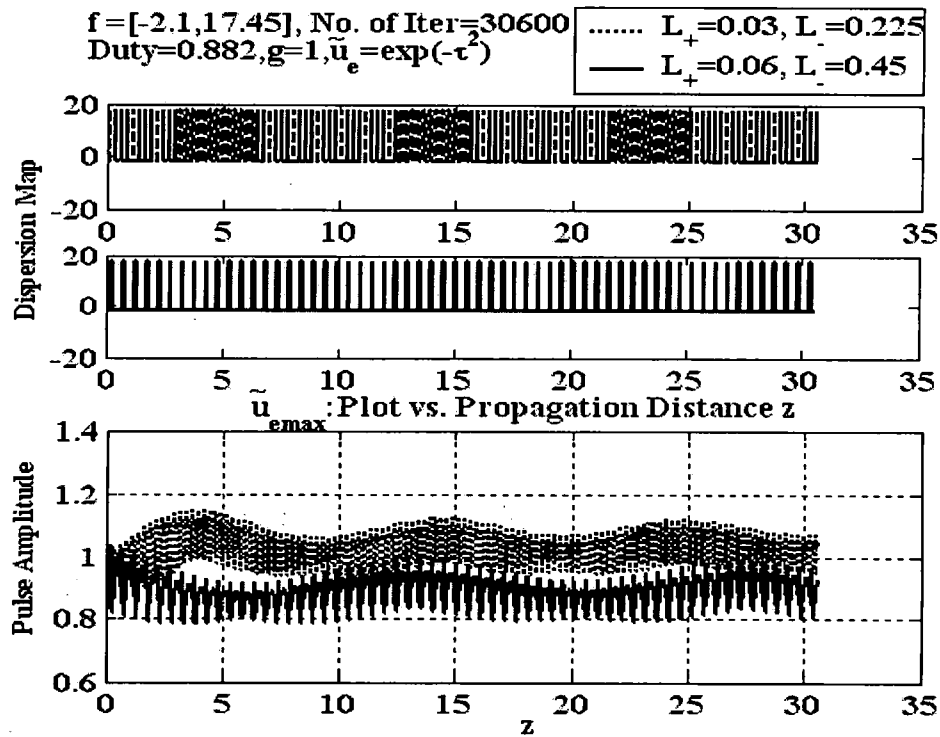


**Figure 7.8:** Variation of the on-axis pulse amplitude for two different dispersion map periods keeping the same amplitude in the anomalous dispersion regime with the initial pulse  $\tilde{u}_e = \exp(-\tau^2)$  using the AWT techniques when propagating according to the accompanying dispersion maps and initial conditions.

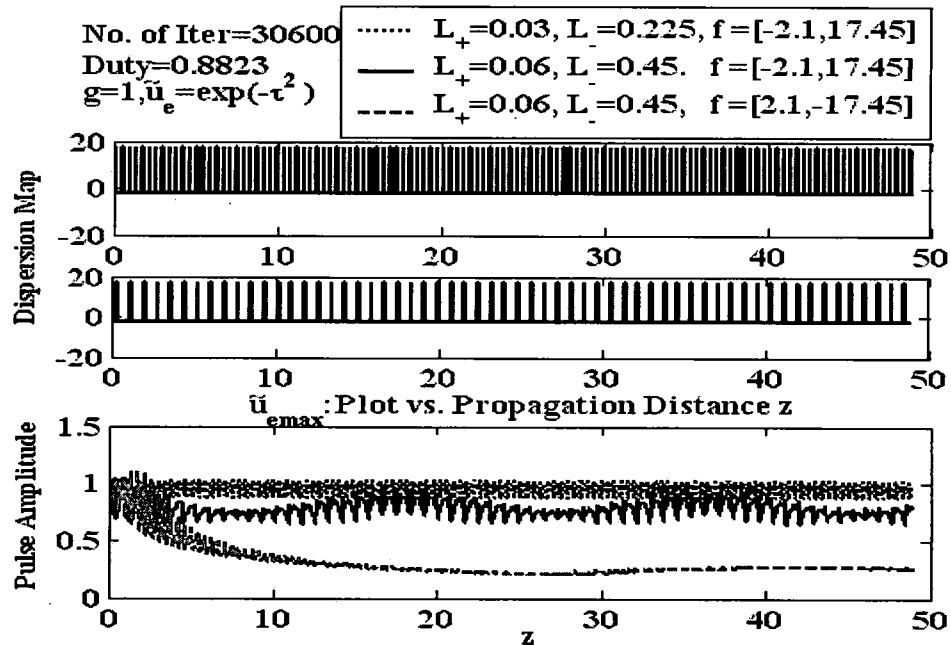


**Figure 7.9:** Variation of the on-axis pulse amplitude for two different dispersion map periods keeping the same amplitude with the initial pulse  $\tilde{u}_e = \exp(-\tau^2)$  using the AWT techniques when propagating according to the accompanying dispersion maps and initial conditions. The first two are in the AD regime and the third one is in the normal regime.

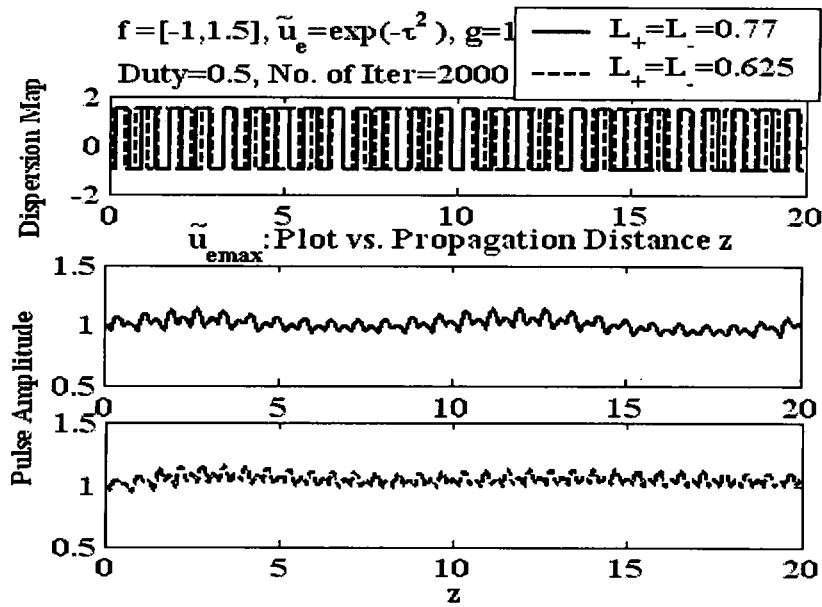


**Figure 7.10:** Variation of the on-axis pulse amplitude for two different dispersion map periods, keeping the same amplitude in the anomalous dispersion regime according to condition in Section 7.2.2.2, with the initial pulse  $\tilde{u}_e = \exp(-\tau^2)$ , using the AWT techniques according to the accompanying initial conditions.

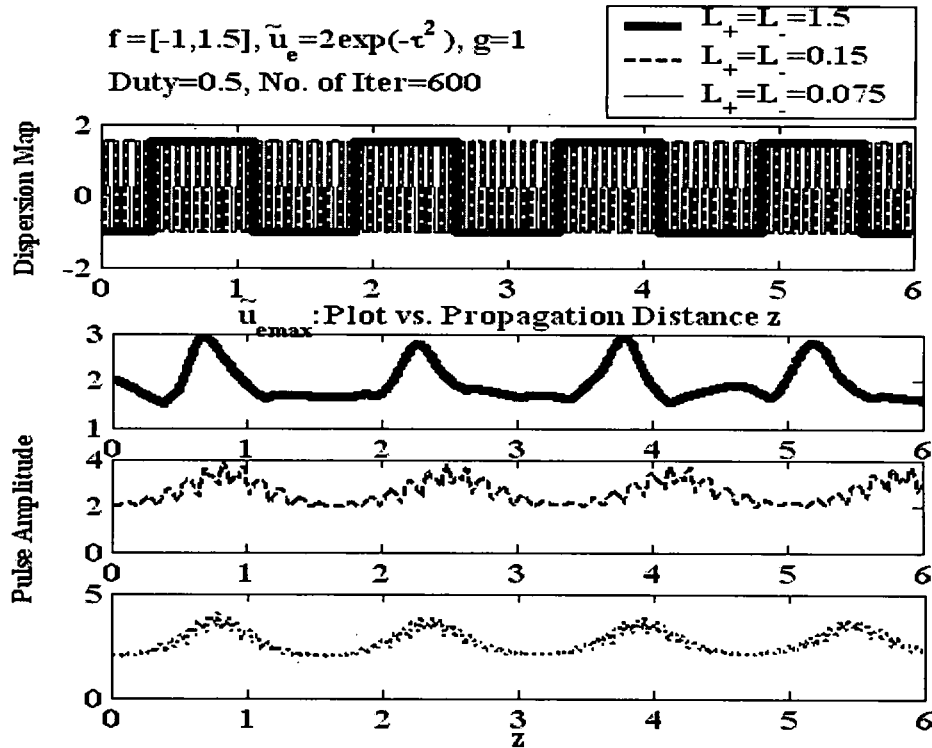


**Figure 7.11:** Variation of the on-axis pulse amplitude for three different dispersion map periods, keeping the same amplitude in the anomalous dispersion regime according to condition in Section 7.2.2.2, with the initial pulse  $\tilde{u}_e = 2\exp(-\tau^2)$ , using the AWT techniques according to the accompanying initial conditions.

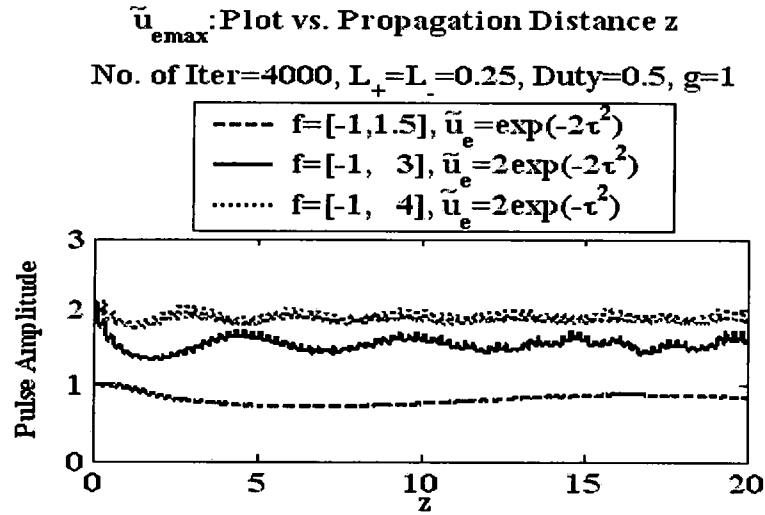


**Figure 7.12:** Variation of the on-axis pulse amplitude for three different dispersion map amplitudes, keeping the same period in the anomalous dispersion regime according to condition in Section 7.2.2.2, with different initial pulses, using the AWT techniques according to the accompanying initial conditions.

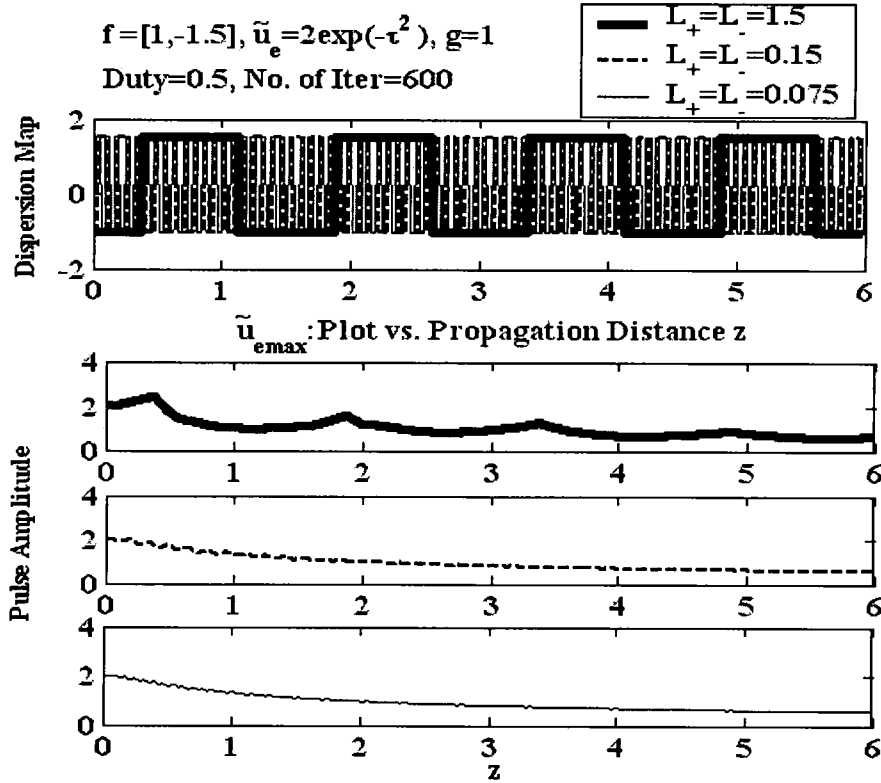


**Figure 7.13:** Variation of the on-axis pulse amplitude for three different dispersion map periods, keeping the same amplitude in the normal dispersion regime contradicting the condition in 7.2.2.2, using the AWT techniques according to the accompanying same initial conditions.



### 7.3 Dispersion Management in 2 and 3 -D

We study the propagation of chirped  $(D+1)$ -dimensional optical pulses in bulk media with periodic dispersion, analytically by using the variational approach, and numerically by using a new numerical technique relying on the adaptive fast Hankel split step (AFHSS) method using cylindrical and spherical symmetry for 2 and 3 dimensions respectively. Stability criteria for  $(2+1)$  and  $(3+1)$ -dimensional solitons are identified, and the long term dynamics of the solitons are studied by the averaged equations obtained using the Kapitza approach. Also, the slow dynamics of the solitons around the fixed points for the width and the chirp are studied. The importance of this work is in generating dispersion managed optical solitons in optical communication. Also, this work is applied to the stabilization of the Bose-Einstein condensate in  $(2+1)$  and  $(3+1)$ -dimensional optical lattice. We compare results of the new numerical technique with those obtained using fast Fourier split step (FFSS) technique.

#### 7.3.1 Introduction

In recent years, dispersion management (DM) techniques have received a lot of attention due to its benefits in high speed nonlinear wave propagation in optical communication systems because it allows one to reach the zero dispersion limit where inter pulse effects are reduced enormously<sup>62-65</sup>. Recently a similar model to DM has been developed for optical beams in a nonlinear wave guide array<sup>129</sup>, where the width and amplitude of discrete spatial solitons evolve periodically in time, thus the system obtained called diffraction management<sup>129</sup>. A bright soliton in  $(1+1)$  dimension in a Kerr medium is unconditionally stable for self-focusing (SF) media, however, it is not the case in  $(2+1)$  and  $(3+1)$  D where they collapse in SF and spreads out in self-defocusing (SDF)

media<sup>61</sup>. Confined wave packets in (3+1) D are often called optical bullets which are an extension of self-trapped optical beams into the temporal domain. It is worth to note that optical bullet generation and stabilization is important in optical communication systems. Recently it has been proven that nonlinearity management in 2D and 3D can arrest collapse or decay of solitons in Kerr type optical media<sup>26,66-68,112</sup> as well as the assumption of non-paraxiality and/or saturating nonlinearity<sup>58,60</sup>. The same can be said about 2D and 3D Bose-Einstein condensates with the sign in front of the cubic nonlinear term subject to periodic sinusoidal modulation in time via the Feshback resonance using the Gross-Pitaevskii equation<sup>111</sup>. Another possibility for stabilization of spatiotemporal solitons (STS) in Kerr media is to use alternating layered structures of the local group velocity dispersion (GVD) instead of the nonlinearity coefficient<sup>65,110,130</sup>. On the experimental front, although neither the 2D planar waveguide solitons nor the 3D STSs in bulk media have been observed, stabilization of (2+1)D discrete vortex solitons in a SF nonlinear medium has been observed in optically induced photonic lattices<sup>110</sup>.

In this Section, we use the adaptive fast Hankel split step (AFHSS) transform developed in Chapter 4 to numerically solve the underlying nonlinear Schrödinger (NLS) equation with dispersion management terms, develop an averaged variational technique to reduce the governing (D+1)-dimensional NLS equation to a coupled set of nonlinear ordinary differential equations (ODEs) and rigorously solve these equations and study their stability in each case. The stability of the dispersion managed soliton is deduced from the stability of the fixed points of the variational equations. These ODEs accurately predict the pulse dynamics in a medium of periodic nonlinearity and/or dispersion variations. This analytical method is used as a guideline for how to select stable initial

conditions for the pulse and the dispersion map, and compare it with the exact numerical technique developed. The results are compared to the step profile case.

The time-dependent paraxial wave equation, in the presence of periodic modulation of dispersion and nonlinearity has the form of a modified (D+1)-dimensional NLS with a dimensionless envelope of the electric field

$$j \frac{\partial \tilde{u}_e}{\partial z} + \frac{f(z)}{2} \frac{1}{r^{D-1}} \frac{\partial}{\partial r} \left( r^{D-1} \frac{\partial \tilde{u}_e}{\partial r} \right) + g(z) |\tilde{u}_e|^2 \tilde{u}_e = 0, \quad (7.28)$$

where  $r = (x^2 + y^2)^{1/2}$  or  $r = (x^2 + y^2 + \tau^2)^{1/2}$  for cylindrical or spherical symmetry of the field distribution respectively, and  $D$  can be 2 or 3, respectively. Assuming a Kerr type unsaturated medium with constant dispersion we should note that if the beam or spatiotemporal pulse energy exceeds a certain critical value  $P = \pi^{D/2} N_0 = 2^{D-1} \pi \int |\tilde{u}_e|^2 r^{D-1} dr = (5.85, 28.87)$  for  $D = (2, 3)$  respectively for an unchirped Gaussian input, small fluctuations of the intensity, beam size or pulse width can grow with propagation and lead to a phenomenon known as beam or spatiotemporal collapse. In other words, the intensity becomes infinitely large at a finite distance as the size of the beam diminishes and tends to zero both in the spatial and temporal domains. The functions  $f(z), g(z)$  are periodic modulation of dispersion and nonlinearity respectively. The above functions can be piece-wise continuous (PWC) and simple harmonic functions of the form  $\vartheta(z) = \vartheta_0 + \vartheta_1 \sin \tilde{\Omega} z$ , and we study both these cases.

### 7.3.2 Variational Technique

In this Section we use the variational approach to describe the wave evolution based on the Lagrangian formalism of classical mechanics in terms of the Lagrangian density<sup>126</sup>

$$\mathcal{L} = \frac{j}{2} \left( \tilde{u}_e^* \frac{\partial \tilde{u}_e}{\partial z} - \tilde{u}_e \frac{\partial \tilde{u}_e^*}{\partial z} \right) r^{D-1} + \frac{f(z)}{2} \left| \frac{\partial \tilde{u}_e}{\partial r} \right|^2 r^{D-1} - \frac{1}{2} r^{D-1} g(z) |\tilde{u}_e|^4, \quad (7.29)$$

where the (D+1) NLS equation can be derived from  $\mathcal{L}$  using the Euler-Lagrange equation

$$\frac{\partial}{\partial z} \frac{\partial \mathcal{L}}{\partial (\partial \tilde{u}_e / \partial z)} + \frac{\partial}{\partial r} \frac{\partial \mathcal{L}}{\partial (\partial \tilde{u}_e / \partial r)} - \frac{\partial \mathcal{L}}{\partial \tilde{u}_e} = 0. \quad (7.30)$$

Note that the application of Eq. (7.30) to the Lagrangian density in Eq. (7.29) generates the NLS equation given in Eq. (7.28). Following the Ritz optimization procedure let us assume the initial profile to be one of the following forms:

$$\tilde{u}_e = \tilde{u}_e(r, z) = A(z) \exp \left[ -\frac{r^2}{2w^2(z)} + jb(z)r^2 \right], \text{ or } \tilde{u}_e(r, z) = A(z) \operatorname{sech} \left( \frac{r}{w(z)} \right) \exp [jb(z)r^2] \quad (7.31)$$

where  $A(z)$  is the amplitude,  $w(z)$  is the beam radius,  $b(z)$  is the wave front curvature, as unknown functions of the propagation distance  $z$ . Following the method in<sup>126</sup>, where we insert the trial functions from Eq. (7.31) into the Lagrangian and by integrating:

$$\begin{aligned} \langle \mathcal{L} \rangle &= \int_0^\infty \mathcal{L} dr = \frac{i}{2} \left( A \frac{dA^*}{dz} - A^* \frac{dA}{dz} \right) w^D \alpha_{D-1} + |A|^2 w^{D+2} \left( \frac{db}{dz} + 2fb^2 \right) \alpha_{D+1} \\ &\quad + \frac{f}{2} |A|^2 w^{D-2} \gamma_{D-1} - \frac{1}{2} w^D \beta_{D-1} g(z) |A|^4, \end{aligned} \quad (7.32)$$

we obtain the reduced Lagrangian, where the  $\alpha$ ,  $\beta$ , and  $\gamma$ 's are given by

$$\alpha_D = \int_0^\infty r^D \exp(-r^2) dr, \beta_D = \int_0^\infty r^D \exp(-2r^2) dr, \gamma_{D-1} = \alpha_{D+1}, \quad (7.33)$$

for a Gaussian ansatz, and

$$\alpha_D = \int_0^\infty r^D \sec h^2(r) dr, \beta_D = \int_0^\infty r^D \sec h^4(r) dr, \gamma_D = \alpha_D - \beta_D, \quad (7.34)$$

for a hyperbolic secant assumption.

We can derive a set of evolution equations called Euler-Lagrange equations taking into account that the variation with respect to the unknowns in the initial profile

should be equal to zero, namely:  $\frac{\delta \langle \mathcal{L} \rangle}{\delta Q} = 0 \Rightarrow \frac{\partial \langle \mathcal{L} \rangle}{\partial Q} - \frac{d}{dz} \left( \frac{\partial \langle \mathcal{L} \rangle}{\partial Q'} \right) = 0$ , where

$Q = (A, w, b, A^*)$ . The evolution equations obtained are given by:

$$|A|^2 w^D = A_0^2 w_0^D = N_0, \quad (7.35a)$$

$$b = \frac{1}{2fw} \frac{dw}{dz}, \quad (7.35b)$$

$$\frac{d\tilde{\phi}}{dz} = \left[ -\frac{\gamma_{D-1}}{\alpha_{D-1}} \frac{f(z)}{w^2} + \left( 1 + \frac{D}{4} \right) g(z) \frac{\beta_{D-1}}{\alpha_{D-1}} |A|^2 \right], \quad (7.35c)$$

$$\frac{d^2 w}{dz^2} = \frac{\gamma_{D-1}}{\alpha_{D+1}} \frac{f^2(z)}{w^3} - \frac{N_0 D \beta_{D-1}}{2\alpha_{D+1}} \frac{f(z)g(z)}{w^{D+1}} + \frac{1}{f(z)} \frac{dw}{dz} \frac{df}{dz}, \quad (7.35d)$$

where  $A(z) = |A(z)| e^{i\tilde{\phi}(z)}$ ,  $N_0$  is the initial pulse energy defined above. In what follows,

we consider the cases where  $g(z) = 1$ .

#### A- The Two-dimensional Case (D=2)

Consider a periodic step function for the dispersion of the form<sup>67</sup>:

$$f(z) = \begin{cases} f_+ & 0 < z < L_+, \\ f_- & L_+ < z < L_+ + L_-. \end{cases} \quad (7.36)$$

Eq. (8d) becomes

$$\frac{d^2 w}{dz^2} = \begin{cases} \frac{F_+}{4w^3}, & 0 < z < L_+, \\ \frac{F_-}{4w^3}, & L_+ < z < L_+ + L_-, \end{cases} \quad (7.37)$$

where,  $F_{\pm} = 4(c_1 f_{\pm}^2 - c_2 f_{\pm})$  and  $c_1 = \frac{\gamma_1}{\alpha_3}$ ,  $c_2 = \frac{N_0 \beta_1}{\alpha_3}$  in the segments  $L_{\pm}$  respectively.

Following the technique used for the nonlinearity management in<sup>67</sup> but for dispersion management instead Eq. (7.37) becomes

$$\left(\frac{d\tilde{v}}{dz}\right)^2 = -F_{\pm} + 8T_{0\pm}\tilde{v}, \quad (7.38)$$

where  $\tilde{v} = w^2$ ,  $T_{0+} = \frac{H_+}{8} = \frac{F_+ + \tilde{v}_0'^2}{8\tilde{v}_0}$ ,  $T_{0-} = \frac{H_-}{8} = \frac{F_- + \tilde{v}_j'^2}{8\tilde{v}_j}$ , is the potential energy, and

$H_{\pm}$  is the Hamiltonian of the system in the corresponding segments. Note that  $\tilde{v}$ ,  $\tilde{v}'$ , must be continuous and if at  $z=0$ ,  $\tilde{v} = \tilde{v}_0$ ,  $\tilde{v}' = \tilde{v}_0'$ , the goal is to have at  $z = L_+ + L_-$ ,  $\tilde{v} = \tilde{v}_0 = \tilde{v}_j$ ,  $\tilde{v}' = \tilde{v}_0' = \tilde{v}_j'$ . Eq. (7.38) can be integrated in the interval  $(0, L_+)$

$$\text{as } \int_{\tilde{v}_0}^{\tilde{v}_j} \frac{d\tilde{v}}{\sqrt{H_+ \tilde{v} - F_+}} = L_+ \Rightarrow \tilde{v}_j = \frac{\left(\frac{L_+ H_+}{2} + \tilde{v}_0'\right)^2 + F_+}{H_+}, \text{ and } \tilde{v}_j' = \left(\tilde{v}_0' + \frac{L_+ H_+}{2}\right), \text{ where } \tilde{v}_j, \tilde{v}_j'$$

are the values of  $\tilde{v}$ ,  $\tilde{v}'$  at  $z = L_+$ , and  $H_+ = \frac{\tilde{v}_0'^2 + F_+}{\tilde{v}_0}$  as can be seen from Eq. (7.38). In a

similar fashion we can integrate Eq. (7.38) in the interval  $(L_+, L_+ + L_-)$ . The result is

tantamount to the replacements  $\tilde{v}_0 \rightarrow \tilde{v}_j$ ,  $\tilde{v}_j \rightarrow \tilde{v}_0$ ,  $\tilde{v}_0' \rightarrow \tilde{v}_j'$ ,  $\tilde{v}_j' \rightarrow \tilde{v}_0'$ , and

$$L_+ \rightarrow L_-, F_+ \rightarrow F_- \text{ and yields the pair of equations } \tilde{v}_0 = \frac{\left(\frac{L_- H_-}{2} + \tilde{v}_j'\right)^2 + F_-}{H_-} \text{ and}$$

$\bar{v}'_0 = \left( \check{v}'_j + \frac{L_- H_-}{2} \right)$  where  $H_- = \frac{\check{v}'_j{}^2 + F_-}{\check{v}_j}$ . Introducing normalizations  $F_r = \frac{F_+}{F_-}$ ,  $L_r = \frac{L_+}{L_-}$ ,

$\check{v}_{jr} = \frac{\check{v}_j}{\sqrt{F_- L_-}}$ ,  $\check{v}'_{jr} = \frac{\check{v}'_j}{\sqrt{F_-}}$ , we arrive after some basic calculations at

$$\begin{cases} \check{v}_{jr} = \frac{[\check{v}'_{0r} + (L/2\check{v}_{0r})(\check{v}'_{0r}{}^2 + F_r)]^2 + F_r}{(\check{v}'_{0r}{}^2 + F_r)/\check{v}_{0r}}, \\ \check{v}'_{jr} = \check{v}'_{0r} + (L/2\check{v}_{0r})(\check{v}'_{0r}{}^2 + F_r) \end{cases}, \quad (7.39a)$$

$$\begin{cases} \check{v}_{0r} = \bar{v}_{0r} = \frac{[\check{v}'_{jr} + (1/2\check{v}_{jr})(\check{v}'_{jr}{}^2 + 1)]^2 + 1}{(\check{v}'_{jr}{}^2 + 1)/\check{v}_{jr}}, \\ \check{v}'_{0r} = \bar{v}'_{0r} = \check{v}'_{jr} + (1/2\check{v}_{jr})(\check{v}'_{jr}{}^2 + 1) \end{cases}, \quad (7.39b)$$

If at  $z = L_+ + L_-$ ,  $\check{v} = \bar{v}_0 = \check{v}_0$ ,  $\check{v}' = \bar{v}'_0 = \check{v}'_0$ , then we arrive at the same starting point. Fixed

points can be found to be  $\check{v}_{0FP} = -\frac{L_r(F_r - 1)}{4\sqrt{L_r + 1}\sqrt{-1 - L_r F_r}}$ ,  $\check{v}'_{0FP} = \frac{\sqrt{-1 - L_r F_r}}{\sqrt{L_r + 1}}$ . Note that

$F_r < 1$  (since  $\check{v}_{0FP} > 0$ ) and  $F_r < -1/L_r$ , for real values of  $\check{v}_{0FP}$ ,  $\check{v}'_{0FP}$ . Since

$F_{\pm} = 4(c_1 f_{\pm}^2 - c_2 f_{\pm})$  this last condition leads to  $\frac{L_+ f_+^2 + L_- f_-^2}{L_+ f_+ + L_- f_-} < \frac{c_2}{c_1}$ , or  $\frac{\bar{f}^2}{\bar{f}} < \frac{c_2}{c_1}$ , where

$\bar{f} = \frac{L_+ f_+ + L_- f_-}{L_+ + L_-}$ , and  $\bar{f}^2 = \frac{L_+ f_+^2 + L_- f_-^2}{L_+ + L_-}$ . Also, it can be easily shown that  $\bar{f}^2 < \overline{f^2}$ .

Hence the condition for fixed points to exist is that  $\bar{f} < \frac{c_2}{c_1} = \frac{N_0 \beta_1}{\gamma_1}$ . Also, it turns out

that  $\bar{f} = \frac{L_+ f_+ + L_- f_-}{L_+ + L_-} = \frac{L_r f_+ + f_-}{L_r + 1} > 0$ , for fixed points to exist. Since

$F_{\pm} = 4(c_1 f_{\pm}^2 - c_2 f_{\pm})$  or  $f_{\pm} = \frac{c_2}{2c_1} \left( 1 \pm \sqrt{1 + \frac{F_{\pm} c_1}{c_2^2}} \right)$ , the average dispersion  $\bar{f}$  becomes

$$\bar{f} = \frac{(L_r + 1) + L_r \sqrt{1 + \frac{c_1 F_+}{c_2^2}} - \sqrt{1 + \frac{c_1 F_-}{c_2^2}}}{2 \frac{c_1}{c_2} (L_r + 1)} > 0. \text{ Note that when } L_r^2 = \frac{c_2^2 + c_1 F_-}{c_2^2 + c_1 F_+}, \text{ then}$$

$$\bar{f} = \bar{f}_{\min} = \frac{c_2}{2c_1} = \frac{N_0 \beta_1}{2\gamma_1}. \text{ Hence } \frac{N_0 \beta_1}{2\gamma_1} < \bar{f} < \frac{N_0 \beta_1}{\gamma_1}.$$

Now let us consider a periodic function for the dispersion of the form  $f(z) = f_0 + f_1 \sin \tilde{\Omega} z$ . From Eqs. (7.35b) and (7.35d) we arrive at the following ODE system

$$\frac{db}{dz} = \frac{c_1 f - c_2}{2w^4} - 2fb^2, \quad (7.40a)$$

$$\frac{dw}{dz} = 2fbw. \quad (7.40b)$$

Following the Kapitza approach where the width  $w$  and the chirp  $b$  has the form  $w = \tilde{w} + \delta w$ ,  $b = \tilde{b} + \delta b$  respectively. After gathering the slowly varying terms apart from the rapidly varying ones, Eqs. (7.40a) and (7.40b) become

$$\frac{d\tilde{w}}{dz} = 2f_0 \tilde{w} \tilde{b} + 2\tilde{w} \delta w f_1 \sin \Omega z + 2\tilde{b} \delta w f_1 \sin \Omega z + 2f_0 \delta w \delta b, \quad (7.41a)$$

$$\frac{d\delta w}{dz} = 2\tilde{w} \tilde{b} f_1 \sin \Omega z + 2f_0 \tilde{w} \delta b + 2f_0 \tilde{b} \delta w, \quad (7.41b)$$

$$\begin{aligned} \frac{d\tilde{b}}{dz} = & \frac{1}{\tilde{w}^4} \left( \frac{c_1 f_0 - c_2}{2} \left( 1 + 10 \frac{\delta w^2}{\tilde{w}^2} \right) - 2c_1 f_1 \frac{\delta w \sin \tilde{\Omega} z}{\tilde{w}} \right) \\ & - 2f_0 \tilde{b}^2 - 2f_0 \delta b^2 - 4\tilde{b} f_1 \delta b \sin \tilde{\Omega} z, \end{aligned} \quad (7.41c)$$

$$\frac{d\delta b}{dz} = \left( \frac{2(c_1 f_0 - c_2)}{\tilde{w}^5} \right) \delta w + \left( \frac{c_1}{2\tilde{w}^4} - 2\tilde{b}^2 \right) f_1 \sin \tilde{\Omega} z - 4f_0 \tilde{b} \delta b. \quad (7.41d)$$

Taking the average, denoted by the symbol  $\langle \dots \rangle$ , of Eqs. (7.41a) and (7.41c) we get



$$\left\langle \frac{d\tilde{w}}{dz} \right\rangle = 2f_0 \langle \tilde{w}\tilde{b} \rangle + 2\langle \tilde{w}\delta w f_1 \sin \tilde{\Omega}z \rangle + 2\langle \tilde{b}\delta w f_1 \sin \tilde{\Omega}z \rangle + 2\langle f_0 \delta w \delta b \rangle, \quad (7.42a)$$

$$\begin{aligned} \left\langle \frac{d\tilde{b}}{dz} \right\rangle = & \left\langle \frac{1}{\tilde{w}^4} \right\rangle \left( \frac{c_1 f_0 - c_2}{2} \left( 1 + 10 \left\langle \frac{\delta w^2}{\tilde{w}^2} \right\rangle \right) - 2c_1 f_1 \left\langle \frac{\delta w \sin \tilde{\Omega}z}{\tilde{w}} \right\rangle \right) \\ & - 2f_0 \langle \tilde{b}^2 \rangle - 2f_0 \langle \delta b^2 \rangle - 4\langle \tilde{b} f_1 \delta b \sin \tilde{\Omega}z \rangle, \end{aligned} \quad (7.42b)$$

Assuming  $\langle \tilde{w}^n \rangle = \tilde{w}^n$ ,  $\langle \tilde{b}^n \rangle = \tilde{b}^n$ ,  $\left\langle \frac{d\tilde{w}}{dz} \right\rangle = \frac{d\tilde{w}}{dz}$ ,  $\left\langle \frac{d\tilde{b}}{dz} \right\rangle = \frac{d\tilde{b}}{dz}$ , and dropping out the  $\langle \sim \rangle$ , Eqs.

(7.42a), (7.42b), (7.41 b), and (7.41d), and becomes

$$\frac{dw}{dz} = 2f_0 w b + 2w \langle \delta w f_1 \sin \tilde{\Omega}z \rangle + 2b \langle \delta w f_1 \sin \tilde{\Omega}z \rangle + 2f_0 \langle \delta w \delta b \rangle, \quad (7.43a)$$

$$\begin{aligned} \frac{db}{dz} = & \frac{1}{w^4} \left( \frac{c_1 f_0 - c_2}{2} \left( 1 + 10 \frac{\langle \delta w^2 \rangle}{w^2} \right) - 2c_1 f_1 \frac{\langle \delta w \sin \tilde{\Omega}z \rangle}{w} \right) \\ & - 2f_0 b^2 - 2f_0 \langle \delta b^2 \rangle - 4b f_1 \langle \delta b \sin \tilde{\Omega}z \rangle, \end{aligned} \quad (7.43b)$$

$$\frac{d\delta w}{dz} = 2w b f_1 \sin \tilde{\Omega}z + 2f_0 w \delta b + 2f_0 b \delta w, \quad (7.43c)$$

$$\frac{d\delta b}{dz} = \left( \frac{2(c_1 f_0 - c_2)}{w^5} \right) \delta w + \left( \frac{c_1}{2w^4} - 2b^2 \right) f_1 \sin \tilde{\Omega}z - 4f_0 b \delta b. \quad (7.43d)$$

Let  $\delta b = S_5 \sin \tilde{\Omega}z + S_6 \cos \tilde{\Omega}z$ ,  $\delta w = S_7 \sin \tilde{\Omega}z + S_8 \cos \tilde{\Omega}z$ ,  $\tilde{\kappa} = 2 \left( \frac{c_1 f_0 - c_2}{w^5} \right)$ ,

$\tilde{\eta} = \left( \frac{c_1}{2w^4} - 2b^2 \right) f_1$ , then a particular solution to Eqs. (7.43c) and (7.43d) can be found

from the following system of linear equations

$$\begin{bmatrix} 0 & 2wf_0 & -\tilde{\Omega} & 2bf_0 \\ 2wf_0 & 0 & 2bf_0 & \tilde{\Omega} \\ \tilde{\Omega} & 4bf_0 & 0 & -\tilde{\kappa} \\ 4bf_0 & -\tilde{\Omega} & -\tilde{\kappa} & 0 \end{bmatrix} \begin{bmatrix} S_5 \\ S_6 \\ S_7 \\ S_8 \end{bmatrix} = \begin{bmatrix} 0 \\ -2wbf_1 \\ 0 \\ \tilde{\eta} \end{bmatrix}. \quad (7.44)$$

The solution of the above system gives

$$S_5 = \frac{-2\tilde{\kappa}wbf_1(2wf_0\tilde{\kappa} + 8b^2f_0^2 + \tilde{\Omega}^2)}{\hat{M}} + \frac{4bf_0(wf_0\tilde{\kappa} + \tilde{\Omega}^2 + 4b^2f_0^2)\tilde{\eta}}{\hat{M}}, \quad (7.45a)$$

$$S_6 = -4 \frac{\tilde{\Omega}b^2wf_1f_0\tilde{\kappa} - \tilde{\Omega}(2wf_0\tilde{\kappa} + \tilde{\Omega}^2 + 4b^2f_0^2)\tilde{\eta}}{\hat{M}}, \quad (7.45b)$$

$$S_7 = \frac{-4b^2f_0wf_1(4wf_0\tilde{\kappa} + 16b^2f_0^2 + \tilde{\Omega}^2)}{\hat{M}} - \frac{2wf_0(2wf_0\tilde{\kappa} + \tilde{\Omega}^2 + 8b^2f_0^2)\tilde{\eta}}{\hat{M}}, \quad (7.45c)$$

$$S_8 = \frac{-2bwf_1\tilde{\Omega}(2wf_0\tilde{\kappa} + \tilde{\Omega}^2 + 16b^2f_0^2) - 4bf_0^2w\tilde{\Omega}\tilde{\eta}}{\hat{M}}, \quad (7.45d)$$

where  $\hat{M} = \tilde{\Omega}^4 + 4wf_0\tilde{\Omega}^2\tilde{\kappa} + 20b^2f_0^2\tilde{\Omega}^2 + 4w^2f_0^2\tilde{\kappa}^2 + 32wf_0^3b^2\tilde{\kappa} + 64b^4f_0^4$ . Assuming  $f_1$  is large and keeping the linear terms in  $\kappa$  and  $b$ , and in the limit of high frequencies  $\tilde{\Omega}^2 \gg \tilde{\kappa}wf_0$ , we get

$$\delta w = \frac{-f_0f_1c_1}{w^3\tilde{\Omega}^2} \sin \tilde{\Omega}z - \frac{2wbf_1\tilde{\Omega}}{\tilde{\Omega}^2} \cos \tilde{\Omega}z, \quad (7.46a)$$

$$\delta b = \frac{2bf_1(c_1f_0 - c_2)}{w^4\tilde{\Omega}^2} \sin \tilde{\Omega}z - \frac{c_1f_1}{2w^4\tilde{\Omega}} \cos \tilde{\Omega}z. \quad (7.46b)$$

Eqs. (7.43a) and (7.43b) become

$$\frac{dw}{dz} = 2wb \left( f_0 + \frac{f_1^2}{\tilde{\Omega}^2} \frac{\hat{\mu}}{w^4} \right), \quad (7.46c)$$

$$\frac{db}{dz} = \frac{\hat{\mu}/2}{w^4} + \frac{4b^2f_1^2\hat{\mu}}{w^4\tilde{\Omega}^2} + \frac{c_1^2f_1^2f_0}{w^8\tilde{\Omega}^2}, \quad (7.46d)$$

where  $\hat{\mu} = c_1 f_0 - c_2$ . In general, collapse occurs if  $\hat{\mu} < 0$ . To see this in the easiest way,

consider the case  $f_0 = 1, D = 2, c_1, c_2$  as defined in Eq. (7.37), we get  $N_0 > \frac{\gamma_1}{\beta_1} = 2$ , which

is the critical power as is well known in the case of a Gaussian input. Fixed points are

found by putting  $db/dz = dw/dz = 0$ , which gives  $b = 0, w = \left( \frac{-2c_1^2 f_1^2 f_0}{\hat{\mu} \tilde{\Omega}^2} \right)^{\frac{1}{4}}$ . Note that

real solutions exist when  $\hat{\mu} < 0$  and  $f_0 > 0$  which is equivalent to  $0 < f_0 < \frac{c_2}{c_1} = \frac{N_0 \beta_1}{\gamma_1}$ , as

is shown in the assumption of periodic step dispersion function previously. The above

system can be simplified if we consider  $\frac{f_1}{\tilde{\Omega}} \ll 1$ . If we substitute Eq. (7.46d) into the

derivative of Eq. (7.46c) we obtain  $\frac{d^2 w}{dz^2} = \frac{f_0 \hat{\mu}}{w^3} + 2 \frac{c_1^2 f_1^2 f_0^2}{w^7 \tilde{\Omega}^2} + \left( \frac{dw}{dz} \right)^2 \left( 1 + \frac{2 f_1^2 \hat{\mu}}{f_0 w^5 \tilde{\Omega}^2} \right)$ ,

which corresponds to the minimum of the effective potential for the evolution of radius

$w$ ,  $T_{eff} = \frac{c_1 f_0^2 - c_2 f_0}{2w^2} + \frac{c_1^2 f_1^2 f_0^2}{3w^6 \tilde{\Omega}^2}$ . Compared to the potential obtained from Eq. (7.37)

namely  $T = \frac{c_1 f_0^2 - c_2 f_0}{2w^2}$  with  $(f = f_0)$ , we find that the last term is the correction term

for dispersion. Note that stabilization is possible when there is a minimum in this

effective potential namely when  $\hat{\mu} < 0$  and  $f_0 > 0$ .

Note that the condition  $\hat{\mu} < 0$  and  $0 < f_0 < \frac{N_0 \beta_1}{\gamma_1}$  is similar to the condition

obtained in the piecewise assumption of the dispersion map namely

$\frac{N_0\beta_1}{2\gamma_1} < \bar{f} < \frac{\bar{f}^2}{f} < \frac{N_0\beta_1}{\gamma_1}$ , where  $\bar{f} = f_0$ . The difference is due to the fact that the

piecewise assumption has many harmonics compared to that of the sinusoidal case.

### B- The Three-dimensional Case (D=3)

Let us consider a periodic function for the dispersion of the form  $f(z) = f_0 + f_1 \sin \tilde{\Omega} z$ . Let  $\varpi = w b$ , then from Eqs. (7.35b) and (7.35d) we arrive at the following ODE system

$$\frac{d\varpi}{dz} = \frac{c_1 f}{w^3} - \frac{c_2}{w^4}, \quad (7.47a)$$

$$\frac{dw}{dz} = 2f\varpi, \quad (7.47b)$$

where  $c_3 = \frac{\gamma_{D-1}}{2\alpha_{D+1}}$ ,  $c_4 = \frac{DN_0\beta_{D-1}}{4\alpha_{D+1}}$ . Following the Kapitza approach where the width  $w$

and the chirp  $\varpi$  has the form  $w = \tilde{w} + \delta w$ ,  $\varpi = \tilde{\varpi} + \delta \varpi$  respectively. Following the same approach and upon making the same assumptions as in the 2D case, Eqs. (7.47a) and (7.47b) become

$$\frac{dw}{dz} = 2f_0\varpi + 2f_1\langle \delta\varpi \sin \tilde{\Omega} z \rangle + 2f_1\langle \delta\varpi \sin \tilde{\Omega} z \rangle, \quad (7.48a)$$

$$\frac{d\varpi}{dz} = \left( \frac{c_3 f_0 w - c_4}{w^4} \right) + \left( \frac{6c_3 f_0 w - 10c_4}{w^6} \right) \langle \delta w^2 \rangle - \frac{3c_3 f_1}{w^4} \langle \delta w \sin \tilde{\Omega} z \rangle, \quad (7.48b)$$

$$\frac{d\delta w}{dz} = 2\varpi f_1 \sin \tilde{\Omega} z + 2f_0 \delta \varpi, \quad (7.48c)$$

$$\frac{d\delta \varpi}{dz} = \left( \frac{-3c_3 f_0 w + 4c_4}{w^5} \right) \delta w + \frac{c_3 f_1}{w^3} \sin \tilde{\Omega} z. \quad (7.48d)$$

Let  $\delta b = S_9 \sin \tilde{\Omega} z + S_{10} \cos \tilde{\Omega} z$ ,  $\delta w = S_{11} \sin \tilde{\Omega} z + S_{12} \cos \tilde{\Omega} z$ ,  $\bar{\kappa} = \left( \frac{-3c_3 f_0 w + 4c_4}{w^5} \right)$ ,

$\bar{\eta} = \left( \frac{c_3 f_1}{w^3} \right)$ , then a particular solution to Eqs. (7.48c) and (7.48d) can be found from the

following system of linear equations

$$\begin{bmatrix} \tilde{\Omega} & 0 & 0 & -\bar{\kappa} \\ 0 & \tilde{\Omega} & \bar{\kappa} & 0 \\ 0 & -2f_0 & \tilde{\Omega} & 0 \\ 2f_0 & 0 & 0 & \tilde{\Omega} \end{bmatrix} \begin{bmatrix} S_9 \\ S_{10} \\ S_{11} \\ S_{12} \end{bmatrix} = \begin{bmatrix} 0 \\ -\bar{\eta} \\ 0 \\ -2f_1 \varpi \end{bmatrix}. \quad (7.49)$$

The solution of the following system gives

$$S_9 = \frac{-2\bar{\kappa}\varpi f_1}{\tilde{\Omega}^2 + 2f_0\bar{\kappa}}, \quad (7.50a)$$

$$S_{10} = \frac{-\bar{\eta}\tilde{\Omega}}{\tilde{\Omega}^2 + 2f_0\bar{\kappa}}, \quad (7.50b)$$

$$S_{11} = \frac{-2\bar{\eta}f_0}{\tilde{\Omega}^2 + 2f_0\bar{\kappa}}, \quad (7.50c)$$

$$S_{12} = \frac{-2\varpi f_1 \tilde{\Omega}}{\tilde{\Omega}^2 + 2f_0\bar{\kappa}}. \quad (7.50d)$$

Hence we obtain the solution

$$\delta w = \frac{-2c_3 f_1 f_0}{w^3 \left[ \tilde{\Omega}^2 + \frac{2f_0(4c_4 - 3c_3 f_0 w)}{w^5} \right]} \sin \tilde{\Omega} z - \frac{-2\varpi \tilde{\Omega} f_1}{\left[ \tilde{\Omega}^2 + \frac{2f_0(4c_4 - 3c_3 f_0 w)}{w^5} \right]} \cos \tilde{\Omega} z, \quad (7.51a)$$

$$\delta \varpi = \frac{-2f_1 \varpi (4c_4 - 3c_3 f_0 w)}{w^5 \left[ \tilde{\Omega}^2 + \frac{2f_0(4c_4 - 3c_3 f_0 w)}{w^5} \right]} \sin \tilde{\Omega} z - \frac{-c_3 f_1 \tilde{\Omega}}{w^3 \left[ \tilde{\Omega}^2 + \frac{2f_0(4c_4 - 3c_3 f_0 w)}{w^5} \right]} \cos \tilde{\Omega} z, \quad (7.51b)$$

Let  $\bar{\mu} = 3c_3 f_0 w - 4c_4$ , and assuming  $\tilde{\Omega}^2 \gg -2f_0 \left( \frac{\bar{\mu}}{w^5} \right) \approx 1$ , we get

$$\frac{dw}{dz} = 2\varpi \left( f_0 - \frac{f_1^2}{\tilde{\Omega}^2} \frac{\bar{\mu}}{w^5} \right), \quad (7.51c)$$

$$\frac{d\varpi}{dz} = \frac{c_3 f_0}{w^3} - \frac{c_4}{w^4} + \frac{3c_3^2 f_1^2 f_0}{w^7 \tilde{\Omega}^2} + \frac{12c_3 f_1^2 f_0}{w^5 \tilde{\Omega}^2} \varpi^2 - \frac{20 f_1^2 c_4}{w^6 \tilde{\Omega}^2} \varpi^2. \quad (7.51d)$$

This system has the Hamiltonian structure with the Hamiltonian given by

$$H = \left( \frac{3c_3 f_0 w - 2c_4}{6w^3} + \frac{c_3^2 f_1^2 f_0}{6\tilde{\Omega}^2 w^6} \right) + \varpi^2 \left( f_0 + \frac{f_1^2 \bar{\mu}}{\tilde{\Omega}^2 w^5} \right), \quad (7.52)$$

from which the equations of motion follow as  $dw/dz = \partial H / \partial \varpi$ ,  $d\varpi/dz = -\partial H / \partial w$ . From this Hamiltonian we can see that the mechanism of collapse suppression resides in the repulsive potential near the small values of width (the 2<sup>nd</sup> term) in the above equation and attractive force induced by the (1<sup>st</sup> term). Note that collapse occurs if  $\bar{\mu} < 0$ . So in

the case  $f_0 = 1$ ,  $D = 3$ ,  $c_1, c_2$  as defined in Eq. (7.47), we get  $\frac{N_0}{w} > \frac{\gamma_2}{2\beta_2}$  which is

equivalent to the condition found in<sup>126</sup> for 3D solitons. Fixed points are found by putting

$d\varpi/dz = dw/dz = 0$ , which gives  $\varpi = 0$ ,  $w^4 - \frac{c_4}{c_3 f_0} w^3 + \frac{3c_3 f_1^2}{\tilde{\Omega}^2} = 0$ . Also, in the case

where we have constant dispersion namely  $f_1 = 0$ , then  $\frac{N_0}{w} = 2\sqrt{2}$ , for the Gaussian case

which is the stationary point for STS as shown in<sup>12</sup>. Eqs. (7.51c) and (7.51d) can be

simplified if we consider  $\frac{f_1}{\tilde{\Omega}} \ll 1$ . We obtain

$\frac{d^2 w}{dz^2} = \frac{2f_0^2 c_3}{w^3} - \frac{2f_0 c_4}{w^4} + \frac{6c_3^2 f_1^2 f_0^2}{w^7 \tilde{\Omega}^2} + \left( \frac{dw}{dz} \right)^2 \left( \frac{6c_3 f_1^2}{w^5 \tilde{\Omega}^2} - \frac{10f_1^2 c_4}{f_0 w^6 \tilde{\Omega}^2} \right)$ , which corresponds to the

minimum of the effective potential

$$T_{eff} = \frac{c_3 f_0^2}{w^2} - \frac{2f_0 c_4}{3w^3} + \frac{c_3^2 f_1^2 f_0^2}{w^6 \tilde{\Omega}^2}. \quad (7.53)$$

Compared to the potential obtained from Eq. (8d) namely  $T = \frac{c_3 f_0^2}{w^2} - \frac{2f_0 c_4}{3w^3}$  with  $(f = f_0)$ , we find that the last term is the correction term for dispersion. Note that stabilization is possible when there is a minimum in this effective potential namely when  $f_0 c_4 > 0$ .

### 7.3.3 Adaptive Fast Hankel Split Step Method

The Hankel transform method adopted is that of <sup>31,94,95</sup> mentioned in Chapter 4. The AFHSS algorithm in Figure 7.14 resembles that in Figure 4.1 and it resembles the symmetrized Fourier split-step technique<sup>59,90</sup>, where we change the longitudinal propagation stepping size  $\Delta z \propto A(z_1)^{-1/s} - A(z_2)^{-1/s} \approx A(z_1)^{-1/s}$  when  $A(z_2) \gg A(z_1)$ , adaptively using Zakharov et al. similarity formula defined in<sup>20</sup> where  $s_z = (2/3, 1/2)$  for  $D = (2, 3)$  respectively, and the grid spatial range  $\Delta r_{max} \propto A(z)^{1-D}$  as indicated in<sup>2</sup> in order to track the varying amplitude of the spatiotemporal pulse in the medium,. We note that periodic focusing/defocusing or beam trapping occurs when we have a sign-alternating dispersive medium and under the conditions stated above.

### 7.3.4 Numerical Results And Conclusion

We now show sample simulation results using the AFHSS method that uses Guizar-Sicairos et al's Hankel transform technique<sup>94,95</sup> and compare it to the adaptive fast Fourier split step (AFFSS) method. All the input functions are of the type mentioned in Eq. (7.31). Figure 7.15 (a), (b) and (c) show the case when  $D=2$  with the parameters  $f = [f_-, f_+] = [-1, 2]$ ,  $\Delta z = 0.001$ ,  $M = 4000$ ,  $A_0 = 1.5$ ,  $w_0 = 1$ , for different values of the

dispersion period ranging from  $L = 0.004$  to  $L = 0.2$ , where  $M$  is the number of iterations. According to the analytical study above these should lead to stable solitons. Figure 7.16(a) when  $D=2$  with the parameters  $f = [-1, 2]$ ,  $\Delta z = 0.001$ ,  $M = 8000$ ,  $A_0 = 1.5$ ,  $w_0 = 1$ ,  $L = 0.04$  shows the beam evolution. Notice that in this case the beam focuses and defocuses periodically. Figure 7.16(b) shows the corresponding on-axis amplitude. Similarly for Figure 17(a) with different dispersion map and parameters  $f = [-2, 4]$ ,  $\Delta z = 0.001$ ,  $M = 8000$ ,  $A_0 = 2$ ,  $w_0 = 1$ ,  $L = 0.002$  shows the  $D=2$  case when there is a periodic focusing and defocusing. Figure 7.18(a-c) shows the comparison of the on-axis amplitude between the AFFSS and the AFHSS for the parameters shown in each inset. Figure 7.19(a) shows the case when  $D=3$  with the parameters  $f = [-2, 4]$ ,  $\Delta z = 0.005$ ,  $M = 4000$ ,  $A_0 = 0.2$ ,  $w_0 = 15$ ,  $L = 4$ , which according to the analytical study above leads to a stable soliton. Figure 19(b) shows the corresponding on-axis amplitude. Figure 7.20(a) shows the case when  $D=3$  with the parameters  $f = [-2, 4]$ ,  $\Delta z = 0.005$ ,  $M = 7200$ ,  $A_0 = 1$ ,  $w_0 = 5$ ,  $L = 0.015$ , which leads to a stable soliton. Figure 7.20(b) shows the corresponding on-axis amplitude. Figure 7.21(a) shows the decay of a 3-D optical pulse with the parameters  $f = [2, -4]$ ,  $\Delta z = 0.005$ ,  $M = 1200$ ,  $A_0 = 2$ ,  $w_0 = 5$ ,  $L = 0.01$ , using AFHSS. Figure 7.21(b) shows the corresponding on-axis amplitude. Figure 7.22(a) shows the collapse of a 3-D optical pulse when  $f = [2, -5]$ ,  $\Delta z = 0.005$ ,  $M = 1800$ ,  $A_0 = 1$ ,  $w_0 = 10$ ,  $L = 0.015$ . Figure 7.23(b) shows the corresponding on-axis amplitude. Note that as a general observation for numerical stability it is preferable that the width or eventually the energy of the pulse and the frequency of the alternating dispersion is large enough.



Finally, we compare computation speeds of the AFHSS and regular (2 and 3)-D FFT. The number of computations in (2 and 3)-D FFT is  $\propto 2N^2 \log_2 N$  and  $N^3 \log_2 N$  respectively. On the other hand we can make the number of computations of Guizar-Sicairos et al's method comparable to Siegman's method<sup>51</sup> namely equal to  $4N \log_2 2N + 2N$  by a priori computing and storing the zeros of the cylindrical or spherical Bessel function. The advantages of Guizar-Sicairos et al's method over Siegman's are the accuracy for the sampled points and a simple retrieval expression. For more comparison between Guizar-Sicairos et al's and Siegman's method, we refer readers to Table 1 in Yu et al.<sup>94</sup>. Also, we note that the use of the adaptive variation of the longitudinal propagation stepping size  $\Delta z$  and the transverse spatial sampling size  $\Delta r_{max}$  according to  $\Delta z \propto A^{-1/s}$  and  $A^{1-D}$  respectively, allow us to track on-axis amplitudes, for the paraxial unsaturated constant nonlinearity case, more precisely than regular 2D and 3D FFT methods. Without the adaptive variation in the case of unsaturated constant nonlinearity media, the numerical methods become unstable, and we witness oscillatory focusing and defocusing of the beam from numerical instability. Typical run times are around 1 and 2 minutes for AFHSS when  $S = 2\pi R_1 R_2 = 200\pi$ , or  $\tilde{S} = 2\pi R_1 R_2 = 800\pi$ , respectively, and 10 minutes and 1 hour for (2 and 3)-D FFT when the mesh size is  $N^2 = (2^8)^2$  and  $N^3 = (2^8)^3$  respectively.

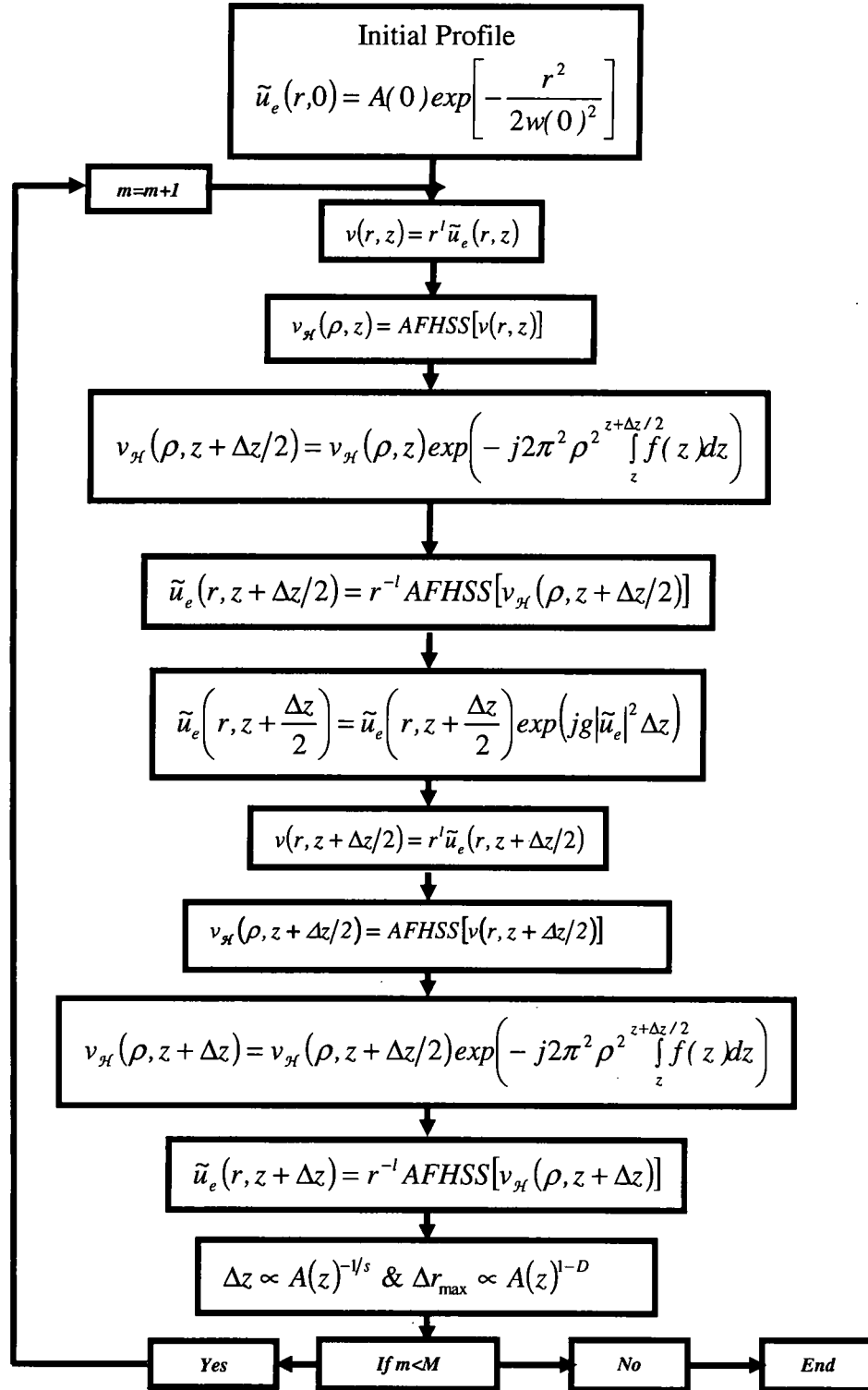


**Figure 7.14:** The AFHSS algorithm, a symmetrized version of the split step FFT using cylindrical or spherical Fourier Bessel transform instead, and using adaptive longitudinal stepping and transverse grid management.

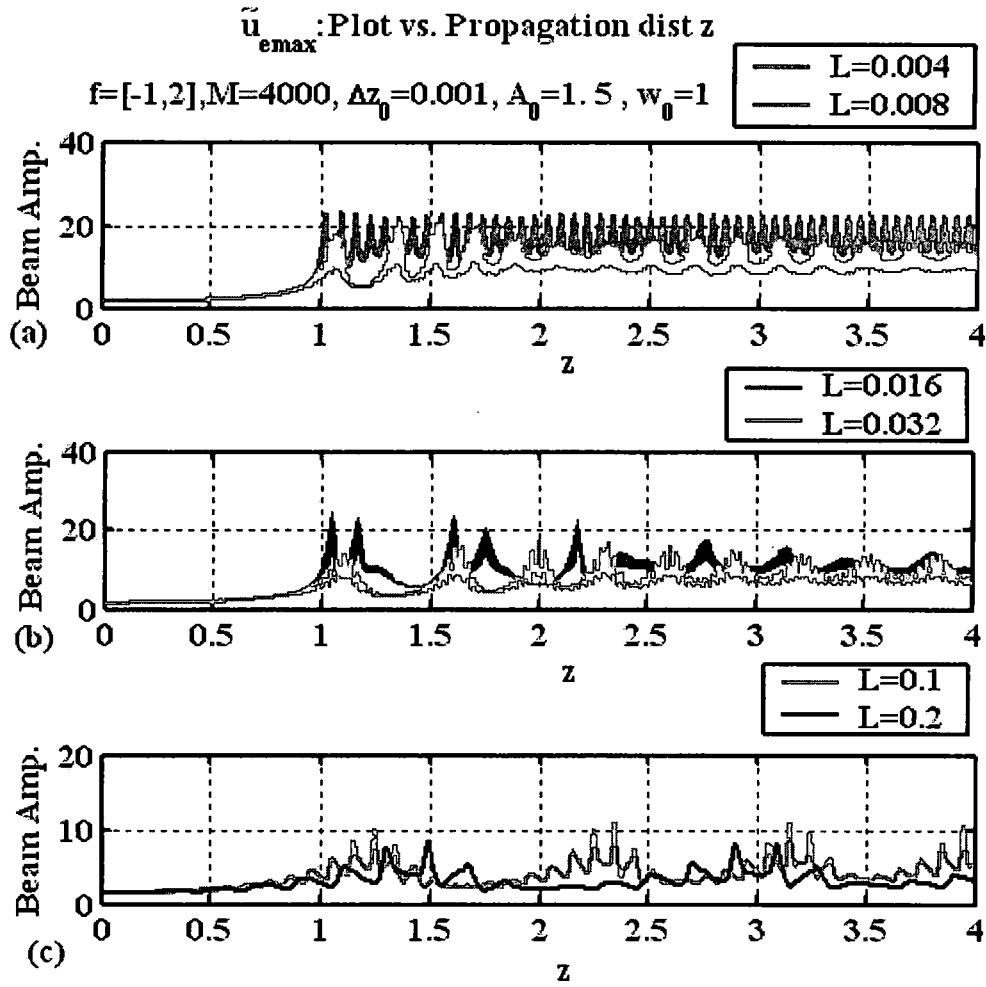


**Figure 7.15:** (a), (b) and (c) on-axis amplitude stable 2-D soliton evolution through the sign alternating dispersion when  $D=2$  with the parameters  $f = [-1,2]$ ,  $\Delta z = 0.001$ ,  $M = 4000$ ,  $A_0 = 1.5$ ,  $w_0 = 1$ , for different values of the dispersion period ranging from  $L = 0.004$  to  $L = 0.2$ , using AFHSS with  $\tilde{S} = 2\pi R_1 R_2 = 2\pi \times 200$  (400 cylindrical samples).

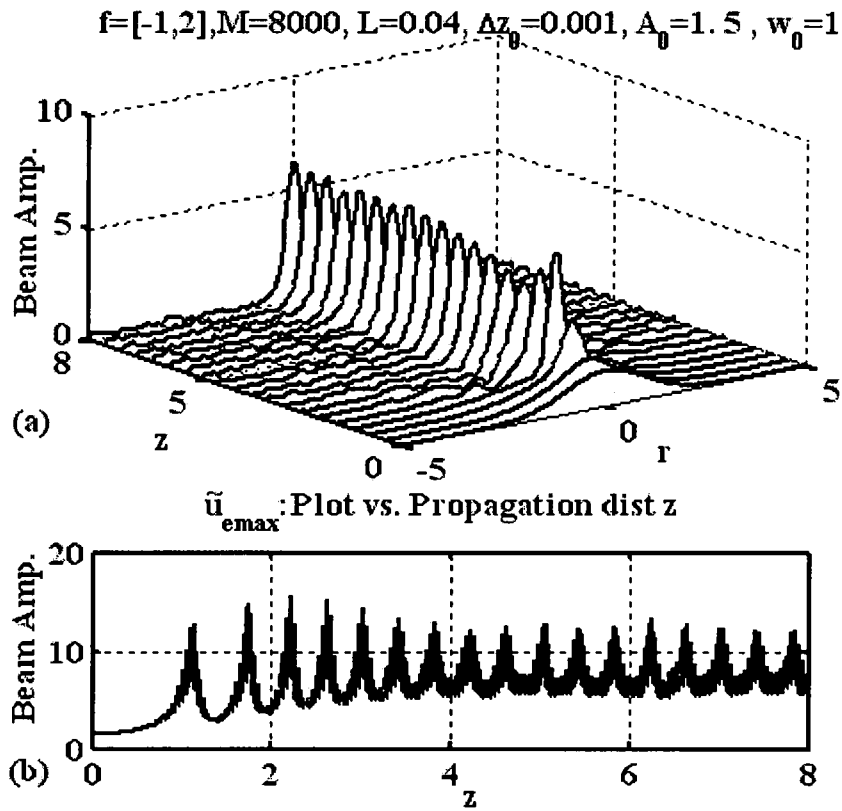


**Figure 7.16:** Stable 2-D soliton generation through the sign alternating dispersion. 3(a) shows the pulse evolution with the parameters  $f = [-1, 2], \Delta z = 0.001, M = 8000, A_0 = 1.5, w_0 = 1, L = 0.04$ . 3(b) shows the on-axis amplitude for both the AFFSS and the AFHSS methods for the same parameters, using AFHSS with  $\tilde{S} = 2\pi R_1 R_2 = 2\pi \times 200$  (400 cylindrical samples).

$$f=[-2,4], M=8000, \Delta z_0=0.001, L=0.002, A_0=2, w_0=1.$$

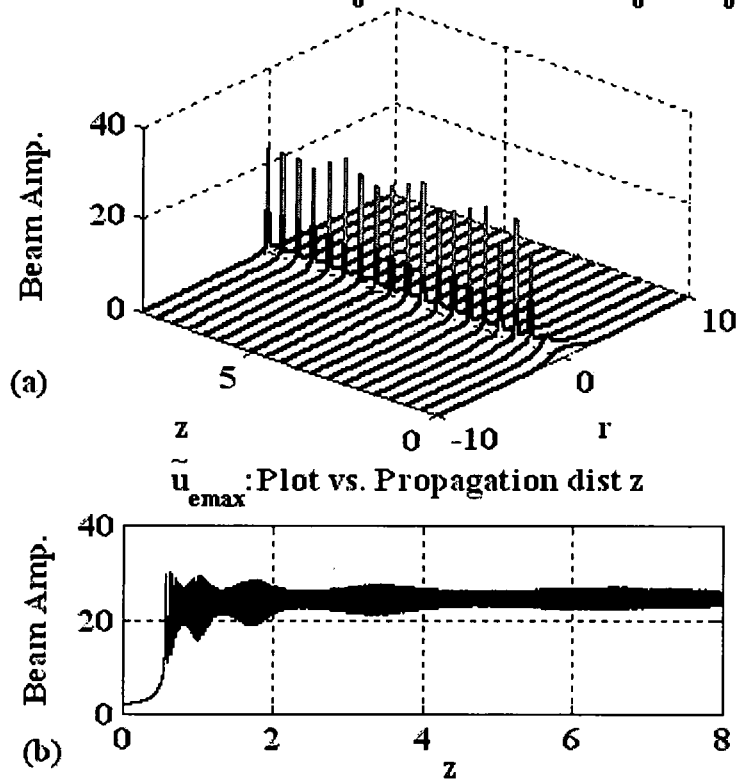


**Figure 7.17:** Stable 2-D soliton generation through the sign alternating dispersion. 4(a) shows the pulse evolution with the parameters  $f = [-2, 4]$ ,  $\Delta z = 0.001$ ,  $M = 8000$ ,  $A_0 = 2$ ,  $w_0 = 1$ ,  $L = 0.002$ . 4(b) shows the on-axis amplitude for the AFHSS methods for the same parameters, using AFHSS with  $\tilde{S} = 2\pi R_1 R_2 = 2\pi \times 200$  (400 cylindrical samples).

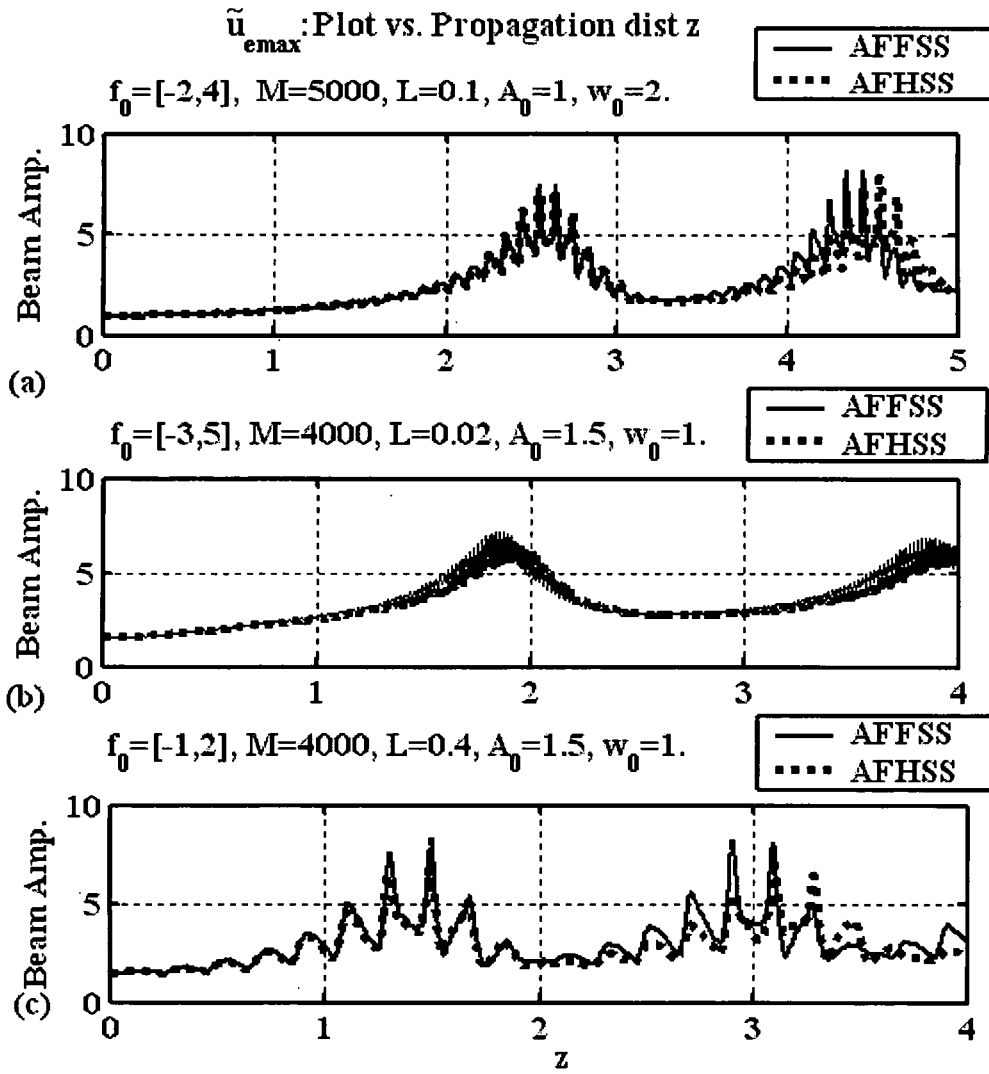


**Figure 7.18:** (a-c) shows the comparison of the on-axis amplitude between the AFFSS and the AFHSS for the parameters shown in each inset, using AFHSS with  $\tilde{S} = 2\pi R_1 R_2 = 2\pi \times 200$  (400 cylindrical samples). and  $N^2 = (2^8)^2$  for the AFFSS 2D mesh.

$M = 4000, L = 4, \Delta z_0 = 0.005, f = [4, -2], w_0 = 15, A_0 = 0.2.$

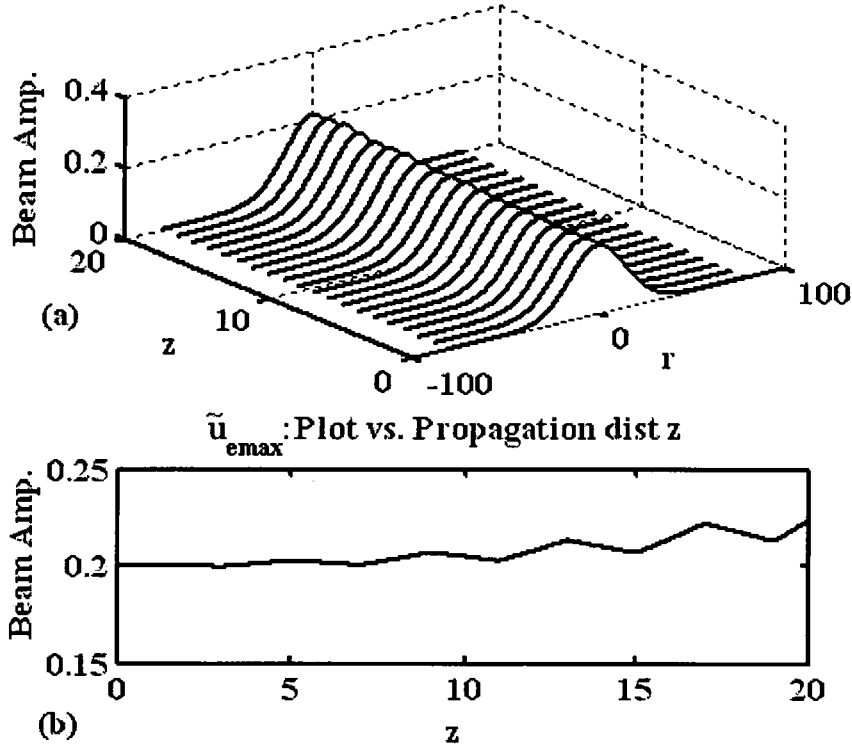


**Figure 7.19:** Stable 3-D soliton generation through the sign alternating dispersion when  $f = [-2, 4], \Delta z = 0.005, M = 4000, A_0 = 0.2, w_0 = 15, L = 4,$  using AFHSS with  $\tilde{S} = 2\pi R_1 R_2 = 2\pi \times 800$  (1600 radial samples). (6a) is pulse evolution. (6b) is on-axis amplitude.

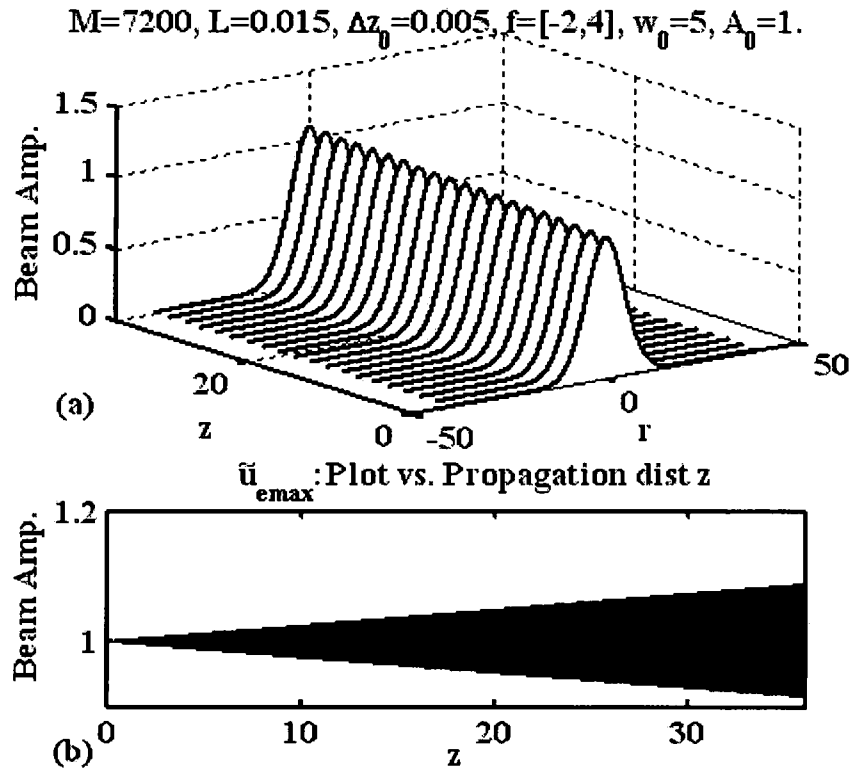


**Figure 7.20:** Stable 3-D soliton generation through the sign alternating dispersion when  $f = [-2, 4]$ ,  $\Delta z = 0.005$ ,  $M = 7200$ ,  $A_0 = 1$ ,  $w_0 = 5$ ,  $L = 0.015$ , using AFHSS with  $\tilde{S} = 2\pi R_1 R_2 = 2\pi \times 800$  (1600 radial samples). (7a) is pulse evolution. (7b) is on-axis amplitude.



$M=1200, L=0.01, \Delta z_0=0.005, f=[-4,2], w_0=5, A_0=2.$

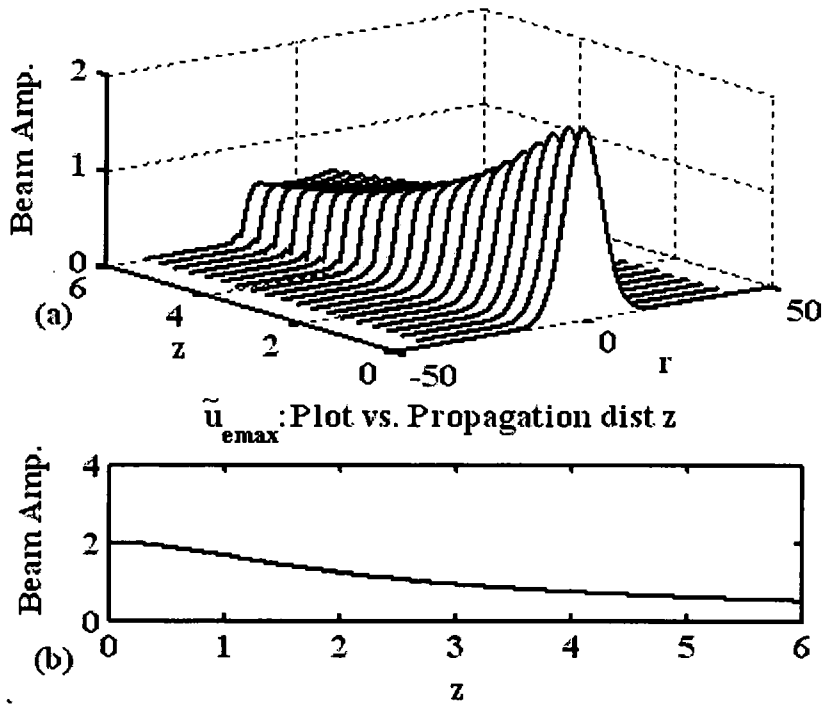


**Figure 7.21:** Decay of a 3-D optical pulse when  $f=[2,-4], \Delta z=0.005, M=1200, A_0=2, w_0=5, L=0.01$ , using AFHSS with  $\tilde{S}=2\pi R_1 R_2=2\pi \times 800$  (1600 radial samples). (8a) is pulse evolution. (8b) is on-axis amplitude.

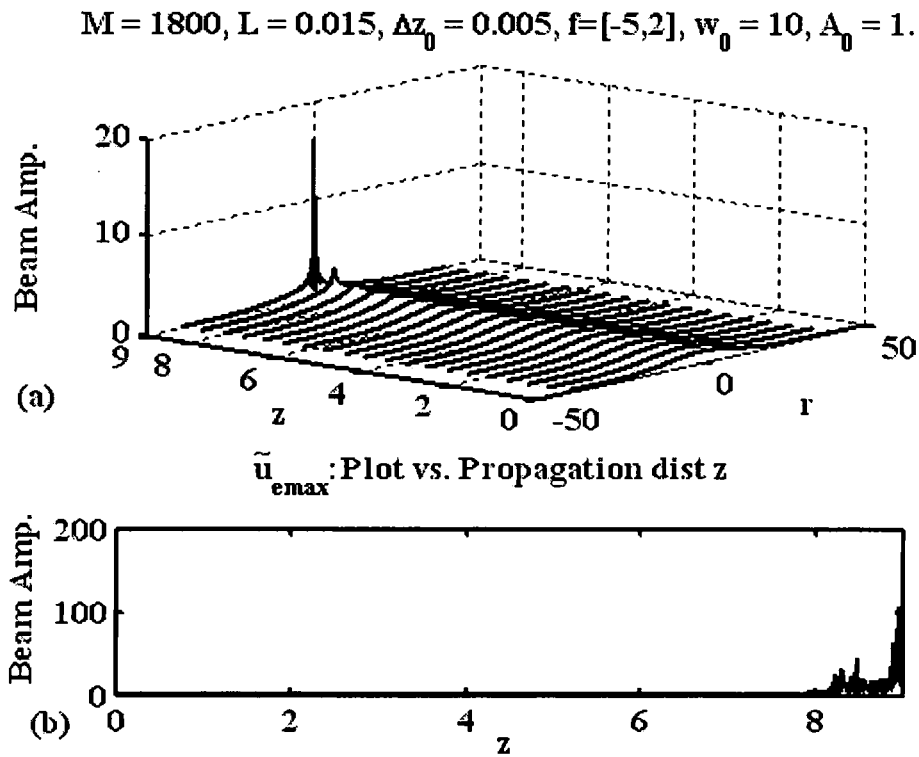


**Figure 7.22:** Collapse of a 3-D optical pulse when  $f = [2, -5], \Delta z = 0.005, M = 1800, A_0 = 1, w_0 = 10, L = 0.015$ , using AFHSS with  $\tilde{S} = 2\pi R_1 R_2 = 2\pi \times 800$  (1600 radial samples). (9a) is pulse evolution. (9b) is on-axis amplitude.

#### 7.4 Summary

In summary, we have outlined a fast and accurate method for tracking the amplitude of a pulse propagating in 1-dimensional dispersion modulated media by utilizing an adaptive wavelet transform. Also, we compared our results with traditional methods used to solve such type of equations. Moreover, relying on the semi-analytical study developed using the Lagrangian dynamics we were able to interpret the analytical results and whether they agree with the numerical simulation developed. Finally we shall mention that speed versus accuracy, is a common trade-off, and as such, a compromise is usually sought. Also, we have studied analytically, by using the variational approach, and

numerically by using a fast and accurate method, to track beams and spatiotemporal propagation of chirped  $(D+1)$ -dimensional optical pulses in bulk media with periodic dispersion.. These novel methods used are better and more accurate results than existing techniques. Based on results for the unsaturated constant dispersion coefficient case, we feel that the AFHSS is the more accurate and faster simulation method<sup>91,117</sup>.

In Chapters 8 we continue with other focusing arrest mechanism namely nonlinearity management which we study numerically using Fourier Bessel transform technique and analytically using the variational technique introduced in Chapters 4 and 5 respectively.

## CHAPTER 8

### NONLINEARITY MANAGEMENT IN 2 AND 3-D

In this Chapter we use the novel techniques devised previously in Chapters 4 and 5 to numerically and analytically solve and study transverse and pulsed optical beam or “light bullet” propagation in a layered alternating self-focusing and self-defocusing medium based on the scalar nonlinear Schrödinger (NLS) equation in two and three dimensions with cylindrical and spherical symmetry respectively. Using fast algorithms for Hankel transform along with adaptive longitudinal stepping and transverse grid management in a symmetrized split-step technique, it is possible to accurately study many nonlinear effects, including the possibility of spatiotemporal collapse, or the collapse-arresting mechanism due to sign alternating nonlinearity coefficient. Also, by using the variational approximation technique, we can prove that stable  $(D + 1)$ -dimensional soliton beams and optical bullets exist in these media.

#### 8.1 Introduction

Self-trapping of  $(D + 1)$  optical beams in a Kerr type nonlinear medium resulting in solitons have been studied extensively in the last decades<sup>18,19,51,108,131</sup>, and it has been shown experimentally and theoretically that a  $(1 + 1)$ -dimensional bright or dark soliton is stable in a Kerr type medium if the nonlinearity is self-focusing (SF) or self-defocusing (SDF) respectively. However, in  $(2 \text{ and } 3 + 1)$ -dimensions in Kerr type media, one cannot have stable solitons or optical bullets. So, if the medium is SDF we have a

spreading of the beam or the optical pulse and if it is SF the stationary beam solution, with a critical power as found in Fibich and Gaeta<sup>23</sup>, or the optical bullet created are unstable and will eventually collapse<sup>61</sup>. There exist a lot of attempts to stabilize the higher dimensional beam and optical bullet propagation through Kerr media by either considering the nonparaxial effect and/or the saturating nonlinearity<sup>58-60</sup>. Also, it has been shown<sup>66</sup> that a beam can be stabilized if the nonlinearity coefficient is weakly modulated along the propagation direction where the beam power oscillates about the modulated critical value. Moreover, a better stabilization occurs if a more radical modulation of the nonlinearity is done based on a periodically alternating SF and SDF layers or even a periodic SF layers with different values of the Kerr coefficient as shown in [67]. Note that in a periodic quadratically nonlinear medium with alternating signs of phase mismatch  $\Delta K$ , it has been shown that the effective cubic nonlinearity coefficient,  $\chi_{eff}^{(3)}(z) \propto (\chi^{(2)})^2 \left( \frac{1 - \exp(-j\Delta K z)}{\Delta K} \right)$ , will also carry the same periodicity with respect to its sign<sup>68</sup>.

Here we extend this model to apply it to optical bullets and also we introduce a novel numerical technique, which we call the adaptive fast Hankel split-step (AFHSS) method, to numerically solve the  $(D + 1)$ -dimensional NLS equation with alternating nonlinearity, which is classically used to model this phenomenon<sup>18,19,23,51,61,108,131</sup>.

The time-dependent  $(D+1)$ -dimensional ( $D=3$ ) paraxial wave equation, in the presence of group velocity dispersion is<sup>18,51,61</sup>:

$$j \frac{\partial u_e}{\partial Z'} + \frac{1}{2k_0} (\nabla_{\perp}^2 u_e) - \frac{k_2}{2} \frac{\partial^2 u_e}{\partial T'^2} + g(Z) |u_e|^2 u_e = 0, \quad (8.1)$$

where  $E$  is the slowly varying envelope of the optical field,  $t$  is the reduced time in a moving frame of reference,  $k_1$  is the group velocity,  $k_0 = \frac{n_0 \omega}{c}$  is the propagation constant,  $k_2$  is the group-velocity dispersion (GVD) parameter, and  $g = \frac{k_0}{n_0} n_2$  is the nonlinear parameter responsible for self-phase modulation (SPM) and is either piecewise continuous in layers of width  $L$  or harmonic function of period  $L$ . Note that  $k_2$  can be positive or negative depending on the nature of the dispersion in the medium, corresponding to normal dispersion (ND) and anomalous dispersion (AD) respectively.

Introducing the following normalization<sup>61</sup> for Eq. (8.1):  $z = \frac{Z'}{L_d}$ ,  $x = \frac{X'}{w_0}$ ,  $y = \frac{Y'}{w_0}$ ,

$\tau = \frac{T'}{(w_0^2 k_0 k_2)^{1/2}}$ ,  $\tilde{u}_e = (L_d)^{1/2} u_e$ ,  $L_d = k_0 w_0^2$ , we arrive at

$$j \frac{\partial \tilde{u}_e}{\partial z} + \frac{1}{2} \left( \nabla_{\perp}^2 \tilde{u}_e - s_d \frac{\partial^2 \tilde{u}_e}{\partial \tau^2} \right) + g(z) |\tilde{u}_e|^2 \tilde{u}_e = 0, \quad (8.2)$$

where  $s_d = \text{sgn}(k_2)$ ,  $w_0$  is the initial transverse spatial width,  $L_d$  is the diffraction length. If we use the spherical symmetry of the field distribution and introduce the radial variable  $r = (x^2 + y^2 + \tau^2)^{1/2}$ , Eq. (8.2) can be written as

$$j \frac{\partial \tilde{u}_e}{\partial z} + \frac{1}{2} \frac{1}{r^{D-1}} \frac{\partial}{\partial r} \left( r^{D-1} \frac{\partial \tilde{u}_e}{\partial r} \right) + g(z) |\tilde{u}_e|^2 \tilde{u}_e = 0, \quad (8.3)$$

where  $D$  can be 1, 2, 3, and  $s_d = -1$  which is the anomalous dispersion regime.

Assuming a Kerr type unsaturated medium we should note that if the beam or spatiotemporal pulse energy exceeds a certain critical value

$\mathcal{N} = \pi^{D/2} N_0 = 2^{D-1} \pi \int |\tilde{u}_e|^2 r^{D-1} dr = (2, 5.85, 28.87)$  for  $D = (1, 2, 3)$  respectively for an

unchirped Gaussian input, small fluctuations of the intensity, beam size or pulse width can grow with propagation and lead to a phenomenon known as beam or spatiotemporal collapse. In other words, the intensity becomes infinitely large at a finite distance as the size of the beam diminishes and tends to zero both in the spatial and temporal domains. There are few known integral invariants for Eq. (8.3) when  $g(z)=1$ ,  $D \geq 2$ . These invariants can be obtained either from the Noether's theorem, or from the symmetry of the NLS equation under gauge, space, and time transformations. Three of these invariants are the energy, Hamiltonian and the momentum, defined as<sup>61</sup>

$$\mathcal{N} = \int |\tilde{u}_e|^2 d^D r, \quad (8.4a)$$

$$\mathcal{H} = \int \left( |\nabla \tilde{u}_e|^2 - F(|\tilde{u}_e|^2) \right) d^D r, \quad (8.4b)$$

$$\mathcal{M} = -j \int \left( \tilde{u}_e^* \nabla \tilde{u}_e - \tilde{u}_e \nabla \tilde{u}_e^* \right) d^D r, \quad (8.4c)$$

where  $F(\tilde{u}_e) = \int_0^{\tilde{u}_e} \xi d\xi$ . Two techniques are traditionally used to study the spatiotemporal collapse. The first is the moment method technique based on the virial theorem and the second may be derived from a variational technique based on the Lagrangian density corresponding to Eq. (8.3). If we stick to the first technique here then the quantity of most interest to us is

$$\frac{d^2 \tilde{\sigma}^2(z)}{dz^2} = \frac{1}{\mathcal{N}} \left( 8\mathcal{H} + 4\mathcal{R} - \frac{4\mathcal{M}^2}{\mathcal{N}} \right), \quad (8.5)$$

due to its relation to the self-focusing effect, where  $\mathcal{R} = \left(1 - \frac{D}{2}\right) \int F(|\tilde{u}_e|^2) r^{D-1} dr < -\frac{\mathcal{N}^2}{2V_p}$

for unsaturated Kerr type media,  $\tilde{\sigma}^2(z) = \langle r^2 \rangle - \langle r \rangle^2$ ,  $\langle r^n \rangle = \frac{\int r^n |\tilde{u}_e|^2 r^{D-1} dr}{\mathcal{N}}$ . For

$D = (2, 3)$ , if the right hand side of Eq. (8.5) is negative or the initial energy exceeds a threshold,  $\mathcal{N}_c \approx 2\pi$ , or  $\mathcal{N}_c \approx \frac{3\pi\sqrt{2\pi}V_\rho w_0}{V_\rho + \pi\sqrt{2\pi}w_0^3}$  respectively, where  $V_\rho$  is a constant

representing the volume in which most of the pulse is located, then the variance  $\sigma^2(z)$  decreases monotonically along the propagation direction, becoming zero at a finite distance associated with the beam or spatiotemporal collapse, at a distance

$$z_c = \left( \frac{\mathcal{N}}{\mathcal{N}_c} - 1 \right)^{-1/2} w_0^3, \text{ and } z_c = w_0 \left( \frac{\mathcal{N}V_\rho}{\mathcal{N}^2 - 4V_\rho \mathcal{H}} \right)^{1/2} \text{ respectively. Zakharov et al}^{20}$$

predict similarity solutions of the form

$$\tilde{u}_e(r, z) \propto \frac{1}{(z_c - z)^s} Q\left(\frac{r}{(z_c - z)^s}\right), \quad (8.6)$$

where  $Q$  is an arbitrary function,  $z_c$  as defined above, and  $s_z = (2/3, 1/2)$  for  $D = (2, 3)$  respectively.

## 8.2 Variational Technique

In this Section we use the variational approach to describe the wave evolution based on the Lagrangian formalism of classical mechanics in terms of the Lagrangian density<sup>60,61,67,126</sup>

$$\mathcal{L} = \frac{j}{2} \left( \tilde{u}_e^* \frac{\partial \tilde{u}_e}{\partial z} - \tilde{u}_e \frac{\partial \tilde{u}_e^*}{\partial z} \right) r^{D-1} + \frac{1}{2} \left| \frac{\partial \tilde{u}_e}{\partial r} \right|^2 r^{D-1} - \frac{1}{2} r^{D-1} g(z) |\tilde{u}_e|^4, \quad (8.7)$$

where the  $(D+1)$  NLS equation can be derived from  $\mathcal{L}$  using the Euler-Lagrange equation

$$\frac{\partial}{\partial z} \frac{\partial \mathcal{L}}{\partial(\partial \tilde{u}_e / \partial z)} + \frac{\partial}{\partial r} \frac{\partial \mathcal{L}}{\partial(\partial \tilde{u}_e / \partial r)} - \frac{\partial \mathcal{L}}{\partial \tilde{u}_e} = 0. \quad (8.8)$$



Note that the application of Eq. (8.8) to the Lagrangian density in Eq. (8.7) generates the NLS equation given in Eq. (8.3). Following the Ritz optimization procedure let us assume the initial profile to be one of the following forms:

$$\tilde{u}_e = \tilde{u}_e(r, z) = A(z) \exp \left[ -\frac{r^2}{2w^2(z)} + jb(z)r^2 \right], \text{ or } \tilde{u}_e(r, z) = A(z) \operatorname{sech} \left[ \frac{r}{w(z)} \right] \exp[jb(z)r^2], \quad (8.9)$$

where  $A(z)$  is the amplitude,  $w(z)$  is the beam radius,  $b(z)$  is the wave front curvature, and are unknown functions of the propagation distance  $z$ . Following the method in Desaix et al <sup>126</sup>, we insert the trial functions from Eqs. (8.9a) and (8.9b) into the Lagrangian and upon integrating, we obtain the reduced Lagrangian:

$$\begin{aligned} \langle \mathcal{L} \rangle = \int_0^\infty \mathcal{L} dr = \frac{i}{2} \left( A \frac{dA^*}{dz} - A^* \frac{dA}{dz} \right) w^D \alpha_{D-1} + |A|^2 w^{D+2} \left( \frac{db}{dz} + 2b^2 \right) \alpha_{D+1} \\ + \frac{1}{2} |A|^2 w^{D-2} \gamma_{D-1} - \frac{1}{2} w^D \beta_{D-1} g(z) |A|^4, \end{aligned} \quad (8.10)$$

where  $\alpha$ ,  $\beta$ , and  $\gamma$  are given by

$$\alpha_D = \int_0^\infty r^D \exp(-r^2) dr, \beta_D = \int_0^\infty r^D \exp(-2r^2) dr, \gamma_{D-1} = \alpha_{D+1}, \quad (8.11)$$

for a Gaussian ansatz, and

$$\alpha_D = \int_0^\infty r^D \operatorname{sech}^2(r) dr, \beta_D = \int_0^\infty r^D \operatorname{sech}^4(r) dr, \gamma_D = \alpha_D - \beta_D, \quad (8.12)$$

for the hyperbolic secant function.

We can derive a set of evolution equations called Euler-Lagrange equations taking into account that the variation with respect to the unknowns in the initial profile should be

equal to zero, namely:  $\frac{\delta \langle \mathcal{L} \rangle}{\delta Q} = 0 \Rightarrow \frac{\partial \langle \mathcal{L} \rangle}{\partial Q} - \frac{d}{dz} \left( \frac{\partial \langle \mathcal{L} \rangle}{\partial Q'} \right) = 0$ , where  $Q = (A, w, b, A^*)$ . The

evolution equations obtained are given by:

$$|A|^2 w^D = A_0^2 w_0^D = N_0, \quad (8.13a)$$

$$b = \frac{1}{2w} \frac{dw}{dz}, \quad (8.13b)$$

$$\frac{d\hat{\phi}}{dz} = \left[ -\frac{\gamma_{D-1}}{\alpha_{D-1}} \frac{1}{w^2} + \left( 1 + \frac{d}{4} \right) \frac{\beta_{D-1}}{\alpha_{D-1}} |A|^2 \right], \quad (8.13c)$$

$$\frac{d^2 w}{dz^2} = \frac{\gamma_{D-1}}{\alpha_{D+1}} \frac{1}{w^3} - \frac{N_0 D \beta_{D-1}}{2 \alpha_{D+1}} \frac{g(z)}{w^{D+1}}, \quad (8.13d)$$

where  $A(z) = |A(z)| \exp[j\hat{\phi}(z)]$ ,  $N_0$  is the initial pulse energy defined above. In what follows, we consider the two and the three-dimensional cases respectively.

#### A- The Two-dimensional Case (D=2)

For this case Eq. (8.13d) becomes:

$$\frac{d^2 w}{dz^2} = \frac{\gamma_1}{\alpha_3} \frac{1}{w^3} - \frac{N_0 \beta_1}{\alpha_3} \frac{g(z)}{w^3} = \frac{\Gamma(z)}{4w^3}, \quad (8.14)$$

where  $\Gamma(z) = 4 \left[ \frac{\gamma_1 - N_0 \beta_1 g(z)}{\alpha_3} \right]$ . Integrating the above equation and assuming

$\Gamma(z) = \Gamma(z_0)$  we get  $\frac{1}{2} \left( \frac{dw}{dz} \right)^2 = -\frac{\Gamma(z_0)}{8w^2} + T_{eff}$ , where  $T_{eff} = \frac{\Gamma(z_0)}{8w^2}$  is the effective

potential of the evolution of the radius  $w$ , i.e.,  $\frac{d^2 w}{dz^2} = -\frac{\partial T_{eff}}{\partial w}$ , and  $T_{0eff} = \frac{\Gamma(z_0)}{8w_0^2} = \frac{\mathcal{H}}{8}$  is

the Hamiltonian of the system. If we consider the case when  $g(z) = g_0$ , a stationary

solution  $\left. \frac{\partial T_{eff}}{\partial w} \right|_{w=w_e} = 0$  of Eq. (8.13d) leads to an equilibrium radius:

$$w_{eN} = \frac{1}{|A|} \left( \frac{\gamma_1}{\beta_1 g_0} \right)^{1/2}. \text{ The stability of the equilibrium solution } w_0 = w_{eN} \text{ can be studied}$$

by the behavior of small amplitude fluctuations around the equilibrium point. Setting

$$w = w_{eN} + \delta w \text{ we get } \frac{d^2}{dz^2} \delta w + \zeta^2 \delta w = 0, \text{ where } \zeta^2 = \left. \frac{\partial^2 T_{eff}}{\partial w^2} \right|_{w=w_0} = \frac{3\Gamma}{4w_0^4} > 0. \text{ Thus when}$$

$g_0 < \frac{\gamma_1}{N_0 \beta_1}$ , the equilibrium solution is stable. This result can also be obtained if we

solve Eq. (8.13d) explicitly. The solution is  $w(z) = w_0 \left[ \frac{z^2 \gamma_1}{\alpha_3 w_0^4} \left( 1 - \frac{\beta_1 g_0 N_0}{\gamma_1} \right) + 1 \right]^{1/2}$ . This

solution is stable when  $g_0 < \frac{\gamma_1}{N_0 \beta_1}$ . Also in Ref. [67] when  $g(z)$  is a piecewise function,

alternating between  $g_+$  and  $g_-$  during the length  $L_+$  and  $L_-$  respectively, equilibrium

solutions exist when  $\bar{g} = \frac{L_+ g_+ + L_- g_-}{L_+ + L_-} > 0$ .

Next we study the stability of Eq. (8.13d) when  $g(z)$  is a harmonic varying function with a dc offset:,  $g(z) = g_0 + g_1 \sin \tilde{\Omega} z$ . Eq. (8.13d) becomes

$$\frac{d^2 w}{dz^2} = \frac{-\bar{\epsilon}_0 + \bar{\epsilon} \sin \tilde{\Omega} z}{w^3}, \quad (8.15)$$

where  $\bar{\epsilon}_0 = \frac{-\gamma_1 + N_0 \beta_1 g_0}{\alpha_3}$ ,  $\bar{\epsilon} = \frac{-N_0 \beta_1 g_1}{\alpha_3}$ . Also, if we make the assumption as in

Kelly<sup>16</sup> that the beam radius  $w$  can be divided into  $w(z) = \tilde{w} + \delta w$ , with  $|\delta w| \ll |\tilde{w}|$ , where

$\tilde{w}$  varies on a slow time scale, and  $\delta w$  is a rapidly varying function with a zero mean

value, then by means of Kapitsa averaging method we derive the following equations from Eq. (8.15)<sup>111</sup>:

$$\frac{d^2 \delta w}{dz^2} = \tilde{w} \bar{\epsilon} \sin \tilde{\Omega} z + 3 \tilde{w}^{-4} \bar{\epsilon}_0 \delta w, \quad (8.16a)$$

$$\frac{d^2 \tilde{w}}{dz^2} = -\tilde{w}^{-3} \bar{\epsilon}_0 - 6 \tilde{w}^{-5} \bar{\epsilon}_0 \langle \delta w^2 \rangle - 3 \tilde{w}^{-4} \bar{\epsilon} \langle \delta w \sin \tilde{\Omega} z \rangle, \quad (8.16b)$$

where  $\langle \bullet \rangle$  is the average over the period  $2\pi / \tilde{\Omega}$ . A particular solution for Eq. (8.16a) is

$$\delta w(z) = \frac{-\bar{\epsilon} \sin \tilde{\Omega} z}{\tilde{w}^3 (\tilde{\Omega}^2 + 3 \tilde{w}^{-4} \bar{\epsilon}_0)}, \quad (8.17)$$

and if we substitute Eq. (8.17) into Eq. (8.16b), we obtain the evolution equation of  $\tilde{w}$ ,

$$\frac{d^2 \tilde{w}}{dz^2} = \tilde{w}^{-3} \left[ -\bar{\epsilon}_0 - \frac{3 \bar{\epsilon}_0 \bar{\epsilon}^2}{(\tilde{\Omega}^2 \tilde{w}^4 + 3 \bar{\epsilon}_0)^2} + \frac{3}{2} \frac{\bar{\epsilon}^2}{(\tilde{\Omega}^2 \tilde{w}^4 + 3 \bar{\epsilon}_0)} \right]. \quad (8.18)$$

Eq. (8.18) will have a stable, fixed point solution given by,

$$\tilde{w}^4 = \frac{1}{\tilde{\Omega}^2} \left[ \frac{3}{4} \frac{\bar{\epsilon}^2}{\bar{\epsilon}_0^2} \left( 1 + \sqrt{1 - \frac{16}{3} \frac{\bar{\epsilon}^2}{\bar{\epsilon}_0^2}} \right) - 3 \bar{\epsilon}_0 \right]. \quad (8.19)$$

Eq. (8.19) has a real value for the average width  $\tilde{w}$  when  $\bar{\epsilon} > \sqrt{6} \bar{\epsilon}_0$ . So for  $g_1 < 0$ , we

must have  $g_1 < \sqrt{6} \left( \frac{\gamma_1}{N_0 \beta_1} - g_0 \right)$ , which agrees with the results obtained in<sup>111</sup>.

## B- The Three-dimensional Case (D=3)

For this case Eq. (8.13d) becomes

$$\frac{d^2 w}{dz^2} = -\frac{\partial T}{\partial w} = \frac{\gamma_2}{\alpha_4} \frac{1}{w^3} - \frac{3 N_0 \beta_2}{2 \alpha_4} \frac{g(z)}{w^4}. \quad (8.20)$$

Integrating the above equation once we get  $\frac{1}{2}\left(\frac{dw}{dz}\right)^2 = -T_{eff} + T_{0eff}$ , where

$T_{eff} = \frac{\tilde{\mu}}{w^2} + \frac{v_z}{w^3}$ , is the effective potential of the evolution of the radius  $w$ ,

$\tilde{\mu} = \frac{\gamma_2}{2\alpha_4}$ ,  $v_z = -\frac{N_0\beta_2 g(z)}{2\alpha_4}$ , and  $T_{0eff} = \frac{\tilde{\mu}}{w_0^2} + \frac{v_z}{w_0^3}$ , is the Hamiltonian of the system. If

we consider the case where  $g(z) = g_0$ , a stationary solution  $\left.\frac{\partial T_{eff}}{\partial w}\right|_{w=w_e} = 0$  of Eq. (8.13d)

leads to an equilibrium radius:  $w_e = \frac{1}{|A|}\left(\frac{2\gamma_2}{3\beta_2 g_0}\right)^{1/2}$ . The stability of the equilibrium

solution  $w_0 = w_e$  can be studied by the behavior of small amplitude fluctuations around

the equilibrium point ( $w = w_e + \delta w$ ), which leads to  $\frac{d^2}{dz^2}\delta w + \hat{\zeta}^2\delta w = 0$ , where

$\hat{\zeta}^2 = \left.\frac{\partial^2 T_{eff}}{\partial w^2}\right|_{w=w_0} = \frac{6\tilde{\mu}}{w^4} + \frac{12v_z}{w^5} > 0$ . So when  $g_0 < \frac{w_0\gamma_2}{2N_0\beta_2}$ , the equilibrium solution is

stable.

Next we study the stability of Eq. (8.13d) when  $g(z)$  is a harmonic varying function with a dc offset:  $g(z) = g_0 + g_1 \sin \tilde{\Omega}z$ . Eq. (8.13d) becomes

$$\frac{d^2 w}{dz^2} = \frac{\tilde{\eta}}{w^3} + \frac{-\hat{\epsilon}_0 + \hat{\epsilon} \sin \Omega z}{w^4}, \quad (8.21)$$

where  $\hat{\epsilon}_0 = \frac{3N_0\beta_2 g_0}{2\alpha_4}$ ,  $\hat{\epsilon} = \frac{-3N_0\beta_2 g_1}{2\alpha_4}$ , and  $\tilde{\eta} = \frac{\gamma_2}{\alpha_4}$ . Following the same procedure as

performed for the two-dimensional case, we get

$$\frac{d^2 \delta w}{dz^2} = (4\hat{\epsilon}_0 \tilde{w}^{-1} - 3\tilde{\eta}) \tilde{w}^{-4} \delta w + \tilde{w}^{-4} \hat{\epsilon} \sin \tilde{\Omega} z, \quad (8.22a)$$

$$\begin{aligned} \frac{d^2 \tilde{w}}{dz^2} = & \tilde{\eta} \tilde{w}^{-3} - \hat{\epsilon}_0 \tilde{w}^{-4} + (6\tilde{\eta} \tilde{w}^{-5} - 10\hat{\epsilon}_0 \tilde{w}) \langle \delta w^2 \rangle \\ & - 4\hat{\epsilon} \tilde{w}^{-5} \langle \delta w \sin \tilde{\Omega} z \rangle. \end{aligned} \quad (8.22b)$$

A particular solution for Eq. (8.22a) is

$$\delta w(z) = \frac{-\tilde{w} \hat{\epsilon} \sin \tilde{\Omega} z}{\tilde{w}^5 \tilde{\Omega}^2 - 3\tilde{\eta} \tilde{w} + 4\hat{\epsilon}_0}. \quad (8.23)$$

Also, if we substitute Eq. (8.23) into Eq. (8.22b), we obtain the evolution equation of  $\tilde{w}$ ,

$$\begin{aligned} \frac{d^2 \tilde{w}}{dz^2} = & \tilde{\eta} \tilde{w}^{-3} - \hat{\epsilon}_0 \tilde{w}^{-4} + \frac{2\hat{\epsilon}^2 \tilde{w}^{-4}}{\tilde{w}^5 \tilde{\Omega}^2 - 3\tilde{\eta} \tilde{w} + 4\hat{\epsilon}_0} \\ & + \frac{\tilde{w}^{-4} \hat{\epsilon}^2 (3\tilde{\eta} \tilde{w} - 5\hat{\epsilon}_0)}{(\tilde{w}^5 \tilde{\Omega}^2 - 3\tilde{\eta} \tilde{w} + 4\hat{\epsilon}_0)^2}. \end{aligned} \quad (8.24)$$

Eq. (8.24) can be written in steady state as

$$\begin{aligned} & \tilde{\eta} \tilde{\Omega}^4 \tilde{w}^{11} - \tilde{\Omega}^4 \hat{\epsilon}_0 \tilde{w}^{10} + 6\tilde{\eta}^2 \tilde{\Omega}^2 \tilde{w}^7 - 14\tilde{\eta} \tilde{\Omega}^2 \hat{\epsilon}_0 \tilde{w}^6 \\ & + 2\tilde{\Omega}^2 \tilde{w}^5 (4\hat{\epsilon}_0^2 + \hat{\epsilon}^2) + 9\tilde{\eta}^3 \tilde{w}^3 - 33\tilde{\eta} \hat{\epsilon}_0 \tilde{w}^2 \\ & + \tilde{\eta} (40\hat{\epsilon}_0^2 - 3\hat{\epsilon}^2) \tilde{w} + 3\hat{\epsilon}_0 \hat{\epsilon}^2 - 16\hat{\epsilon}_0^3 = 0. \end{aligned} \quad (8.25)$$

Eq. (8.25) is solved for the initial conditions  $\Delta z = 0.01$ ,  $A_0 = 0.18$ ,  $w_0 = 10$ ,  $g_0 = 1$ ,  $g_1 = -4$ ,  $L_+ = L_- = 0.2$  as shown in Section 8.4 below, where one of the steady state real positive roots for the average pulse width  $\tilde{w} \approx 10$  which agrees with the initial condition  $w_0 = 10$ , assumed. Also note that the above equation with the same initial conditions but

with the exception of  $\varepsilon_0 < 0$  this time admits no physical solution, which is in agreement with<sup>111</sup>.

### 8.3 Adaptive Fast Hankel Split Step Method

The AFHSS algorithm in Figure 8.1 resembles the symmetrized Fourier split-step technique<sup>59,90</sup>, where we change the longitudinal propagation stepping size  $\Delta z \propto A(z_1)^{-1/s} - A(z_2)^{-1/s} \approx A(z_1)^{-1/s}$  when  $A(z_2) \gg A(z_1)$ , adaptively using Zakharov *et al*<sup>20</sup> similarity formula defined in Eq.(8.6), and the grid spatial range  $\Delta r_{\max} \propto A(z)^{1-D}$  as indicated in<sup>2</sup> in order to track the varying amplitude of the D-dimensional pulse in the medium. We note that periodic focusing/defocusing or beam trapping occurs when we have a sign-alternating Kerr nonlinearity medium and under the conditions stated above.

### 8.4 Numerical Results

We now show sample simulation results using the AFHSS method that uses Guizar-Sicairos *et al*'s Hankel transform technique<sup>95</sup>. All the input functions are of the type mentioned in Eqs. (8.9a) and (8.9b). Figure 8.2 shows the case when  $D=2$  with the parameters  $\Delta z = 0.01, A_0 = 0.2, w_0 = 10, g_0 = 0.5, g_1 = -1.5, L_+ = L_- = 0.1$ , which according to the analytical study above leads to a stable soliton. Similarly Figure 8.3 with the parameters  $\Delta z = 0.01, A_0 = 2.1, w_0 = 1, g_0 = 1, g_1 = -2, L_+ = L_- = 0.01$ . Notice that in these cases the beam focuses and defocuses periodically. Figure 8.4 with  $\Delta z = 0.01, A_0 = 1, w_0 = 1, g_0 = 1.7, g_1 = -2.7, L_+ = L_- = 0.4$  shows the  $D=2$  case when there is decay. Figure 8.5 with  $\Delta z = 0.01, A_0 = 3, w_0 = 1, g_0 = 1.5, g_1 = -0.5, L_+ = L_- = 0.1$ , shows the  $D=2$  case when the optical pulse still self focuses.

Figure 8.6 shows the variation of the main beam ( $D=2$ ) period  $\Lambda_z$  with respect to the nonlinearity map period  $L = [0.02, 0.04, 0.08, 0.16, 0.32]$ , with the initial widths  $w_0 = [1, 1.5, 2, 2.5]$  as a parameter, but keeping the same initial beam power  $N_0 = 2.1^2$ . The chosen parameters satisfy the stability criteria for  $D=2$  solitons. Superposed on the data are empirical fits of the form  $\Lambda_z = \hat{c}_1 + \hat{c}_2 L^\zeta$  obtained through fitting the first, third and fifth points for each  $w_0$ , and suggests that both sublinear as well as superlinear variations are possible. We speculate that there may exist a value of  $w_0$  for a given  $N_0$  where the variation of the soliton period is linear *w.r.t.* the period of the nonlinearity map. Note that the study of the variation of the main soliton period with respect to the nonlinearity map was made feasible due to the fast algorithm developed, since data collection with traditional techniques takes time because every point in the figure is the result of a complete simulation runtime. More on computation times appears later on in the paper. Figure 8.7 shows the case when  $D=3$  with the following parameters:  $\Delta z = 0.01$ ,  $A_0 = 0.18$ ,  $w_0 = 10$ ,  $g_0 = 1$ ,  $g_1 = -4$ ,  $L_+ = L_- = 0.2$ , which according to the analytical study above leads to a stable soliton, but for  $\approx 40$  diffraction lengths we see a 10% focusing in the numerical solution. Figure 8.8 with  $\Delta z = 0.01$ ,  $A_0 = 0.5$ ,  $w_0 = 5$ ,  $g_0 = 1$ ,  $g_1 = -1$ ,  $L_+ = L_- = 0.2$ , shows the  $D=3$  case when the optical pulse self focuses. Figure 8.9 shows the decay case when  $\Delta z = 0.01$ ,  $A_0 = 1$ ,  $w_0 = 10$ ,  $g_0 = -1$ ,  $g_1 = -4$ ,  $L_+ = L_- = 0.2$ . Note that as a general observation for numerical stability it is preferable that the width or eventually the energy of the pulse and the frequency of the alternating nonlinearity is large enough. Finally, we compare computation speeds of the AFHSS and regular (2 and 3)-D FFT. The number of



computations in (2 and 3)-D FFT is  $\propto 2M^2 \log_2 M$  and  $M^3 \log_2 M$  respectively. On the other hand we can make the number of computations of Guizar-Sicairos et al's method comparable to Siegman's method<sup>91</sup> namely equal to  $4M \log_2 2M + 2M$  by a priori computing and storing the zeros of the cylindrical or spherical Bessel function. The advantages of Guizar-Sicairos et al's method over Siegman's are the accuracy for the sampled points and a simple retrieval expression. For more comparison between Guizar-Sicairos et al's and Siegman's method, we refer readers to Table 1 in Yu et al.<sup>94</sup>. Also, we note that the use of the adaptive variation of the longitudinal propagation stepping size  $\Delta z$  and the transverse spatial sampling size  $\Delta r_{max}$  according to  $\Delta z \propto A^{-1/s}$  and  $A^{1-D}$  respectively, allow us to track on-axis amplitudes, for the paraxial unsaturated constant nonlinearity case, more precisely than regular (2 and 3)-D FFT methods. Without the adaptive variation in the case of unsaturated constant nonlinearity media, the numerical methods become unstable, and we witness oscillatory focusing and defocusing of the beam from numerical instability. Typical run times are around 1 minute for AFHSS when  $\tilde{S} = 2\pi R_1 R_2 = 800\pi$ , 10 minutes and 1 hour for (2 and 3)-D FFT when the mesh size is  $M^2 = (2^{10})^2$  and  $M^3 = (2^{10})^3$  respectively.

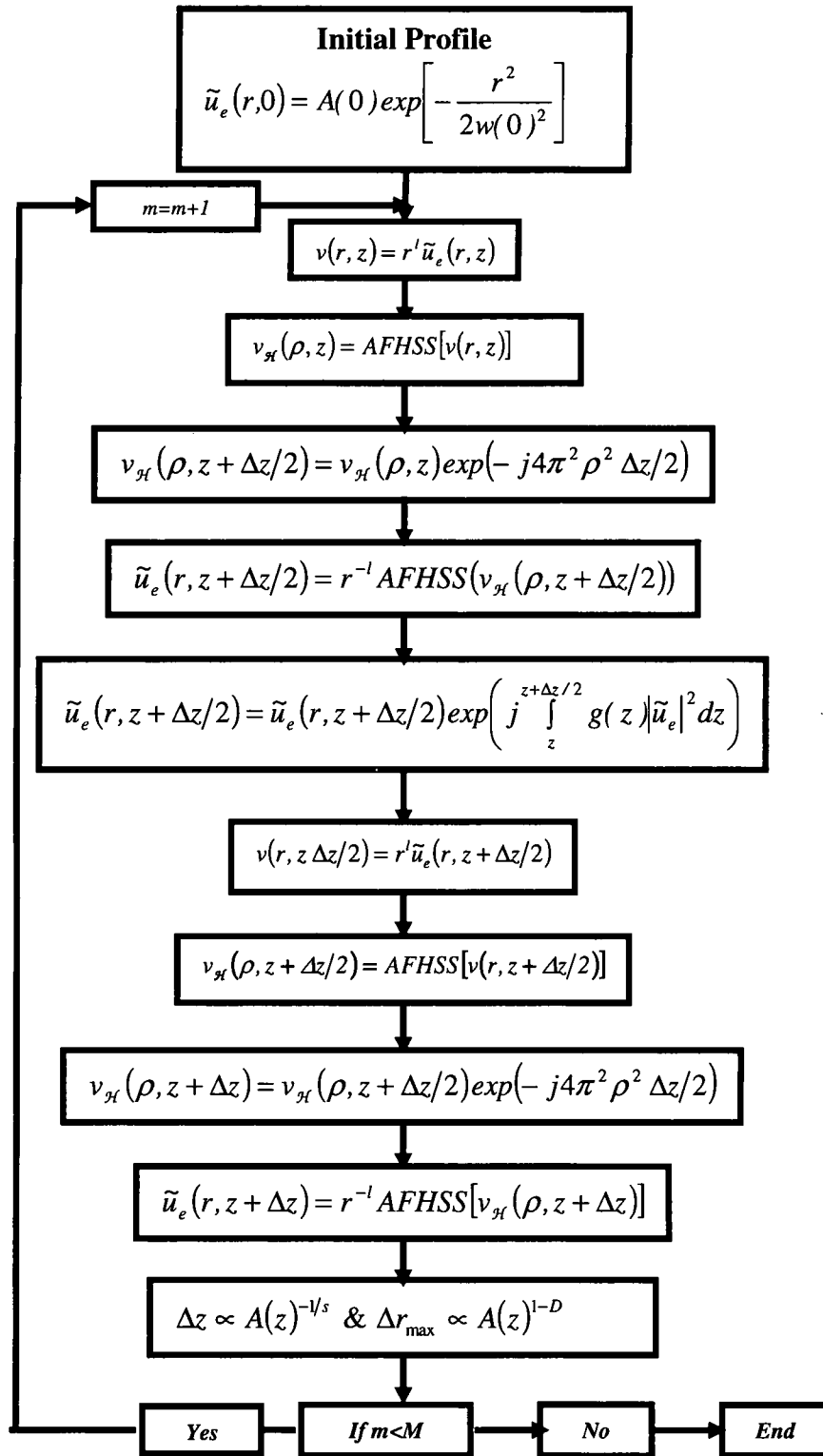


**Figure 8.1:** The AFHSS algorithm, a symmetrized version of the split step FFT using cylindrical or spherical Fourier Bessel transform instead, and using adaptive longitudinal stepping and transverse grid management.

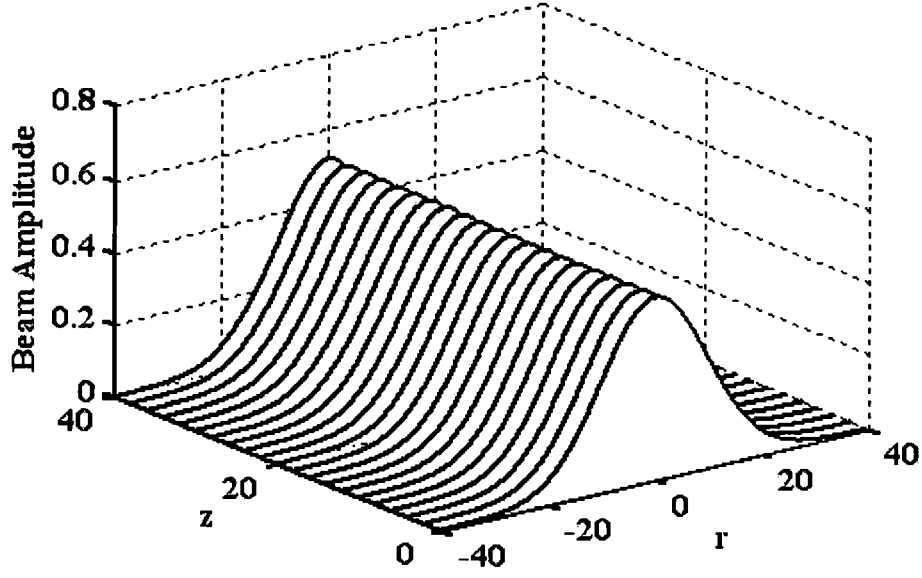


**Figure 8.2:** Stable 2-D soliton generation through the sign Alternating nonlinearity when  $\Delta z = 0.01$ ,  $A_0 = 0.2$ ,  $w_0 = 10$ ,  $g_0 = 0.5$ ,  $g_1 = -1.5$ ,  $L_+ = L_- = 0.1$ , using AFHSS with  $\tilde{S} = 2\pi R_1 R_2 = 2\pi \times 800$  (1600 cylindrical samples).

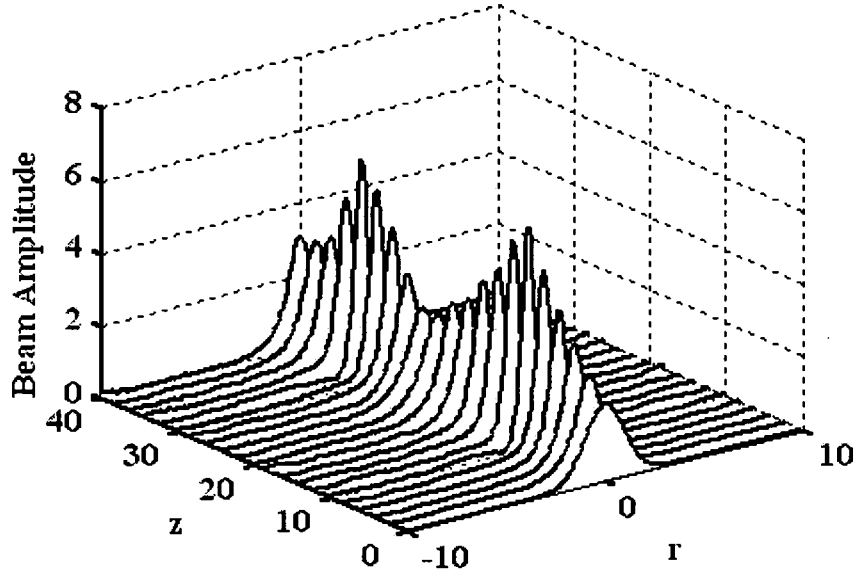


**Figure 8.3:** Stable 2-D soliton generation through the sign Alternating nonlinearity when  $\Delta z = 0.01$ ,  $A_0 = 2.1$ ,  $w_0 = 1$ ,  $g_0 = 1$ ,  $g_1 = -2$ ,  $L_+ = L_- = 0.01$ , using AFHSS with  $\tilde{S} = 2\pi R_1 R_2 = 2\pi \times 800$  (1600 cylindrical samples).

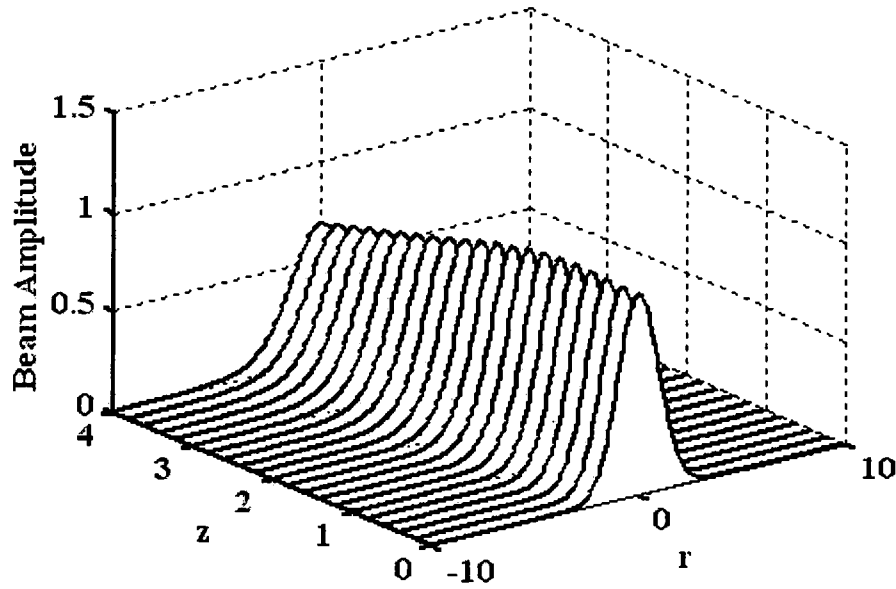


**Figure 8.4:** Decay of 2-D beams when  $\Delta z = 0.01$ ,  $A_0 = 1$ ,  $w_0 = 1$ ,  $g_0 = 1.7$ ,  $g_1 = -2.7$ ,  $L_+ = L_- = 0.4$ , using AFHSS with  $\tilde{S} = 2\pi R_1 R_2 = 2\pi \times 800$  (1600 cylindrical samples).

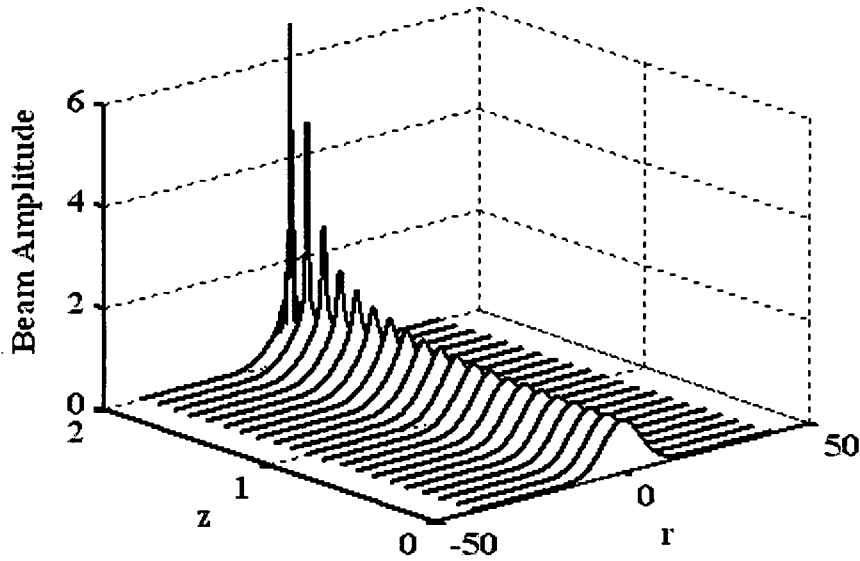


**Figure 8.5:** Self-focusing of a 2-D optical pulse when  $\Delta z = 0.01$ ,  $A_0 = 3$ ,  $w_0 = 1$ ,  $g_0 = 1.5$ ,  $g_1 = -0.5$ ,  $L_+ = L_- = 0.1$ , using AFHSS with  $\tilde{S} = 2\pi R_1 R_2 = 2\pi \times 800$  (1600 radial samples).

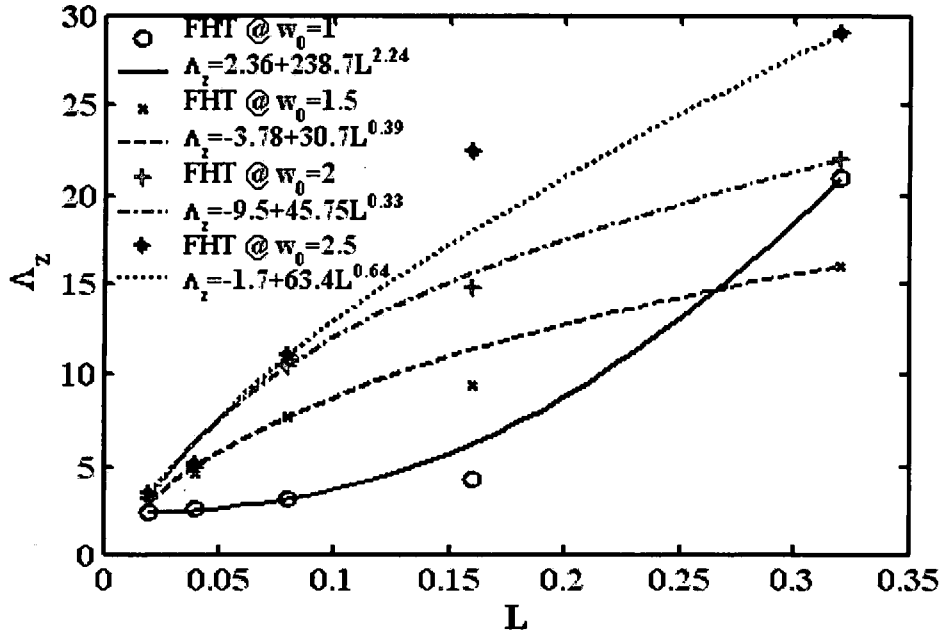


**Figure 8.6:** The variation of the main beam ( $D=2$ ) period  $\Delta_z$  with respect to the nonlinearity map period  $L = [0.02, 0.04, 0.08, 0.16, 0.32]$ , for different initial width ranging from  $w_0 = [1, 1.5, 2, 2.5]$  keeping the same initial beam power  $N_0$ . Superposed on the data are empirical fits of the form  $\Delta_z = c_1 + c_2 L^S$  obtained through fitting the first, third and fifth points for each  $w_0$ .

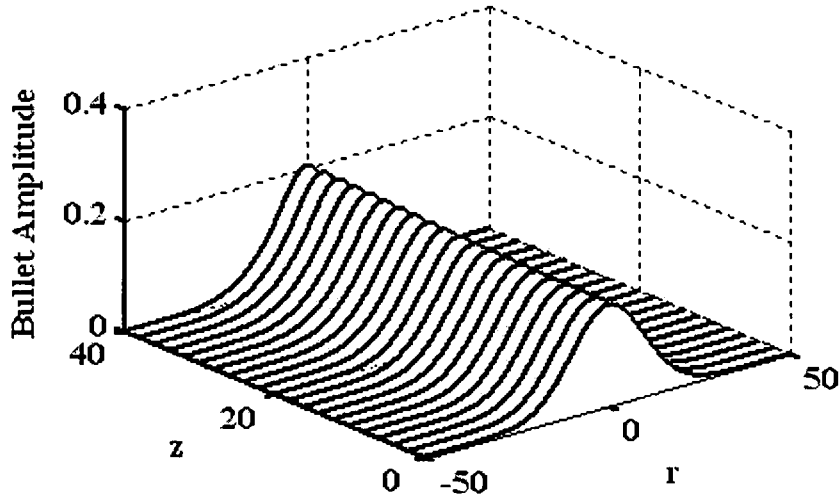


**Figure 8.7:** Stable 3-D soliton generation through the sign Alternating nonlinearity when  $\Delta z = 0.01$ ,  $A_0 = 0.18$ ,  $w_0 = 10$ ,  $g_0 = 1$ ,  $g_1 = -4$ ,  $L_+ = L_- = 0.2$ , using AFHSS with  $\tilde{S} = 2\pi R_1 R_2 = 2\pi \times 800$  (1600 radial samples).

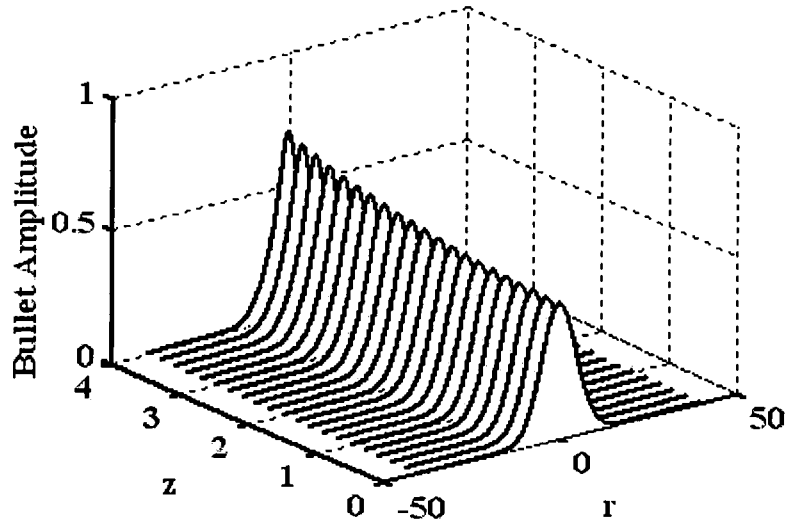


**Figure 8.8:** Self-focusing of a 3-D optical pulse when  $\Delta z = 0.01$ ,  $A_0 = 0.5$ ,  $w_0 = 5$ ,  $g_0 = 1$ ,  $g_1 = -1$ ,  $L_+ = L_- = 0.2$ , using AFHSS with  $\tilde{S} = 2\pi R_1 R_2 = 2\pi \times 800$  (1600 radial samples).

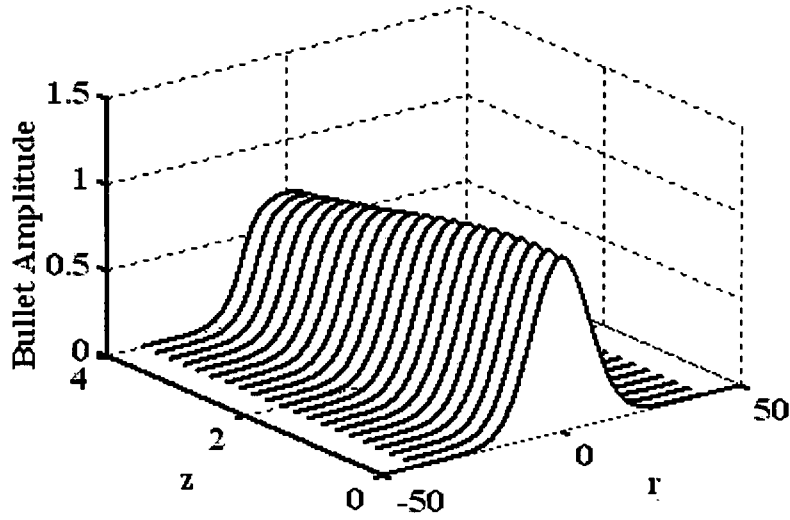


**Figure 8.9:** Decay of a 3-D optical pulse when  $\Delta z = 0.01$ ,  $A_0 = 1$ ,  $w_0 = 10$ ,  $g_0 = -1$ ,  $g_1 = -4$ ,  $L_+ = L_- = 0.2$ , using AFHSS with  $\tilde{S} = 2\pi R_1 R_2 = 2\pi \times 800$  (1600 radial samples).

## 8.5 Summary

In summary, we have outlined a fast and accurate method for tracking beams and spatiotemporal pulse propagation in a sign-alternating Kerr nonlinearity medium in which the beam or spatiotemporal collapse is expected for the paraxial unsaturated medium approximation, and to cyclic focusing and defocusing in the sign-alternating nonlinearity case. These novel methods developed in previous Chapters are useful in order to obtain better and more accurate results than existing techniques. Based on results for the unsaturated constant nonlinearity coefficient case, we feel that the AFHSS is the more accurate and faster simulation method<sup>91,117</sup>. We have also postulated variation of the soliton period as a function of the nonlinearity period for the  $D=2$  case.

In the next Chapter we summarize what we did in this work and give some suggestions for future work.

## **CHAPTER 9**

### **CONCLUSION AND FUTURE WORK**

#### **9.1 Conclusions**

As mentioned in Chapter 1, the purpose of this work is to develop and compare between existing numerical techniques for different evolution equations which exhibit singularity, or has been traditionally difficult to tackle with conventional techniques and developing an analytical technique to study the pulse dynamics and stability of the solitons. The two techniques namely, the Hankel transform or pseudo-spectral technique, and the Galerkin Wavelet technique and their variations, using temporal, spatial and level adaptation, are discussed in conjunction with the pulse and/or beam propagation in nonlinear dispersive or diffractive media, and their underlying physical phenomena.

In this work we have managed to:

- Generate dispersion /nonlinearly managed optical solitons in optical communication.
- Study high speed comm. and inter pulse effects reduction due to zero dispersion limit.
- Minimize DM pulse radiation reduction due to amplitude compensating fiber loss.
- Reduce Modulation instability in bandwidth and in gain.
- Jitter reduction due to collisions between signals in different channels (WDMS).



- Study the stabilization of the Bose-Einstein condensate in  $(D+1)$ -dimensional optical lattice.
- Provide stabilizing pulse propagation for very long distances and many other effects.
- Study stability using Variational technique which was developed for:
  - A- Dispersion management.
  - B- Nonlinearity management .
  - C- Saturating nonlinearity.
- Develop two new numerical technique based on Fourier Bessel split-step and wavelet methods to:
  - A- Track more accurately pulses, beams and spatiotemporal pulses where collapse is expected.
  - B- Obtain faster results than existing techniques.
  - C- Use adaptability and scalability to solve various number and forms of equations.

## 9.2 Future Work

What we are planning to do next, is to apply these methods (whenever it is possible) to different problems as outlined in Table 9.1.

**Table 9.1:** Plan for future work.

TASK	Timeline [0 – 1]									
	0.1	0.2	0.3	0.4	0.5	0.6	0.7	0.8	0.9	1
1. Nonlinear X-waves.										
2. Stable Vortex solitons by competing quadratic-cubic or cubic-quintic nonlinearities.										
3. Dynamics of coupled solitons.										
4. Stable 3-D optical solitons in 2-D photonic lattice.										
5. Stable spinning optical solitons in 3-D.										

## REFERENCES

1. A. Korpel and P. Banerjee, "A heuristic guide to nonlinear dispersive wave equations and soliton-type solutions," *Proc. of the IEEE*, **72**, No. 9, pp. 1109-1130 (1984).
2. G. Fibich and B. Ilan, "Discretization effects in the nonlinear Schrödinger equation," *App. Num. Math.*, **44**, pp. 63-75 (2003).
3. T. Taha and M. Ablowitz, "Analytical and numerical aspects of certain nonlinear evolution equations: II, Numerical nonlinear Schrödinger equation," *J. of Comp. Phys*, **55**, pp. 203-230 (1984).
4. P. Sulem, C. Sulem, and A. Patera, "Numerical simulation of singular solutions to the 2-dimensional cubic Schrödinger equation," *Comm. on Pure and App. Math.*, **37**, pp. 755-78 (1984).
5. G. Akrivis, V. Dougalis, O. Karakashian, and W. McKinney, "Galerkin finite element methods for the nonlinear Schrödinger equation," *Adv. in Comp. Math. and its Appl.*, World Scientific, Singapore, pp. 85-106 (1993).
6. C. Canuto, Y. Hussaini, A. Quarteroni, and T. Zang, *Spectral Methods in Fluid Dynamics*. Springer-Verlag, New York, NY (1988).
7. M. Stedham and P. P. Banerjee, "Detailed resolution of the nonlinear Schrödinger equation using the full adaptive wavelet transform," *SPIE Proc.*, **4056**, pp. 24-28 (2000).
8. G. Nehmetallah and P.P. Banerjee, "Analysis of Nonlinear Dispersive Optical Propagation Using Adaptive Wavelet Transform," Great Lakes Photonics Symposium, June 7-11 (2004).
9. I. Daubechies, "Orthonormal bases of compactly supported wavelets," *Comm. on Pure and App. Math.*, **41**, pp. 909-996 (1988).
10. I. Daubechies, *Ten Lectures on Wavelets*. CBMS\_NSF Regional Conference Series in Applied Mathematics, SIAM, Philadelphia, PA (1992).
11. A. Cohen, I. Daubechies, and J. Feauveau, "Biorthogonal basis of compactly supported wavelets," *Comm. on Pure and App. Math.*, **45**, pp. 485-560 (1992).
12. G. Beylkin, R. Coifman, and V. Rokhlin, "Fast wavelet transform and numerical algorithms I," *Comm. on Pure and App. Math.*, **44**, pp. 141-183 (1991).
13. S. Mallat, "Multiresolution approximation and wavelets," *Trans. of Am. Math. Soc.*, **315**, pp. 69-87 (1989).

14. J. de Oliveira, M. de Moura, J. Hickmann, and A. Gomes, "Self-steepening of optical pulses in dispersive media," *JOSA B*, **9**, pp. 2025-2027 (1992).
15. C. Zaspel, "Optical solitary wave and shock solutions of the higher order nonlinear Schrödinger equation," *Phy. Rev. Lett.*, **82**, pp. 723-726 (1999).
16. P. Kelly, "Self-focusing of optical beams," *Phys. Rev. Lett.*, **15**, pp. 1005-1008 (1965).
17. D. McLaughlin, "Focusing singularity of the cubic Schrödinger equation," *Phys. Rev. A*, **34**, No. 2, pp. 1200-1210, 1986.
18. R. Chiao, E. Garmire, and C. Townes, "Self-trapping of optical beams," *Phys. Rev. Lett.*, **13**, 479-482 (1964).
19. V. E. Zakharov and D. Shabat, "Exact theory of two-dimensional self-focusing and one-dimensional self-modulation of waves in nonlinear media," *Sov. Phys. JETP*, **34**, 62-69 (1972).
20. V. Zakharov, V. Sobolev, and V. Synakh, "Character of singularity and stochastic phenomena in self-focusing," *ZhETF Pis. Red.*, **14**, No. 10, 564-568 (1971).
21. R. Glassy, "On the blowing up of solutions to the Cauchy problem for nonlinear Schrödinger equations," *J. of Math. Phys.*, **18**, No. 9, 1794-1797, (1977).
22. G. Fibich and G. Papanicolaou, "Self-focusing in the perturbed and unperturbed nonlinear Schrödinger equation in critical dimension," *SIAM J. of App. Math.*, **60**, 183-240 (1999).
23. G. Fibich and A. Gaeta, "Critical power for self-focusing in bulk optical media and in hollow waveguides," *Opt. Lett.*, **25**, No. 5, 335-337 (2000).
24. P. P. Banerjee, G. Nehmetallah, and M. Chatterjee, "Numerical Modeling of Cylindrically Symmetric Nonlinear Self-focusing Using an Adaptive Fast Hankel Split-step Method," *Opt. Comm.* **249**, 293-300 (2005).
25. G. Nehmetallah, and P. P. Banerjee, "Stabilization of a (D+1)-dimensional Dispersion Managed Solitons in Kerr Media by an Alternating Dispersion Structure," *JOSA B*, **23**, 2, 203-211 (2006).
26. G. Nehmetallah, and P. P. Banerjee, "Numerical Modeling of (D+1)-dimensional Solitons in a Sign Alternating Nonlinear Medium Using an Adaptive Fast Hankel Split Step Method," *JOSA B* **22**, 10, 2200-2207 (2005).

27. G. Nehmetallah, and P. P. Banerjee, "Numerical Modeling of Spatiotemporal Solitons Using an Adaptive Spherical Fourier Bessel Split Step Method," *Opt. Comm.* 257, 197-205 (2006).
28. G. Nehmetallah, P.P. Banerjee, "Analysis of Spatial and Spatio-temporal Soliton Propagation Using a Fast Adaptive Fourier-Bessel Transform Technique," *Proc. Int. Conf. on Opt. and Optoelectronics, India, IT-NLO 1, Dec. (2005).*
29. G. Nehmetallah and P.P. Banerjee, "An Adaptive Spherical Fourier Bessel Split-step Method for Tracking Optical Bullets," *Proc. SPIE Int. Soc. Opt. Eng.* 5892 (2005).
30. J. Cooley and J. Tukey, "An algorithm for the machine calculation of complex Fourier series," *Math. Comp.*, **19**, 297-301 (1965).
31. I. Sneddon, *The Use of Integral Transform*, McGraw-Hill, New York, NY (1972).
32. L. Andrews and B. Shivamoggi, *Integral Transforms for Engineers*. SPIE The Int. Soc. for Opt. Eng., Bellingham, Washington (1998).
33. R. Bracewell, *Fourier Transform and Its Applications*. Revised 2<sup>nd</sup> Ed., McGraw Hill, New York, NY (1986).
34. E. Brigham, *The Fast Fourier Transform*. Prentice Hall, Englewood Cliffs, NJ (1974).
35. O. Rudenko and S. Soluyan, *Theoretical Foundations of Nonlinear Acoustics*. Consultant Bureau, New York, NY (1977).
36. R. Beyer, *Nonlinear Acoustics*. Dept. of the Navy, Washington, DC (1974).
37. P. Banerjee and T. Poon, *Principles of Applied Optics*. Richard D. Irwin, Inc., Homewood, IL (1991).
38. G. Agrawal, *Nonlinear Fiber Optics*. Academic Press, San Diego, CA (1995).
39. N. Akhmediev and A. Ankiewicz, *Solitons: Nonlinear Pulses and Beams*. Chapman & Hall, Boundary Row, London, UK (1997).
40. M. Goldman, "Strong turbulence of plasma waves," *Rev. of Mod. Phys.*, **56**, No. 4, 709-735 (1984).
41. M. Goldman, K. Rypdal, and B. Hafizi, "Dimensionality and dissipation in Langmuir collapse," *Phys. of Flu.*, **23**, No. 5, 945-955 (1980).
42. V. Zakharov, "Collapse of Langmuir waves," *Sov. Phys. JETP*, **35**, 908-914 (1972).

43. B. Herbst and J. Weidman, "Split-step methods for the solution of the nonlinear Schrödinger equation," *SIAM J. on Num. Anal.*, **23**, 485-507 (1986).
44. J. Sanz-Serna, "An explicit finite difference scheme with exact conservation properties," *J. of Comp. Phys.*, **47**, 199-210 (1982).
45. G. Fibich, W. Ren, and X. Wang., "Numerical simulations of self-focusing of ultrafast laser pulses," *Phys. Rev. E*, **67**, No. 056603 (2003).
46. J. Dendy, "An alternating direction method for Schrödinger equation," *SIAM J. on Num. Anal.*, **14**, No. 6, 1028-1032 (1977).
47. W. Bao, F. Sun, and G. Wei, "Numerical methods for the generalized Zakharov system," *J. of Comp. Phys.*, **190**, 201-228 (2003).
48. G. Whitham, *Linear and Nonlinear Waves*. Wiley, New York, NY (1974).
49. N. Zabusky and M. Kruskal, "Interaction of solitons in a collisionless plasma and the recurrence of initial states," *Phys. Rev. Lett.*, **15**, No. 6, 240-243 (1965).
50. R. Dodd, J. Eilbeck, J. Gibbon, and H. Morris, *Solitons and Nonlinear Wave Equations*. Academic Press Inc., New York, NY (1982).
51. Y. Silberberg, "Collapse of optical pulses," *Opt. Lett.*, **15**, No. 22, 1282-1284 (1990).
52. P. Goorjian and Y. Silberberg, "Numerical simulations of light bullets using the full-vector time-dependent nonlinear Maxwell equations," *JOSA B*, **14**, No. 11, 3253-3260 (1997).
53. S. Akhmanov, A. Sukhonorov, and R. Khoklov, "Self-focusing and self-trapping of intense light beams in a nonlinear medium," *J. of Exp. Theor. Phys. USSR*, **50**, 1537-1549 (1966).
54. J. Rothenberg, "Space-time focusing: Breakdown of the slowly varying envelope approximation in the self-focusing of femtosecond pulses," *Opt. Lett.*, **17**, 1340-1342 (1992).
55. J. Soto-Crespo, and N. Akhmediev, "Description of the self-focusing and collapse effects by a modified nonlinear Schrödinger equation," *Opt. Comm.*, **101**, No. 3, 223-230 (1993).
56. P. Banerjee, *Nonlinear Optics: Theory, Numerical Modeling, and Applications*. Marcel Dekker, Inc., New York, NY (2003).

57. T. Poon and P. Banerjee, *Contemporary Optical Image Processing with MATLAB* Elsevier Science Ltd., New York, NY (2001).
58. G. Fibich, "Small Beam Nonparaxiality Arrests Self-Focusing of Optical Beams," *Phys. Rev. Lett.* **76**, 4356-4359 (1996).
59. M. Feit and J. Fleck, "Beam nonparaxiality, filament formation, and beam breakup in the self-focusing of optical beams," *JOSA B* **5**, 633-640 (1988).
60. V. Skarka, V. Berezhiani, and R. Miklaszewski, "Spatiotemporal soliton propagation in saturating nonlinear optical media," *Phys. Rev. E* **56** 1080-1087 (1997).
61. Y. Kivshar, and G. Agrawal, *Optical Solitons*, (Academic Press: San Diego, CA 2003).
62. F. Kh. Abdullaev, and J. G. Caputo, "Validation of the variational approach for chirped pulses in fibers with periodic dispersion," *Phys. Rev. E* **58**, 6637-6648 (1998).
63. J. N. Kutz, P. Holmes, S. G. Evangelides Jr., and J. P. Gordon, "Hamiltonian dynamics of dispersion-managed breathers," *JOSA B* **15**, 87-96 (1998).
64. V. Cautaerts, A. Maruta, and Y. Kodama, "On the dispersion managed soliton," *Chaos* **10**, 515-528 (2000).
65. F. Kh. Abdullaev, B. B. Baizakov, and M. Salerno, "Stable two-dimensional dispersion-managed soliton," *Phys. Rev. E* **68**, 066605 (2003).
66. L. Berge, V.K. Mezentsev, J. Juul Rasmussen, P.L. Christiansen, and Yu. B. Gaididei, "Self-guiding light in layered nonlinear media," *Opt. Lett.* **25**, 1037-1039 (2000).
67. I. Towers and B. A. Malomed, "Stable (2+1)-dimensional solitons in a layered medium with sign-alternating Kerr nonlinearity," *JOSA B* **19**, 537-543 (2002).
68. G. I. Stegeman, M. Sheik-Bahae, E. W. Van Stryland, G. Assanto, "Large nonlinear phase shifts in second-order nonlinear-optical processes," *Opt. Lett.* **18**, 13-15 (1993).
69. H. Matthies and O. Kayser-Herold, *Lecture Notes: Introduction to PDEs and Numerical Methods*. Institute of Scientific Computing, Tech. Univ. Braunschweig (2002).

70. G. Whitham and B. Fornberg, "A numerical and theoretical study of certain nonlinear wave phenomena," *Philosophical Transactions, Royal Society London*, **289**, 373-403 (1978).
71. R. Schilling and S. Harris, *Applied numerical methods for engineers*. Brooks/Cole Pacific Grove, CA (2000).
72. H. Resnikoff and R. Wells, *Wavelet Analysis: The Scalable Structure of Information*. Springer-Verlag, New York, NY (1998).
73. M. Holmstrom and J. Walden, "Adaptive wavelet methods for hyperbolic PDEs," Department of Scientific Computing, Uppsala University, Sweden (1995).
74. J. Restrepo and G. Leaf, "Wavelet Galerkin discretization of hyperbolic equations," *J. of Comp. Phys.*, **122**, 118-128 (1995).
75. G. Chiavassa, and J. Liandrat, "Fully adaptive wavelet algorithm for parabolic partial differential equations," *App. Num. Math.*, **36**, 333-358 (2001).
76. J. Liandrat and J. Tchamitchian, "Resolution of the 1-D regularized Burgers equation using a spatial wavelet approximation algorithm and numerical results," ICASE Report, No. 90-83 (1990).
77. O. Vasilyev and S. Paolucci, "A dynamically adaptive multilevel wavelet Collocation method for solving partial differential equations in a finite domain," *J. of Comp. phys.*, **125**, 498-512 (1996).
78. O. Vasilyev, S. Paolucci, and M. Sen, "A multilevel wavelet collocation method for solving partial differential equations in a finite domain," *J. of Comp. Phys.*, **120**, 33-47 (1995).
79. O. Vasilyev and C. Bowman, "Second-generation wavelet collocation method for solution of partial differential equations," *J. of Comp. Phys.*, **165**, 660-693 (2000).
80. K. Amaratunga, J. Williams, S. Qian, and J. Weiss, "Wavelet Galerkin solutions for one dimensional partial differential equations," *Int. J. for Num. Meth. in Eng.*, **37**, 2703-2716 (1992).
81. L. Jameson, "On the wavelet optimized finite difference method," ICASE Report, supported by AFOSR Grant 93-1-0090 (1993).
82. B. Alpert, G. Beylkin, D. Gines, and L. Vozovoi, "Adaptive solution of partial differential equations in multiwavelet bases," *J. of Comp. Phys.*, **182**, 149-190 (2002).



83. I. Pierce and L. Watkins, "Modeling optical pulse propagation in nonlinear media using wavelets," Proc. of IEEE Int. Symp. on Time-Frequency and Time-Scale Anal., Paris, France, 361-338 (1996).
84. M. Misiti and Y. Misiti, *Wavelet Toolbox: User's Guide*. The MathWorks, Inc. Natick, MA (2002).
85. G. Beylkin and J. Keiser, "On the adaptive numerical solution of nonlinear partial differential equations in wavelet bases," J. of Comp. Phys, **132**, 233-259 (1997).
86. W. Shann, "Quadrature rules needed in Galerkin-wavelets methods," Chinese Mathematics Society Annual Meeting, (1993).
87. G. Beylkin, "On the representation of operators in bases of compactly supported wavelets," SIAM J. on Num. Anal., **6**, No. 6, 1716-1740 (1992).
88. L. Gagnon, J. Lina, and B. Goulard, "Application of complex Daubechies wavelets to numerical simulation of a nonlinear signal propagation model," Proceedings of the 7<sup>th</sup> IEEE Signal Processing Work Shop on Statistical Signal and Array Processing, Quebec, 251-254 (1994).
89. B. Suter and R. Hedges, "Understanding fast Hankel transforms," JOSA A., **18**, No. 3, 717-720 (2001).
90. M. Lax, J. H. Batteh, and G. P. Agrawal, "Channeling of intense electromagnetic beams ", J. Appl. Phys. **52**, 109-125 (1981).
91. Siegman, "Quasi-fast Hankel transform," Opt. Lett., **1**, No.1, 13-15 (1977).
92. V. Magni, G. Cerullo, and S. De Silvestri, "High-accuracy fast Hankel transform for optical beam propagation," JOSA A, **9**, 2031-2033 (1992).
93. D. Gardner, G. Gardner, G. Lausch, and W. Meinke, "Method for the analysis of multi-component exponential decays," J. of Chem. Phys., **31**, 987 (1959).
94. L. Yu, M. Huang, M. Chen, W. Chen, W. Huang, and Z. Zhu, "Quasi-discrete Hankel transform," Opt. Lett., **23**, No.6, 409-411 (1998).
95. M. Guizar-Sicairos, and J. Gutiérrez-Vega, "Computation of quasi-discrete Hankel transform of integer order for propagating optical wave fields", JOSA A, **21**, 53-58 (2004).
96. A. Ferrari, "Fast Hankel transform of order zero," JOSA A, **10**, 1872-1874 (1993).
97. G. Arfken, and H. Weber, *Mathematical Methods for Physicists*, Academic Press, Inc., Sandiego, Ca (1995).

98. R. Weinstock, *Calculus of Variations*, Dover Publications, Inc., New York, NY (1974).
99. H. Goldstein, *Classical Mechanics*, Addison-Wesley, Reading, MA (1980).
100. R. Chiao, E. Garmire and C. Townes, "Self-trapping of optical beams," *Phys. Rev. Lett.* **13**, 479-482 (1964).
101. P. Sulem, C. Sulem and A. Patera, "Numerical simulation of singular solutions to the 2-dimensional cubic Schrödinger equation," *Comm. Pure Appl. Math.* **37**, 755-778 (1984).
102. S. Chi and Q. Guo, "Vector theory of self-focusing of an optical beam in Kerr media" *Opt. Lett.* **20**, 1598-1600 (1995).
103. D.W. McLaughlin, G.C. Papanicolaou, C. Sulem and P.L. Sulem, "Focusing singularity of the cubic Schrödinger equation," *Phys. Rev. A* **34**, 1200-1210 (1986).
104. M.I. Weinstein, "Nonlinear Schrödinger equation and sharp interpolation estimates" *Comm. Math. Phys.* **87**, 567-576 (1983).
105. R.T. Glassey, "On the blowing up of solutions to the Cauchy problem for nonlinear Schrödinger equations," *J. Math. Phys.* **18**, 1794-1797 (1977).
106. G. Agrawal and M. Lax, "End correction in the quasi-fast Hankel transform for optical propagation problems" *Opt. Lett.* **6**, 171-173 (1981).
107. W. Ren and X-P Wang, "An iterative Grid Redistribution Method for Singular Problems in Multiple Dimensions," *J. Comp. Phys.* **159**, 246-273 (2000).
108. O. Budneva, V. Zakharov, and V. Synakh, "On some models of wave collapse," *Sov. J. Plasma Phys.* **1**, 335 (1975).
109. X. Liu, L.J. Qian, and F.W. Wise, "Generation of Optical Spatiotemporal Solitons," *Phys. Rev. Lett.* **82**, 4631 (1999).
110. S. K. Adhikari, "Stabilization of a  $(3 + 1)$ -dimensional soliton in a Kerr medium by a rapidly oscillating dispersion coefficient," *Phys. Rev. E* **71**, 016611 (2005).
111. F. K. Abdullaev, J. G. Caputo, R.A. Kraenkel, and B.A. Malomed, "Controlling collapse in Bose-Einstein condensates by temporal modulation of the scattering length," *Phys. Rev. A* **67**, 013605 (2003).
112. S. K. Adhikari, "Stabilization of a light bullet in a layered Kerr medium with sign-changing nonlinearity," *Phys. Rev. E* **70**, 036608 (2004).

113. D. Mihalache, D. Mazilu, F. Lederer, Y. V. Kartashov, L.-C. Crasovan, and L. Torner, "Stable three-dimensional spatiotemporal solitons in a two-dimensional photonic lattice," *Phys. Rev. E* **70**, 055603 (2004).
114. I. Towers, A.V. Buryak, R. A. Sammut, B. A. Malomed, L.-C. Crasovan, and D. Mihalache, "Stability of spinning ring solitons in the cubic-quintic nonlinear Schrodinger equation," *Phys. Lett. A* **288**, 292 (2001).
115. B. A. Malomed, D. Mihalache, F. Wise, and L. Torner, "Spatiotemporal optical solitons," *J. Opt. B: Quantum Semiclass. Opt.* **7** R53 (2005).
116. X. Cao, G. Agrawal, and C. McKinstrie, *Phys. Rev. A* **49**, 4085 (1994).
117. J. Talman, "Numerical Fourier and Bessel transform in logarithmic variables", *J. Comp. Phys.* **29**, 35 (1978).
118. N.J. Smith, F.M. Knox, N.J. Doran, K. J. Blow, and I. Bennion, "Enhanced power solitons in optical fibers with periodic dispersion management," *Electron. Lett.* **32**, 54-55 (1996).
119. N.J. Smith, N.J. Doran, F.M. Knox, and W. Forysiak, "Energy-scaling characteristics of solitons in strongly dispersion-managed fibers," *Opt. Lett.* **21**, 1981-1983 (1996).
120. I. Gabitov, E. G. Shapiro, and S.K. Turitsyn, "Optical pulse dynamics in fiber links with dispersion compensation," *Opt. Commun.* **134**, 317-329 (1997).
121. I. Gabitov, E. G. Shapiro, and S.K. Turitsyn, "Asymptotic breathing pulse in optical transmission system with dispersion compensation," *Phys. Rev. E* **55**, 3624-3633 (1997).
122. J. H. B. Nijhof, N.J. Doran, W. Forysiak, and F.M. Knox, "Stable soliton-like propagation in dispersion managed systems with net anomalous, zero and normal dispersion," *Electron. Lett.* **33**, 1726 (1997).
123. A. Hasegawa and Y. Kodama, "Guiding-center soliton in optical fibers," *Opt. Lett.* **15**, 1443-1445 (1990).
124. D. Anderson, "Variational approach to nonlinear pulse propagation in optical fibers," *Phys. Rev. A* **27**, 3135-3145 (1983).
125. M. J. Ablowitz and G. Biondini, "Multiscale pulse dynamics in communication systems with strong dispersion management," *Opt. Lett.* **23**, 1668-1670 (1998).
126. M. Desaix, D. Anderson, and M. Lisak, "Variational approach to collapse of optical pulses," *JOSA B* **8**, 2082-2086 (1991).

- 127. B. A. Malomed, "Pulse propagation in a nonlinear optical fiber with periodically modulated dispersion: variational approach," *Opt. Comm.* **136**, 313 (1997).
- 128. M. Ablowitz and Z. Muslimani, "Discrete diffraction managed spatial solitons," *Phys. Rev. Lett.* **87**, 254102 (2001).
- 129. M. Ablowitz and Z. Muslimani, "Discrete diffraction managed spatial solitons," *Phys. Rev. Lett.* **87**, 254102 (2001).
- 130. M. Matuszewski, M. Trippenbach, B.A. Malomed, E. Infeld, and A.A. Skorupski, "Two-dimensional dispersion-manages light bullets in Kerr media," *Phys. Rev. E* **70**, 016603 (2004).
- 131. A. Hasegawa and F. Tappert, "Transmission of stationary nonlinear optical pulses in dispersive dielectric fibers. I. Anomalous dispersion," *Appl. Phys. Lett.* **23**, 171-172 (1973).

## APPENDIX A

### USEFUL HANKEL TRANSFORM PROPERTIES

Some Hankel Transform properties:

- $\mathcal{H}_l\{f(ar); \rho\} = \frac{1}{a^2} \mathcal{H}_l\left\{f\left(\frac{\rho}{a}\right); \rho\right\}.$
- $\mathcal{H}_l\left\{\frac{1}{r} f(r); \rho\right\} = \frac{\rho}{2\nu} [\mathcal{H}_{l+1}\{f(r); \rho\} + \mathcal{H}_{l-1}\{f(r); \rho\}], l > \frac{-1}{2}.$
- $\mathcal{H}_l\{f'(r); \rho\} = \frac{-\rho}{2\nu} [(l+1)\mathcal{H}_{l-1}\{f(r); \rho\} - (l-1)\mathcal{H}_{l+1}\{f(r); \rho\}]$
- $\mathcal{H}_l\{f''(r); \rho\} = \frac{\rho^2}{4} \left[ \left( \frac{l+1}{l-1} \right) \mathcal{H}_{l-2}\{f(r); \rho\} - 2 \frac{l^2-3}{l^2-1} \mathcal{H}_l\{f(r); \rho\} + \left( \frac{l-1}{l+1} \right) \mathcal{H}_{l+2}\{f(r); \rho\} \right].$
- $\mathcal{H}_0\{f''(r); \rho\} = -\frac{\rho^2}{4} [\mathcal{H}_{-2}\{f(r); \rho\} + 6\mathcal{H}_0\{f(r); \rho\} + \mathcal{H}_2\{f(r); \rho\}]$
- $\mathcal{H}_l\left\{r^{l-1} \frac{d}{dr} [r^{1-l} f(r)]; \rho\right\} = -\rho \mathcal{H}_{l-1}\{f(r); \rho\}.$
- $\mathcal{H}_l\left\{\frac{1}{r^{l+1}} \frac{d}{dr} [r^{l+1} f(r)]; \rho\right\} = \rho \mathcal{H}_{l+1}\{f(r); \rho\}.$
- $\mathcal{H}_0\left\{\frac{1}{r} \frac{d}{dr} [rf(r)]; \rho\right\} = \mathcal{H}_0\left\{\frac{f(r)}{r} + \frac{df(r)}{dr}; \rho\right\} = \rho \mathcal{H}_1\{f(r); \rho\}.$

- $\mathcal{H}_1\left\{\frac{1}{r^2}\frac{d}{dr}[r^2 f(r)]; \rho\right\} = \mathcal{H}_1\left\{\frac{2f(r)}{r} + \frac{df(r)}{dr}; \rho\right\} = \rho \mathcal{H}_2\{f(r); \rho\}$
- $\mathcal{H}_l\left\{\frac{1}{r^{l+1}}\frac{d}{dr}\left[r^{2l+1}\frac{d}{dr}\left(\frac{1}{r^l}f(r)\right)\right]; \rho\right\} = \mathcal{H}_l\left\{\frac{d^2 f}{dr^2} + \frac{1}{r}\frac{df}{dr} - \frac{l^2 f}{r^2}; \rho\right\} = -\rho^2 \mathcal{H}_l\{f(r); \rho\}.$
- $\mathcal{H}_0\left\{\frac{1}{r}\frac{d}{dr}[rf'(r)]; \rho\right\} = -\rho^2 \mathcal{H}_0\{f(r); \rho\}.$
- $\mathcal{H}_1\left\{\frac{d^2 f}{dr^2} + \frac{1}{r}\frac{df}{dr} - \frac{f}{r^2}; \rho\right\} = -\rho^2 \mathcal{H}_1\{f(r); \rho\}.$

## APPENDIX B

### MATLAB CODE

#### B.1 Wavelet Transform Codes

##### B.1.1 NLS Equation in 1-D

```
%*****
%FWT on the NLS equation  $i\frac{du}{dt} + \alpha \frac{d^2u}{dx^2} + \nu |u|^2 u = 0$ 
%x=linspace(-
3,3,1000);u=exp(2*x.^2);[c,L]=wavedec(u,3,'sym6');A=wrcoef('a',c,L,'sym6',3);
%plot(x,u,'x',x,A,'r')
%-----Claculate the wavelet-----
xmax=16;
level=3;
alpha=1/2;
nu=1;
deltat=5*10^(-5);
maxtime=2;
iter=3;
wav='sym6';
[phi,psi,xval]=wavefun(wav,iter);
hval=xval(2)-xval(1);
MX=max(xval);
s=1;
% mm=0;
% jump=10^(s+1);
flag=1;
for t=0:deltat:maxtime
    if flag==1
        flag=0;
        thresh=2^(level-3)*10^-5;
        phin=2^(level/2)*phi;
        psin=2^(level/2)*psi;
        lenphi=length(phin);
        shift=floor(lenphi/MX);
        N=xmax*2^level-(MX-1);
        lenPHI=(N-1)*shift+lenphi;
```

```

x=linspace(-xmax/2,xmax/2,lenPHI);
h=x(2)-x(1);
%-----Clculate the initial approximation of u-----
if t==0
    ua=3*sech(x);
end
t=0;
for L=1:N
    aold(1,L)=h*ua((L-1)*shift+1:(L-1)*shift+lenphi)*phin';
end
for L=1:N
    b(1,L)=h*ua((L-1)*shift+1:(L-1)*shift+lenphi)*psin';
end
u0=zeros(1,lenPHI);
for L=1:N
    u0(1,(L-1)*shift+1:(L-1)*shift+lenphi)=u0(1,(L-1)*shift+1:(L-
    1)*shift+lenphi)+aold(1,L)*phin;
end
figure
plot(x,ua,'k',x,u0,'r');
title(strcat('xmax=',num2str(xmax),'alpha=',num2str(alpha),'nu=',num2str(nu),'maxtime
=',num2str(maxtime),'deltat=',num2str(deltat),'level=',num2str(level),'iter=',num2str(iter
),'time=',num2str(t)));
%----Calculate KM Matrix for sym6
load sym6KMburg3;
for L=1:N
    for K=1:N
        if abs(L-K)<MX
            KM(L,K)=sym6KMburg3(K-L+MX)*2^(2*level);
        end
    end
end
%-----
load sym6LambdaNLS3;
end
% U=zeros(floor(maxtime/(jump*deltat))+1,lenPHI);
%----Calculate C Matrix-----
C=zeros(N,N);
for L=1:N
    for K=1:N
        if abs(L-K)<MX
            for m=1:N
                if abs(m-K)<MX & abs(L-m)<MX
                    for n=1:N
                        if abs(n-K)<MX & abs(L-n)<MX & abs(m-n)<MX

```



```

        C(L,K)=C(L,K)+aold(1,n)*2^(level)*sym6LambdaNLS3(K-
        L+MX,m-L+MX,n-L+MX)*conj(aold(1,m));
    end
end
end
end
end
end
end
end

% % for L=1:N
% % for K=1:N
% % if abs(L-K)<MX
% % Mat(L,K)=deltat*(nu*C(L,K) +
alpha*sym6KMburg3(KL+MX)*2^(2*level));
% % end
% % end
% % end
% %a=a+i*a*Mat;

anon=aold+i*deltat*aold*nu*C;
alin=anon+i*deltat*anon*alpha*KM;
anew=alin;
aold=anew;
if max(abs(aold))>50
    u=zeros(1,lenPHI);
    for L=1:N
        u(1,(L-1)*shift+1:(L-1)*shift+lenphi)=u(1,(L-1)*shift+1:(L-
        1)*shift+lenphi)+abs(aold(1,L))*phi;
    end
    figure
    plot(x,u0,'r',x,u,'k');
    title(strcat('xmax=',num2str(xmax),'alpha=',num2str(alpha),'nu=',num2str(nu),'maxtime
    =',num2str(maxtime),'deltat=',num2str(deltat),'level=',num2str(level),'iter=',num2str(iter
    ),'time=',num2str(t)));
    break;
end
u=zeros(1,lenPHI);
for L=1:N
    u(1,(L-1)*shift+1:(L-1)*shift+lenphi)=u(1,(L-1)*shift+1:(L-
    1)*shift+lenphi)+abs(aold(1,L))*phin;
end
for L=1:N
    b(1,L)=h*u((L-1)*shift+1:(L-1)*shift+lenphi)*psin';
end
if max(abs(b))>thresh

```

```

    max(abs(b));
    level=level+1;
    flag=1;
    ut=interp(u,2);
    ua=ut(1:length(ut)-1);
    % a=interp(a,2);
end
% if t == (mm*jump*deltat)
%     u=zeros(1,lenPHI);
%     for L=1:N
%         u(1,(L-1)*shift+1:(L-1)*shift+lenphi)=u(1,(L-1)*shift+1:(L-
%             1)*shift+lenphi)+abs(aold(1,L))*phin;
%     end
%     mm=mm+1;
%     U(mm,:)=u;
% end
if t==deltat*10^(s+1) | t==deltat*10^(s+2) | t==deltat*10^(s+3) |
    t==deltat*10^(s+4) | t==0.5 | t==0.75 | t==1.5 | t==1.75 | t==2
    u=zeros(1,lenPHI);
    for L=1:N
        u(1,(L-1)*shift+1:(L-1)*shift+lenphi)=u(1,(L-1)*shift+1:(L-
            1)*shift+lenphi)+abs(aold(1,L))*phin;
    end
    end
    figure
    plot(x,u0,'r',x,u,'k');

title(strcat('xmax=',num2str(xmax),'alpha=',num2str(alpha),'nu=',num2str(nu),'maxtime
=',num2str(maxtime),'deltat=',num2str(deltat),'level=',num2str(level),'iter=',num2str(iter
),'time=',num2str(t)));
end
end
% figure
% S=size(U);
% % tp=[0:1:S(1)-1];
% tp=linspace(0,maxtime,S(1));
% [X,T]=meshgrid(x,tp);
% mesh(X,T,U);
%
title(strcat('xmax=',num2str(xmax),'alpha=',num2str(alpha),'nu=',num2str(nu),'maxtime
=',num2str(maxtime),'deltat=',num2str(deltat),'level=',num2str(level),'iter=',num2str(iter
),'time=',num2str(t)));
%*****

```

### B.1.2 NLS Equation in 2-D: Self-focusing Phenomena

```

%*****

```

```

%FWT on the self-focussing NLS equation
%i*du/dt+1/tao*du/dtao+alpha*d^2u/dtao^2+nu*|u|^2*u=0
%-----Claculate the wavelet-----
Pcr=1.86225;
xmax=6;
level=3;
deltat0=0.00001;
maxtime=0.5;
iter=3;
NS=45000;
wav='sym6';
% umax(1)=4;%(6*Pcr)^0.5;
% ua=umax(1)*exp(-x.^2);
[phi,psi,xval]=wavefun(wav,iter);
hval=xval(2)-xval(1);
MX=max(xval);
s=1;
% mm=0;
% jump=10^(s+1);
flag=1;
LL=NS/10;
umax(1)=4;%(6*Pcr)^0.5;
con=deltat0*(umax(1)^(3/2));
di=0;
for t=0:1:NS
    if flag==1
        flag=0;
        thresh=5*10^-(level+3);
        phin=2^(level/2)*phi;
        psin=2^(level/2)*psi;
        lenphi=length(phin);
        shift=floor(lenphi/MX);
        N=xmax*2^level-(MX-1);
        lenPHI=(N-1)*shift+lenphi;
        x=linspace(-xmax/2,xmax/2,lenPHI);
        h=x(2)-x(1);
        %-----Claculate the initial approximation of u-----
        if t==0
            ua=umax(1)*exp(-x.^2);
            for L=1:N
                aold(1,L)=h*ua((L-1)*shift+1:(L-1)*shift+lenphi)*phin';
            end
            for L=1:N
                b(1,L)=h*ua((L-1)*shift+1:(L-1)*shift+lenphi)*psin';
            end
            u=zeros(1,lenPHI);

```

```

for L=1:N
    u(1,(L-1)*shift+1:(L-1)*shift+lenphi)=u(1,(L-1)*shift+1:(L-
    1)*shift+lenphi)+aold(1,L)*phin;
end
figure
plot(x,ua.^2,'k',x,u.^2,'r');

title(strcat('xmax=',num2str(xmax),'maxtime=',num2str(maxtime),'deltat0=',num2str(del
tat0),'level=',num2str(level),'NS=',num2str(NS),'time=',num2str(t)));
E0=sum(abs(u((lenPHI+1)/2:lenPHI)).^2.*x((lenPHI+1)/2:lenPHI))
%since cylindrical coordinates
end
%----Calculate KM Matrix for sym6
load sym6KMburg3;
for L=1:N
    for K=1:N
        if abs(L-K)<MX
            KM(L,K)=sym6KMburg3(K-L+MX)*2^(2*level);
        end
    end
end
%-----calculate the TM matrix
iterf=5;
wav='sym6';
[phif,psif,xvalf]=wavefun(wav,iterf);
MXf=max(xvalf);
phif=2^(level/2)*phif;
lenphif=length(phif);
%%%%%%%%%%
phif=phif(1:lenphif-1);
lenphif=length(phif);
%%%%%%%%%%
shiftf=floor(lenphif/11);
N=xmax*2^level-(MXf-1);
lenPHIf=(N-1)*shiftf+lenphif;
xf=linspace(-xmax/2,xmax/2,lenPHIf);
hf=xf(2)-xf(1);
dphif=diff(phif)/hf;
dphif(lenphif)=dphif(lenphif-1);
for c=1:1:N
    PHIf(c,(c-1)*shiftf+1:(c-1)*shiftf+lenphif)=phif;
    dPHIf(c,(c-1)*shiftf+1:(c-1)*shiftf+lenphif)=dphif;
end
for L=1:N
    for K=1:N
        if abs(L-K)<MXf

```

```

        TM(L,K)=hf*sum(1./(xf((L-1)*shiftf+1:(L-1)*shiftf+lenphif)).*dPHIf(L,(L-
        1)*shiftf+1:(L-1)*shiftf+lenphif).*PHIf(K,(L-1)*shiftf+1:(L-
        1)*shiftf+lenphif));
    end
end
clear phif psif xvalf iterf TMa lenPHIf shiftf dphif lenphif PHIf dPhIf eps hf xf;
%-----
load sym6LambdaNLS3;
end
%U=zeros(floor(maxtime/(jump*deltat))+1,lenPHI);
%----Calculate C Matrix-----
C=zeros(N,N);
for L=1:N
    for K=1:N
        if abs(L-K)<MX
            for m=1:N
                if abs(m-K)<MX & abs(L-m)<MX
                    for n=1:N
                        if abs(n-K)<MX & abs(L-n)<MX & abs(m-n)<MX
                            C(L,K)=C(L,K)+aold(1,n)*2^(level)*sym6LambdaNLS3(K-
                            L+MX,m-L+MX,n-L+MX)*conj(aold(1,m));
                        end
                    end
                end
            end
        end
    end
end
deltat=con/(umax(t+1)^(3/2));
di=di+deltat;
%deltat=0.205/(t+1)*(maxtime-1/(umax(t+1)^(3/2)));
%  anew=aold+i*aold*deltat*(C+KM+TM);
%  aold=anew;
anon=aold+i*deltat*aold*C;
alin=anon+i*deltat*anon*(KM+TM);
aold=alin;
u=zeros(1,lenPHI);
for L=1:N
    u(1,(L-1)*shiftf+1:(L-1)*shiftf+lenphif)=u(1,(L-1)*shiftf+1:(L-
    1)*shiftf+lenphif)+abs(aold(1,L))*psin';
end
for L=1:N
    b(1,L)=h*u(1,(L-1)*shiftf+1:(L-1)*shiftf+lenphif)*psin';
end
umax(t+2)=max(abs(u));

```

```

if umax(t+2)>10^3
    max(abs(b))
    figure
    plot(x,abs(u).^2,'k');

    title(strcat('xmax=',num2str(xmax),'deltat=',num2str(deltat),'level=',num2str(level)
    ',num of steps=',num2str(NS),'di=',num2str(di),'time step=',num2str(t)));
    ylabel('Beam Intensity')
    xlabel('\tau')
    disp('blow up');
    break;
end
if max(abs(b))>thresh
    max(abs(b))
    figure
    plot(x,ua,'r',x,u,'k');
title(strcat('xmax=',num2str(xmax),'alpha=',num2str(alpha),'nu=',num2str(nu),'maxtime
=',num2str(maxtime),'deltat=',num2str(deltat),'level=',num2str(level),'iter=',num2str(iter
),'time=',num2str(t)));
    level=level+1;
    flag=1;
    at=aold(ceil(N/4):floor(3*N/4));
    aold=interp(at,2);
    xmax=xmax/2;
end
%      if t == (mm*jump*deltat)
%          u=zeros(1,lenPHI);
%          for L=1:N
%              u(1,(L-1)*shift+1:(L-1)*shift+lenphi)=u(1,(L-1)*shift+1:(L-
%              1)*shift+lenphi)+abs(aold(1,L))*phin;
%          end
%          mm=mm+1;
%          U(mm,:)=u;
%      end
if rem(t,LL)==0 | t== 10 | t==100 | t==1000 | t== 3000 | t== 5000 | t== 10000
    max(abs(b))
    figure
    plot(x,abs(u).^2,'k');

    title(strcat('xmax=',num2str(xmax),'deltat=',num2str(deltat),'level=',num2str(level)
    ',num of steps=',num2str(NS),'di=',num2str(di),'time step=',num2str(t)));
    ylabel('Beam Intensity')
    xlabel('\tau')
    E=sum(abs(u>((lenPHI+1)/2:lenPHI)).^2.*x((lenPHI+1)/2:lenPHI))
end
end
end

```

```

% figure
% S=size(U);
% % tp=[0:1:S(1)-1];
% tp=linspace(0,maxtime,S(1));
% [X,T]=meshgrid(x,tp);
% mesh(X,T,U);
di
figure
zprop=linspace(0,di,t+2);
plot(zprop,umax.^2)
title(strcat('Psimax:Plot vs. Propagation Time t ',Tr*=',num2str(di)));
ylabel('Beam Intensity')
xlabel('t')
Ef=sum(abs(u((lenPHI+1)/2:lenPHI)).^2.*x((lenPHI+1)/2:lenPHI))
clear all;
%*****

```

### B.1.3 Self-steepening Eq.

```

%*****
%FWT on the NLS equation  $i\sigma \frac{d(|u|^2 u)}{dt} + \nu |u|^2 u = 0$ 
%-----Claculate the wavelet-----
xmax=6;
level=3;
sigma=1/2;
nu=1;
deltat=10^(-5);
maxtime=1;
iter=3;
wav='sym6';
[phi,psi,xval]=wavefun(wav,iter);
hval=xval(2)-xval(1);
MX=max(xval);
s=2;
flag=1;
t=0;
%for t=0:deltat:maxtime
if flag==1
    flag=0;
    thresh=(level-2)*10^(-5);
    phin=2^(level/2)*phi;
    psin=2^(level/2)*psi;
    lenphi=length(phin);
    shift=floor(lenphi/MX);
    N=xmax*2^level-(MX-1);
    lenPHI=(N-1)*shift+lenphi;
    x=linspace(-xmax/2,xmax/2,lenPHI);

```

```

h=x(2)-x(1);
%-----Calculate the initial approximation of u-----
if t==0
    ua=exp(-1/2*x.^2);
    for L=1:N
        aold(1,L)=h*ua((L-1)*shift+1:(L-1)*shift+lenphi)*phin';
    end
    for L=1:N
        b(1,L)=h*ua((L-1)*shift+1:(L-1)*shift+lenphi)*psin';
    end
    u=zeros(1,lenPHI);
    for L=1:N
        u(1,(L-1)*shift+1:(L-1)*shift+lenphi)=u(1,(L-1)*shift+1:(L-
            1)*shift+lenphi)+aold(1,L)*phin';
    end
    figure
    plot(x,ua,'k',x,u,'r');

title(strcat('xmax=',num2str(xmax),',sigma=',num2str(sigma),'\nu=',num2str(nu),',maxtime=
',num2str(maxtime),',deltat=',num2str(deltat),',level=',num2str(level),',iter=',num2str(it
er),',time=',num2str(t)));
    load sym6LambdaNLS3;
    load sym6selfsteep3;
end
end
%----Calculate C Matrix-----
C=zeros(N,N);
ST=zeros(N,N);
for L=1:N
    for K=1:N
        if abs(L-K)<MX
            for m=1:N
                if (abs(m-K)<MX && abs(L-m)<MX)
                    for n=1:N
                        if (abs(n-K)<MX && abs(L-n)<MX && abs(m-n)<MX)
                            C(L,K)=C(L,K)+aold(1,n)*2^(level)*sym6LambdaNLS3(K-
                                L+MX,m-L+MX,n-L+MX)*conj(aold(1,m));
                            ST(L,K)=ST(L,K)+aold(1,n)*2^(2*level)*sym6selfsteep3(K-
                                L+MX,m-L+MX,n-L+MX)*conj(aold(1,m));
                        end
                    end
                end
            end
        end
    end
end
end
end
end
end
end

```



```

aold=aold+deltat*aold*(i*nu*C-sigma*ST);
if max(abs(aold))>20
    u=zeros(1,lenPHI);
    for L=1:N
        u(1,(L-1)*shift+1:(L-1)*shift+lenphi)=u(1,(L-1)*shift+1:(L-
            1)*shift+lenphi)+abs(aold(1,L))*phin;
    end
    figure
    plot(x,u,'k');

title(strcat('xmax=',num2str(xmax),'sigma=',num2str(sigma),'nu=',num2str(nu),'maxtime=
e=',num2str(maxtime),'deltat=',num2str(deltat),'level=',num2str(level),'iter=',num2str(it
er),'time=',num2str(t)));
    break;
end
u=zeros(1,lenPHI);
for L=1:N
    u(1,(L-1)*shift+1:(L-1)*shift+lenphi)=u(1,(L-1)*shift+1:(L-
        1)*shift+lenphi)+abs(aold(1,L))*phin;
end
for L=1:N
    b(1,L)=h*u(1,(L-1)*shift+1:(L-1)*shift+lenphi)*psin';
end
if max(abs(b))>thresh
    max(abs(b));
    u=zeros(1,lenPHI);
    for L=1:N
        u(1,(L-1)*shift+1:(L-1)*shift+lenphi)=u(1,(L-1)*shift+1:(L-
            1)*shift+lenphi)+abs(aold(1,L))*phin;
    end
    figure
    plot(x,ua,'r',x,u,'k');
title(strcat('xmax=',num2str(xmax),'sigma=',num2str(sigma),'nu=',num2str(nu),'maxtime=
e=',num2str(maxtime),'deltat=',num2str(deltat),'level=',num2str(level),'iter=',num2str(it
er),'time=',num2str(t)));
    level=level+1;
    flag=1;
    aold=interp(aold,2);
    %ut=interp(u,2);
    %ua=ut(1:length(ut)-1);
end
if t==deltat*10^(s+1) | t==2*deltat*10^(s+1) | t==5*deltat*10^(s+1) | t==0.5
    |t==0.55| t==0.75 |t== maxtime
    u=zeros(1,lenPHI);
    for L=1:N

```

```

        u(1,(L-1)*shift+1:(L-1)*shift+lenphi)=u(1,(L-1)*shift+1:(L-
        1)*shift+lenphi)+abs(aold(1,L))*phi;
    end
    figure
    plot(x,u,'k');
    title(strcat('xmax=',num2str(xmax),'sigma=',num2str(sigma),'nu=',num2str(nu),'maxtime=
    ',num2str(maxtime),'deltat=',num2str(deltat),'level=',num2str(level),'iter=',num2str(it
    er),'time=',num2str(t)));
    end
end
clear all;
%*****

```

#### B.1.4 Dispersion Management in 1-D

```

%*****
%FWT on the DMSS using NLS equation:
%      i*du/dt+i*1/2*alpha(t)u+1/2*beta2(t)*d^2u/dx^2+gamma*|u|^2*u=0
%-----Claculate the wavelet-----
xmax=10;
level=3;
deltat=10^(-5);
duty=1-6/51;
maxtime=0.8;
% beta=[-4,4];
beta=[-2.1,17.45];
gamma=1;
alpha=0;
NS=80000;
period=NS/2;
% umax(1)=1;
% ua=umax(1)*exp(-x.^2);
%-----
for m=0:NS-1
    if period*duty/2<=rem(m,period)& rem(m,period)<= period-period*duty/2
        beta2(m+1)=beta(2);
    else
        beta2(m+1)=beta(1);
    end
end
end
tt=[0:1:NS-1]*deltat;
%-----
iter=3;
wav='sym6';
[phi,psi,xval]=wavefun(wav,iter);
hval=xval(2)-xval(1);
MX=max(xval);

```

```

phi=2^(level/2)*phi;
lenphi=length(phi);
shift=floor(lenphi/MX);
N=xmax*2^level-(MX-1);
lenPHI=(N-1)*shift+lenphi;
x=linspace(-xmax/2,xmax/2,lenPHI);
h=x(2)-x(1);
%----Calculate KM Matrix for sym6
load sym6KMburg3;
for L=1:N
    for K=1:N
        if abs(L-K)<MX
            KM(L,K)=sym6KMburg3(K-L+MX)*2^(2*level);
        end
    end
end
%-----Clculate the initial approximation of u-----
umax(1)=1;
ua=umax(1)*exp(-x.^2);
t=0;
for L=1:N
    aold(1,L)=h*ua((L-1)*shift+1:(L-1)*shift+lenphi)*phi';
end
u0=zeros(1,lenPHI);
for L=1:N
    u0(1,(L-1)*shift+1:(L-1)*shift+lenphi)=u0(1,(L-1)*shift+1:(L-1)*shift+lenphi)+aold(1,L)*phi;
end
% figure
% plot(x,ua,x,u0,'r');
%-----
load sym6LambdaNLS3;
%-----Loop-----
di=0;
for t=0:1:NS-1
    %di=di+deltat;
    %----Calculate C Matrix-----
    C=zeros(N,N);
    for L=1:N
        for K=1:N
            if abs(L-K)<MX
                for m=1:N
                    if (abs(m-K)<MX && abs(L-m)<MX)
                        for n=1:N
                            if (abs(n-K)<MX && abs(L-n)<MX && abs(m-n)<MX)

```

```

        C(L,K)=C(L,K)+aold(1,n)*2^(level)*sym6LambdaNLS3(K-
        L+MX,m-L+MX,n-L+MX)*conj(aold(1,m));
    end
end
end
end
end
end
anon=aold+i*deltat*aold*gamma*C;
alin=anon+i*deltat*anon*(1/2*beta2(t+1)*KM);% -1/2*deltat*alpha*anon;
aold=alin;
u=zeros(1,lenPHI);
for L=1:N
    u(1,(L-1)*shift+1:(L-1)*shift+lenphi)=u(1,(L-1)*shift+1:(L-
    1)*shift+lenphi)+abs(aold(1,L))*phi;
end
umax(t+2)=max(abs(u));
if umax(t+2)>10
    figure
    plot(x,abs(u).^2,'k');
    title(strcat('time
step=',num2str(t),'deltat=',num2str(deltat),'level=',num2str(level),'time=',num2str(t),'pe
riod=',num2str(period*deltat)));
    ylabel('pulse amplitude')
    xlabel('\tau')
    disp('blow up');
    break;
end
if rem(t,period)==0 | rem(t,period/2)==0
    figure
    plot(x,u0,'r',x,u,'k');
    title(strcat('time
step=',num2str(t),'deltat=',num2str(deltat),'level=',num2str(level),'time=',num2str(t),'pe
riod=',num2str(period*deltat)));
end
end
figure
subplot(2,1,1)
plot(tt,beta2);
subplot(2,1,2)
di=NS*deltat;
zprop=linspace(0,di,t+2);
plot(zprop,umax)
title(strcat('\Psi_{max}:Plot vs. Propagation Time t'
',Tr=',num2str(di),'period=',num2str(period*deltat)));

```

```

ylabel('pulse amplitude')
xlabel('t')
%-----Clculate the final value of u-----
%clear all;
%*****

```

## B.2 Fourier Bessel Transform Codes

```

%*****

```

### B.2.1 Non-paraxial NLS Equation

```

%*****
%Yu fast Hankel transform function
%yfht
function g=yfht(g1,C,jn,R1,R2,L)
%forward transform
if L==0
F1=R1*g1.*abs(besselj(1,jn)).^(-1);
F2=C*F1;
g=F2.*abs(besselj(1,jn))/R2;
% figure(3)
% plot(r2m,f2)
%inverse transform
else
F2=R2*g1.*abs(besselj(1,jn)).^(-1);
IF1=C'*F2;
g=IF1.*abs(besselj(1,jn))/R1;
end
%*****
% Yu method for Hankel transform applied on Self-focusing of beams using the

```

### NLS Eq.

```

%*****
clear all;
load jnR1_10R2_200;
R1=10;
R2=2000/R1;
umax(1)=4;
w0=1/(2^0.5);
q=1;
M=220;
delz=0.01;
lambda=0.001257;
eps=(lambda/(4*pi*w0))^2;
% eps=10^-3;
S=2*pi*R1*R2;

```

```

N=length(jn);
S=jn(length(jn))+jn(2)-jn(1);
%C=2/S*besselj(0,(jn*jn')/S).*(abs(besselj(1,jn).^(-1))*(abs(besselj(1,jn).^(-1)))));
load Yucmatrix2000;
r1n=jn/(2*pi*R2);
r2m=jn/(2*pi*R1);
f1=umax(1)*exp(-r1n.^2/(2*w0^2));
f1(length(f1))=0;
L=M/10;
con=delz*(umax(1)^(2));
figure
plot([-fliplr(r1n),r1n],[fliplr(f1),f1].^2,'b');
title(strcat('\Deltaz_0=',num2str(delz),'\psi_0 =4*exp(-r^2/(2w_0^2))'));
ylabel('Beam Intensity')
u=f1;
E0=sum(abs(f1).^2.*r1n)
zprop(1)=0;
for k=1:M
delz=con/(umax(k)^(2));
zprop(k+1)=zprop(k)+delz;
w=exp(-i/(2*eps)*(1-(1-16*eps*pi^2*r2m.^2).^0.5)*delz/2);
hu=yfht(u,C,jn,R1,R2,0).*w;
u=yfht(hu,C,jn,R1,R2,1);
uint=(u.*conj(u)+conj(u).*u)/2;
qr=exp(-i/(2*eps)*(1-(1+4*eps*uint).^0.5)*delz);
u=u.*qr;
hu=yfht(u,C,jn,R1,R2,0).*w;
u2=yfht(hu,C,jn,R1,R2,1);
u2(length(u2))=0;
umax(k+1)=abs(u2(1));
I=find(abs(u2)<(umax(k+1)/exp(1)));
r=r1n(I(1));
eps=(lambda/(4*pi*r))^2 ;
% -----
if rem(k,L)==0
% fr=[-fliplr(r1n),r1n];
% ur=[fliplr(u2),u2];
% figure
% %semilogy(fr,abs(ur).^2,'b');
% plot(fr,abs(ur).^2,'b');
%title(strcat('\Deltaz=',num2str(delz),',z_r_c=',num2str(zprop(k+1)),',\psi_m_a_x^2=',nu
m2str(umax(k+1)^2)));
% ylabel('Beam Intensity')
% xlabel('r')
E=sum(abs(u2).^2.*r1n)
end

```

```

% if umax(k+1)< 0.95*umax(k)
%     display(strcat('blow up=',num2str(zprop(k+1))));
%     break;
% end
    u=u2;
end
zr=zprop(length(zprop));
figure
plot(zprop,umax.^2)
title(strcat('\psi_m_a_x^2:Plot vs. Propagation dist z' ',z_r_c =',num2str(zr)));
ylabel('Beam Intensity')
xlabel('z')
Ef=sum(abs(u).^2.*r1n)
clear all
%*****

```

## B.2.2 Saturating Nonlinearity Equation

```

%*****
%Sicairos spherical Bessel transform method: SSBT
function g=SSBT(g1,C,jn,R1,R2,L,mu)
%forward transform
if L==0
F1=R1*g1.*abs(besselj(mu+1,jn)).^(-1);
F2=C*F1;
g=F2.*abs(besselj(mu+1,jn))/R2;
% figure(3)
% plot(r2m,f2)
%inverse transform
else
F2=R2*g1.*abs(besselj(mu+1,jn)).^(-1);
IF1=C'*F2;
g=IF1.*abs(besselj(mu+1,jn))/R1;
end
%*****
% Sicairos method for spherical Bessel transform applied on optical bullets using the
NLS eq
clear all;
R1=40;R2=40;
umax(1)=0.6;
w0=4.8;
M=1500;
alpha=1;
%uint=uint-alpha*uint.^2;
%uint=uint./(1+alpha*uint);
delz0=0.08;
L=M/20;

```

```

q=1;
S=2*pi*R1*R2;
mu=1/2;
mm=0;
jn=pi*[1:1:2*R1*R2]';
N=length(jn);
S=jn(length(jn))+jn(2)-jn(1);
% C=2/S*besselj(mu,(jn*jn')/S).*(abs(besselj(mu+1,jn).^(-
1))*(abs(besselj(mu+1,jn).^(-1)))));
load Scmatrix1600;
r1n=jn/(2*pi*R2);
r2m=jn/(2*pi*R1);
f1=umax(1)*exp(-r1n.^2/(2*w0^2));
f1(length(f1))=0;
%BPM method
u0r=[flipud(f1);f1].^2;
figure(1)
% subplot(1,3,1)
plot([-flipud(r1n);r1n],u0r,'b');
title(strcat('\Delta z_0=',num2str(delz0),'\psi_0 =',num2str(umax(1)),'*exp(-
r^2/2w_0^2)'));
ylabel('Beam Intensity')
u=f1;
E0=sum(abs(f1).^2.*r1n.^2)
zprop(1)=0;
delz=delz0;
% con=delz*(umax(1)^(1/2));
for k=1:M
% delz=con/(umax(k)^(1/2));
zprop(k+1)=zprop(k)+delz;
w=exp(-i*4*pi^2*r2m.^2*delz/2);
u=r1n.^(1/2).*u;
hu=SSBT(u,C,jn,R1,R2,0,mu).*w;
u=r1n.^(-1/2).*SSBT(hu,C,jn,R1,R2,1,mu);
% nonlinear part
uint=(u.*conj(u)+conj(u).*u)/2;
uint=uint-alpha*uint.^2;
% uint=uint./(1+alpha*uint);
qr=exp(i*q*uint*delz);
u=u.*qr;
% linear part
u=r1n.^(1/2).*u;
hu=SSBT(u,C,jn,R1,R2,0,mu).*w;
u2=r1n.^(-1/2).*SSBT(hu,C,jn,R1,R2,1,mu);
u2(length(u2))=0;
umax(k+1)=abs(u2(1));

```



```

if rem(k,L)==0
    mm=mm+1;
    ur=[flipud(u2);u2];
    U(:,mm+1)=abs(ur).^2;
%    figure
%    plot(fr,abs(ur).^2,'b');
    E=sum(abs(u2).^2.*r1n.^2)
end
% if umax(k+1)< 0.8*umax(k)
%     display(strcat('blow up=',num2str(zprop(k+1))));
%     break;
% end
    u=u2;
end
fr=[-flipud(r1n);r1n];
zr=zprop(length(zprop));
U(:,1)=u0r;
S=size(U);
figure
[Fr,Zprop]=meshgrid(linspace(0,zr,S(2)),fr);
mesh(Zprop,Fr,U);
title(strcat('\Deltaz=',num2str(delz),'z_r=',num2str(zprop(M)),'\psi_m_a_x^2=',num2str(
umax(M+1)^2)));
xlabel('Beam Intensity')
xlabel('r')
figure
waterfall(Zprop,Fr,U);
title(strcat('\Deltaz=',num2str(delz),'z_r
=',num2str(zprop(M)),'\psi_m_a_x^2=',num2str(umax(M+1)^2)));
xlabel('Beam Intensity')
xlabel('r')
figure
plot(zprop,umax.^2)
title(strcat('\psi_m_a_x^2:Plot vs. Propagation dist z' ',z_r=',num2str(zr)));
ylabel('Beam Intensity')
xlabel('z')
Ef=sum(abs(u).^2.*r1n.^2)
clear all
%*****

```

## **B.2.3 Dispersion Management in 2 and 3D**

### **B.2.3.1 2D Case**

```

%*****
% Yu method for Hankel transform applied on alternating dispersion media beams
% NLS:  $i \frac{du}{dz} + \frac{1}{2} f(z) (u_{rr} + \frac{1}{r} u_r) + |u|^2 u = 0$ 

```

```

%-----
% beta=number of cycles
% period=length of one cycle, L+=period*Deltaz*duty;
clear all;
load jnR1_10R2_20;
R1=40;
f0=[-3,5];
delz0=0.005;
M=800;
beta=200;
period=M/beta;
umax(1)=1.5;
w0=1;
duty=0.5;
mm=0;
R2=200/R1;
S=2*pi*R1*R2;
N=length(jn);
S=jn(length(jn))+jn(2)-jn(1);
%C=2/S*besselj(0,(jn*jn')/S).*(abs(besselj(1,jn).^(-1))*(abs(besselj(1,jn).^(-1))))';
load Yucmatrix200;
r1n=jn/(2*pi*R2);
r2m=jn/(2*pi*R1);
LL=M/20;
f1=umax(1)*exp(-r1n.^2/(2*w0^2));
f1(length(f1))=0;
u0r=[flipud(f1);f1];
fr=[-flipud(r1n);r1n];
% figure
% plot(fr,u0r,'b');
% title(strcat('\Deltaz_0=',num2str(delz0),'\psi_0 =4*exp(-r^2)'));
% ylabel('Beam Intensity')
%-----
for m=1:M
    if period*duty/2<=rem(m,period)& rem(m,period)< period-period*duty/2
        f(m)=f0(2);
    else
        f(m)=f0(1);
    end
end
t=[0:1:M-1]*delz0;
%-----
u=f1;
E0=sum(abs(f1).^2.*r1n)
zprop(1)=0;
delz=delz0;

```

```

for m=1:1:M-1
    zprop(m+1)=zprop(m)+delz;
    w=exp(-i*f(m)*4*pi^2*r2m.^2*delz/4);
    hu=yfht(u,C,jn,R1,R2,0).*w;
    u=yfht(hu,C,jn,R1,R2,1);
    u(length(u))=0;
    uint=(u.*conj(u)+conj(u).*u)/2;
    qr=exp(i*uint*delz);
    u=u.*qr;
    hu=yfht(u,C,jn,R1,R2,0).*w;
    u2=yfht(hu,C,jn,R1,R2,1);
    u2(length(u2))=0;
    umax(m+1)=abs(u2(1));
    if rem(m,LL)==0
        mm=mm+1;
        ur=[flipud(u2);u2];
        U(:,mm+1)=abs(ur);
        E=sum(abs(u2).^2.*r1n)
    end
    u=u2;
end
fr=[-flipud(r1n);r1n];
zr=zprop(length(zprop));
U(:,1)=u0r;
SS=size(U);
[Fr,Zprop]=meshgrid(linspace(0,zr,SS(2)),fr);
% figure
% mesh(Zprop,Fr,U);
% title(strcat('\Deltaz=',num2str(delz),',z_r
=',num2str(zprop(M)),',\psi_m_a_x=',num2str(umax(M))));
% xlabel('Beam Amp')
% xlabel('r')
figure
waterfall(Zprop,Fr,U);
title(strcat('\Deltaz=',num2str(delz),',z_r=',num2str(zprop(M)),',\psi_m_a_x=',num2str(umax(M))));
xlabel('Beam Amp')
xlabel('r')
figure
subplot(2,1,1);
plot(t,f);
subplot(2,1,2);
plot(zprop,umax)
title(strcat('\psi_m_a_x:Plot vs. Propagation dist z',',z_r=',num2str(zr)));
ylabel('Beam Amp')
xlabel('z')

```

```
Ef=sum(abs(u).^2.*r1n)
```

```
clear all
```

```
%*****
```

### B.2.3.2 3D Case

```
%*****
```

```
% Sicairos method for spherical Bessel transform applied on optical bullets using the  
NLS eq
```

```
% applied on alternating dispersion media using the NLS eq
```

```
% NLS:  $i \frac{du}{dz} + f(z)/2 * (d^2/dr^2 + (D-1)/r * d/dr)u + |u|^2 u = 0$ 
```

```
% beta=number of cycles
```

```
% period=length of one cycle, L+=period*Deltaz*duty;
```

```
clear all;
```

```
R1=40;R2=20;
```

```
M=1800;
```

```
beta=600;
```

```
period=M/beta;
```

```
duty=0.5;
```

```
delz0=0.005;
```

```
f0=[-5,3];
```

```
w0=10;
```

```
umax(1)=1;
```

```
mm=0;
```

```
L=M/20;
```

```
S=2*pi*R1*R2;
```

```
mu=1/2;
```

```
jn=pi*[1:1:2*R1*R2]';
```

```
N=length(jn);
```

```
S=jn(length(jn))+jn(2)-jn(1);
```

```
% C=2/S*besselj(mu,(jn*jn')/S).*(abs(besselj(mu+1,jn).^(-1))*(abs(besselj(mu+1,jn).^(-1)))));
```

```
load Scmatrix800;
```

```
r1n=jn/(2*pi*R2);
```

```
r2m=jn/(2*pi*R1);
```

```
f1=umax(1)*exp(-r1n.^2/(2*w0^2));
```

```
f1(length(f1))=0;
```

```
%-----
```

```
for m=1:M
```

```
    if period*duty/2<=rem(m,period)& rem(m,period)< period-period*duty/2
```

```
        f(m)=f0(2);
```

```
    else
```

```
        f(m)=f0(1);
```

```
    end
```

```
end
```

```
t=[0:1:M-1]*delz0;
```

```
% -----
```

```

%BPM method
u0r=[flipud(f1);f1];
% figure
% plot([-flipud(r1n);r1n],u0r,'b');
% title(strcat('\Deltaz_0=',num2str(delz0),'\psi_0 =',num2str(umax(1)),'*exp(-
r^2/2w_0^2)'));
% ylabel('Beam Amplitude')
u=f1;
E0=sum(abs(f1).^2.*r1n.^2)
zprop(1)=0;
delz=delz0;
for m=1:M-1
    zprop(m+1)=zprop(m)+delz;
    w=exp(-i*f(m)*4*pi^2*r2m.^2*delz/4);
    u=r1n.^(1/2).*u;
    hu=SSBT(u,C,jn,R1,R2,0,mu).*w;
    u=r1n.^(-1/2).*SSBT(hu,C,jn,R1,R2,1,mu);
    % nonlinear part
    uint=(u.*conj(u)+conj(u).*u)/2;
    qr=exp(i*uint*delz);
    u=u.*qr;
    % linear part
    u=r1n.^(1/2).*u;
    hu=SSBT(u,C,jn,R1,R2,0,mu).*w;
    u2=r1n.^(-1/2).*SSBT(hu,C,jn,R1,R2,1,mu);
    u2(length(u2))==0;
    umax(m+1)=abs(u2(1));
    if rem(m,L)==0
        mm=mm+1;
        ur=[flipud(u2);u2];
        U(:,mm+1)=abs(ur);
    %    figure
    %    plot(fr,abs(ur).^2,'b');
    E=sum(abs(u2).^2.*r1n.^2)
    end
    u=u2;
end
fr=[-flipud(r1n);r1n];
zr=zprop(length(zprop));
U(:,1)=u0r;
SS=size(U);
[Fr,Zprop]=meshgrid(linspace(0,zr,SS(2)),fr);
% figure
% mesh(Zprop,Fr,U);
%title(strcat('\Deltaz=',num2str(delz),',z_r=',num2str(zprop(M)),',\psi_m_a_x=',num2str(
umax(M))));

```

```

% xlabel('Beam amplitude')
% xlabel('r')
figure
waterfall(Zprop,Fr,U);
title(strcat('\Deltaz=',num2str(delz),',z_r=',num2str(zprop(M)),',\psi_m_a_x=',num2str(u
max(M))));
xlabel('Beam Amplitude')
xlabel('r')
figure
subplot(2,1,1);
plot(t,f);
subplot(2,1,2);
plot(zprop,umax)
title(strcat('\psi_m_a_x:Plot vs. Propagation dist z' ',z_r=',num2str(zr)));
ylabel('Beam Amplitude')
xlabel('z')
Ef=sum(abs(u).^2.*r1n.^2)
clear all
%*****

```

## **B.2.4 Nonlinearity Management in 2 and 3-D**

### **B.2.4.1 2D Case**

```

%*****
% Yu method for Hankel transform applied on alternating Kerr media beams using the
NLS Eq
% NLS: $i\frac{du}{dz} + \frac{1}{2}(\frac{d^2}{dr^2} + (D-1)/r \frac{d}{dr})u + \gamma(z)|u|^2u = 0$ 
%-----
clear all;
load jnR1_10R2_20;
%%rem(m,2)==0
delz0=0.01;
M=320;
beta=20;% beta=number of cycles
gamma0=[3,-1];
period=M/beta;% period=length of one cycle, L+=period*Deltaz*duty;
umax(1)=4.2;
w0=0.5;
duty=0.5;
mm=0;
R1=20;
R2=200/R1;
S=2*pi*R1*R2;
N=length(jn);
S=jn(length(jn))+jn(2)-jn(1);
%C=2/S*besselj(0,(jn*jn')/S).*(abs(besselj(1,jn).^(-1))*(abs(besselj(1,jn).^(-1))))';

```

```

load Yucmatrix200;
r1n=jn/(2*pi*R2);
r2m=jn/(2*pi*R1);
LL=M/20;
f1=umax(1)*exp(-r1n.^2/(2*w0^2));
f1(length(f1))=0;
u0r=[flipud(f1);f1];
fr=[-flipud(r1n);r1n];
figure
plot(fr,u0r,'b');
title(strcat('\Deltaz_0=',num2str(deltz0),'\psi_0 =4*exp(-r^2)'));
ylabel('Beam Intensity')
%-----
for m=0:M-1
    if period*duty/2<=rem(m,period)& rem(m,period)< period-period*duty/2
        gamma(m+1)=gamma0(2);
    else
        gamma(m+1)=gamma0(1);
    end
end
%-----
u=f1;
E0=sum(abs(f1).^2.*r1n)
zprop(1)=0;
delz=deltz0;
for k=1:1:M
    zprop(k+1)=zprop(k)+delz;
    w=exp(-i*4*pi^2*r2m.^2*delz/2);
    hu=yfht(u,C,jn,R1,R2,0).*w;
    u=yfht(hu,C,jn,R1,R2,1);
    u(length(u))=0;
    uint=(u.*conj(u)+conj(u).*u)/2;
    qr=exp(i*gamma(k)*uint*delz);
    u=u.*qr;
    hu=yfht(u,C,jn,R1,R2,0).*w;
    u2=yfht(hu,C,jn,R1,R2,1);
    u2(length(u2))=0;
    umax(k+1)=abs(u2(1));
    if rem(k,LL)==0
        mm=mm+1;
        ur=[flipud(u2);u2];
        U(:,mm+1)=abs(ur);
        E=sum(abs(u2).^2.*r1n)
    end
    u=u2;
end

```

```

fr=[-flipud(r1n);r1n];
zr=zprop(length(zprop));
U(:,1)=u0r;
SS=size(U);
[Fr,Zprop]=meshgrid(linspace(0,zr,SS(2)),fr);
figure
waterfall(Zprop',Fr',U');
title(strcat('\Deltaz=',num2str(deltz),',z_r=',num2str(zprop(M)),',\psi_m_a_x=',num2str(u
max(M+1)))));
xlabel('Beam Amp')
xlabel('r')
figure
plot(zprop,umax)
title(strcat('\psi_m_a_x:Plot vs. Propagation dist z' ',z_r=',num2str(zr)));
ylabel('Beam Amp')
xlabel('z')
Ef=sum(abs(u).^2.*r1n)
clear all
%*****

```

#### **B.2.4.2 3D Case**

```

%*****
% Sicairos method for spherical Bessel transform applied on optical bullets using the
NLS eq
% applied on alternating kerr media using the NLS eq
% NLS: i*du/dz+1/2*(d^2/dr^2+(D-1)/r*d/dr)u+gamma(z)*|u|^2*u=0
clear all;
R1=50;R2=20;
deltz0=0.01;
gamma0=[-3,5];
M=2000;
beta=50;% beta=number of cycles
period=M/beta;% period=length of one cycle, L+=period*Deltaz*duty;
duty=0.5;
umax(1)=0.18;
w0=15;
mm=0;
L=M/20;
S=2*pi*R1*R2;
mu=1/2;
jn=pi*[1:1:2*R1*R2]';
N=length(jn);
S=jn(length(jn))+jn(2)-jn(1);
% C=2/S*besselj(mu,(jn*jn')/S).*(abs(besselj(mu+1,jn).^(-1))*(abs(besselj(mu+1,jn).^(-
1)))));
load Scmatrix1000;

```



```

r1n=jn/(2*pi*R2);
r2m=jn/(2*pi*R1);
f1=umax(1)*exp(-r1n.^2/(2*w0^2));
f1(length(f1))=0;
%-----
for m=1:M
    if(period/2<=rem(m,period))&(rem(m,period)<period)
        gamma(m)=gamma0(2);
    else
        gamma(m)=gamma0(1);
    end
end
t=[0:1:M-1]*delz0;
u=f1;
E0=sum(abs(f1).^2.*r1n.^2)
zprop(1)=0;
delz=delz0;
for k=1:M
    zprop(k+1)=zprop(k)+delz;
    w=exp(-i*4*pi^2*r2m.^2*delz/2);
    u=r1n.^(1/2).*u;
    hu=SSBT(u,C,jn,R1,R2,0,mu).*w;
    u=r1n.^(-1/2).*SSBT(hu,C,jn,R1,R2,1,mu);
    % nonlinear part
    uint=(u.*conj(u)+conj(u).*u)/2;
    qr=exp(i*gamma(k)*uint*delz);
    u=u.*qr;
    % linear part
    u=r1n.^(1/2).*u;
    hu=SSBT(u,C,jn,R1,R2,0,mu).*w;
    u2=r1n.^(-1/2).*SSBT(hu,C,jn,R1,R2,1,mu);
    u2(length(u2))=0;
    umax(k+1)=abs(u2(1));
    if rem(k,L)==0
        mm=mm+1;
        ur=[flipud(u2);u2];
        U(:,mm+1)=abs(ur);
    %    figure
    %    plot(fr,abs(ur).^2,'b');
    E=sum(abs(u2).^2.*r1n.^2)
    end
    u=u2;
end
fr=[-flipud(r1n);r1n];
zr=zprop(length(zprop));
U(:,1)=u0r;

```

```

SS=size(U);
[Fr,Zprop]=meshgrid(linspace(0,zr,SS(2)),fr);
figure
waterfall(Zprop,Fr,U);
title(strcat("\Deltaz=",num2str(deltz),'z_r=',num2str(zprop(M)),'\psi_m_a_x=',num2str(u
max(M+1))));
xlabel('Beam Amplitude')
xlabel('r')
figure
plot(zprop,umax)
title(strcat("\psi_m_a_x:Plot vs. Propagation dist z' ',z_r=',num2str(zr)));
ylabel('Beam Amplitude')
xlabel('z')
Ef=sum(abs(u).^2.*r1n.^2)
clear all
%*****

```

R702032871